HgTe nanocrystals and graphene quantum dots for THz optoelectronics : intraband absorption, carrier dynamics and coherent THz emission

Thibault Apretna

SORBONNE UNIVERSITÉ

THÈSE DE DOCTORAT
DE SORBONNE UNIVERSITÉ

Spécialité : Physique

École doctorale nº397: Physique et Chimie des Matériaux

réalisée sous la direction de Juliette MANGENEY

au Laboratoire de Physique de l'Ecole Normale Supérieure

LPENS
LABORATOIRE DE PHYSIQUE
DE L'ÉCOLE NORMALE SUPÉRIEURE

présentée par

Thibault APRETNA

Sujet de la thèse :

HgTe nanocrystals and graphene quantum dots for THz optoelectronics : Intraband absorption, carrier dynamics and coherent THz emission

soutenue le 28 mars 2023

devant le jury composé de :

M.	LAMPIN Jean-François,	Dir. de recherche,	IEMN,	Président
M.	SAUVAGE Sébastien,	Dir. de recherche,	C2N,	Rapporteur
M.	TEPPE Frédéric,	Dir. de recherche,	L2C,	Rapporteur
M.	FERREIRA Robson,	Dir. de recherche,	LPENS,	Examinateur
M.	LHUILLIER Emmanuel,	Dir. de recherche,	INSP,	Examinateur
Mme	MANGENEY Juliette,	Dir. de recherche,	LPENS,	Directrice de thèse

Remerciements

De part l'unicité du sujet qu'elle traite, une thèse est un exercice qui se veut bien souvent solitaire, ce qui vient s'ajouter à l'ensemble des difficultés inhérentes au doctorat. Ainsi, s'entourer des bonnes personnes, tant d'un point de vue scientifique que personnel me semble indispensable au bon déroulement d'une thèse. J'ai pour ma part eu la chance d'être entouré de nombreuses personnes qui m'ont grandement aidé dans ce travail de thèse et qui ont permis que celui-ci aboutisse. Aussi, je souhaiterais prendre le temps de remercier tous ceux sans qui cela n'aurait pas été possible.

Tout d'abord, je tiens à remercier ma directrice de thèse Juliette, pour son encadrement durant ces trois années plein de bienveillance et d'enthousiasme, pour sa confiance dans ma manière d'organiser mes projets de recherche, mais aussi pour son recul scientifique, sa capacité à identifier les points bloquants dans les expériences et à intuiter les aspects à creuser.

Je souhaiterais ensuite remercier les membres de mon jury pour leurs différentes contributions dans mon travail de thèse. Tout d'abord les deux rapporteurs, Sébastien Sauvage et Frédéric Teppe pour leur lecture minutieuse ayant permis d'affiner les travaux présentés ci-dessous et de mettre en lumière de nombreuses perspectives. Je remercie également les examinateurs, Jean-Francois Lampin pour ses commentaires et ses questions pertinentes, Emmanuel Lhuillier de m'avoir permis d'étudier ces nanocristaux qui n'ont eu de cesse de me surprendre et enfin Robson Ferreira pour sa pédagogie limpide et son travail théorique autour de la modélisation des nanocristaux de HgTe, ou plutôt ces "gros bébés" pour le citer.

Je tiens a remercier également les chercheurs du laboratoire avec qui j'ai eu la chance de travailler et d'échanger : Sukhdeep pour ses facultés de chef d'orchestre dans ce grand concert que représente une salle de manip, Francesca pour ses explications limpides et Louis-Anne pour sa disponibilité et son enthousiasme.

Je remercie les différentes équipes du laboratoire qui ont joué un rôle indispensable dans la mise en place de mes expériences : L'équipe de salle blanche, Michaël Rosticher, José Palomo et Aurélie Pierret pour leur disponibilité et leur investissement dans le développement des différents processus de fabrication d'échantillons. Merci à l'équipe de cryogénie - Florent Perrin et Olivier Andrieu, grâce à qui je n'ai jamais manqué d'hélium même au milieu de crises géopolitiques ! Merci a Pascal Morfin, Arnaud Leclercq et Pascal Pace d'avoir permis à mes échantillons d'être au bon endroit, ni trop chaud ni trop froid.

Je remercie les personnes de l'administration du laboratoire et de l'ED397 de ne pas avoir exacerbé ma phobie admistrative et tout particulièrement à Hakima Si-Bachir de m'avoir guidé si adroitement à travers les arcanes d'Adum.

Merci à tous les doctorants et post-doctorants que j'ai eu la chance de côtoyer : Tout

d'abord mon mentor Sylvain qui m'a transmis la fibre de la spectroscopie résolue en temps dans une ambiance méditerranéenne des plus agréables. Niloufar pour sa confiance et sa délicatesse. Romaine, avec qui j'ai pu partager mon amour pour les peluches. Simon pour son sens physique aussi juste que ses traits d'esprit. Enzo pour sa jovialité même dans les plus sombres journées d'alignement optique. Sans oublier Elisa, Aurélie, Pavel, Solen, Joaquin, Jacques, Minoosh, Martin, Chao, Seonggil, Pan-hui, Hadrien, Adrien, Anna, Etienne et Ali. Merci à mes deux poulains Bastien et Ismaël avec qui j'ai pris beaucoup de plaisir à travailler ! Merci à Virginia du pot de m'avoir servi et re-servi avec tant d'abondance au détriment de ma productivité postméridienne.

Je souhaiterais bien sûr remercier mes amis qui m'ont permis de voir mon doctorat sous autant d'angles différents que leurs profils sont riches et variés : Guilhem, pour son prestige, sa ponctualité chaque midi au pot, mais surtout pour sa curiosité et son bagoût ! La fine équipe de Montpellier : Florent, Pierre-Louis, Arnaud, Antonin, Manon, Anna, Pauline et Agathe pour avoir prétendu comprendre ce sur quoi je travaillais. Les amis de Centrale : Andy, Emeric, Céline, Anne-Claire, Michelle, Léo, Karim, Paul, Anais pour avoir également prétendu comprendre ce sur quoi je travaillais. Merci également aux barcelonais Réjane et Adrien et à Bakr.

Merci à McFly, Guigui, Adrien et toute l'équipe de Nation qui m'ont permis de contre-balancer la lourdeur des équations par la légèreté d'une planche de bois et de quatre roues sous les pieds.

Je remercie évidemment ma famille pour leur soutien. Ma mère pour toutes ces longues discussions après lesquelles on se sent vif. La branche mexicaine avec mon frère Yaya, ma belle soeur Dayana et mes neveux Mateo et Esteban avec qui passer du temps est si ressourçant. Merci a Badr de renforcer la part scientifique de notre famille. Je ne pourrais remercier suffisament ma soeur Pauline, qui me connait mieux que moi même et qui a toujours été d'un soutien sans faille. Un merci tout particulier à mon neveu Shems-Eddine qui a assisté à sa première soutenance de thèse à l'âge de deux mois.

Enfin, je souhaiterais remercier *my partner in crime* Julie, qui m'accompagne si bien depuis des années, qui a su m'ouvrir les yeux sur mon besoin de poursuivre ce projet, et qui s'est montrée indispensable dans la réalisation de celui-ci. Merci pour tout.

PS : Je souhaiterais remercier Coherent d'avoir arrêté de produire le Micra-10, épargnant ainsi aux futurs doctorants les problèmes d'un laser femtoseconde peu robuste. Je remercie également Newport et Thorlabs pour les boîtes de photonic food et de lab snacks, même si je persiste a croire que les paquets de TUC n'étaient pas indispensables.

Introduction

Over the last century, the developments performed in the field of electromagnetic waves have given birth to a remarkably large variety of technologies. Indeed, applications such as 5G communication, X-ray imaging, or LCD screens make all use of electromagnetic waves. Yet, a noticeable difference between these waves is their various frequencies. When looking at the electromagnetic spectrum, we can note that the frequency range (i.e. the energy range) of the electromagnetic applications spans over more than 10 orders of magnitude. In order to cover such a wide range of frequencies and energies, various technologies have been developed. In particular, a common distinction can be made between two well-established fields : On the one hand, we have electronics-based technologies used for low frequency domains such as radio frequencies and microwaves. On the other hand, we find photonics technologies, which dominate higher frequency domains like visible or infrared. However electronics and optics do not overlap, and are separated by an intermediate spectral range which is defined as the THz domain. This specific spectral range, which lies typically from 0.1 THz and 30 THz, cannot be explored and exploited with conventional electronic or optic devices, so that it is often referred to as the "THz gap". Indeed, devices based on existing technologies in the microwave or optical fields suffer a drop in efficiency when pushed to the THz spectral range. For example, there are fundamental limits to high frequency electronic systems due to the limited switching time of transistors, or to lasers emitting at lower frequencies due to material band gaps. As a result, the THz technology does not have the same level of maturity as its bordering domains. Nevertheless, this spectral domain has aroused strong interest of the scientific community for several decades owing to its promising applications.

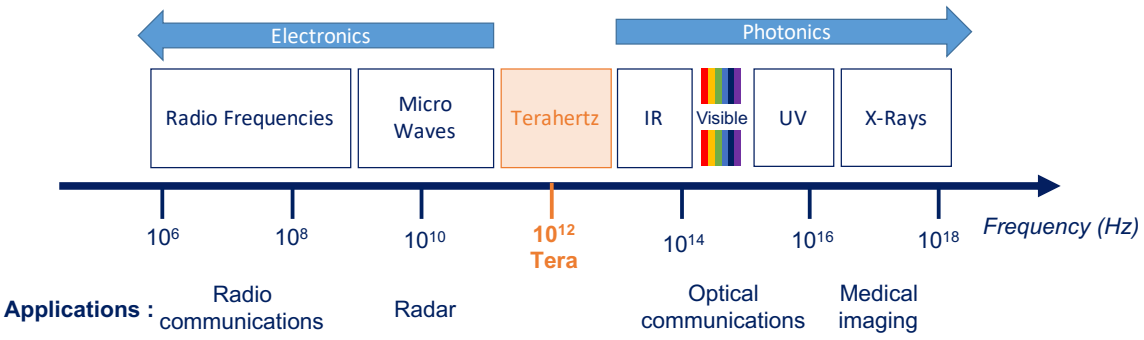

Fig. 0.1 *Diagram of the elecromagnetic spectrum.*

For instance, from the telecommunication perspective, THz frequencies represent an unexploited spectral range that could both solve the upcoming problem of saturated telecom-

munication bandwidths, and enable ultrafast wireless data transfer. Also the low energy of THz photons make them non-ionizing and therefore suitable for bio-medical applications. Numerous investigations regarding various applications such as skin cancer diagnosis, illicit drug detection in mails, security screening at airport, semi-conductor inspection and characterization have therefore already been reported [1–6]. From fundamental science perspective, many elementary process in matter, such as the interaction of electrons, spins and phonons as well as rotational modes of molecules possess resonances frequencies in the THz spectral range. Therefore, spectroscopy at THz frequencies has become an exciting technique for probing and characterizing a variety of low-energy physical phenomena [7], that are relevant for a wide range of disciplines including physics, chemistry, astronomy, and medicine.

This plethora of potential applications has motivated intense research devoted to the development of components, devices and instrumentation operating at THz frequencies. As a consequence, a wide variety of THz sources and detectors have emerged, that now successfully cover the entire THz domain. However, while these technological developments have allowed for active research in the THz domain, current THz sources still suffer from drawbacks that prevent their proliferation outside laboratory. For example, as mentioned earlier, technologies based on the adaptation of microwaves and infrared sources, such as IMPATT diodes or semiconductor lasers, are pushed to their limits at THz frequencies. Other available alternatives of THz emitters, such as photoconductive antennas or quantum cascade lasers (QCL), involve either femtosecond lasers or cryogenic temperatures and are thus relatively bulky, which is not compatible with commercial applications. The research of new materials and concepts as well as the development of novel technologies are thus essential to exploit these specific THz waves. In this challenging context, my thesis project aims at evaluating the potential of innovative quantum dots for the development of new optoelectronic emitters operating at THz frequencies.

Quantum dots are nanomaterials in which charge carriers are confined in the three directions of space. The carrier confinement leads to a complete discretization of the energy levels of the quantum dot, as in an isolated atom. These "artificial atoms" are of great interest because of their adjustable optical properties according to the size of the quantum dot. Thus, quantum dots have been widely exploited over the last decades for the development of optoelectronic devices operating from the ultraviolet down to the mid-infrared spectral range. However, quantum dots with optical properties in the THz range are still in their infancy, due to several technological and instrumental challenges associated with the very low energy of THz photons. Indeed, while most optoelectronic applications of quantum dots are based on the tunability of their interband transitions, this approach is hard to implement in the THz spectral range, even for materials with a sufficiently narrow gap, due to thermal broadening of carrier populations which tends to equalize the populations of the two levels involved in a THz transition and thus to reduce the interband process efficiency. Also, to activate interband transitions at THz frequencies, the Fermi level of the quantum dot, should lie very close to zero which is hard to technologically implement and control. Moreover, to obtain energy level spacings between quantized states that match the low energy of THz photons, quantum dots must be relatively large, typically several tens of nm, which raises issues regarding their fabrication.

In my thesis work, we study two new types of large quantum dots, HgTe nanocrystals

and graphene quantum dots. These two material systems have the advantage of being zero bandgap semiconductors (semi-metals), which is favorable to the study of low energy transitions. In addition, the fabrication of both types of quantum dots is relatively accessible today, which should enable the exploitation of the flexibility of electronic state engineering of quantum dots to tune their optical properties at THz frequencies.

The first part of this PhD work concerns the study of **large HgTe nanocrystals (NCs)**. This study was motivated by the recent breakthrough reported by Goubet *et al.* [8] of a colloidal synthesis procedure allowing the production of large HgTe nanocrystals with a typical size up to a hundred nanometers. From technological perpective, colloidal synthesis is particularly attractive as it is low-cost and colloidal nanocrystals can be easily manipulated. The most attractive optical feature of large HgTe nanocrystals is the presence of an absorption resonance at low frequency, that can be tuned from 60 THz down to 4 THz. This absorption is attributed to intraband transitions (the 0 D counterpart of the intersubband transition in the doped quantum well structure), that are made possible by the self-doped nature of these large nanocrystals. The work presented here aims at exploring the low frequency absorption and the carriers dynamics in these promising HgTe nanocrystals as well as their potential for coherent THz emission, properties that are crucial for their possible integration into futur THz optoelectronic devices.

The second part of this PhD work is devoted the study of **large graphene quantum dots (GQD)**. Graphene is a 2D material which exhibits very peculiar electronic properties such as a gapless band structure or a linear dispersion relation that sharply contrasts with the parabolic structure observed in most semiconductors and a high carrier mobility. Its remarkable properties have already aroused significant interest in the THz scientific community so that the development of graphene based THz devices is intensively investigated [9–11]. Most notably, the study of hot carrier dynamics in graphene has demonstrated the onset of a population inversion at low energy under intense optical excitation, suggesting that THz lasing could be possible [12]. However, Auger recombination processes in graphene limit the lifetime of this population inversion to a few hundred femtoseconds, making it suitable only for amplification of short pulses [13, 14]. Our motivation to study graphene quantum dots comes from their great potential to effectively address this current limitation. The strategy adopted here is to take advantage of the quantum confinement effects to tailor the carrier dynamics in graphene quantum dots. The full discretization of electronic states could efficiently inhibit Auger recombination processes by limiting the available final states. In this context, the objectives of this PhD project are to study large GQDs in order to improve the understanding of quantum confinement effects in these large circular nanodisks on their optical properties at THz frequencies.

The present thesis is organized in five chapters :

Chapter 1 provides a short overview of the field of semiconductor nanocrystals. Based on the particule in a box model, we give first insights on the effects of spatial confinement on the energy levels of electrons in conventional semiconductors where the effective mass model applies. We then present the different types of fabrication of nanocrystals and detail the characteristics and advantages of colloidal synthesis. This is followed by a brief review of nanocrystals applications. The last part of the chapter presents HgTe nanocrystals and the

recent development of large HgTe NCs that show optical absorption at very long wavelength, i.e. in the THz spectral range.

Chapter 2 presents an in-depth study of the optical properties of large HgTe nanocrystals. Based on THz-Time Domain Spectroscopy (TDS) and Fourier Transform Infrared Spectroscopy (FTIR) measurements, we demonstrate a broad resonance in the absorption spectrum of these nanocrystals, centered around 4.5 THz. We then develop a microscopic model and fully interpret this absorption at THz frequencies as the result of multiple intraband transitions of single carriers between quantized electronic states. The last part of the chapter is devoted to the study of the influence of the temperature on the THz absorption.

Chapter 3 concerns the study of the photoresponse and the dynamics of hot carriers in HgTe nanocrystals. We present optical-pump THz-probe measurements performed on large HgTe nanocrystals. We report on a relatively long recombination time of non-equilibrium carriers, of the order of a few picoseconds, and then interpret the different relaxation and recombination processes at stake in the hot carrier dynamics. We finally study the influence of the temperature on the hot carrier dynamics.

Chapter 4 presents coherent THz emission from HgTe nanocrystals under femtosecond optical excitation. We detail measurements performed under various experimental configurations. We then develop a formalism describing the second-order nonlinear processes that allows us to determine the physical phenomena involved in the measured THz coherent emission.

Chapter 5 is devoted to theoretical and experimental work on the optical properties at THz frequencies of large graphene quantum dots. The beginning of the chapter provides a brief overview of the properties of monolayer graphene and motivates the study of GQDs. We then present the theoretical investigation of the electronic and optical properties of large circular GQDs based on a tight-binding modeling, which predicts an intraband absorption resonance from large GQDs in the THz spectral range. The last part of the chapter addresses the experimental work performed in order to measure this predicted absorption resonance. We start by presenting the clean-room process that has been developed for the fabrication of arrays of large circular GQD. We then present the issues encountered in probing small absorption feature at THz frequencies and the optimisation we performed to improve the spectroscopic set-up. Finally, we report on the transmission measurements of an array of large GQDs at THz frequencies.

Contents

Chapter 1

Introduction to Nanocrystals

With the increasing deployment of nanotechnology and nanomaterials in modern society, nanocrystals (NCs) are expected to play a central role in the next generation of devices such as liquid crystal displays, light-emitting diodes, lasers, and luminescent solar concentrators. This statement is the result of several decades of growth development, which now allows the synthesis of a wide range of materials in the form of NCs. Technological advances also enable control of NCs chemistry and quantum confinement of carriers, and thus fine-tuning of their optical and electrical characteristics. NCs are operating in a spectral range from ultraviolet to mid-infrared, and are currently integrated in a wide variety of devices (solar cells, LEDs) with some mass applications. NCs are becoming a viable alternative to traditional semiconductors offering a high spectral tunability combined with ease of processing and transfer (spin coating, inkjet printing). However, despite these intensive efforts devoted to the synthesis and the integration of a large variety of NCs, NCs with optical properties in the THz spectral range remain early bird of development. A main part of my doctoral project aims at evaluating the potential of state-of-the-art HgTe NCs for the development of optoelectronic devices operating in the THz spectral range.

In this introductory chapter, I will present the electronic structures of NCs. Then, I will briefly present the different methods to synthesis NCs. I will discuss on the application fields of semiconducting NCs. At last, I will present recent developement of large NCs that have revealed optical absorption at very long wavelength, in the THz spectral range. All the results that are presented in these sections are already well known. My objective is to clarify the basic concepts and the general context of semiconducting NCs.

1.1 Electronic properties of Nanocrystals

The study of an isolated atom reveals that its electrons can only occupy discrete energy states. In the case of a crystal, because of the periodic spatial arrangement of atoms, the energy levels are arranged into bands. These bands, fully described by the band theory, represent ranges of accessible energy states and are separated by gaps of forbidden energies for electrons. One can define two important bands, relevant for electronics and optoelectronics, the valence band and the conduction band that are the bands near the Fermi level of the crystal. In a semiconductor or insulator crystal, the Fermi level is surrounded by a band

gap, E_{bulk}, referred to as the band gap to distinguish it from the other band gaps in the band structure. The closest band above the band gap is called the conduction band, E_{CB}, and the closest band beneath the band gap is called the valence band, E_{VB}. In a semimetal, the conduction and the valence bands overlap and the bandgap energy is zero. In a metal, the Fermi level lies within one or more allowed bands and the distinction between valence and conduction bands is meaningless.

1.1.1 Dispersion relation of bulk materials

The relation between the energy of an electron and its wavevector k is described by the dispersion relation. In the case of a free electron, the dispersion relation is parabolic and expressed as $E = \hbar^2 k^2/(2m_e)$, with $\hbar$ the reduced Planck constant, k the electron wavevector, and m_e the electron mass. However, in the case where the electron is in a crystal, i.e. subject to the periodic potential of the crystal lattice, the potential of the crystal renormalizes this parabolic dependence. Considering a semiconductor with a direct band gap at the Γ point, and defining the origin of energy at the top of the valence band, the relation dispersions for the electrons (i.e., in conduction band) and for the holes (i.e., invalence band) are then:

$$E_{CB}(k) = \frac{\hbar^2 k^2}{2m_e^*} + E_{bulk} \qquad E_{VB}(k) = -\frac{\hbar^2 k^2}{2m_h^*} \tag{1.1}$$

where m_e^* and m_h^* are the effective mass for electrons and holes respectively and E_{CB} and E_{VB}, the energy of the electronic states in the conduction and valence band respectively. Those parabolic bands are represented in Figure 1.2 by solid lines.

During the absorption of photons whose energy is higher than the band gap, an electron from the valence band is promoted to the conduction band. The electron/hole pair created by this process is bounded by the Coulombic interaction and called an exciton. The average distance between the two bound photo-generated charges is given by the Bohr model and called the exciton Bohr radius defined by :

$$a_0^* = \frac{\varepsilon_r}{m_{eh}^*}\frac{\varepsilon_0 h^2}{\pi e^2} \qquad \text{with} \qquad m_{eh}^* = \frac{m_e^* m_h^*}{m_e^* + m_h^*} \tag{1.2}$$

where ε_0 is the vacuum permittivity, ε_r the relative dielectric permittivity of the crystal and e the elementary charge.

When at least one of the dimensions of the crystal becomes smaller than the Bohr radius a_0^*, the crystal starts to exhibit quantum confinement effects.

1.1.2 Quantum confinement effects

To get insight in quantum confinement effect, let us consider a NC as a cubic box with size L of the order of magnitude of a_0. We derive the Schrödinger equation for a particle in an infinite potential box. The $\overrightarrow{e_x}$, $\overrightarrow{e_y}$ and $\overrightarrow{e_z}$ axis correspond to the cube edges as represented in Figure 1.1.a). The potential V is defined as follow :

$$V(x,y,z) = \begin{cases} 0 & \text{if } (x,y,z) \in [0,L]^3 \\ \infty & \text{otherwise} \end{cases}$$

We define $\overrightarrow{r} = x\overrightarrow{e_x} + y\overrightarrow{e_y} + z\overrightarrow{e_z}$. The wavefunction is cancelled when the potential is infinite, i.e. outside the box. When the potential energy is zero inside the box, the wavefunction obeys the time-independent Schrödinger equation for a particle of mass m_0 :

$$-\frac{\hbar^2}{2m_0}\nabla^2\psi(r) + V(r)\psi(r) = E\psi(r) \tag{1.3}$$

This equation can be modified for a particle of mass m_0 free to move in the 3-dimensional space with zero potential energy resulting in the quantum mechanical description of free motion in three dimensions:

$$-\frac{\hbar^2}{2m_0}\left(\frac{d^2\psi(r)}{dx^2} + \frac{d^2\psi}{dy^2} + \frac{d^2\psi}{dz^2}\right) = E\psi(r) \tag{1.4}$$

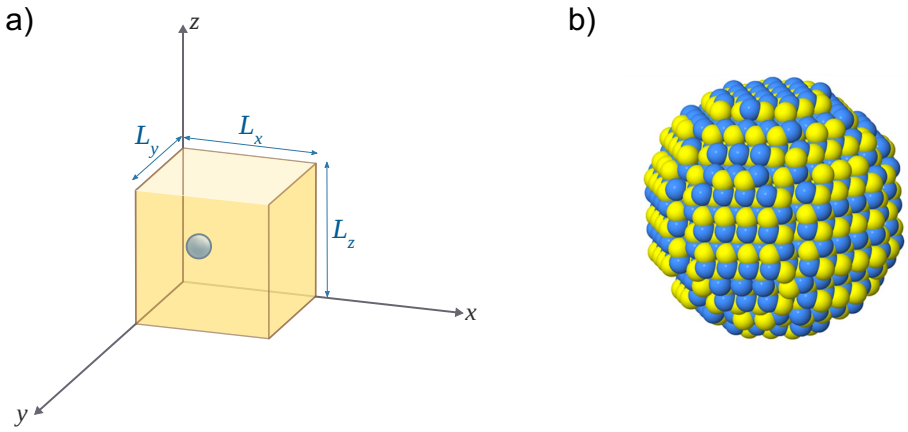

Fig. 1.1 *a) Scheme of a particle in a semiconductor cubic box of size L with infinite barriers. b) Scheme of the atomic structure of a nanocrystal.*

We use the separation of variables technique to solve this equation, which consists in writing the wavefunction as a product of individual function for each variable $\psi(x,y,z) = X(x)Y(y)Z(z)$, where each function X, Y, Z depends on its own variable only. We thus obtain :

$$\left(-\frac{\hbar^2}{2m_0X(x)}\frac{d^2X(x)}{dx^2}\right) + \left(-\frac{\hbar^2}{2m_0Y(y)}\frac{d^2Y(y)}{dx^2}\right) + \left(-\frac{\hbar^2}{2m_0Z(z)}\frac{d^2Z(z)}{dz^2}\right) = E \tag{1.5}$$

Since E is constant, each term has to be equal to its own constant so that :

$$-\frac{\hbar^2}{2m_0X(x)}\frac{d^2X(x)}{dx^2} = E_x \; ; \; -\frac{\hbar^2}{2m_0Y(y)}\frac{d^2Y(y)}{dx^2} = E_y \; ; \; -\frac{\hbar^2}{2m_0Z(z)}\frac{d^2Z(z)}{dz^2} = E_z \tag{1.6}$$

with $E_x + E_y + E_z = E$. Since the box is a cube, the three components E_x, E_y and E_z are equivalent.

We solve the first of the three equations using the boundary and normalization conditions. We find an infinite set of solutions for $X_n(x)$ with $n \in \mathbb{N}^*$ defined as:

$$X_n(x) = \begin{cases} \sqrt{\frac{2}{L}}\sin(\frac{n\pi x}{L}) & \text{if } 0 \leq x \leq L \\ 0 & \text{otherwise} \end{cases}$$

with the corresponding energy $E_{x_n} = \frac{n^2h^2}{8m_0L^2}$. Using normalization wavefunction equation for each variable, we find that the eigenfunctions inside the box are defined by a set of three quantum numbers (l,m,n) $\in \mathbb{N}^{*3}$ and have the following form :

$$\psi_{l,m,n}(r) = \sqrt{\frac{8}{L^3}} \sin(\frac{l\pi x}{L}) \sin(\frac{m\pi y}{L}) \sin(\frac{n\pi z}{L}) \tag{1.7}$$

the corresponding total energies are expressed as :

$$E_{l,m,n} = \frac{h^2}{8m_0} \left(\frac{l^2 + m^2 + n^2}{L^2} \right) \tag{1.8}$$

If now we consider a cubic box made of a crystal, the potential V is not null anymore and has the periodicity of the lattice. The parabolic effective mass approximation consists in the following approximation :

$$-\frac{\hbar^2}{2m_0}\nabla^2\psi(r) + V_{Lattice}(r)\psi(r) = E\psi(r) \iff -\frac{\hbar^2}{2m_e^*}\nabla^2\psi(r) = E\psi(r)$$

The corresponding wavevectors and energies are quantized and defined by :

$$E_{l,m,n} = \frac{\hbar^2\pi^2}{2m^*L^2}(l^2 + m^2 + n^2) \tag{1.9}$$

where m^* is either the effective electron (m_e^*) or hole (m_h^*) mass.

The energy of the particle is quantized and the lowest possible energy of a particle is not zero. The band gap energy of the NC, $E_{G_{QD}}$, is then modified by the quantum confinement and is expressed as :

$$E_{G_{NC}} = E_{bulk} + \frac{3\hbar^2\pi^2}{2m_e^*L^2} + \frac{3\hbar^2\pi^2}{2m_h^*L^2} = E_{G,Bulk} + \frac{3\hbar^2\pi^2}{2m_{eh}^*L^2} \tag{1.10}$$

where $m_{eh}^* = m_e^*m_h^*/(m_e^* + m_h^*)$. In the framework of this model, the Coulomb interaction between the electron and the hole is neglected because it is often very weak compared to the confinement energy. The spatial extension of the electron-hole pair is then limited by the size of the particle and not by the spatial extension of the Coulomb interaction.

The second term on the right hand side of Equation 1.10 is often referred to as the confinement energy E_C. One can note that $E_C(L) \propto \frac{1}{L^2}$. On Figure 1.2, we see the discretization of the energy levels in a semiconductor NC starting from the simplified band structure of the bulk material.

This simple model gives a good description of the tunability of the optical properties of NCs by varying their sizes. Indeed, as shown in Figure 1.3, by varying the size of the NC it is possible to tune the energy distribution of the electronic states, and therefore the energy of transitions between electronic levels. Besides, due to the large difference between the effective masses of electrons and holes, which makes the dispersion of the valence band generally much smaller than that of the conduction band, the energy states are closer together in the

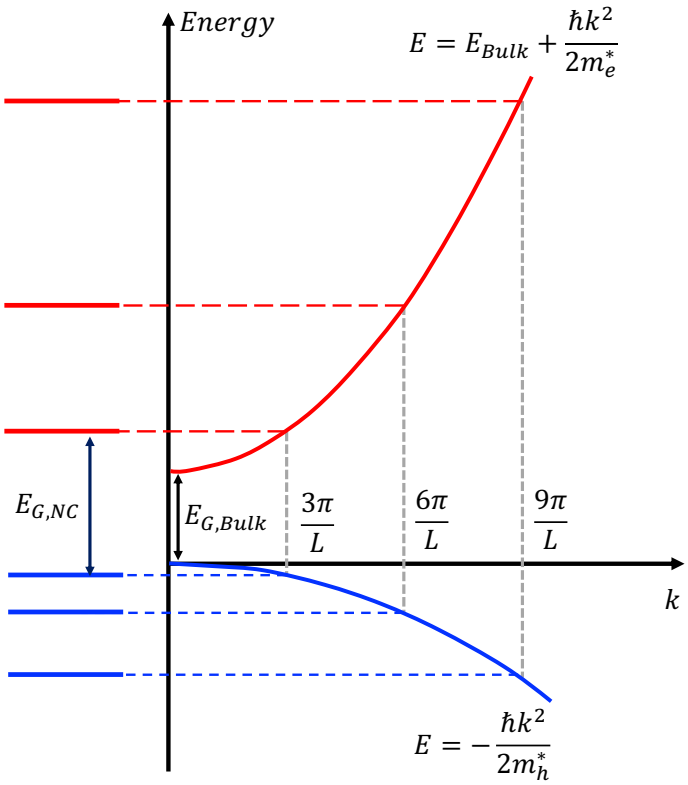

Fig. 1.2 *Band diagram of a semiconductor in the parabolic approximation (thick lines). Quantum confinement transforms the parabolic bands in discrete, non-dispersive levels for a cubic nanoparticle of length L.*

valence band and can often be considered as a quasi-continuum of states.

In this thesis work, we aim at studying the optical properties of NCs at low energy, i.e. the THz spectral range, and therefore large NCs with typical sizes of 80 nm - 100 nm will be investigated to address low energy transitions.

1.2 Synthesis of Nanocrystals

As described in the previous section, NCs offer a large and easy spectral tunability owing to quantum confinement effects. Their application fields have been largely extended over the past decades thanks to rapid progress realized in their synthesis. Two approaches exist for their synthesis 1.4. First, the "top-down" techniques which consist in creating a nanostructure of desired size starting from the bulk semiconductor. This is notably the case of lithographic or epitaxial growth techniques. These methods allow the production of large quantities of NCs with good control over the size and uniformity of the NCs. However, they require sophisticated and expensive equipment and highly specialized know-how. Also, these NCs can suffer other drawbacks like the difficulty to separate them from their substrates, or

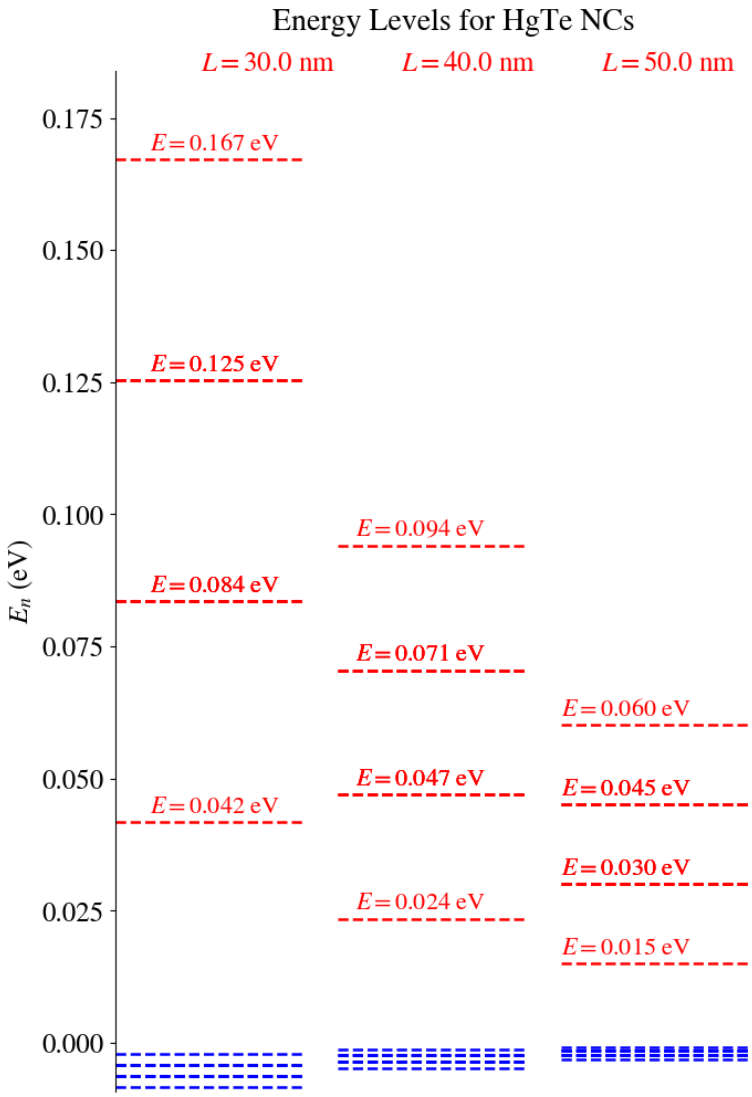

Fig. 1.3 *Distribution of the first energy levels of a HgTe NC calculated from the model of a 1-dimensional box in an infinite potential, assuming* m_e*=0.03*m_0 *and* m_h*=0.6*m_0 *for three distinct NC sizes L=30 nm, L=40 nm and L=50 nm.*

the small number of NCs produced per batch. Secondly, the "bottom-up" approaches, which consist in assembling crystalline units to obtain NCs of desired size. This is the case of soft chemistry techniques such as colloidal synthesis, which allow to obtain monodisperse NCs with a good reproducibility at a low cost.

In this thesis work, we studied NCs prepared by chemical approaches (bottom-up). It is a colloidal synthesis performed by the group of E. Lhuillier at INSP (Sorbonne University). This method has been investigated for more than 30 years [16], successive breakthroughs were made and nowadays, colloidal synthesis benefits from a high level of maturity. A very important development in the synthesis of NCs took place in the early 1990s with the use

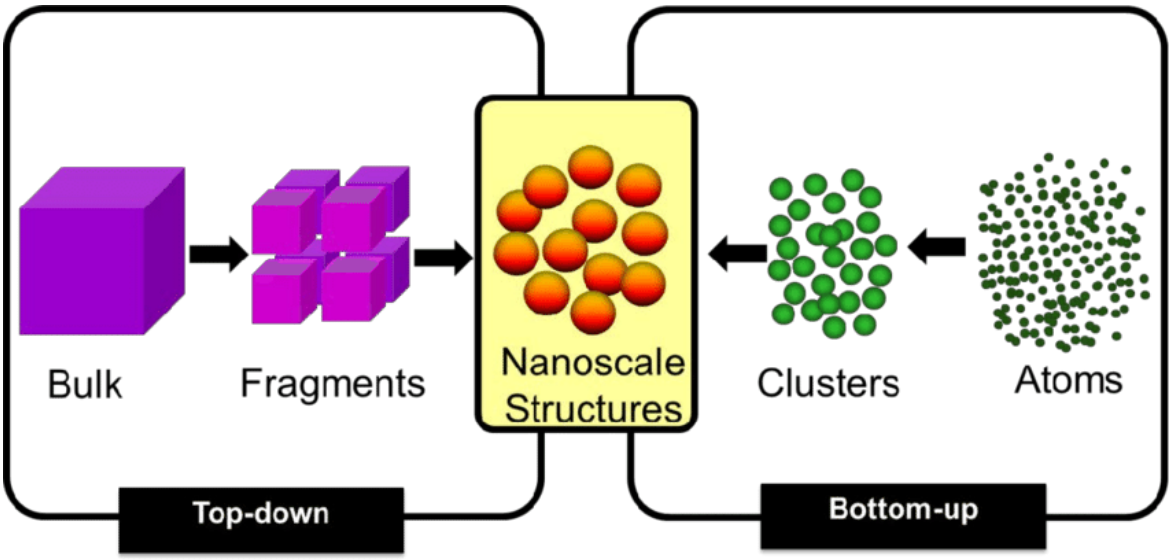

Fig. 1.4 *Reproduced from Reference [15]. Illustration of the top-down and bottom-up approaches for fabrication of nanocrystals.*

of non-aqueous solvents and capping ligands to stabilize the products against maturation, carrying out the reaction at high temperature to ensure good crystallinity and separating the nucleation and particle growth steps, and thus obtaining particles of uniform size [17, 18]. Colloidal synthesis involves a series of chemical reactions, during which different ions are mixed and self-assembled under controlled temperature and pressure to form colloidal suspensions. Most colloidal synthesis of NCs follow the same major principles with a dissolution of the precursor, a fast nucleation followed by a controlled growth of particles as illustrated in Figure 1.5 (from C. Greboval manuscript thesis) [19]. Not only does the colloidal synthesis make possible the fabrication of NCs of many different types of materials, with various shapes and with molecule-like manipulability without any substrate requirement, but it is also a very low-cost process in comparison with others techniques. Indeed, a standard chemistry equipment enables the synthesis of very reproducible NCs batches of important quantities. Current investigations on larger-scale colloidal synthesis aim to give NCs a key role in the future of quantum dots technology [20].

One peculiar and distinct characteristic of colloidal NCs is the presence of ligands binding to the surface atoms all around the nanocrystal (see Figure 1.6 a) and b)). Ligands are long organic molecules which play multiple roles. Their first role is to be introduced in the solution as a quenching compound. Their great affinity with surface atoms makes them bind to them, terminating their dangling bonds. They limit access to precursors. The NCs are then isolated from the reacting compounds and the reaction stops. Organic capping has been of great use to prevent uncontrolled growth and agglomeration, resulting in better control on size and shape. Growing anisotropic shapes can be achieved by using the convenient ligands which would block reaction on certain facets while letting the nanostructures grow on other ones. After the reaction is stopped, ligands still play their passivating role. They act as a coating to the semiconductor core and modulate its interaction with the environment. Most

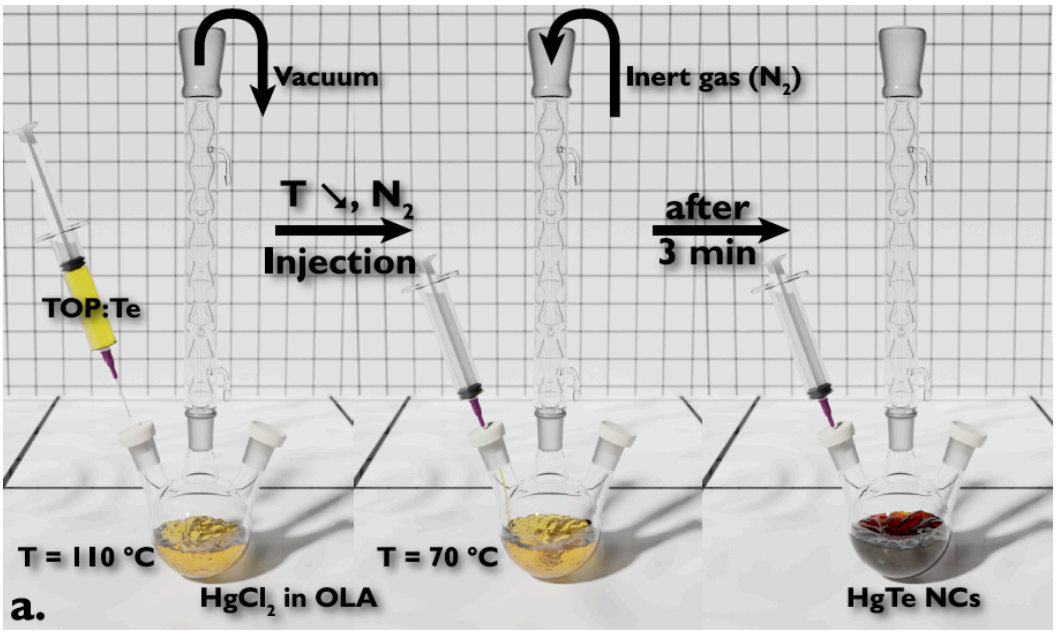

Fig. 1.5 *Reproduced from C. Greboval thesis manuscript [19]. Schematic representing the main steps of the synthesis of HgTe NCs, from left to right: degassing of the hot solvent and dissolution of the mercury precursor, adjustment of the temperature to the reaction temperature and passage under inert atmosphere, followed by the injection of the tellurium precursor. After 3 minutes, the solution is brown and ligands are added to stop the reaction.*

notably, they ensure colloidal stability, and facilitate manipulation of the NCs. The latter is particularly important when it comes to integration into devices. Interactions between the semiconductor core and the ligands can modify electrical and optical properties of colloidal NCs [21]. Indeed, surface chemistry has an impact on energy transfer mechanisms from NCs to ligands, and thus on dynamics of carriers. This can result in an enhanced or in a quenched photoluminescence of the NCs, depending on the recombination channels induced by the ligands [22]. Thus, surface chemistry of NCs is a productive field of research, with various axis of investigations such as the shape and manipulability of the produced NCs, or even their carrier dynamics [23].

1.3 Application of Nanocrystals

As previously mentioned, for more than four decades, NCs have been widely studied, resulting in important advances in fundamental and applied science. They have reached a high technological maturity, which has even lead to their integration into a wide variety of devices [25] or a variety of scientific and commercial applications [26, 27]. For instance, their tunable and narrow photoluminescence has lead to the development of nanocrystal-based Light Emitting Diodes covering the entire visible range, and now integrated into display devices commercially available [28]. By varying the materials, size or shape of the NCs, photodetectors based on NCs have emerged with operating range spanning from the UV

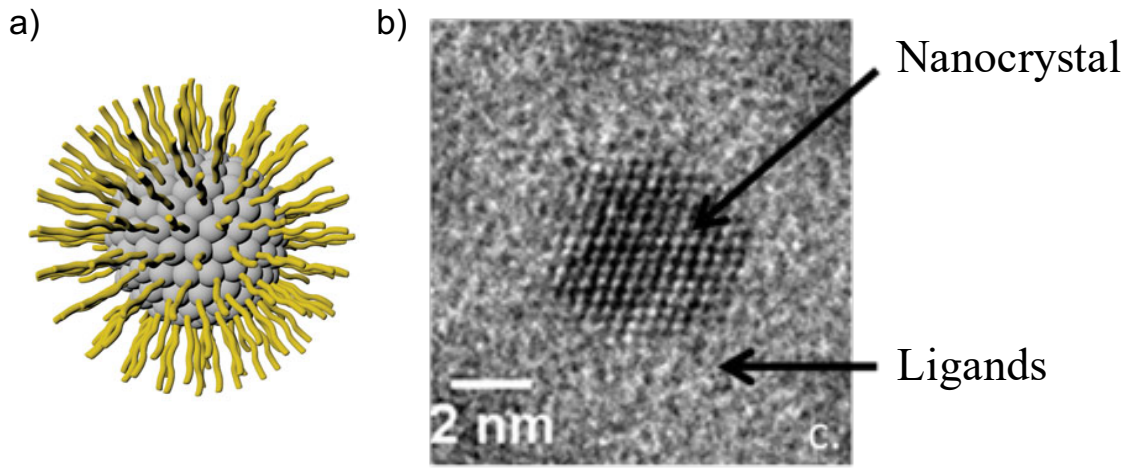

Fig. 1.6 *a) Schematic of a NC whose surface is covered with ligands; b) High-resolution electron microscopy image of a HgSe NC: the crystallized part appearing dark in the center corresponds to the HgSe NC, the light part on the outside corresponds to the amorphous ligands (from B. Martinez thesis manuscript [24]).*

frequencies down to infrared ones [29–31]. Improvements in the synthesis have also enabled the development of more complicated core-shell structures. Such structures are particularly promising for applications in catalysis [32], but also in the biomedical field [33], for cell imaging [34, 35] or drug delivery [36, 37]. The engineering of the electronic properties of NCs is also investigated for the development of photovoltaic solar cells with high energy conversion efficiency [38, 39], but also for future battery technologies [40]. Also, NCs could play an important role in the development of more environment friendly technologies.

Regarding their spectral range, most of the applications of NCs have been focused on the visible and near-infrared range. However, in the mid-infrared spectral range, current technologies are based on expensive epitaxially grown semiconductors and therefore colloidal NCs are of significant interests for the design of low-cost optoelectronic devices. For instance, the development of LIDAR requires a significant cost reduction and current quantum dots infrared photodetectors are limited by the size and low density of quantum dots grown by epitaxy or CVD. To extend the spectral range of NCs, narrow band gap semiconductors such as chalcogenides are required. Indeed, even if the bandgap energy can be adjusted by the particle size (as discussed previously), its minimum value is limited by the bandgap energy of the bulk material. Therefore, mercury chalcogenides HgX (with X=S, Se or Te) are perfect candidates to develop NCs operating in the mid-infrared spectral range due to their narrow band gaps and high process maturity. Rogach *et al.* were the first to report the growth of such narrow bandgap NCs and obtained very small particles with a bandgap corresponding to 1300 nm [41]. Then, by synthesis larger size NCs, the NCs field has been extended from the near-infrared to the mid-infrared [42–48]. The optical features of such NCs, relying on interband processes, was extended up to 12 μm by the addition of a regrowth step [49].

To further extend the optical characteristics of NCs and reach the hardly accessible THz

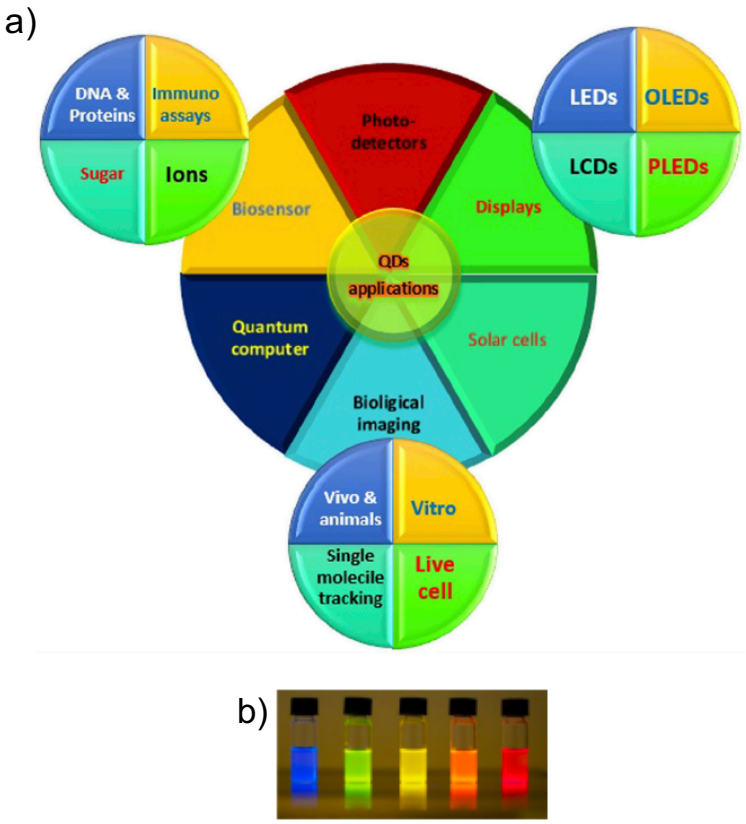

Fig. 1.7 *a) Examples of application of NCs. b) CdSe CQDs of different sizes in solution, illuminated with UV light (©Nexdot)*

spectral range, mercury telluride (HgTe) NCs appear to be a very promising material because in its bulk form, HgTe is a zero-band gap semiconductor, which means that the bandgap of HgTe NCs can potentially be reduced to zero eV. In addition, a recent breakthrough was reported by Goubet et al. [8], namely the development of a high-temperature procedure for HgTe NCs producing large self-doped HgTe NCs that exhibit intraband absorption (the 0 D counterpart of the intersubband transition in the doped quantum well structure) that can be tuned from 60 THz down to 4 THz. This recent work, which opens up interesting prospects for expanding the application fields of NCs, represents the basis of this thesis work.

1.4 HgTe Nanocrystals

In this thesis work, we have studied the optical properties of large semimetal mercury telluride (HgTe) NCs in the THz frequency range. This work has been done in close collaboration with Emmanuel Lhuillier's group from the Paris Institute of Nanosciences (INSP, Sorbonne University), which has grown all the HgTe NCs presented in this thesis.

1.4.1 HgTe bulk properties

HgTe can be seen as a limit case of the famous ternary material Mercury Cadmium Telluride, $Hg_{1-x}Cd_xTe$ with $x = 0$, which is vastly used for infrared detection. It is a chalcogenide made of Hg^{2+} cations and Te^{2-} anions. It has a zinc blende structure that can be viewed as two face-centered cubic structures, each one corresponding to respectively Hg^{2+} and Te^{2-}, with the second one being displaced from the first one by one quarter of a body diagonal, as represented in Figure 1.8.a). As for every zinc-blende crystal, HgTe is non-centrosymmetric. In its bulk form, it has a peculiar electronic structure. Indeed, the high symmetry Γ_6 band, which usually plays the role of the conduction band in other semiconductors, lies under the Γ_8 bands as represented in Figures 1.8 b) and c). Energy gap being usually defined as $E_G = E_{\Gamma_6} - E_{\Gamma_8}$ is thus negative in the case of HgTe and is approximately equal to -0.3 eV. HgTe is said to have an inverted band structure. The upper Γ_8 band with positive dispersion forms the conduction band and the lower one with negative dispersion forms the valence band [50]. These two bands touch at the center of the Brillouin zone, and when HgTe is intrinsic, the Fermi level lies in between. HgTe is then a semi-metal with an effective energy gap equals to 0 eV. The conduction band is highly dispersive with an associated effective mass m_e^*= 0.03 m_0, while the valence band is much less dispersive, ie $m_h^*/m_e^* >> 1$. From Equation 1.2 and $\varepsilon_r = 20.5$ [51], it is then possible to derive the effective Bohr radius of the exciton in HgTe, $a_0^* = 40$ nm, which is large compared to exciton Bohr radius in many other semiconductors.

1.4.2 Optical properties of HgTe Nanocrystals

As discussed previously, in HgTe material, the absence of the bandgap theoretically allows to obtain a bandgap energy only due to confinement and thus reduced down a very small energy. Figure 1.9 shows the infrared absorption spectrum of HgTe NCs of different sizes [52]. The smallest ones (a few nanometers in diameter) have a first excitonic peak that is in the near infrared around 1 μm. By increasing the size to about 20 nm, this excitonic peak is shifted to the mid-infrared near 5 μm. Even if one can theoretically obtain a band gap energy as small as one wishes, several difficulties appear when one wants to go further than the mid-infrared. The first one is practical since it is difficult to obtain large stable colloidal HgTe NCs, without aggregating. However, even by working on the stability, the second difficulty is related to the material itself. The more the size of the NCs is increased, the closer the Fermi level is to the conduction band (reinforcement of the n character), up to the point where the Fermi level is above the first level of the conduction band [53]. Consequently, the interband transition between the $1S_h$ and $1S_e$ levels is made impossible because of the filling of the $1S_e$ level and an intraband transition between the $1S_e$ and $1P_e$ levels appears. This phenomenon is called self-doping as no extrinsic impurities are introduced in the NCs during the synthesis. We observe in Figure 1.9 the emergence of an intraband absorption for large HgTe NCs (size>20-30 nm) with a resonance peak that can reach the THz spectral range.

The origin of doping in self-doped NCs is believed to be linked to NC reduction by the environment. HgTe NCs are made of an intrinsic material with an excess of Hg2+ on the surface [54]. Depending on the ligands, this excess of positive charges might be partly screened, but the density of ligands will remain lower than the surface density of cations. This causes the bands to bend downwards and favors the injection of free electrons [55].

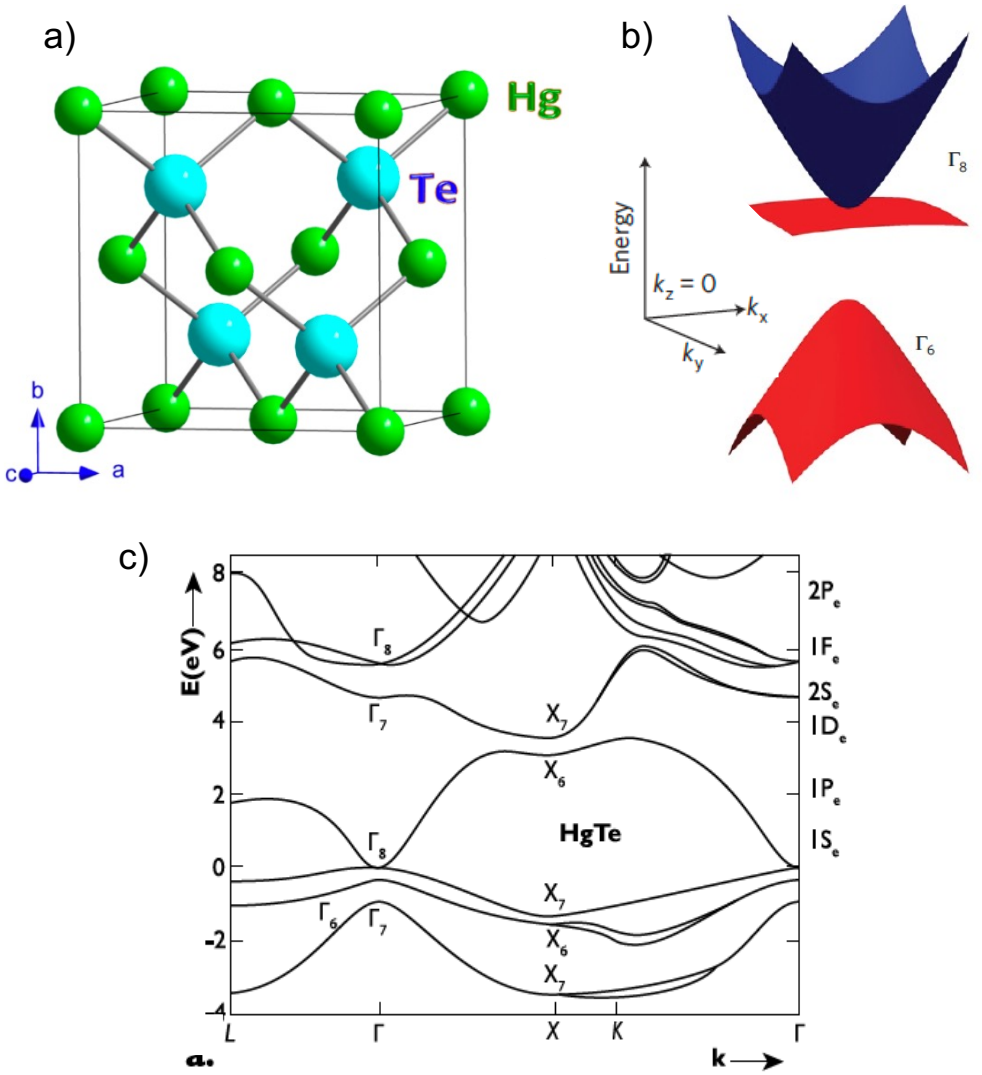

Fig. 1.8 *a) HgTe crystal structure. It corresponds to a zinc blende structure which can be viewed as two face-centered cubic structures, each one corresponding to respectively Hg2+ (blue) and Te2- (red), with the second one being displaced from the first one by one quarter of a body diagonal. b) and c) HgTe bulk band structure. It is said to have an inverted band gap since the Γ_6 band, which usually plays the role of the conduction band in other semiconductors, lies under the Γ_8 bands. Adapted from C. Greboval thesis manuscript [19].*

A more electrochemical way to understand this self-doping process is the combination of a large work function of HgTe [56], with the narrow band gap nature, bringing the conduction band below the Fermi level of the environment and leading to a degenerate doping in HgTe NCs. Ligands do not actually add charges in the system but rather tune the position of the states so that electronic states of the conduction band lie under the Fermi level. To tune the carrier density, a strategy is the control of the hgTe NCs surface chemistry.

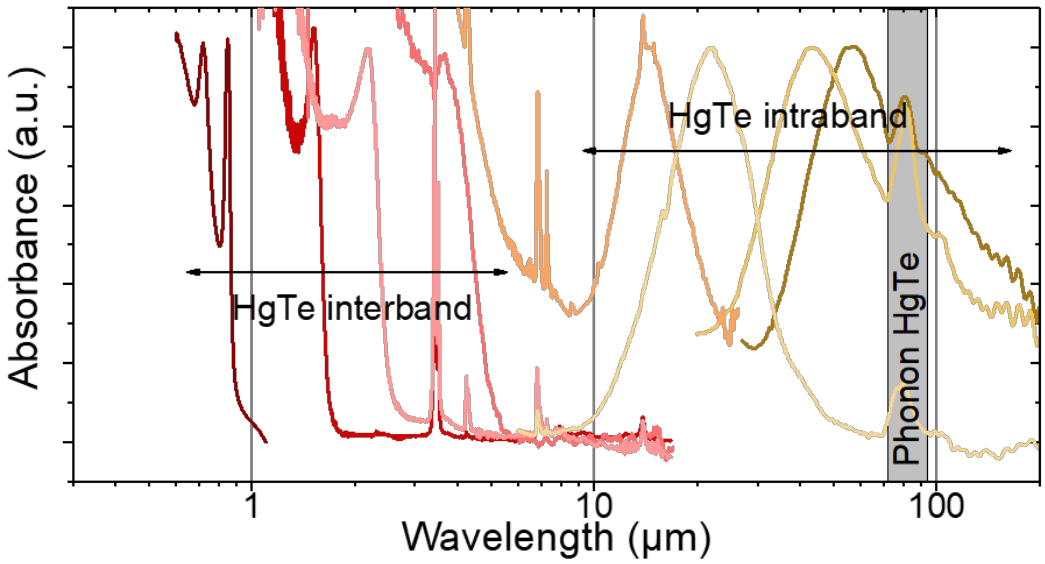

Fig. 1.9 *From C. Greboval thesis manuscript [19]. Absorption spectra of undoped HgTe NCs and doped HgTe NCs are shown for different sizes, highlighting the extreme tunability of this material.*

Chapter 2

Intraband absorption in self-doped HgTe nanocrystals

As discussed in the previous chapter, using semimetals, the NCs field has been recently extended to long wavelengths. In a material such as HgTe, the absence of a band gap makes that the energy of the electronic states at the band edge results only from the quantum confinement effect. Another striking development is the appearing of doped NCs presenting intraband absorption (the 0D counterpart of intersubband transition in doped quantum well structure). Such transitions offer an alternative way to explore mid-infrared and far-infrared spectral range. Goubet *et al.* have recently demonstrated that such transitions in the case of large HgTe NCs can be pushed in the THz spectral range [8]. Before considering THz photonics applications of large HgTe NCs, it is necessary to master their optical response, and, as much as possible, to understand their evolution as a function of the size of the NCs, their crystal structure, their shape, their surface passivation (organic ligands, semiconductor heterostructure) and temperature. In this context, a main objective of this thesis project is to go beyond the pioneering work on large HgTe NCs and to study in-depth the absorption properties in the THz spectral range of large HgTe NCs.

In this chapter, we will first motivate the in-depth study of THz absorption. Secondly, the results of the absorption of self-doped large HgTe NCs in the full THz spectral range will be presented. They were obtained using both THz time-domain spectroscopy (THz-TDS) and Fourier transform infrared spectroscopy (FTIR). Then, we will introduce a microscopic model we have developed which includes both quantum confinement and thermal carrier distribution effects. The interpretation of the measured THz absorbance using our microscopic model and the respective contributions of the intraband excitations of individual carriers versus the collective excitations will be discussed. Last, we will present the investigation of the THz intraband absorption in large HgTe NCS as a function of temperature. This chapter includes parts of our complete article [57].

2.1 Motivation of this work

The unique features of the large HgTe NCs developed by Lhuillier's team is their very low frequency absorption due to their self-doped nature. The tunability of their absorption

resonance up to 4THz is very promising for THz technology. Since electrons are involved in this absorption feature, the actual nature of this low frequency absorption is a challenging question of great interest. Indeed, two main regimes have been identified in smaller NCs absorbing at higher frequencies [58]. In some cases, when the doping is low enough, this absorption can be attributed to intraband absorption, i.e. carrier excitation between quantized states. The second regime occurs when the number of electrons involved is higher. In this case, the Coulomb repulsion energy starts to overcome the confinement energy, and the electrons can no longer be considered as independent. They undergo collective excitations, which correspond to a plasmonic regime.

The same question remains to be elucidated for HgTe NCs, whose large size and optical characteristics in the THz spectral range are unprecedented. Indeed, revealing the nature of the absorption is crucial to develop THz optoelectronic devices based on these NCs, as the different phenomena may or may not be suitable for certain applications. For example, plasmonic effects are expected to occur on a much shorter time scale than intraband processes, making them less suitable for photodetection applications.

2.2 Synthesis, structural and electrical properties

The NCs studied in this thesis work have been synthesized by Emmanuel Lhuillier's group from the Paris Institute of Nanosciences (Sorbonne University), following the procedure described in Reference [8]. The major improvement over conventional hot injection processes, is the use of less reactive precursors: $HgCl_2$ for the mercury halide and trioctylphosphine telluride ($C_{24}H_{51}PTe$). This advanced process results in a better control, enabling the synthesis of large NCs. These two precursors are mixed and injected in a hot (300 °C) solvent solution oleylamine, used as coordinating solvent. After 5 minutes, ligands are introduced to quench the reaction. Here, dodecanethiol ($CH_3(CH_2)_{11}SH$) is used. The solution then follows successive steps of washing, and ends up in a solution of chloroform. The HgTe particles are capped with 1-dodecanethiol ligands of typical length 1.5-2 nm. These insulating long-chain organic ligands surrounded each HgTe NC strongly limit the carrier hopping between neighboring NCs.

The shape, size and dispersion of the grown HgTe NCs have been characterized using electron microscope images and X-Ray diffraction measurements by the group of Emmanuel Lhuillier. The Scanning Electron Microscopy (SEM) and Transmission Electron Microscopy (TEM) images, shown in Figure 2.1.a) and Figure 2.1.b) indicate that the NCs are not uniform and have various shapes, roughly spherical for the smallest ones, and more angular for larger sizes. From these electron microscopy images, we estimate the distribution in size of the NCs as represented in Figure 2.1.c). The size of the HgTe NCs exhibit an important dispersion with an mean value $L \sim 90$ nm.

From the X-Ray diffraction patterns, shown in Figure 2.2.a), we can also estimate the mean size of the NCs, L, by considering the Scherrer equation expressed as $L = K\lambda/(Hcos(\theta))$, where K is a shape factor (0.93 in our case), H the full width at half maximum of the considered peak, and θ the corresponding Bragg angle. The mean size obtained

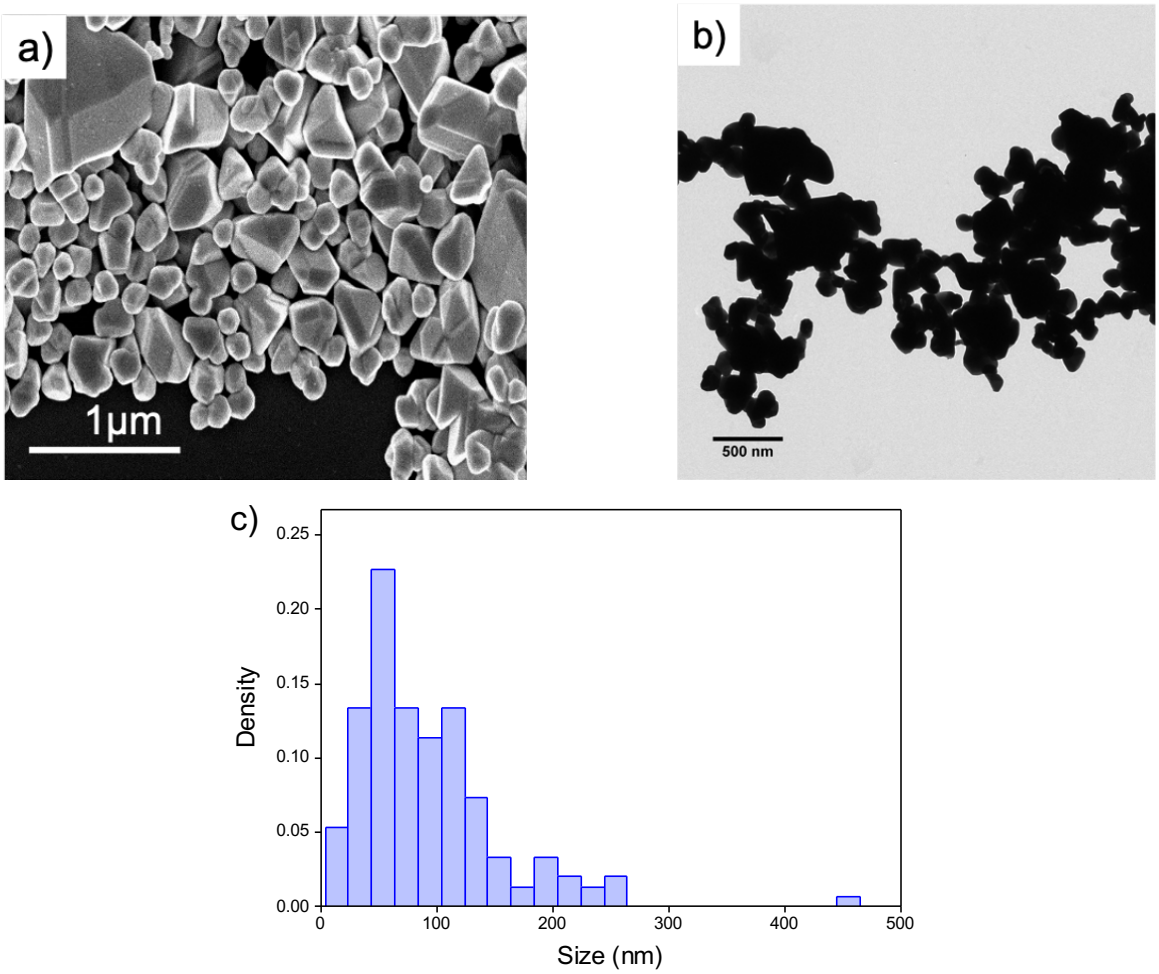

Fig. 2.1 *a) Scanning Electron Microscopy (SEM) Image. b) Transmission Electron Microscopy (TEM) Image. c) Histogram representing the distribution in size of the large HgTe NCs deduced from Figures a) and b).*

by XRD is L $\sim$ 92 nm, which is fully consistent with the mean size deduced from SEM and TEM analysis. This mean size value suggests that the largest NCs, of the order of μm in size, are likely polycrystalline. Raman spectroscopy measurements were also conduced by Emmanuel Lhuillier's team. The Raman spectrum of the NCs, presented in Figure 2.2.b), exhibits several peaks with a transverse optical phonon (TO) at 120 cm^{-1} corresponding to 3.6 THz.

The charge transport in the THz NCs have also been probed by Emmanuel Lhuillier's team using a field-effect transistor configuration. A scheme of the device is shown in the inset of Figure 2.3. The current-gate voltage characteristic, reported in Figure 2.3, shows the ambipolar conductance with both hole and electron conduction and confirms the n-doped nature of these large HgTe NCs, with a carrier density of up to several carriers per nanoparticle [8]. The on/off ratio is low (<4), which is consistent with the expected large

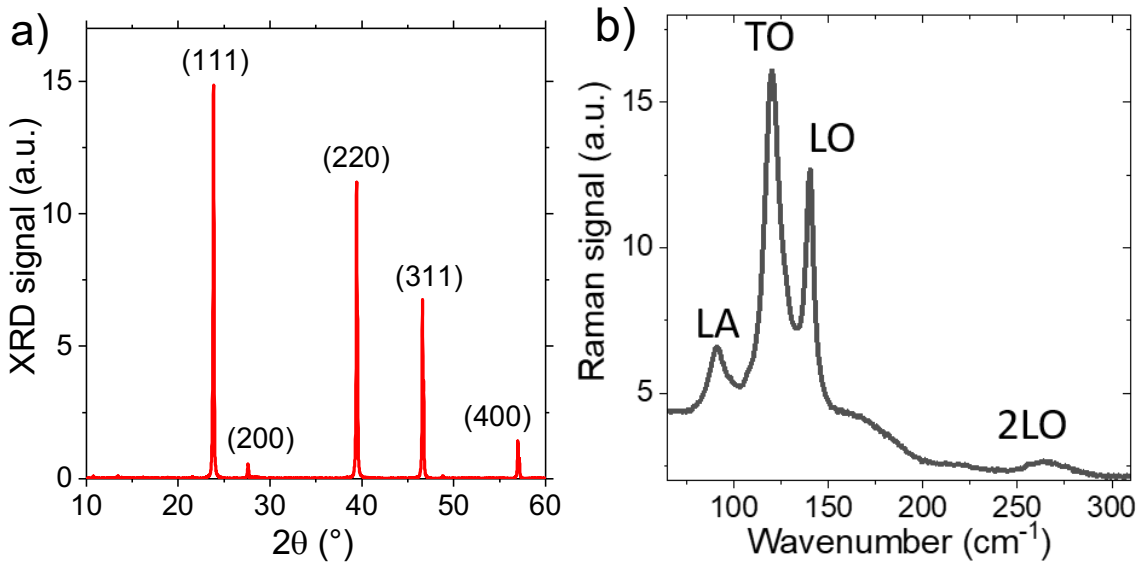

Fig. 2.2 *a) X-Ray diffraction pattern of large HgTe nanocrystals. b) Raman spectrum of a thin film made of large HgTe NCs.*

thermally activated carrier density.

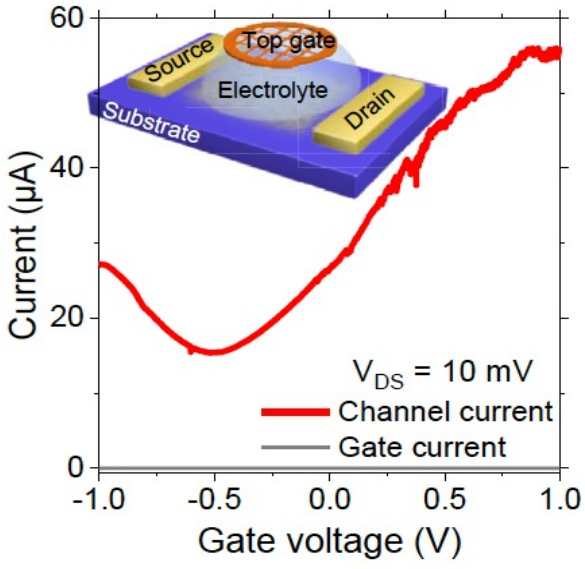

Fig. 2.3 *From Reference [57]. Drain and Gate currents as a function of gate voltage for a thin film made of large HgTe NCs used as the channel of an electrolytic transistor. Inset is a scheme of the field-effect transistor.*

2.3 Probing intraband absorption of self-doped HgTe NCs film

Spectroscopy is the measurement of optical properties of a material as a function of frequency. Such measurements provide insightful informations about material characteristics for a wide range of applications. Among the numerous existing spectroscopy methods at THz frequencies, two of them have been used in frame of this PhD work : Time Domain Spectroscopy (TDS) and Fourier Transform Infrared Spectroscopy (FTIR). These two different techniques measure different quantities and cover different spectral ranges thus providing complementary information. In particular, THz TDS experiments give access to the optical properties of materials in the low frequency part of the THz spectral range, typically from 0.1 to 4 THz. In contrast, FTIR spectroscopy probe the optical properties of materials over a very broadband range from 4 THz to more than 40 THz. In this section, I will first present our investigation of the optical properties of large HgTe NCs films in the full THz spectral range using THz time domain spectroscopy and FTIR spectroscopy systems.

2.3.1 Samples Preparation

All the measurements presented in this chapter were performed on composite films composed of these large HgTe NCs and their surrounding medium of dodecanethiol ligands and air. Due to the long wavelength of THz radiation (300 μm at 1 THz), probing optical properties of NCs in the THz spectral range requires large area composite films. Even if the THz probe beam is focused down to the diffraction limit, HgTe NCs samples in the mm scale are needed. The great manipulability of the NCs has made the fabrication of large size HgTe NCs films fairly simple. Indeed, we have processed the HgTe NCs films by depositing successive droplets of colloidal solution containing the NCs on a bare substrate. We have used either silicon or quartz substrates. Although being relatively simple, the fabrication process suffers some inconveniences. In particular, homogeneous thickness over the whole film surface is hard to achieve. Spin coating is not effective as it expels the NCs to the edges or outside the substrate, leaving very few particles in the center. Measuring the thickness of the film is also a critical issue. The use of a Dektak profilometer was investigated but the measurements were not satisfactory because, even with the tip force set to its minimum, it passed through the film instead of following the surface. Thus, we estimate the HgTe NCs film thickness using an optical microscope (see Figure 2.4.a)) and find a typical thickness of $\sim$ 10 μm. The HgTe NCs films deposited on the substrates are then glued to copper sample holders using PMMA (see Figure 2.4.b)) to be adapted to our instrumentation.

2.3.2 Absorbance at low-frequency using THz-TDS

Description of the THz-TDS set-up The development of mode-locked femtosecond lasers has greatly contributed to the expansion of THz Time Domain Spectroscopy (TDS) experiments, as the short time scale of the laser pulses enables punctual access to slower oscillating THz frequencies. A schematic of the THz TDS set-up is depicted in Figure 2.5. More in-depth descriptions of specific parts are presented in Appendix A. The principle of THz-TDS works as follows: a modelocked femtosecond laser produces a pulse train of femtosecond pulses. In our case, we use a Ti:Sapphire oscillator that delivers horizontally polarized optical pulses with a duration of $\sim$15 fs, a center wavelength of λ_0 $\sim$800 nm with a spectral bandwidth of $\sim$100 nm at a repetition rate of 80 MHz. The average power is about 850 mW.

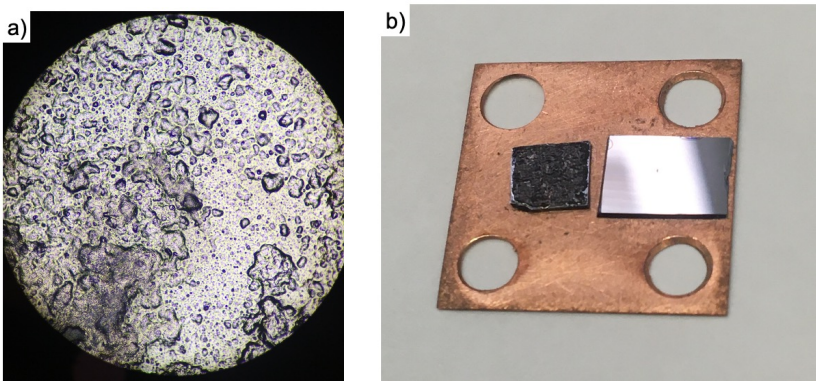

Fig. 2.4 *a) Optical microscope image of a composite film of large HgTe NCs deposited on a Si substrate. b) Composite film of large HgTe NCs deposited on a Si substrate and a reference Si bare substrate glued on a copper sample holder*

The optical beam is separated in two arms by a beam splitter (80/20). The first one is used for the generation of THz pulses while second one is used for the detection of THz pulses. The first red beam illuminates an electrically biased photoconductive antenna (PCA), which generates THz pulses, i.e. transient THz electric fields. The emitted THz pulses are collected and focused onto the samples under characterization using a pair of parabolic mirrors. After passing through the samples, using an other pair of parabolic mirrors, the THz pulses are collected and focused onto an electro-optic crystal used as a THz detector. The second red beam propagates along a second arm, called the "probe line". A motorized delay line installed along this arm enables the adjustment of the optical path length. This second red beam is focused on the electro-optical crystal and is spatially superimposed on the THz pulses. The optical pulses of the second beam therefore interact strongly in the electro-optical crystal with the THz pulses that have passed through the samples. The THz pulses induce birefringence in the electro-optical crystal due to second-order nonlinear effects, which mainly modify the phase of the red pulses. By proceeding to polarization measurements of the optical pulses we are able to record the THz electric field in the electro-optic crystal. The duration of the optical pulses being much shorter than the one of the THz pulses, one gets a "punctual" measurement of the THz electric field.

By swiping the delay line positions, one can reconstruct a discrete time domain measurement of the THz field as shown in Figure 2.6.a). In other words, we are able to synchronously sample the transient THz electric field and reconstruct its temporal profile. The temporal waveform can be further translated using Fast Fourier Transform into then amplitude and the phase spectra of the THz radiation. The complex refractive index of the sample under investigation (i.e. the absorption and the dispersion) is then directly obtained, with a single measurement, without requiring the use of Kramers-Kronig relation [59]. We use two different types of electro optic-crystal, a 2 mm-thick ZnTe crystal and a 100 μm-thick GaP crystal. For a more detailed description of the THz generation and THz detection techniques, cf Appendix A.1 and A.2. The THz beam path is enclosed in a box purged by dry air to reduce the humidity down to 0.1 %, thus strongly reducing the THz absorption by the water molecules in the ambient air. The temporal resolution set by the delay line step between two

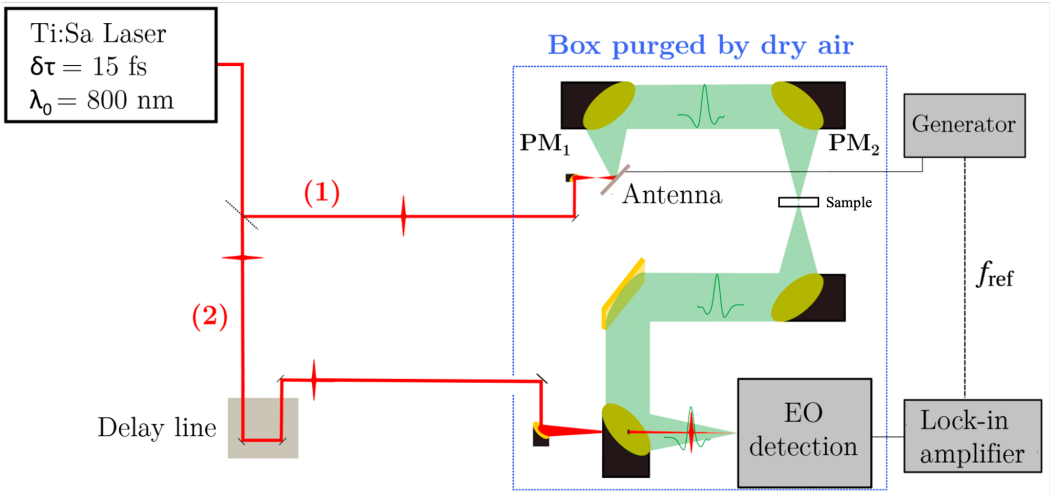

Fig. 2.5 *Sketch of the experimental THz-TDS setup. The optical beam is depicted in red and the THz beam in green. The area where the THz pulse is generated and propagates is placed in a box purged by dry air in order to reduce THz absorption induced by water molecules in the air.*

consecutive acquired points is 8 fs and the time windowing is set to avoid any reflection from the substrate, the photoconductive antenna and the electro-optic crystal. The performances of our advanced THz TDS system is highlighted in Figure 2.6.b) that reports the amplitude spectra of the THz pulses recorded with the two distinct electro-optic crystals. We observe that the detection bandwidth of our THz-TDS system ranges from 0.1 THz to 4.9 THz using the ZnTe crystal, (black curve) with a signal-to-noise ratio of 600, and from 0.1 to 5.8 THz using the GaP crystal with signal-to-noise ratio of 200 (red).

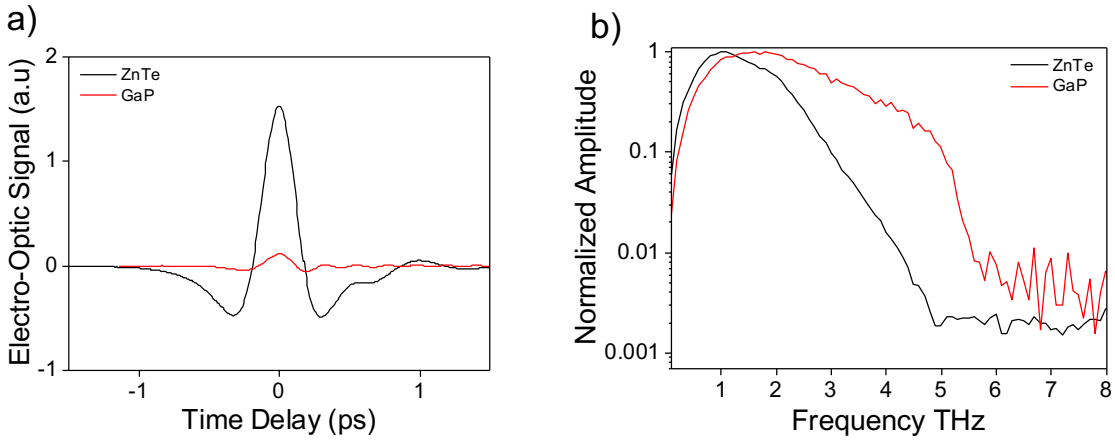

Fig. 2.6 *a) Temporal waveforms of electric fields measured by TDS for two different electro-optic crystals (2mm ZnTe in black and 100µm GaP in red). b) Amplitude spectra obtained by FFT of the time-resolved electric field amplitudes.*

Transmission measurements To probe the optical properties of large HgTe NCs at low frequencies, we measure the transmittance of the composite films, composed by the HgTe NCs surrounded by ligands and air, using the THz-TDS system. For these measurements, the HgTe composite films are deposited on a high-resistivity silicon substrate, which is transparent to THz frequencies, and we use a bare high-resistivity silicon substrate as a reference sample. Note that the thickness of the film, measured using an optical microscope, is $\approx 13.2\mu m$. Our THz TDS set-up operates in a transmission configuration, so that THz pulses propagates through the samples before being acquired.

The THz pulses transmitted through a HgTe NCs sample (red line) shows a temporal shift and a decrease of the electric field relative to the pulse transmitted through a reference sample (black line), as reported in Figure 2.7.a). The observed additional delay is a feature of the real part of the refractive index while the attenuation is related to the imaginary part of the refractive index (absorption). Applying a Fast Fourier Transform on these recorded time-resolved electric fields, we obtain the amplitude spectra presented in Figure 2.7.b).

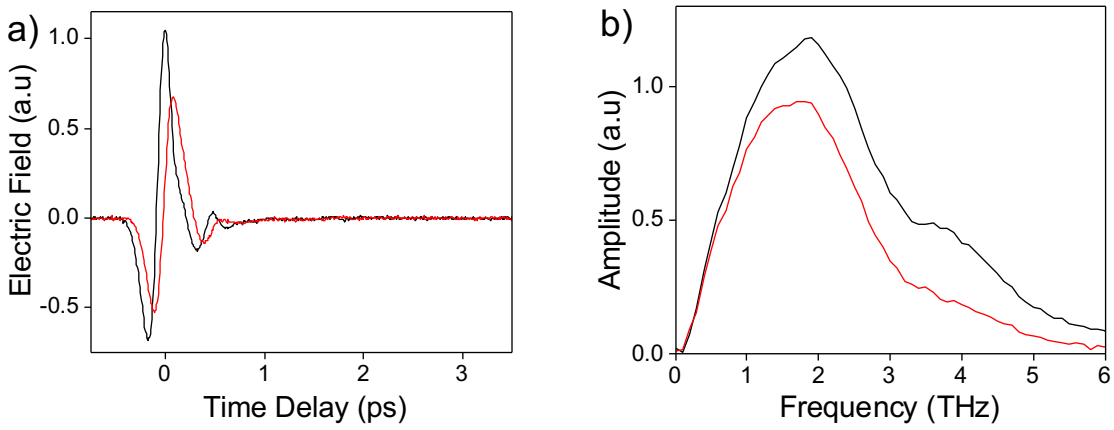

Fig. 2.7 *a) Temporal waveforms of the THz pulses transmitted through the HgTe NCs film sample (red line) and through the Si substrate reference sample (black). b) Corresponding amplitude spectra obtained by fast Fourier transform of the temporal traces.*

The ratio of the two amplitude spectra provides the amplitude transmittance of the composite film in the frequency domain, expressed as :

$$t_o(\omega) = \frac{E_{Sample}(\omega)}{E_{ref}(\omega)} \tag{2.1}$$

The transmittance amplitude, plotted in Figure 2.8.a), provides interesting preliminary insight. We observe that $t_o(\omega)$ decreases with increasing frequency. We proceed to similar measurements for several HgTe NCs film of different thickness. We observe that $t_o(\omega)$ gets smaller as the thickness of the composite film is increased, as observed in Figure 2.8.b).

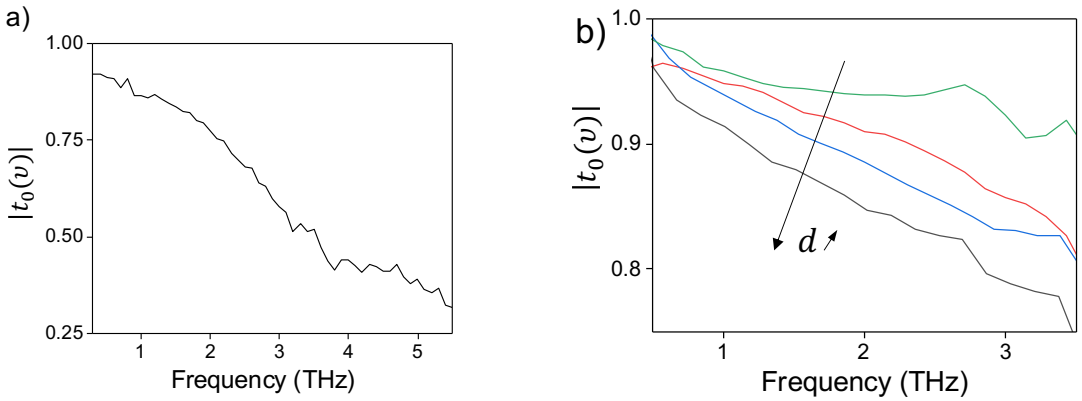

Fig. 2.8 *a) Spectrum of the transmittance amplitude* $|t_o(\omega)| = E_{Sample}(\omega)/E_{ref}(\omega)$ *b) Spectrum of the transmittance amplitude* $|t_o(\omega)| = E_{Sample}(\omega)/E_{ref}(\omega)$ *for various thickness of the composite film.*

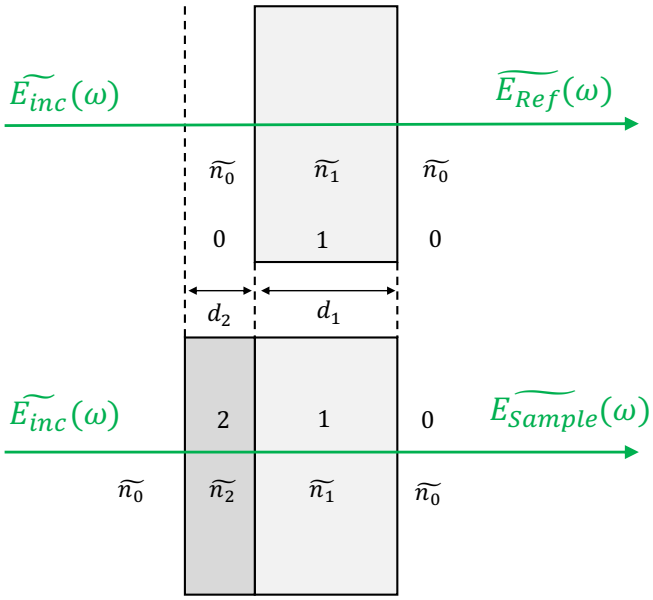

Fig. 2.9 *Sketch of reference and sample signal propagation through respectively a bare substrate (upper part) and through a film on a substrate (lower part).*

As mentioned previously, the main advantage of the THz-TDS system is that it gives access to the amplitude and phase of the transmittance of the probed samples, which allows the determination of the complex refractive index of the material in a single measurement, unlike in contrast to usual spectroscopy systems (such as FTIR spectroscopy). It is possible to calculate the relation between the measured THz waveforms and the complexe refractive index of the composite film [59]. Let us start with the the electric field incident on the sample and the reference, denoted $\tilde{E}_{inc}(\omega)$. A scheme of the electric field propagation through the sample and the reference is illustrated in Figure 2.9.

As the THz electric field propagates through different materials and encounters interfaces,

its phase and amplitude are modified. We label the different mediums by the following numbers:

- 0 ⇔ Lab environnement (air or vacuum)
- 1 ⇔ Substrate (high-resistivity silicon substrate)
- 2 ⇔ Composite HgTe NCs film.

The complex refractive index of the medium j is given by $\tilde{n_j} = n_j + ik_j$ with $(n_j, k_j) \in \mathbb{R}^2$. Thus, we can express the propagation terms in a medium j of thickness d as:

$$\tilde{P}_j(\omega,d) = e^{(i\frac{\tilde{n}_j d\omega}{c})}$$

Since the THz electric field crosses interfaces, transmission and refraction at the interfaces must be considered. We define the Fresnel transmission and reflexion coefficients for the THz electric field going from medium i to medium j:

$$\tilde{t}_{i,j} = \frac{2\tilde{n}_i}{\tilde{n}_i + \tilde{n}_j} \text{ and } \tilde{r}_{i,j} = \frac{\tilde{n}_i - \tilde{n}_j}{\tilde{n}_i + \tilde{n}_j}$$

Let us now express $\tilde{E}_{Sample}(\omega)$ and $\tilde{E}_{Ref}(\omega)$ as function of the incident electric field $\tilde{E}_0(\omega)$. For clarity purpose, we do not write the frequency dependences.

$$\tilde{E}_{Ref} = \tilde{E}_0\tilde{P}_0(d_2)\tilde{t}_{01}\tilde{P}_1(d_1)\widetilde{FP}_{101}(d_1)\tilde{t}_{10}$$

$$\tilde{E}_{Sample} = \tilde{E}_0\tilde{t}_{02}\tilde{P}_2(d_2)\widetilde{FP}_{021}(d_2)\tilde{t}_{21}\tilde{P}_1(d_1)\widetilde{FP}_{210}(d_1)\tilde{t}_{10}$$

where :

$$\widetilde{FP}_{jkl} = \sum_{m=0}^{M} (\tilde{r}_{kl}\tilde{P}_k(d_k)\tilde{r}_{kj}\tilde{P}_k(d_k))^m \tag{2.2}$$

which corresponds to the Fabry-Perot term arising from the multiple internal reflexion of light propagating in a medium k surrounded by mediums j and l. The transmittance in field is given by $\tilde{t}_0(\omega) = \tilde{E}_{Sample}(\omega)/\tilde{E}_{Ref}(\omega)$. Thus, one can write the formula :

$$\tilde{t}_0 = \frac{\tilde{t}_{02}\tilde{t}_{21}\tilde{P}_2(d_2)\widetilde{FP}_{021}(d_2)\widetilde{FP}_{210}(d_1)}{\tilde{t}_{01}\tilde{P}_0(d_2)\widetilde{FP}_{010}(d_1)} \tag{2.3}$$

This formula links the measured THz waveforms with the effective complex refractive index of the the HgTe NCs composite film, which is the only unknown parameter. However, as we will see, this formula can be further simplified owing to the temporal windowing we applied to the measurements. Indeed, the high-resistivity silicon substrate has a thickness of d_{Si}=285μm and has a very low dispersive refractive index in the THz range, with an average value of ≈ 3.418 [60–62]. Therefore, the reflection of the THz pulses within the substrate in the recorded time-resolved electric fields, corresponding to m=1 in $FP_{210}(d_1 \approx 285\mu m)$ and $FP_{010}(d_1 \approx 285\mu m)$, is delayed by:

$$\Delta t = \frac{2d_{Si}n_{Si}}{c} \approx 6.5 \text{ ps}$$

The factor 2 results from the round-trip of the reflected THz pulses in the silicon substrate. This first reflection of the THz pulses within the silicon substrate is observed in the measurement of the temporal waveform over 10 ps range, as displayed in Figure 2.10. Indeed, the delay between the main electric field peak and the first echo is consistent the calculated Δt. Therefore, to exclude any internal reflection of the THz pulses within the silicon substrate, we perform a temporal windowing by restraining the temporal range of the recording to 6 ps after the main peak. Thus only the term m=0 must be considered in $\widetilde{FP}_{210}$ and $\widetilde{FP}_{010}$, which are then equal to 1. Conversely, as the thickness of the HgTe NCs film is much thinner ($\approx$ 13.2 μm), we can assume that every successive reflection within the composite film is recorded during the defined temporal window of 6 ps. As a result, M=∞ in Equation 2.2 and $\widetilde{FP}_{021} = \frac{1}{1-\tilde{r}_{21}\tilde{r}_{20}\widetilde{P}_2^2(d_2)}$. The Equation 2.3 can then be simplified into:

$$\tilde{t}_0(\omega) = \frac{2(1+n_{Si})\tilde{n}_{eff}(\omega)}{(1+\tilde{n}_{eff}(\omega))(n_{Si}+\tilde{n}_{eff}(\omega))} e^{i(\tilde{n}_{eff}(\omega)-1)d\frac{\omega}{c}} \frac{1}{1-\tilde{r}_{21}\tilde{r}_{20}e^{2i\tilde{n}_{eff}(\omega)d\frac{\omega}{c}}} \tag{2.4}$$

with $\tilde{r}_{21}$ and $\tilde{r}_{20}$ the amplitude reflection coefficient at the interface film-Si and air-film respectively. So far, we assume that the substrates of the sample and the reference has exactly the same thickness. In reality, slight changes in the thickness of the high-resistivity silicon wafer exist. We extract the thickness of the sample and reference substrates by probing the delay between the main electric field peak and the first echo for the sample and the reference. We assume that the time delay is directly proportional to the substrate thickness as the dispersion of the silicon in the THz range is extremely low. The thickness difference Δd_{sub} between the sample and the reference substrates can be taken into account by adding the following phase term $e^{i\Delta d_{sub}(n_{Si}-1)\frac{\omega}{c}}$ in the Equation 2.4.

Determination of the complex refractive index of the composite film To extract the complex refractive index $\tilde{n}_{eff} = n_{eff} + ik_{eff}$ of the HgTe NCs composite film from the amplitude and phase of the transmittance, we use an usual approach, which consists in minimizing the error function defined by $\delta(n_{eff},k_{eff}) = \delta\rho^2 + \delta\phi^2$ with $\delta\rho = ln(|t_{theo}(\omega)|) - ln(|t_{meas}(\omega)|)$ and $\delta\phi = arg(t_{theo}(\omega)) - arg(t_{meas}(\omega))$ (from https://thz.yale.edu/resources). Figure 2.11 reports the real and imaginary parts of the effective complex refractive index of the film, extracted from our analysis. We observe that Re($\tilde{n}_{eff}$) slowly decreases with increasing frequency. It remains close to the HgTe bulk value ($n_{HgTe} \sim$ 3-4) [63–66] but higher than the values of films composed of 10 nm-size HgTe NCs (n $\approx$ 2.3) [67]. We observe a clear rise of Im($\tilde{n}_{eff}$) as the frequency increases, reaching a plateau above 3.5 THz.

From the determination of the complex refractive index $\tilde{n}_{eff}$, we calculate the absorbance A of the composite film, defined as the percentage of the light intensity which is absorbed that can be expressed as :

$$A = \frac{4\pi \mathrm{Im}\left[\tilde{n}_{eff}\right] d}{\lambda} \tag{2.5}$$

where d is the thickness of the composite film and equal to 13.2μm. The low-frequency absorbance spectra is reported in Figure 2.12. As expected, the absorbance increases with the increase of the frequency.

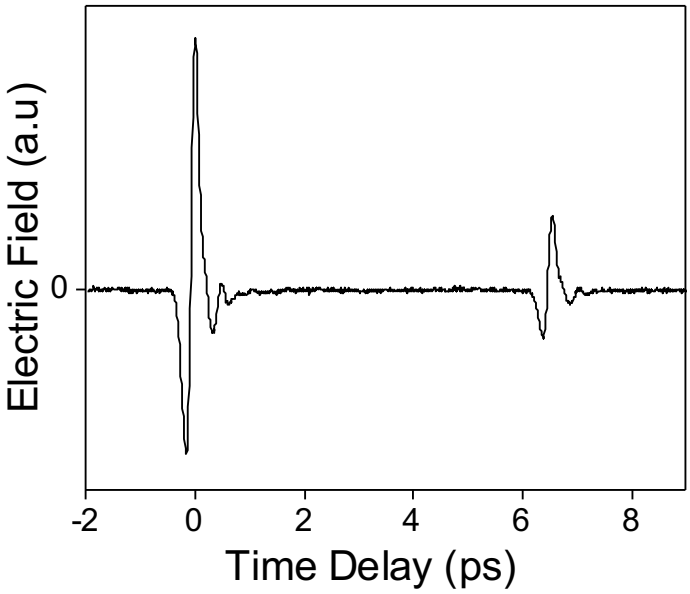

Fig. 2.10 *Temporal waveform of a THz pulse transmitted through a high resistivity silicon substrate. A second signal is measured 6.5 ps after the main peak which is the result of the first internal reflexion within the silicon substrate.*

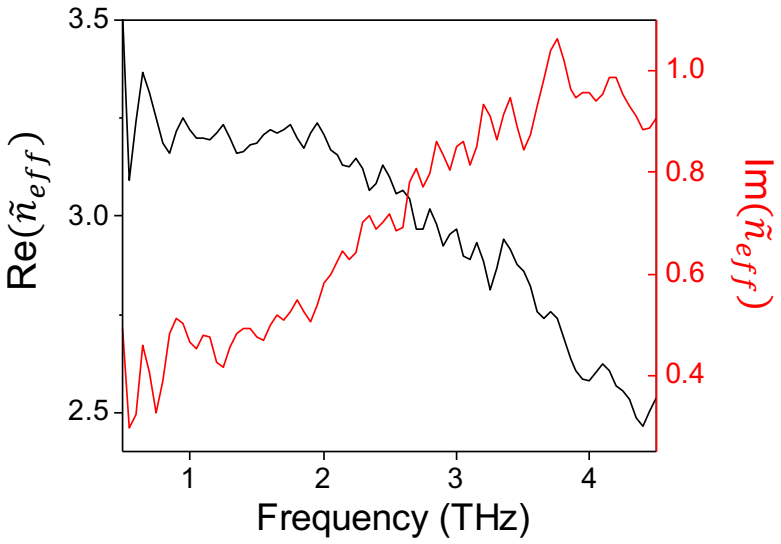

Fig. 2.11 *Real and imaginary parts of the complex refractive index $\tilde{n}_{eff}$ of the composite film composed of NCs and their surrounding environment made of ligands and air. The real part decreases slowly, remaining close to the HgTe bluk values. The imaginary part increases with the frequency, reaching a plateau above 3.5 THz.*

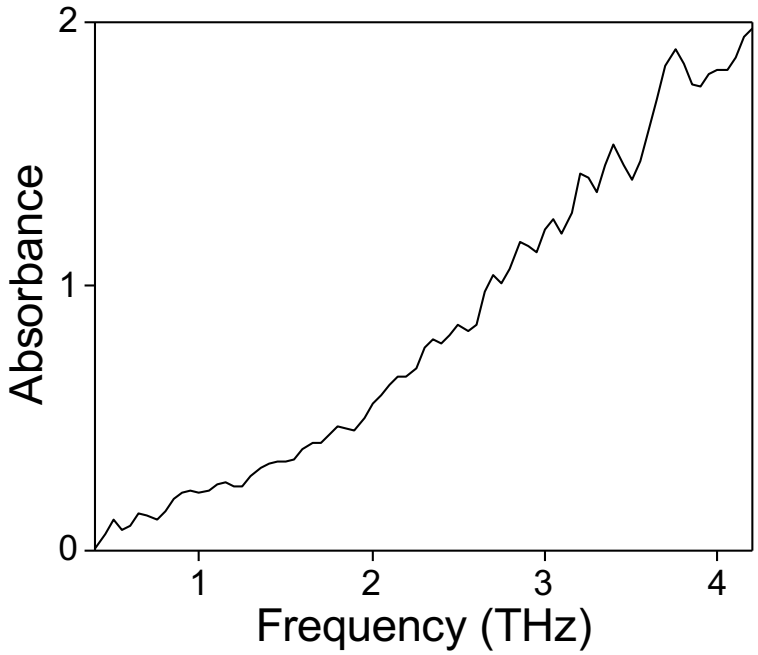

Fig. 2.12 *Absorbance spectrum of the NC film obtained by THz-Time Domain Spectroscopy.*

2.3.3 Absorbance at high-frequency using FTIR Spectroscopy

To extend the investigated spectral range to 40 THz (i.e. 1335 cm^{-1}), we measure the absorbance of the composite film using a Fourier transform infrared (FTIR) spectrometer. Indeed, tandard FTIR system benefits from a very broad bandwidth, which can extend from the visible/near infrared range down to 120 cm^{-1} (i.e. 4 THz).

Description of FTIR spectrometer In FTIR system, the sample under investigation is illuminated by white light delivered by a thermal light source, a Globar SiC globar in our case. The light is collimated and passed through a Michelson interferometer, as sketched in Figure 2.13. The interferometer consists of a beamsplitter, transmitting half of the beam while reflecting the other half. One of these two beams is reflected by a fixed mirror whereas the other one is reflected by a moving mirror. Position of the latter can be adjusted and measured precisely with a He-Ne laser. The two reflected beams pass once again through the beamsplitter. This results in one beam going to the detector and one going back to the source. In transmission configuration, the sample under investigation is placed along the beam propagating towards the detector. As the moving mirror is translated, the optical path in the second arm varies, and constructive and destructive interferences occur successively.

A typical FTIR measurement consists of a detected intensity for a set of mirror positions and is called an interferogram. In the theoretical case of a single frequency source, as the mirror is translated, the measured interference pattern exhibits oscillations. The associated spatial frequency is directly proportional to the inverse of the wavelength, called the wavenumber and expressed in cm^{-1}. For broadband sources, the interferogram is the sum of

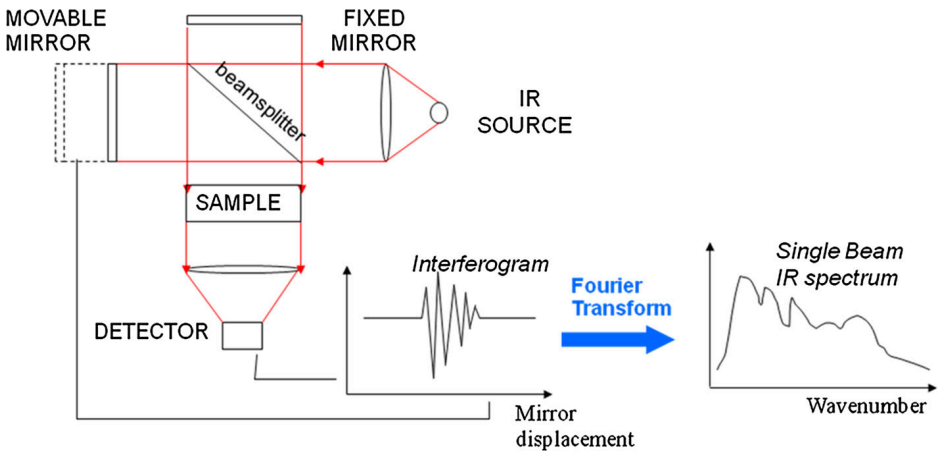

Fig. 2.13 *Scheme of a conventional FTIR spectrometer in transmission configuration.*

all the oscillations corresponding to each frequency. By applying a Fast Fourier Transform (FFT) to the interferogram, one obtain a discrete spatial frequency spectrum. Frequency resolution is set by the inverse of the achievable optical path difference (OPD) between the two arms of the Michelson interferometer, while the OPD resolution sets an upper limit to the measurable frequencies according to Shannon criteria. It is possible to change the thermal light source, the beamsplitter and the detector to adapt the spectrometer to the frequency range of interest. Unlike THz-TDS experiment, which gives access to the amplitude and phase of the electric field, FTIR experiment provides only a measurement of the intensity spectrum.

Transmission measurements We use a Bruker Vertex 70 as FTIR spectrometer in transmission configuration to investigate the optical properties of the HgTe NCs film at high frequencies. A first measurement consists in recording the interferogram with the composite film deposited on its substrate as a sample, and a second one with the bare high-resistivity silicon substrate as the sample. The ratio of the first spectrum by the second one gives the transmittance spectrum in intensity. We make the assumption that the transmittance is linked to the absorbance by the relation $T(\omega) = 1 - A(\omega)$ as the HgTe NCs composite film is highly absorbing. Figure 2.14 shows the absorbance spectrum from 1330 cm^{-1} to 120 cm^{-1} of the HgTe NCs sample obtained by FTIR spectroscopy.

We observe two distinct regimes. At high energy (>700 cm^{-1}), a broad absorption is observed attributed to interband transitions in the HgTe NCs between the lower and upper Γ_8 bands, as transitions between the Γ_6 and the upper Γ_8 bands can not be addressed at these frequencies. Also, the feature observed here happens at frequencies much higher than what was predicted by Equation 1.10. This can be attributed to the n-doping of the NCs, which blue-shifts and smoothens the resonance. A first estimation based on this blue-shift indicates a Fermi level of about 75meV. Below 400 cm^{-1} (i.e. 50 meV or 12 THz or 25 µm), there is a large absorption resonance, non-symmetrical, centered at 148 cm^{-1} (∼4.5 THz). This absorption is attributed to intraband transitions in the self-doped HgTe NCs [41, 48]. We

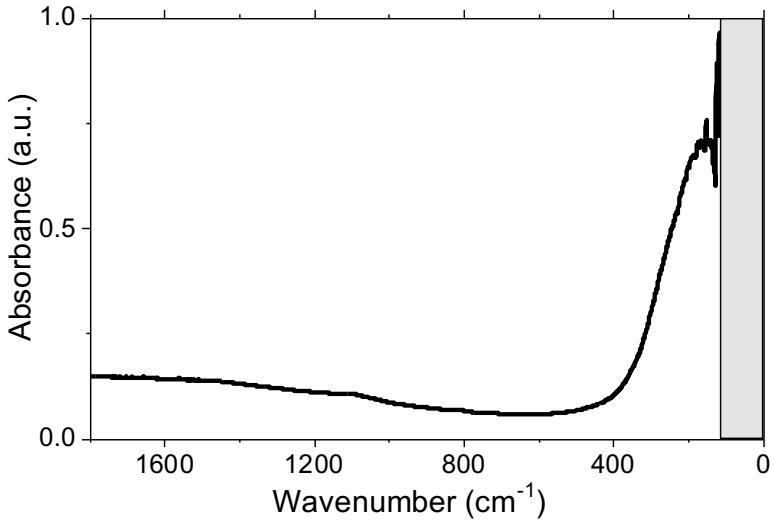

Fig. 2.14 *Absorption spectrum of a NC film obtained by FTIR spectroscopy. It exhibits a large absorption feature under 10THz, which is attributed to the n-doped nature of the NCs. The higher frequency interband feature happens for wavenumbers >700cm^{-1}.*

attribute the narrow absorption resonace observed at 120 cm^{-1} to the additional transverse optical (TO) phonon absorption, consistently with the Raman spectrum (see Figure 2.2.b)).

We now merge the low-frequency and high-frequency measurements obtained with THz TDS and FTIR systems respectively. As these two measurements were performed independently, we report them in arbitrary values in Figure 2.15. The relative values of the two sets of data have been arbitrarily matched in their overlapping spectral region. We uniquely obtain a broad absorption spectrum of the large HgTe NCs film with including the full THz spectral range, from 53 THz down to 0.4 THz.

In this section, we have reported the full (enlarge) absorbance spectrum of the composite HgTe NCs film, which displays interband absorption in the mid-infrared range and a broad intraband absorption resonance in the THz spectral range. To gain insight into the physical origin of the THz absorption resonance, we present in the next section a microscopic model of intraband processes in large and self-doped HgTe NCs.

2.4 Modeling of intraband absorption of self-doped HgTe NCs film

In previous works, the THz absorption resonance is attributed to intraband transitions made possible by the intrinsic electronic doping of large HgTe NCs. This raises a question about the physical origin of this low energy absorption resonance: is it the result of intraband absorption described by a 1 electron Hamiltonian or do collective plasmonic effects already occur? This question is of utmost importance for the realization of THz optoelectronic devices based on large HgTe NCs. To provide answers, we model the absorption cross section of the self-doped HgTe NCs film using a particle-in-a-box model and taking into account

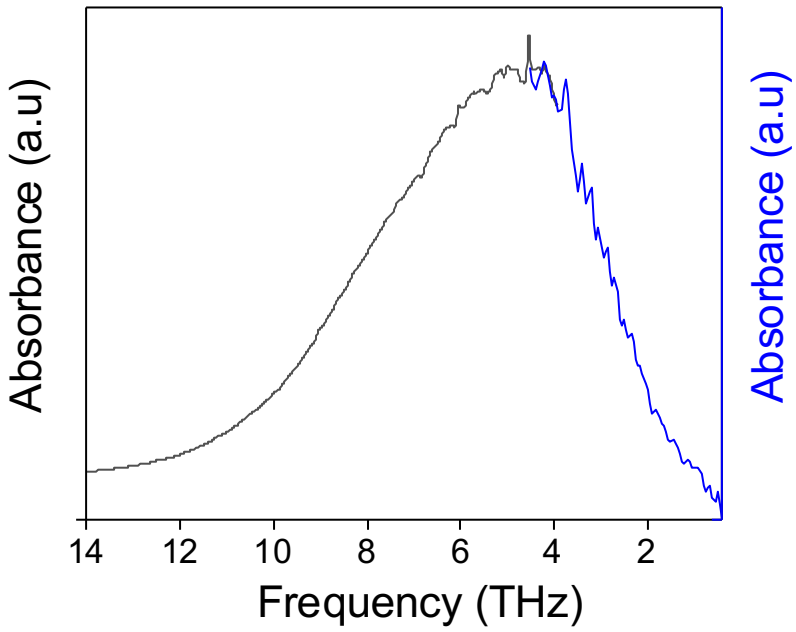

Fig. 2.15 *Full intraband absorbance spectrum obtained by matching the measurements obtained from FTIR (grey line) and TDS (blue line) measurements.*

thermal carrier distribution effects. By confronting our prediction with experimental results, we identify the relative contribution of multiple single carrier intraband transitions between quantized states and collective excitations.

2.4.1 Particle-in-a-Box quantum model

While tight-binding theory is powerful in providing accurate calculation of cross section absorption[68], we develop here a simple effective mass model of a doped NC based on charge carriers confined to a three-dimensional box of size L with the objective of providing intuitive understanding. The electrons are considered as free in the absence of electric field (the interactions with their environment are contained in the effective mass m_e^* =0.03 m_0 for HgTe). As presented in section 1.1.2, the electron wavefunctions $\Psi(r)$ are defined by a set three quantum numbers (l,m,n)$\in \mathbb{N}^{*3}$ given by:

$$\Psi_{l,m,n}(r) = \sqrt{\frac{8}{L^3}} \sin\left(\frac{l\pi}{L}x\right) \sin\left(\frac{m\pi}{L}y\right) \sin\left(\frac{n\pi}{L}z\right)$$

with the corresponding energy :

$$E_{l,m,n} = \frac{\hbar^2\pi^2}{2m_e^*L^2}(l^2+m^2+n^2)$$

These energy values are the eigenvalues of the unperturbed Schrödinger equation. Also, in the model, we account for the distribution of the electrons in the NC, which are at

thermal equilibrium. The electrons are distributed over energy states following a Fermi–Dirac statistics given by:

$$f_{\mathrm{FD}}(E_{l,m,n}) = \frac{1}{e^{(E_{l,m,n}-\mu)/k_BT}+1}$$

with μ the chemical potential of the NC. This consideration is motivated by the fact that the energy level spacing in these large NCs is quite low with regards with thermal energy k_BT, which makes many states partially occupied. In previous works reported in the literature, the effect of thermal carrier distribution among the NC states was disregarded, as small NCs of typically <10 nm sizes were investigated with characteristic level spacings largely surpassing k_BT [69]. Here, we distinctively take into account population effects, i.e. thermal carrier distribution effect, as the largest NCs have a denser energy spectrum.

2.4.2 Intraband susceptibility of the composite film

We now consider the interaction of the NC with the incident optical field $\overrightarrow{E}$ of pulsation ω in the THz spectral range and polarized along $\overrightarrow{z}$. We assume the electric dipolar approximation, as the wavelength of the electric field considered here is very large compared to the size of the NC and thus neglect the spatial variation of $\overrightarrow{E}_z$. The intraband polarization $\overrightarrow{P}_{intra}$ in the NC induced by the incident electric field $\overrightarrow{E}_z = E_0 e^{i\omega t}\overrightarrow{e_z}$ is defined by:

$$\overrightarrow{P}_{intra} = \epsilon_0 \chi_{intra} \overrightarrow{E}_z = -\frac{e\langle z\rangle}{V_{NC}}\overrightarrow{e_z} \tag{2.6}$$

where χ_{intra} is the intraband complex susceptibility of an NC, $-e\langle z\rangle$ is the thermal average of the electron dipole along the electric field polarisation direction and V_{NC} the volume of the NC. To determine χ_{intra}, we calculate $\langle z\rangle$ using density matrix formulation of quantum mechanics because this allows to take into account the statistical thermal distribution of electrons on the different eigenstates. In this formalism, the average value of the position operator for the electron, $\hat{z}$, is expressed as :

$$\langle \hat{z}\rangle = Tr(\hat{\rho}\,\hat{z}) \tag{2.7}$$

The time-evolution of $\hat{\rho}$ is described by :

$$\frac{\partial\hat{\rho}}{\partial t} = -\frac{i}{\hbar}[\hat{\mathrm{H}},\hat{\rho}] - \gamma(\hat{\rho}-\hat{\rho}^{st}) \tag{2.8}$$

The first term corresponds to the regular equation of motion for the density matrix. Here, $\hat{H} = \hat{H}_0 + \hat{\mathrm{V}}$ is the Hamiltonian of the system and $\hat{H}_0$ the Hamiltonian of the free (unperturbated) NC with eigenstates $|\Psi_{l,m,n}\rangle$ and associated energies E_{lmn} so that $\hat{H}_0|\Psi_{l,m,n}\rangle = E_{l,m,n}|\Psi_{l,m,n}\rangle$. $\hat{V}$ is a (semiclassical) perturbing Hamiltonian that represents the energy of interaction of the NC with the incident applied radiation field, expressed as $\hat{V} = -\overrightarrow{\mu}.\overrightarrow{E}$ where $\overrightarrow{\mu}$ denotes the electric dipole moment operator of the NC. In our experimental condition, $\hat{V} = eE_0e^{-i\omega t}\langle\hat{z}\rangle$.

The second term of Equation 2.8 corresponds to the phenomenological part, which tends to make the system come back to equilibrium, with a corresponding damping factor γ that represents the interaction with the thermal reservoir. It takes into account scattering events,

such as phonon interaction. Note that $\gamma = \frac{1}{T}$, where T can be seen as the time required for the system to come back to equilibrium when the electric field is no longer applied. We assume damping constant γ to be energy independent.

Since we consider a perturbative interaction, one can write, in the approximation of a linear response that $\hat{\rho} \approx \hat{\rho}^{(0)} + \hat{\rho}^{(1)}$ with $\hat{\rho}^{(0)} = \hat{\rho}^{(st)}$ the density matrix of the unperturbed system in a stationary state, so that $\langle \Psi_{l,m,n} | \rho^{(0)} | \Psi_{l',m',n'} \rangle = f_{\mathrm{FD}} \delta_{l,l'}, \delta_{m,m'} \delta_{n,n'}$ is the occupancy probability of state $|\Psi_{l,m,n}\rangle$.
For more convenience, in the following derivation, we introduce the notations:
$|\Psi_i\rangle = |\Psi_{l,m,n}\rangle \quad ; \quad |\Psi_f\rangle = |\Psi_{l',m',n'}\rangle \quad ; \quad E_i = E_{l,m,n} \quad ; \quad E_f = E_{l',m,'n'}$

Here, we only present the main steps of the calculation, a more detailed description is presented in Appendix B.1. Considering only the first order terms of Equation 2.8, we obtain:

$$\frac{\partial \hat{\rho}^{(1)}}{\partial t} \approx -\frac{i}{\hbar} \left\{ [\hat{H}_o, \hat{\rho}^{(1)}] + [\hat{V}, \hat{\rho}^{(0)}] + \right\} - \gamma \hat{\rho}^{(1)} \tag{2.9}$$

Using matrix elements, Equation 2.9 writes :

$$\frac{\partial \rho^{(1)}_{i,f}}{\partial t} = -\frac{i}{\hbar} \left\{ \underbrace{\langle \Psi_i | [\hat{H}_o, \hat{\rho}^{(1)}] | \Psi_f \rangle}_{1} + \underbrace{\langle \Psi_i | [\hat{V}, \hat{\rho}^{(0)}] | \Psi_f \rangle}_{2} + \right\} - \gamma \rho^{(1)}_{i,f} \tag{2.10}$$

$$1 : \langle \Psi_i | [\hat{H}_o, \hat{\rho}^{(1)}] | \Psi_f \rangle = (E_i - E_f)\ \rho^{(1)}_{i,f}$$
$$2 : \ \langle \Psi_i | [\hat{V}, \hat{\rho}^{(0)}] | \Psi_f \rangle = V_{i,f}\ (f_{\mathrm{FD}}(E_f) - f_{\mathrm{FD}}(E_i))$$

Replacing 1 and 2 in Equation 2.10 yields (cf. B.1.1) :

$$\frac{\partial \rho^{(1)}_{i,f}}{\partial t} = -\frac{i}{\hbar}(E_i - E_f)\rho^{(1)}_{i,f} - \frac{i}{\hbar}\left(f_{\mathrm{FD}}(E_f) - f_{\mathrm{FD}}(E_i)\right) V_{i,f} - \gamma \rho^{(1)}_{i,f} \tag{2.11}$$

We now focus on the derivation of $V_{i,f}$. Equation 2.11 can now be expressed as follow :

$$\frac{\partial \rho^{(1)}_{i,f}}{\partial t} = -\frac{i}{\hbar}(E_i - E_f - i\gamma\hbar)\rho^{(1)}_{if} - \frac{i}{\hbar}\left(f_{\mathrm{FD}}(E_f) - f_{\mathrm{FD}}(E_i)\right) e z_{i,f} E_z e^{-i\omega t} \tag{2.12}$$

Equation 2.12 is a first order differential equation on $\rho^{(1)}_{i,f}$. The resolution of this equation is presented in B.1.2 and leads to :

$$\rho^{(1)}_{i,f}(t) = eE_z(t) z_{i,f} \frac{f_{\mathrm{FD}}(E_i) - f_{\mathrm{FD}}(E_f)}{E_i - E_f - \hbar\omega - i\hbar\gamma} \tag{2.13}$$

It is then possible to express $\langle \hat{z} \rangle$:

$$\langle \hat{\mathrm{z}} \rangle = Tr(\hat{\rho}\, \hat{\mathrm{z}}) = 2 \sum_{i,f} \rho_{i,f} \mathrm{z}_{f,i} \approx 2 \sum_{i,f} \left(\rho^{(0)}_{i,f} z_{f,i} + \rho^{(1)}_{i,f} z_{f,i} \right) \tag{2.14}$$

Note that the factor 2 in front of the right hand side terms accounts for the spin degeneracy. As mentioned earlier, the stationary part of the density matrix gives $\rho^{(0)}_{i,f} = f_{\mathrm{FD}} \delta_{i,f}$. Thus

$\rho^{(0)}_{i,f} z_{f,i} = f_{\mathrm{FD}}\delta_{i,f}\langle\Psi_f|\hat{z}|\Psi_i\rangle = 0$ since $\langle\Psi_i|\hat{z}|\Psi_i\rangle = 0$ as the $|\Psi_i\rangle$ wavefunction presents parity. Equation 2.14 becomes:

$$\langle\hat{\mathrm{z}}\rangle = 2\sum_{i,f}\rho^{(1)}_{i,f}\mathrm{z}_{fi} = 2eE_z(t)\sum_{i,f}\frac{f_{\mathrm{FD}}(E_i) - f_{\mathrm{FD}}(E_f)}{E_i - E_f - \hbar\omega - i\hbar\gamma}|z_{if}|^2$$

We can now express the linear susceptibility of an NC:

$$\chi_{intra}(\omega) = -\frac{2e^2}{\varepsilon_0 V_{NC}}\sum_{i,f}\frac{f_{\mathrm{FD}}(E_i) - f_{\mathrm{FD}}(E_f)}{E_i - E_f - \hbar\omega - i\hbar\gamma}|z_{i,f}|^2 \tag{2.15}$$

We now detail $|\Psi_i\rangle$, $|\Psi_f\rangle$, E_i and E_f by reintroducing the three quantum numbers (l,m,n). We can rewrite the Equation 2.14 as:

$$\langle\hat{z}\rangle = 2\sum_{ll',mm',nn'}\rho^{(1)}_{\substack{(l,m,n)\\(l',m,'n')}}\langle\Psi_{l',m',n'}|\hat{z}|\Psi_{l,m,n}\rangle \tag{2.16}$$

The eigenstates form an orthonormal basis, thus $\langle\Psi_{l',m',n'}|\Psi_{l,m,n}\rangle = \delta_{l,l'},\delta_{m,m'}\delta_{n,n'}$. In our model, the position operator $\hat{z}$ for the electron is related to quantum number n. Therefore, Equation 2.16 can be simplified into :

$$\langle\hat{z}\rangle = 2\sum_{l}\sum_{m}\sum_{nn'}\rho^{(1)}_{\substack{(l,m,n)\\(l,m,n')}}\langle\Psi_{l,m,n'}|\hat{z}|\Psi_{l,m,n}\rangle = 2\sum_{l}\sum_{m}\sum_{nn'}\rho^{(1)}_{\substack{(l,m,n)\\(l,m,n')}}z_{n',n} \tag{2.17}$$

As detailed in annexe B.2, the calculation of $z_{n'n}$ leads to:

$$z_{n'n} = \begin{cases} 0 & \text{if } n' \text{ and } n \text{ have the same parity} \\ \frac{2L}{\pi^2}\left[\frac{1}{(n'+n)^2} - \frac{1}{(n'-n)^2}\right] & \text{otherwise} \end{cases} \tag{2.18}$$

Here, we can see that the selection rules naturally appear from the calculations. Equation 2.13 becomes :

$$\langle\hat{z}\rangle = 2eE_z(t)\sum_{l}\sum_{m}\sum_{\substack{nn'\\n\neq n'}}\frac{f_{\mathrm{FD}}(E_{l,m,n}) - f_{\mathrm{FD}}(E_{l,m,n'})}{E_{l,m,n} - E_{l,m,n'} - \hbar\omega - i\hbar\gamma}|z_{n',n}|^2 \tag{2.19}$$

and we obtain for the linear susceptibility of an NC :

$$\chi_{intra}(\omega) = -\frac{2e^2}{\varepsilon_0 V_{NC}}\sum_{l}\sum_{m}\sum_{\substack{nn'\\n\neq n'}}\frac{f_{\mathrm{FD}}(E_{l,m,n}) - f_{\mathrm{FD}}(E_{l,m,n'})}{E_{l,m,n} - E_{l,m,n'} - \hbar\omega - i\hbar\gamma}|z_{n',n}|^2 \tag{2.20}$$

Absorbance of the composite film From the intraband susceptibility χ_{intra}, we can calculate the permittivity of the HgTe NCs film:

$$\varepsilon(\omega) = 1 + \chi(\omega) = 1 + \chi_{inter}(\omega) + \chi_{intra}(\omega) \tag{2.21}$$

The total susceptibility also includes interband transitions. From Figure 2.14, it is clear that the interband resonance (>20 THz) is far away from the low-energy spectral range (0.3 to 10 THz) studied here. Thus, $\chi_{inter}(\omega)$ is described as a constant offset $\varepsilon_\infty - 1$ over the frequency range of interest. Thus, the permittivity reduces:

$$\varepsilon(\omega) = \varepsilon_\infty + \chi_{intra}(\omega) \tag{2.22}$$

Equation 2.20 is now substituted into this expression to obtain the permittivity of an HgTe NC :

$$\varepsilon(\omega) = \varepsilon_\infty - \frac{2e^2}{\varepsilon_0 V_{NC}} \sum_l \sum_m \sum_{\substack{nn' \\ n \neq n'}} \frac{f_{\mathrm{FD}}(E_{l,m,n}) - f_{\mathrm{FD}}(E_{l,m,n'})}{E_{l,m,n} - E_{l,m,n'} - \hbar\omega - i\hbar\gamma} |z_{n',n}|^2 \tag{2.23}$$

To link the calculated permittivity of the NCs to the experimental absorption of the HgTe NCs film, we calculate the absorption cross-section. Indeed, for a HgTe NC of size much smaller than the wavelength in the medium, the optical extinction is dominated by absorption of light. In the quasi-static approximation, one has [70]:

$$C_{abs,NC}(\omega) = V_{NC} k_m Im\left[\frac{\varepsilon(\omega) - \varepsilon_{em}}{\varepsilon_{em} + b(\varepsilon(\omega) - \varepsilon_{em})}\right] \tag{2.24}$$

where $k_m = \frac{\omega\sqrt{\varepsilon_m}}{c}$ is the light wavevector in the host medium, ε_{em} the relative permittivity of the surrounding medium and b a shape-dependent parameter accounting for the local-field effect. We neglect interference effects from different NCs in the composite film. In the calculation, we take $\varepsilon_\infty = 16$, $\varepsilon_{em} = 2$ (dodecanethiol ligands and air). For a cubic NC, the value of b is not analytical; we use b = 1/3 (value for a spherical particle) in the calculations, which is not expected to change the physical meaning of the results [69]. Equation 2.24 can be rewritten as :

$$C_{abs,NC}(\omega) = 3V_{NC} k_m Im\left[\frac{\varepsilon(\omega) - \varepsilon_{em}}{2\varepsilon_{em} + \varepsilon(\omega)}\right] \tag{2.25}$$

In order to include the inhomogeneous distribution of sizes of the NCs, we calculate the average absorption cross section :

$$C_{abs} = \sum_n P_n C_{abs,NC}(\omega, L_n)$$

where $P_n = N_n/N_{NC}$ is the normalized inhomogeneous distribution of sizes with N_n the number of NCs of size L_n and N_{NC} the total number of NCs in the composite film. It is important to stress that all the NCs share the same chemical potential μ regardless of their size since they are embedded in the same environment. Thus, it is the number of electrons in the NCs that evolves with the NC size, such that larger NCs host a larger number of electrons. For independent NCs and neglecting scattering effects [70], the absorbance $A(\omega)$ of the composite medium is expressed as :

$$A(\omega) \approx \sum nN_n C_{abs}(\omega, L_n)/S \tag{2.26}$$

where S is the surface of the THz beam incident on the composite film.

2.4.3 Interpretation of the experimental results

We first analyze the experimental results with our full quantum-mechanical model. The two adjustable parameters are μ and γ and their values were set to allow the best fit of the overall spectral shape of the experimental data. Figure 2.16 shows the result of calculations of the normalized absorbance of the composite film, $A(\omega)$ (red line), for a chemical potential μ=35 meV and a broadening of γ=10 meV and an inhomogeneous size distribution of the NCs similar as the one presented in Figure 2.1.c). The calculations capture all the key experimental features (blue circles), including the peak frequency and the asymmetric broadening of the absorbance resonance.

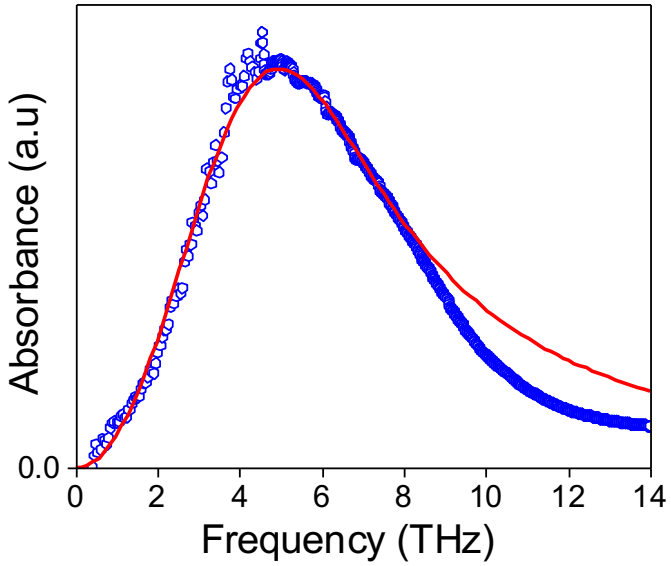

Fig. 2.16 *Calculations based on the full quantum-mechanical model of the normalized absorbance of the composite film, A(ω) (red line), for a chemical potential μ = 35 meV, a broadening of γ = 10 meV, a size distribution reported in Figure 2.1.c) and experimental data obtained from THz-TDS and FTIR measurements (blue dots).*

From the model, for a fixed chemical potential, it is possible to calculate the number of electrons in the NCs, $N_e(L)$, as a function of their sizes, and obtain the corresponding carrier density, $n_e(L)$, using :

$$N_e(L) = 2 \sum_{l,m,n} f_{FD}(E_{l,m,n}) \text{ and } n_e(L) = N_e(L)/L^3$$

These two quantities are represented in Figure 2.17 for μ=35 meV. We find that the carrier density increases with the NC size, with values in the range of $\sim$1-2$\times 10^{17}$cm^{-3} for NCs with sizes less than 100 nm. The obtained densities are much lower than those of metals with typical values $\sim 10^{22}$cm^{-3}.

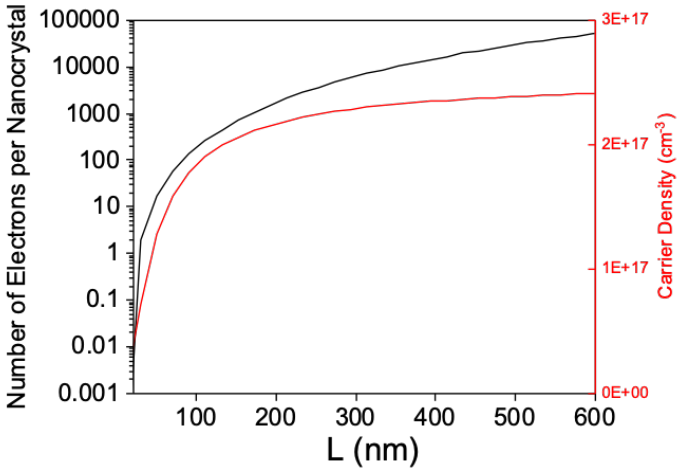

Fig. 2.17 *Number of electrons per nanocrystal (black) and corresponding carrier density (red) as a function of the nanocrystal size for a doping level μ=35meV. The carrier density of an nanocrystal with the average size L=90 nm is* $\approx 1.8\ 10^{17} cm^{-3}$.

Since the composite film is composed of NCs with large size dispersion, it is interesting to study the influence of the size of the NC on its optical response. The absorption cross section per unit volume of an individual NC, expressed as $C_{abs}(\omega,L)/V_{NC}$, is plotted in Figure 2.18.a) for various sizes of NCs ranging from 50 nm up to 1μm. The profiles show a blue-shift as the size of the NCs decreases as expected for quantum confinement effects since the energy level spacing is $\propto L^{-2}$. More quantitatively, the peak frequency exhibits the same $\propto L^{-2}$ dependence, as observed in Figure 2.18.b). Interestingly, we observe that the size dispersion only partly accounts for the broadness of the measured absorption of the NC film. As X-Ray diffraction measurements suggested that the largest NCs could actually be polycrystalline, we have also tried to fit the absorbance spectrum with a cropped size distribution that did not take largest NC into account. By considering only the NCs with a size $\leq$140 nm in the distribution from Figure 2.1.c), we obtain a satisfactory fit but with a chemical potential of μ=8meV. Indeed, since larger NCs exhibit absorption features at lower frequencies, not considering them may be counterbalanced by a smaller chemical potential that induces a transition at lower frequencies.

To evaluate the interplay between quantum mechanical transitions and collective excitations, let us study the permittivity of the NCs deduced from the fit of data with our microscopic model. We calculate the permittivity of a NC of size L=90 nm with μ=35 meV and γ=10 meV and plot its real and imaginary parts in Figure 2.19. We observe that Im[$\varepsilon(\omega)$] displays a resonant profile and vanishes at ω=0, while Re[$\varepsilon(\omega)$] has a positive value at ω=0 and displays a damped dispersive profile up to a frequency close to the maximum one for Im[$\varepsilon(\omega)$]. Importantly, Re[$\varepsilon(\omega)$] remains positive over the entire range. This tendency indicates the absence of localized plasmon resonance. Indeed, from Equation 2.25, the criteria on the permittivity for the appearance of a plasmon resonance is given by $|\varepsilon + 2\varepsilon_m|$

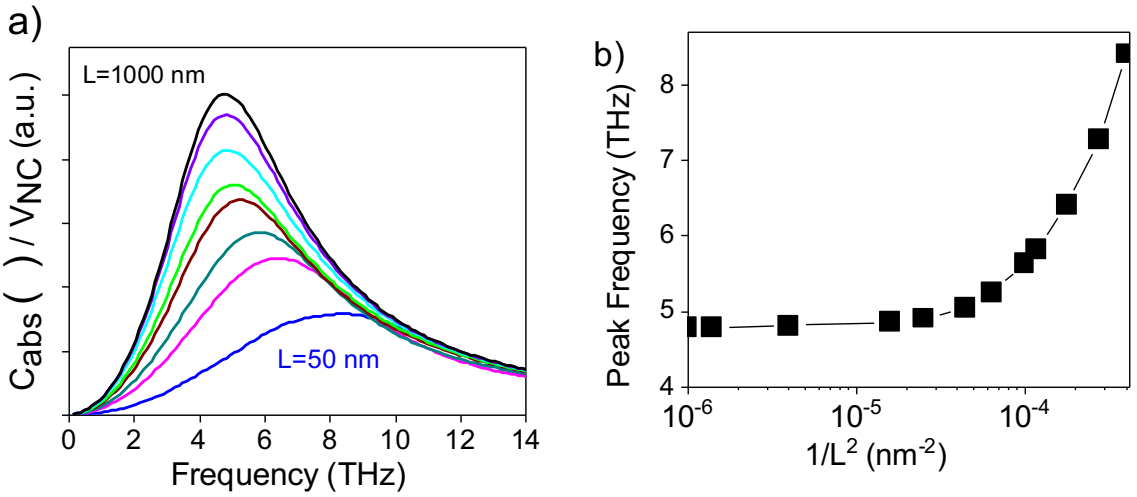

Fig. 2.18 *a) Absorption cross-section per unit volume of individual nanocrystals of various sizes. We have used the same values μ=35meV and γ=10meV than those from the previous fit. b) Peak frequency of $C_{abs}(L)$ as a function of $1/L^2$ in semi-log scale.*

is minimum (or vanishes). This condition can be simplified into :

$$Re[\varepsilon(\omega)] = -2\varepsilon_m \tag{2.27}$$

This relationship is called the Fröhlich condition, which corresponds to resonant excitation of a localized surface plasmon [70, 71]. In the self-doped HgTe NCs, investigated here, the Fröhlich condition is never met as Re$[\varepsilon(\omega)]$ remains positive for all frequencies. Consequently, the absorption does not have a pole preventing the existence of localized plasmon resonance.

Let us investigate here the possibility to induce plasmonic effects in large HgTe NCs through the increase of the doping level based on theoretical predictions. To this purpose, we calculate the minimum doping level require for the plasma contribution to become large enough to meet the Fröhlich criterion. We find that, for a NC of size L=90 nm, the chemical potential should reach $\mu \approx 130$ meV as illustrated in Figure 2.20, which reports the permittivity and the absorbance of such a highly doped NC. The plasmonic resonance occurs at higher frequencies ($\sim$ 10 THz) than the absorption resonance resulting from multiple intraband transitions of single carriers between quantized states and the shape of the resonance is more symmetrical. This result provides a strong hint on the fact that the measured absorption in self-doped large HgTe NCs is mostly explained by the multiple intraband transitions of single carriers between quantized states rather than collective excitation. Moreover, it highlights that, by increasing the doping level by using for instance an electrolyte gate, collective effects could be switch on, opening the way to the study of quantum plasmons in large HgTe NCs.

Another peculiar characteristic of the estimated permittivity of self-doped HgTe NCs is the broad resonant profile of Im$[\varepsilon]$ even for a relatively weak damping rate ($\gamma \approx$10 meV).

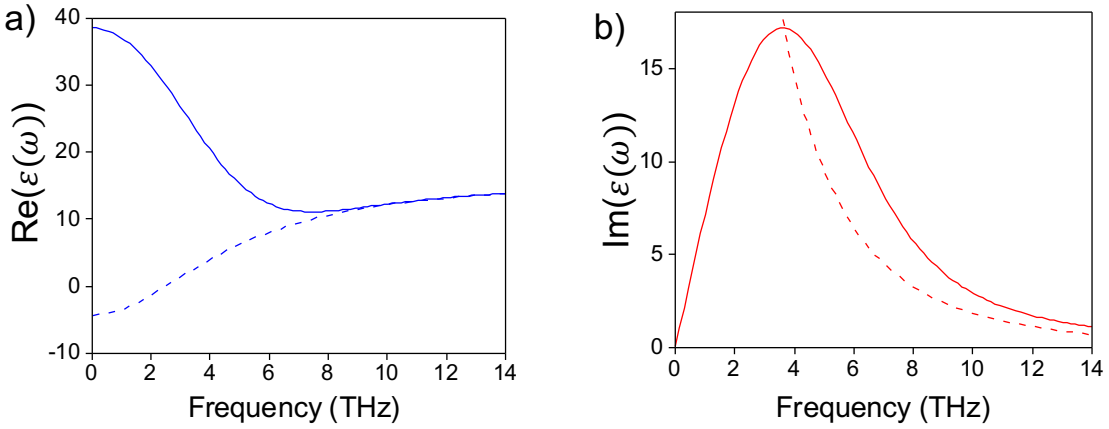

Fig. 2.19 *Real a) and imaginary b) parts of $\varepsilon(\omega)$ of the permittivity obtained by the quantum model for a NC of size L=90nm with μ=35meV, γ=10meV. The dashed lines correspond are the real and imaginary parts based on a classical Drude model with the same parameters.*

We explain this broadening by the low energy level spacing ΔE in these large size NCs with regards to the thermal carrier redistribution. Indeed, for a NC of size L=90 nm, $\Delta E \approx$1.5 meV$< \mu \in$ [8 meV-35 meV]$<k_bT\sim$25 meV, which leads to a large number of states partially populated and thus available for the dipolar transitions.

Also, we compare the calculated permittivity based on our quantum model with a classical Drude permittivity described by :

$$\varepsilon_{Drude} = \varepsilon_\infty + \frac{\omega_p^2}{\omega^2 + i\frac{2\gamma}{\hbar}} \text{ with } \omega_p^2 = \frac{n_e e^2}{m_e^* \varepsilon_0} \text{ the plasma pulsation}$$

The calculated Drude permittivity for a NC of size L=90 nm with μ=35 meV, γ=10 meV and the corresponding n_e (see Figure 2.17) is plotted in Figure 2.19. One can note that, at frequencies of interest in this work, the classical Drude permittivity strongly differs from the one obtained by our model. These differences, both in the real and imaginary parts of the permittivity, indicate that the response of the NCs is definitely different from those of the bulk material. It shows the contribution of quantum confinement effects, even for such large NCs. Indeed, as discussed in previous works [72], such marked deviations of the permittivity from the Drude model predictions can be traced back to the intraband transitions among the confined NC energy levels.

2.5 Temperature dependence of the intraband absorption

As shown in previous section, large self-doped HgTe NCs have the peculiarity that the thermal energy at room temperature exceeds the energy level spacings, which imposes the introduction of the Fermi-Dirac distribution statistic for carriers in the quantum model. By thermally populating the energy levels above the chemical potential and thus allowing

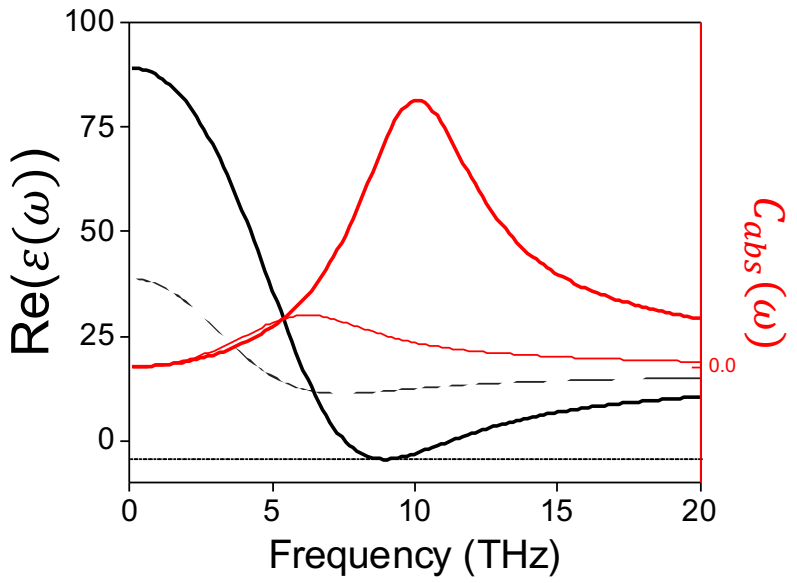

Fig. 2.20 *Real part of the permittivity (black curves) and Absorbance (red curves) of nanocrystals with μ=35meV (thin curves) and μ=130meV (thick curves). For μ=130meV the permittivity decreases down to -2ε_m=-4, reaching the Fröhlich condition. It exhibits a plasmonic resonance absorption centered at ≈10THz, which is much higher than the resonance measured at ≈5THz*

various transitions to become accessible, the temperature plays an important role in the intraband optical response of self-doped HgTe NCs. These considerations motivated us to study more deeply the influence of temperature on the THz absorption of these large HgTe NCs. In this section, we will present low frequency transmission measurements performed at temperatures ranging from 4 K to 300 K and we will detail the analysis of these results with respect to theoretical predictions.

2.5.1 Experimental set-up

We use our THz-TDS set-up and place the HgTe NCs film sample and the bare silicium substrate onto a cryostat with optical access to control the temperature of the samples. The cryostat is cooled down using a flux of liquid helium and the temperature is adjusted with a controller. The range of accessible temperature goes from 4 K up to room temperature. The HgTe NCs film studied here has been synthesized following the same procedure as the one described in section 2.2, although HgTe NCs do not come from the same batch. Note that doping and dispersion can slightly vary from a batch to another. However, differences of size dispersion among samples is mainly caused by the poor reproductibility of the film deposition methods rather than differences between batches. Inhomogeneities across the film surface induced by size dispersion of the HgTe NCs and fluctuation of the film thickness pose a problem for measurements at different temperatures due to the thermal contraction of the cold finger in the cryostat. Indeed, thermal contraction causes significant shifts in the position of the sample with respect to the incident THz beam when the temperature changes.

This effect is depicted in Figure 2.21 which shows a typical vertical shift in sample position of 1 mm between a temperature of 300 K and 4 K. To avoid measurement errors due to the inhomogeneous sample effects, we glue the two samples, the HgTe NCs film and the silicon substrate, on a single sample holder which has two holes separated by 4 mm. The thermal shrinkage between the two holes of the sample holder is negligible compared to the overall displacement. Thus the position of the HgTe NCs film is defined by a constant translation vector from the position of the reference sample on which we perform a calibration of its precise position with respect to the incident THz beam for each temperature.

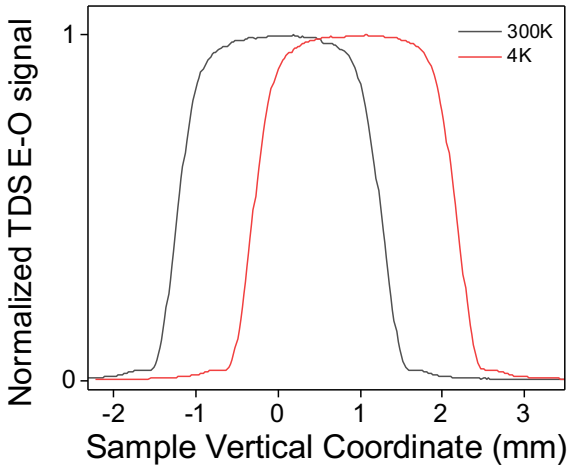

Fig. 2.21 *Normalized vertical scan of a THz-TDS electro-optic (E-O) signal set at a time delay τ_1 corresponding to the maximum amplitude after propagation through a silicon substrate glued on top of a holed sample holder. The sample holder hole diameter is 2.5mm. As the temperature decreases, the cold finger in the cryostat thermally retracts, shifting the sample towards higher position. Displacements as high as 1mm have been measured between 300K and 4K*

2.5.2 Probing intraband absorption from 20 K to 300 K

We first determine the sample and reference silicon substrate thickness by measuring the delay between the main peak of the transient electric field and the first echo, using a temporal windowing of 10 ps. We obtain $d_{\text{sample,sub}}$=500.7μm and $d_{\text{ref,sub}}$=500.9 μm. The thickness of the deposited HgTe NCs film is estimated using an optical microscope to $d_{\text{film}} \approx 5.3\mu m$. Then, we measure the transient electric fields transmitted through the composite film sample and through the reference sample at different temperatures. Applying a Fourier transform on the recorded time-resolved electric fields, we obtain the amplitude transmittance spectra of the HgTe NCs film for different temperatures. Figure 2.22.a) shows the measured transmittance spectra for temperature ranging from 300 K down to 65 K. Figure 2.22.b) shows the corresponding absorbance spectra obtained following the same procedure as described in section 2.3.2.

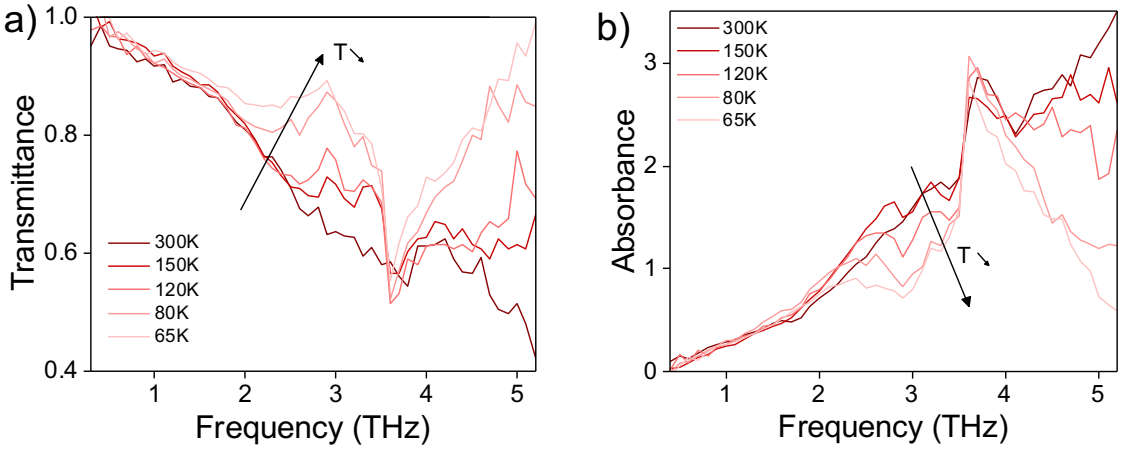

Fig. 2.22 *Transmittance spectra a) and corresponding absorbances spectra b) of large HgTe QD as function of temperature for [300K - 65K] . In both graphs, lower temperatures correspond to lighter curves. As the temperature is decreased, the overall intraband absorbance seem to diminish while the center frequency redshifts. Additionally, a strong and sharp absorption peak is unveiled with its center frequency corresponding to the optical phonon measured in Raman spectroscopy.*

We observe that the absorption characteristic at T=300 K resembles that measured in Figure 2.15 even if the HgTe NCs are from another batch. However, the absorption plateau at high frequency is not yet reached in our accessible spectral range, indicating that the resonance occurs at frequencies higher than 5 THz. We also notice the presence of an additional absorption peak at 3.6 THz, which corresponds to the energy of the transverse optical phonons at 120 cm^{-1} (see Figure 2.2.b)). As the temperature decreases, we observe that the intraband absorption is constant from 0.4 THz up to 2 THz for all temperatures but above 2 THz, the intraband absorption progressively decreases and its spectral shape strongly changes. Also, our measurements reveal that the optical phonon absorption peak remains of constant amplitude when the temperature decreases and dominates the total absorption at T=65 K. Indeed, around 3.6 THz, the consecutive curves are precisely superimposed, which demonstrates that the amplitude and the spectral position of the transverve optical phonon peak is independent of the temperature. These tendencies indicate that the transmittance spectra result from two main effects: an intraband absorption linked to transitions between electronic states, whose efficiency is reduced with the decrease of temperature, and an additional absorption around 3.6 THz attributed to the excitation of the transverse optical phonon.

As the temperature is decreases below 65 K, we observe a non-intuitive evolution of the absorbance with the temperature, (see Figure 2.23.b)). Indeed, the absorbance spectra for a temperature of 50 K and 20 K do not continue to decrease; on the contrary, they increase and show a profile very similar to the transmittance at 300 K. We made sure that this is not due to a problem related to the temperature controller by checking the evolution of the

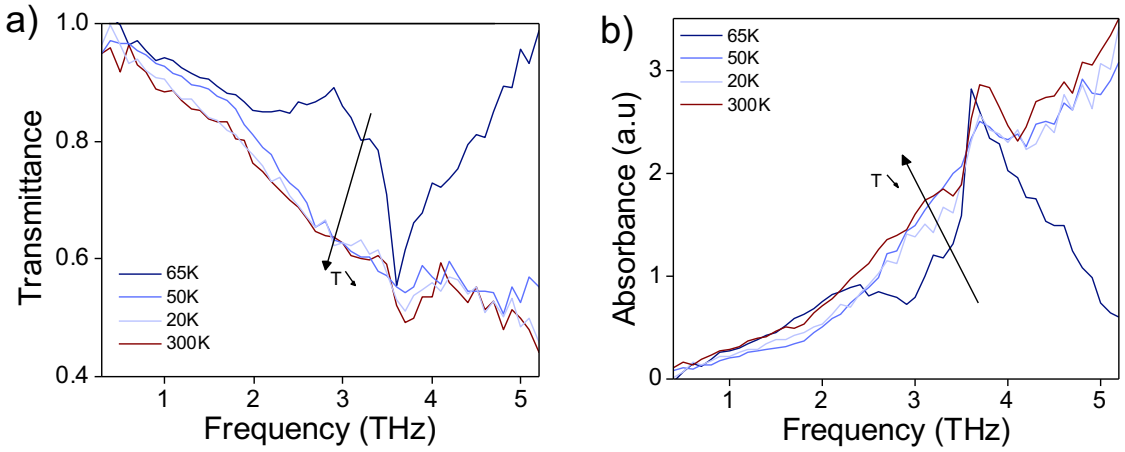

Fig. 2.23 *Transmittance spectra a) and corresponding absorbances spectra b) of large HgTe QD as function of temperature for [65K - 20K] . In both graphs, lower temperatures correspond to lighter curves. In contrast with the trend of the first temperature domain, decreasing the temperature here results in an enhancement of the absorption that seems to go back to the feature at 300K (in brown).*

transmittance spectra of the reference sample. As expected, the measured THz absorption of the silicon substrate decreases with the decrease of the temperature, providing a counter measurement of the temperature in the cryostat during experiments. Therefore, we observe that the evolution of the transmittance spectra with the temperature exhibit very specific features, which can be separated into two main temperature regions, above and below a critical temperature of T=65 K.

2.5.3 Confrontation of data with theoretical prediction

We now interpret these results using the quantum model of the intraband absorption in a NC. Figure 2.24.a) reports the absorbance spectra from 0 to 10 THz, predicted by the quantum model for temperatures of T=4 K, T= 120 K and T=300 K. The parameters used here are μ=8 meV and γ=10 meV and the size distribution is the same as the one presented in Figure 2.1.c). We observe that the absorbance of large HgTe NCs is predicted to strongly depend on the temperature. Indeed, as the temperature decreases, the absorbance decreases over the whole spectral range and the absorption peak is shifted towards low frequencies. For instance, from 300 K to 20 K, the absorption is decreased by more than a factor 10 and the peak frequency evolves from 5 THz down to 2.5 THz. We attribute these significant changes in the intraband absorption to the dependance of the carrier distribution with the temperature. Indeed as the temperature is lowered, less electronic states are thermally populated, and thus fewer transitions are available. This strong dependance on the temperature of the intraband absorption is specific to large NCs as the energy level spacings are comparable or less than thermal energy between T=4 K and T=300 K.

Then, we compare the measured absorbance spectra for temperature T=300 K, T=120 K and T=65 K with the simulated absorbance spectra for μ=20 meV, γ=10 meV and for a size

distribution of NCs truncated to L≥100nm. The later assumption is motivated by the fact that the X-ray diffraction datas indicate that larger NCs could actually be polycrystalline and that, for the HgTe NCs batch used in this study, the absorption resonance at room temperature occurs at high frequencies. Figure 2.24.b) shows that the quantum model based on multiple intraband transitions of single carriers between quantized states only partially explains the experimental results of the temperature dependence of the transmittance. Indeed, over the temperature range from 300 K to 65 K, if we exclude the absorption resonance by optical phonons around 3.6 THz, the predicted absorption spectra reproduce well the experimental characteristics, namely a strong reduction of the absorption when the temperature is reduced as well as a shift towards low frequencies. However, our model does not include the contribution of optical phonon to the absorption and therefore cannot reproduce the narrow transverse optical phonon resonance. More curiously, our model fails to reproduce the evolution of absorption spectra for temperatures below T=65 K.

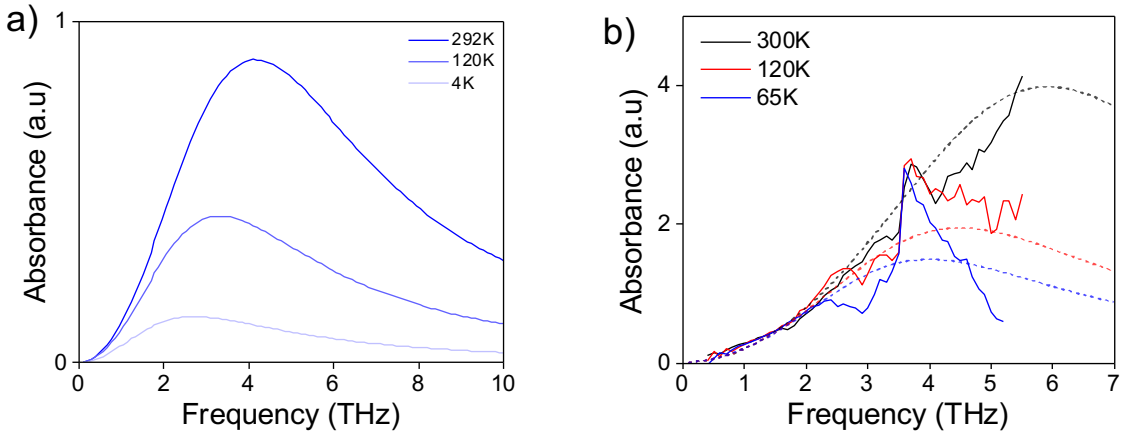

Fig. 2.24 *a) Absorbance spectra simulations based on the quantum model of intraband transitions of single carriers between quantized states. The parameters used here are μ=8meV and γ=10meV. The size distribution is the same as the one presented in Figure 2.1.c). b) Measured absorbance spectrums for temperatures T=292K, 120K and 20K. Simulations are plotted in dashed lines and have been obtained with μ=20meV and γ=10meV and a truncated distribution where L≤100nm*

Note that in our analysis, we assume that the broadening parameter γ is independent of temperature. However, γ is expected to be temperature dependent and further experiments need to be performed to get insight in the dependence of the broadening parameter with the temperature.

2.6 Conclusion

In conclusion, we have studied the optical properties of large self-doped HgTe NCs in the full THz spectral range combining THz-TDS and FTIR spectroscopy experiments. We have showed a broad THz resonant absorption centered at ∼4.5 THz. To interpret the experimental results, we have developed a quantum model that both account for the confinement

of the carriers and their thermal distribution.

From the confrontation of theoretical predictions with data, we showed that the THz absorption results from multiple intraband transitions of single carriers between quantized states and that collective excitations are negligible in self-doped THz HgTe NCs. Also, the model indicates that even at these large sizes of NCs, quantum confinement effects still have a significant contribution. Moreover, our analysis has provided an estimation of the chemical potential of these self doped NCs that falls in the range of few tens of meV while plasmonic regime is expected to occur for chemical potential in the range of a hundred of meV. Finally, we investigated the influence of temperature on the THz absorption properties. We highlighted two distinct regimes separated by a critical temperature $T_{critical} = 65$K. For temperatures above $T_{critical}$, the evolution of the absorption with temperature appears to be due to changes in the Fermi-Dirac distribution of carriers with temperature and to narrow absorption by transverse optical phonons. For temperature below than $T_{critical}$, the THz absorption increases as the temperature decreases, which can not be explained by the quantum model.

From a technological perspective, these large HgTe NCs are very promising for the development of THz emitters and THz detectors as they exhibit a unique intense THz absorption and as they are easy to synthesize and manipulate. Also, as a perspective, we plan to investigate the quantum plasmonic regime, and to this aim, we are currently developing new devices made of large HgTe NCs, which include an electrolytic gate to control the chemical potential and thus the doping level in the HgTe NCs. The control of the chemical potential in HgTe NCs is very promising for understanding the interaction between quantum mechanical transitions and collective excitations and to pave the way for on-demand activation of quantum collective effects. From a theoretical point of view, the current model should be enriched by including the absorption by optical phonons and also a temperature dependence of the parameter γ.

Chapter 3

Dynamics of Hot Carriers under optical illumination

3.1 Motivation of this work

In the previous chapter, we demonstrated that large HgTe NCs exhibit broad THz absorption, which makes them promising for the development of active and passive THz devices such as transmitters and detectors. Another property that plays a crucial role in the performance of THz devices is the lifetime of non-equilibrium carriers. Indeed, physical mechanisms such as carrier relaxation and recombination will dictate the potential of materials for the realization of THz devices based on intraband transitions. For example, for the realization of a THz laser, carrier lifetimes of at least a few tens of picoseconds are required to achieve long-lived optical gain. For the development of THz photodetectors, the carrier dynamics will directly impact the response speed of the detectors.

Despite the intensive work done to study the hot carrier dynamics in small HgTe NCs, the relaxation and recombination dynamics of non-equilibrium carriers in large HgTe NCs has not been studied so far. However, determining, understanding and finally controlling the relaxation and recombination dynamics of non-equilibrium carriers in large HgTe NCs would be of great interest for fundamental studies of elementary processes and of paramount importance for the development of optoelectronic devices. In order to probe the carrier dynamics in large HgTe NCs, we extended the initial configuration of the THz-TDS experiment by adding an optical pump line to perform optical pump-THz probe experiments. In such pump-probe experiment, an optical pump pulse is used to generate non-equilibrium carriers in the HgTe NCs film, which changes the intraband absorption; a THz probe pulse is then used to map the relaxation, the cooling and return to thermodynamic equilibrium of the hot carriers with subpicosecond resolution.

In this chapter, we will first describe the principle of the optical pump-THz probe experiments, then we will present the photoresponse of large HgTe NCs at THz frequencies under optical excitation at 800 nm wavelength. We will then report on the measurements of the dynamics of hot carriers in these large HgTe NCs and finally on the evolution of the hot carrier dynamics with the temperature.

3.2 Optical Pump THz Probe Experiments

The optical pumpTHz probe set up is depicted in Figure 3.1. It is an extension of the THz-TDS set-up presented in section 2.3.2. The principle of the optical pump-THz probe configuration is to make use of an additionnal femtosecond optical pulse to illuminate the sample. This additional beam is obtained by adding a beam splitter that split the optical beam before it illuminates the THz antenna. In order to get enough power for the pump line while preserving a sufficient signal-to-noise ratio of the THz TDS spectroscopy, the beam splitter ratio is set to 70 % in reflection (for the optical beam incident on the photoconductive antenna) and 30 % in transmission (for the optical beam used as a pump). This third beam, named optical pump, is propagating through a second delay line and focused onto the HgTe NCs sample in order to generate non-equilibrium carriers. The THz pulses generated by the photoconductive antenna are used to probe the HgTe NCs sample out-of-equilibrium and are then detected by the electro-optic detection. The second delay line allows us to adjust the optical path length of the optical pump, which results in a tunable time delay τ_2 between the pulses of the optical pump and THz probe. Since the change in absorption induced by the optical pump is weak, we modulate the optical pump beam with an optical chopper. Two lenses (f=75mm) are used to both focus the pump beam onto the optical chopper, and control its diameter at the surface of the HgTe NCs sample.

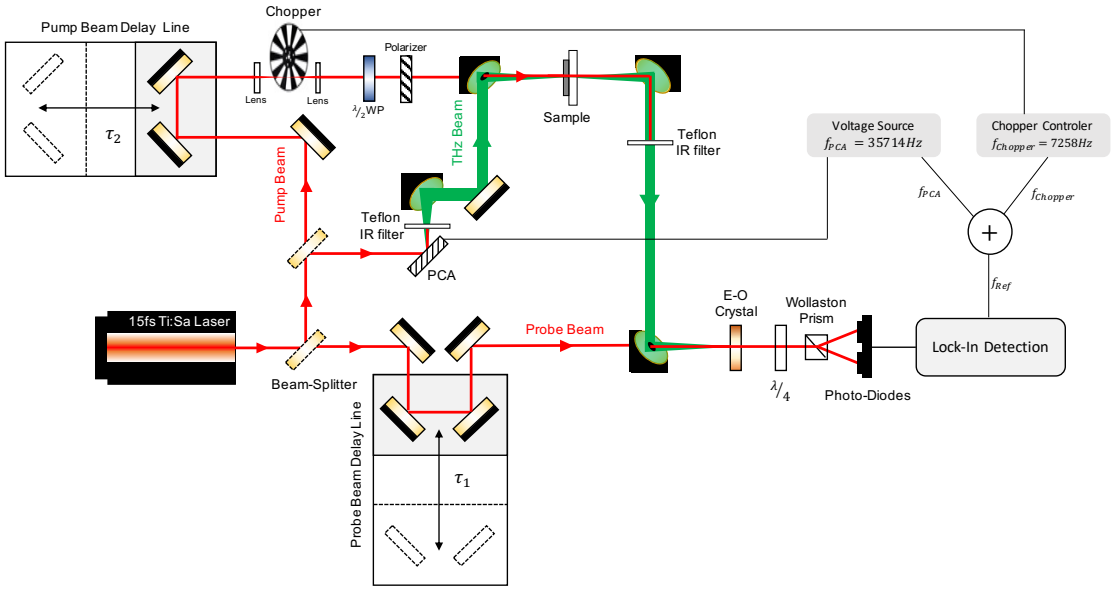

Fig. 3.1 *Scheme of the experimental Optical Pump TeraHertz Probe set-up. The optical beam is depicted in red and the THz beam in green.*

The radius R_{pump} of the optical pump beam on the HgTe NCs sample is ∼125 μm. The maximum red pump power is P_{pump} ∼230 mW. This corresponds to a fluence of Φ:

$$\Phi = \frac{P_{pump}}{f_{rep} S_{pump}}$$

where f_{rep}=80 MHz the repetition rate of the laser and $S_{pump} = \pi R_{pump}^2$ the surface of the pump beam. We find Φ ∼6 μJcm^{-2}. A half-waveplate and a polarizer are added along

the pump beam path to allow fine tuning of the optical pump fluence from $6\mu\text{Jcm}^{-2}$ to extinction by rotating the waveplate. If not indicated, the fluence value is set to its maximum value of $6\mu Jcm^{-2}$. Both the optical beam incident onto the THz photoconductive antenna (PCA) and the pump beam are modulated. We use a electronic microcircuit programmed to synchronize the two modulations and to send a reference frequency equals to the sum of the two modulation frequencies $f_{PCA} + f_{Chopper}$ to a lock-in amplifier. We also made sure that the modulation frequency of the PCA (f_{PCA} = 35.714 kHz) is not a multiple of the modulation frequency of the optical chopper ($f_{chopper}$=7.258 kHz) to avoid an harmonic artefact at the sum frequency. To improve the signal-to-noise ration of the measurements, we use a 2 mm-thick ZnTe crystal as electro-optic detector, which provides a high sensitivity at the expense of a narrower bandwidth. We denote by τ_1 the delay time of the THz-TDS experiment and by τ_2 the delay time between the optical pump and the THz probe beam. We detect the signal ΔE at the sum frequency and thus the measured signal corresponds to:

$$\Delta E(\tau_1,\tau_2) \propto E_{ON}(\tau_1,\tau_2) - E_{OFF}(\tau_1,\tau_2) = E_{ON}(\tau_1,\tau_2) - E_{OFF}(\tau_1)$$

where $E_{ON}(\tau_1,\tau_2)$ is the detected signal when the HgTe NCs sample is illuminated by the optical pump pulses and $E_{OFF}(\tau_1,\tau_2)$ when it is not. Therefore $E_{OFF}(\tau_1,\tau_2)$ is the transient electric field measured by the regular THz TDS measurement, and does not depend on the pump beam delay, and will be denoted $E_{OFF}(\tau_1)$ thereafter. Two different types of measurements are achievable in this optical pump-THz probe configuration as illustrated in Figure 3.2 in the case of a bulk GaAs substrate sample used for set-up calibration.

- 1) The pump-probe time delay τ_2 is fixed and τ_1 is swept. We measure the change of the detected transient THz electric field induced by the optical pump, i.e. the photoresponse at THz frequencies. The signals recorded during these measurements are referred to as "differential signals". They contain the full spectrum information.

- 2) τ_1 is fixed at a time of interest and τ_2 is swept. In general τ_1 is set at the time corresponding to the peak of the differential signal. When τ_2 is swept, we measure the dynamics of the differential signal as a function of the pump-probe time delay. Note that the measured quantity is averaged over the whole THz spectral range since τ_1 is fixed at the differential signal peak.

3.3 Photoresponse of HgTe nanocrystals

In the frame of the following optical pump-THz probe experiments, the silicon substrate of the HgTe NCs film has been replaced by a z-cut quartz substrate, to avoid any absorption of the red pump by the substrate. To this aim, the HgTe NCs were deposited on z-cut quartz substrates with a thickness of ∼500 μm. We first proceed to the measurement of the photoresponse of large HgTe NCs film under optical excitation at 800 nm wavelength. The normalized differential signal $\Delta E(t,\tau_2)$ for a fixed pump-probe delay τ_2=2 ps after the pump excitation is shown in Figure 3.3.a) (red curve). The amplitude of the differential signal is about 50 times lower than $E_{OFF}(t)$ obtained by regular TDS (without illumination).We observe that $\Delta E(t,\tau_2)$ shows a faster transient than the THz electric field pulse transmitted without illumination $E_{OFF}(t)$, with a derivative-like temporal shape. This behavior can also

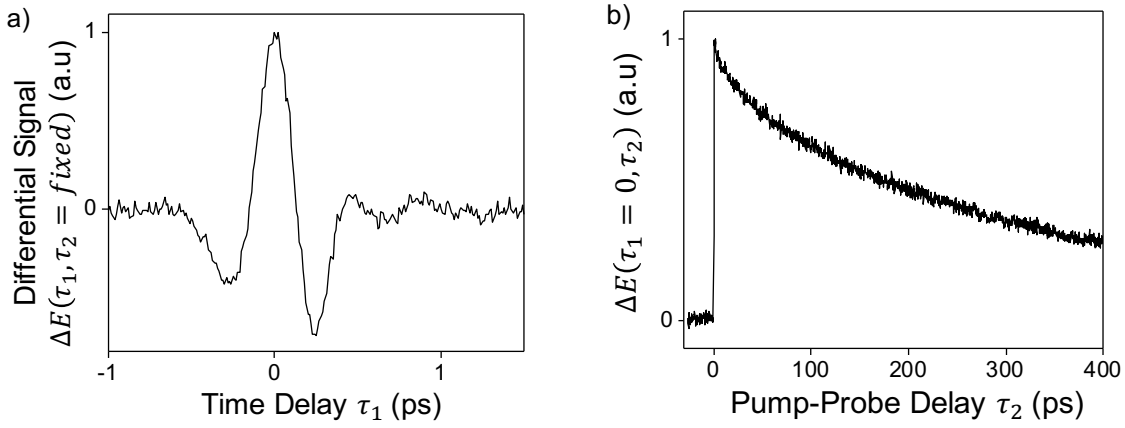

Fig. 3.2 *Two different types of differential signal obtainable with Optical Pump Terahertz Probe (OPTP) measurements a) when the probe delay τ_1 is swept at a fixed τ_2 b) when the pump-probe delay τ_2 is swept at a fixed probe delay τ_1. Measurements were conducted on a bulk GaAs substrate, used for the optimization of the spatial overlap of the THz and red beams. Dynamics of hot carriers in GaAs spreads over hundreds of picoseconds.*

be seen on the amplitude spectrum of the pump-induced change in transmission, represented in Figure 3.3.b) and defined as :

$$\frac{\Delta t(\omega)}{t_0(\omega)} = \frac{\Delta E(\omega)}{E_{ref}(\omega)} \frac{E_{ref}(\omega)}{E_{OFF}(\omega)} = \frac{\Delta E(\omega)}{E_{OFF}(\omega)}$$

Indeed, $\Delta t(\omega)/t_0(\omega)$ shows a monotonic decrease with the frequency from 0.4 to 3 THz, which is fully consistent with the derivative-like shape observed in the temporal domain. Here $\Delta E(\omega)$ is the fast Fourier transform of $\Delta E(t,\tau_2)$ for a fixed τ_2. An important feature of $\Delta t/t_0$ is that it is negative, meaning that the transmitted signal diminishes as a result of photoexcitation, which can be interpreted as an increase of the absorption. This photoinduced absorption increases with the frequency. We also study the evolution of the $\Delta t/t_0$ peak in the temporal domain as a function of pump fluence, reported in Figure 3.4. The peak amplitude of $\Delta t/t_0$ at the peak of the THz pulse follows a square root law with the incident fluence. This indicates that the intensity transmittance peak $\Delta T/T_0 = (\Delta t/t_0)^2$ scales linearly with the pump excitation fluence and consequently with the photoexcited carrier density.

3.4 Dynamics of hot carriers

We then investigate the dynamics of the observed photoinduced change in THz transmission of the HgTe NCs. For this purpose, we measure $\Delta t/t_0$ by varying the pump-probe delay τ_2 for a fixed τ_1 set at the differential signal amplitude peak as shown in Figure 3.5.a) for a pump fluence of 6 μJcm^{-2}. The temporal evolution of $-\Delta t/t_0$ first rises with a characteristic time of $\sim$2 ps, which is highlighted in Figure 3.5.b), then reaches a maximum, followed by a decay over the next few tens of picoseconds. The decay of $-\Delta t/t_0$ after the initial rise is

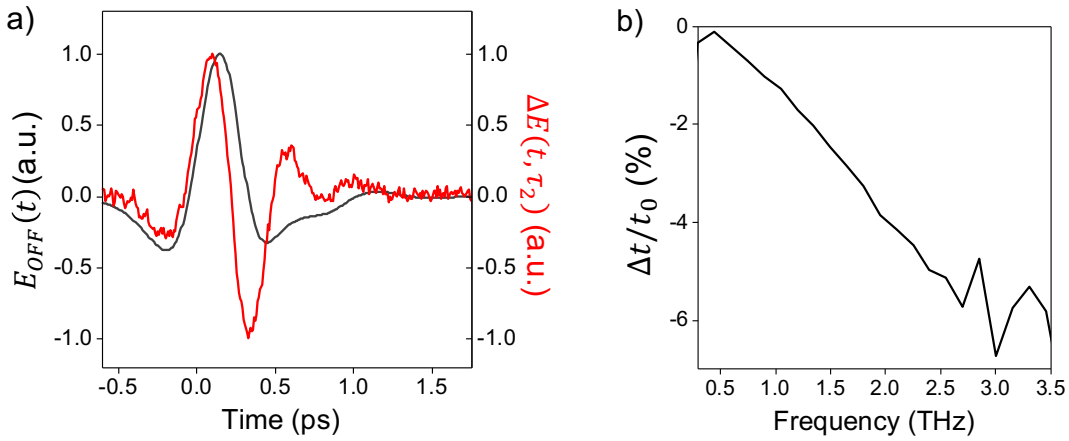

Fig. 3.3 *a) Normalized pulse transmitted through the HgTe composite film $E_{OFF}(t)$ without optical pumping corresponding to a regular TDS measurements (black curve), and normalized differential signal $\Delta E(t,\tau_2)$ for τ_2=2ps after the optical pumping (red curve). b) Corresponding amplitude spectrum of the pump-induced change in transmission defined as $\Delta t(\omega)/t_0(\omega) = \Delta E(\omega)/E_{OFF}(\omega)$.*

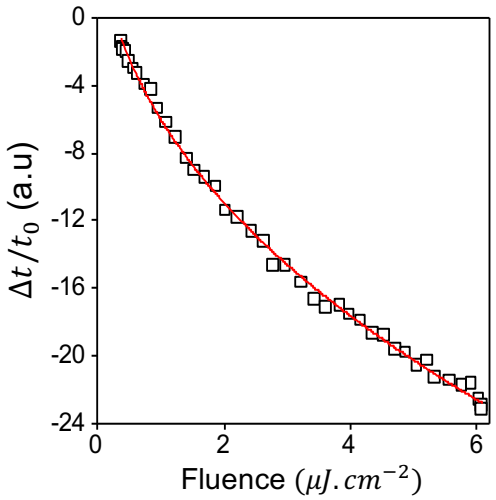

Fig. 3.4 *Influence of the incident optical pump fluence on the amplitude peak of $\Delta t/t_0$. The red line corresponds to a square root law fit.*

well fitted by a mono-exponential decay function (red curve in Figure 3.5.a)). We extract a characteristic decay time $\tau \approx 6$ps.

We perform similar measurements for different pump fluences, ranging from 0.08 to 6 μJcm^{-2}. The dynamics of $-\Delta t/t_0$ exhibit the same rise time of 2 ps, followed by a mono-exponential decay but which slows down significantly as the pump fluence increases. Figure

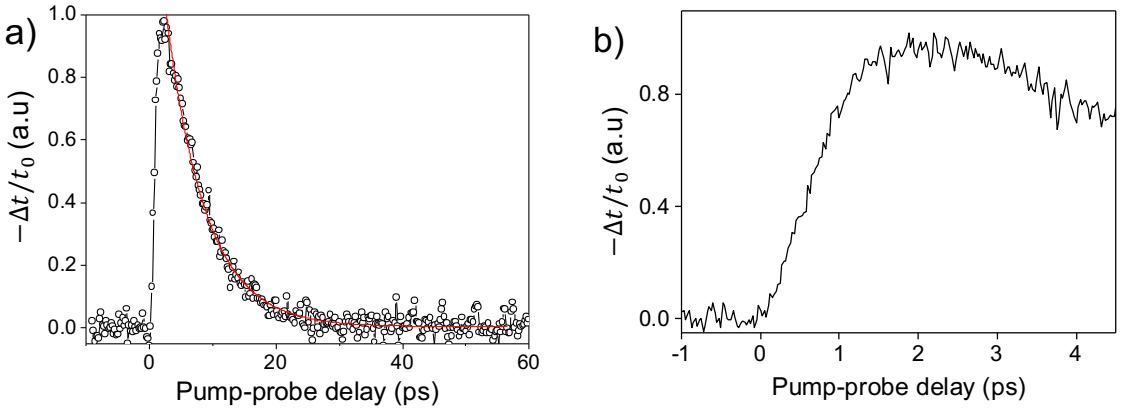

Fig. 3.5 *a) Dynamical measurement of the change in transmission $-\Delta t/t_0$ of the HgTe film as a function of the pump-probe delay time τ_2 for a fluence of 6 $\mu J.cm^{-3}$. Mono-exponential decay fit is plotted in red. b) Zoom of the graph a) into the first two picoseconds after the optical excitation.*

3.6.a) reports the recombination times extracted from the dynamics of $-\Delta t/t_0$ as a function of the pump fluence. We observe that the decay time increases linearly with increasing the pump fluence. Since these measurements are performed at a fixed delay time τ_1, they do not provide information on the spectral dependence of the dynamics of $-\Delta t/t_0$. Thus, we perform measurements of $\Delta t/t_0$ as a function of τ_1 for successive pump probe delay τ_2. After applying a FFT, we obtain the spectra of $\Delta t/t_0(\omega)$ spectra, which give information about the decay dynamics at different frequencies. Figure 3.6.b) shows the spectra of $\Delta t/t_0(\omega)$ for pump-probe delay τ_2 ranging from 2 ps to 9 ps. We observe that the photoinduced transmission change is progressively suppressed over the entire bandwidth of the THz probe. Thus, the frequency dependence of $\Delta t/t_0(\omega)$ is constant for all-optical pump fluences.

3.5 Interpretation

Measurements of the photoresponse and the hot carrier dynamics in large HgTe NCs provide new insight that will be discussed in this section. First of all, the changes observed in the transmission are induced by the optical pump, which generates electron-hole pairs at high energies. Let us estimate the photoexcited carrier density n_{photo} for an incident pump fluence is 6 μJcm^{-2} :

$$n_{photo} \approx \frac{P_{abs}}{f_{rep} E_{pump} V} \approx 2.10^{16} cm^{-3} \tag{3.1}$$

where P_{abs} is the absorbed optical pump power, E_{pump}=1.53 eV the photon energy set at the center wavelength of the pump pulse spectrum (810nm), V=eS_{pump}, e the thickness of the HgTe NCs film $\approx 10\mu$m and f_{rep}= 80 MHz the repetition rate of the femtosecond Ti:Sa laser. We estimate P_{abs}=200 mW by measuring the pump power difference before and after the HgTe NCs sample. Note that this calculation overestimates n_{photos} as we neglect reflection and scattering by the HgTe NCs of the pump radiation. However, we find that the photoexcited carrier density n_{photos} is one order of magnitude lower than the electron density

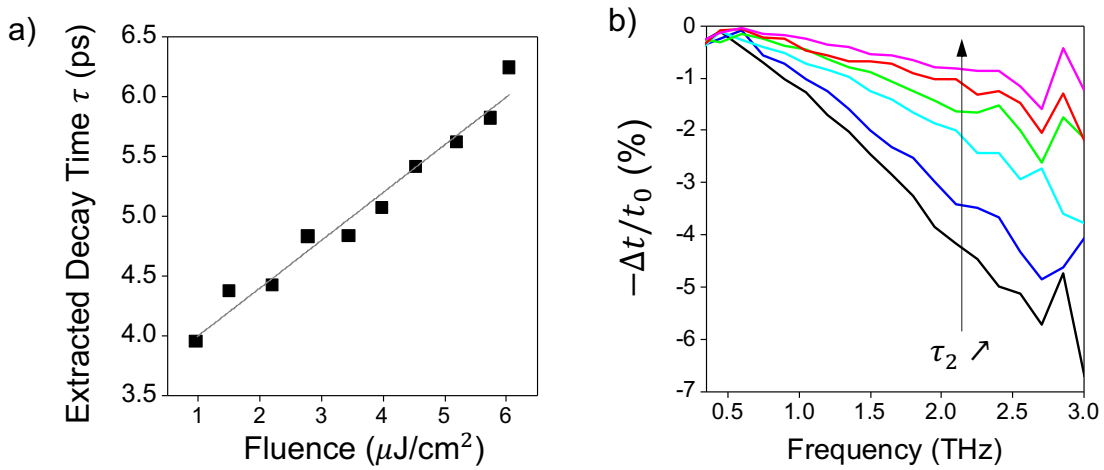

Fig. 3.6 *a) Decay time parameter τ extracted from mono exponential fits of the decay part of $-\Delta t/t_0$ for as a function of optical fluences, ranging from 0.08 to 6$\mu J.cm^{-3}$ b) Amplitude spectrum of the differential transmittance $-\Delta t(\omega)/t_0(\omega)$ measured at different pump probe delay τ_2 from 2ps to 9ps.*

n_e due to self-doping (see section 2.4.3), suggesting that the effect of the optical pump pulses is a small perturbation.

We interpret the experimental observations as follow. We describe the involved physical processes by considering four time windows dependent on the pump-probe delay τ_2, as schematically depicted in Figure 3.7:

1. **System at equilibrium : τ_2<0**
   Before the HgTe NCs film is photoexcited, the carriers are at thermal equilibrium and distributed according to a Fermi-Dirac statistic, with a chemical potential for electrons μ ∼35 meV.

2. **Photoexcitation of carriers: 0<τ_2<100fs**
   When the optical pump pulses illuminate the HgTe NCs film around τ_2=0, electron-hole pairs are created. This process takes place during the 100 fs following optical excitation. As the energy of the pump photons is high (1.53 eV), the photoexcited electrons (respectively holes) are pushed high into the conduction band (respectively deep into the valence band). During this time frame, the THz absorption does not change significantly.

3. **Relaxation: 100 fs<τ_2<2 ps**
   After their initial photoexcitation at high energy, the electrons/holes are both redistributed via intraband processes and cooled down to low energy states close to the chemical potential. This time frame corresponds to the initial rise time of 2 ps depicted in Figure 3.5.b). We attribute the intraband processes to intraband carrier-carrier and electron-optical phonon scattering in the HgTe NCs, consistently with the time scale of 2 ps. Indeed, the weak confinement energies and high density of states in large NCs

(≈100nms diameters) lead to the efficient carrier–carrier scattering between the photoexcited carriers and the carriers in the Fermi sea, and to efficient electron–phonon coupling as even the lowest electronic states are separated by only one or two optical-phonon energies. During these intraband processes, the THz absorption resulting from the intraband transitions of electrons between quantized states increases, thus leading to an increase of the differential signal ΔE. This increase of the THz absorption is explained by the change in the occupation of the electronic states close to the chemical potential after photoexcitation compared to prior.

At $\tau_2 \sim 2$ ps, most of the photocarriers have relaxed down to energy states near μ and ΔE reaches its maximum. The change in the transmission induced by the pump excitation is about 1/50, which is consistent with the low photocarriers density estimated in Equation 3.1 in comparison with the doping carrier density n_e. On the other hand, the invariance of the rise time with pump fluence suggests that the photoexcited carrier density is low enough not to saturate the intraband relaxation channels.

4. **Decay : τ_2>2 ps**
The photoexcited carriers are then trapped and recombination processes start. These physical processes tend to restore the carrier distribution to its equilibrium value. Consequently, the THz absorption decreases back to its original value, as observed in Figure 3.5.a).

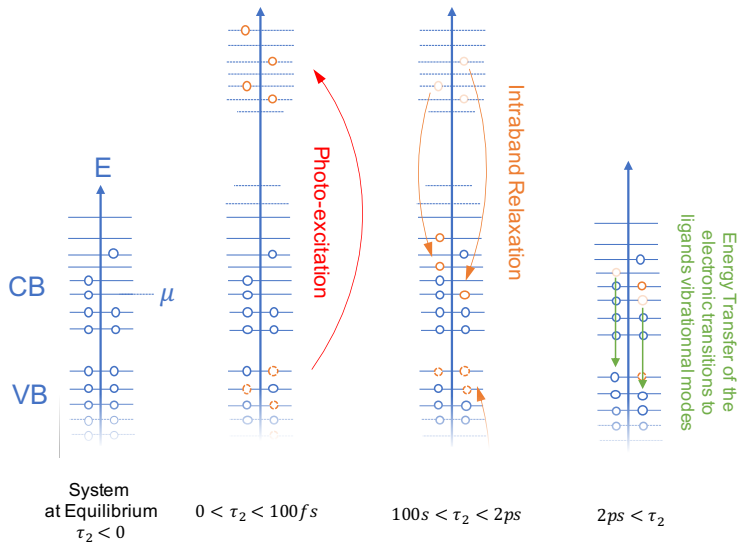

Fig. 3.7 *Schematic of the hot carriers dynamics involved in the photoexcitation of HgTe nanocrystals.*

Understanding the physical mechanisms that may be at the origin of these picosecond recombination processes is particularly important for the development of optoelectronic devices based on these HgTe NCs, such as photodetectors or light emitting diodes. For example, the photoluminescence quantum yield of NCs is limited by any recombination that differs from the desired radiative recombination. Based on our measurements, we discuss the different

physical mechanisms that can be responsible for the recombination of hot carriers in the large HgTe NCs. The recombination pathways can be divided into two main categories: the radiative and non-radiative decays.

Radiative recombinations :

Radiative recombinations involve the emission of a photon. These mechanisms are mainly dictated by the intrinsic properties of the NC (material, quantum confinement ...). Here, we consider interband radiative recombination that consists in the recombination of electron-hole pair via the emission of a photon. In these large HgTe NCs, such recombination processes fall in the nanosecond range [49, 73]. They are thus considered irrelevant here since the measured dynamics occur on a much shorter picosecond timescale.

Non-Radiative recombinations :

Let us now focus on the non-radiative recombinations. They consist in the irreversible transfer of an electron-hole pair energy into some other excitations, which are ultimately dissipated into heat. One can distinguish two types of non-radiative recombinations. The first one of non-radiative recombination involves processes that occur within the NC. The second type of non-radiative recombination comprises transfers of energy from the NC excitation to others excitations in the surrounding of the nanoparticle. Such process are part of FRET (Fröster resonance energy transfer) mechanisms. They are thus clearly dictated by the environnement of the NC, which underlines the crucial role of the synthesis and the used ligands/solvent on the carrier dynamics in the nanoparticles.

Non-radiative recombination process within the NC :

We consider two main non-radiative recombination mechanisms within the NC.

1. The first one is Auger Recombination, which consists in the recombination of an electron-hole pair, but rather than being converted into radiation, the recombination energy is transferred to another charge carrier, which is excited into a higher energy level. However, Auger recombination processes lead to faster decay at higher incident fluence [74], while we have measured the opposite tendency (see Figure 3.6.a)). Moreover, interband Auger recombination time τ_{Auger} are expected on a notably longer timescale in large HgTe NCs. Indeed, the Auger coefficient C_A scales as $C_A = \gamma r^3$ with γ= 1.2× 10^{-9} cm^3/s, giving for an NC of 100 nm radius, $\tau_{Auger} = V^2/(8C_A)$ in the microsecond range[75, 76]. Thus, Auger recombination can be disregarded in the carrier dynamics studied here.

2. The second non-radiative process consists in an electron-hole pair that recombines and transfer its energy to vibrations of the lattice, i.e to optical phonons. However, in our case, the total energy involved in the interband recombination is related to the large interband energy gap (>1 000 cm^{-1}), which is much higher than the energy of the optical phonons, around 120 cm^{-1}. Therefore, recombination involving electron-phonon scattering would require the creation of a large number of phonons, which is improbable.

FRET recombination :

In FRET recombinations, the NC excitation energy is transferred to an excitation in the surrounding of the nanoparticle. The HgTe NCs studied here are capped with dodecanethiol ligands. Such molecules are made of successive C-H compounds. Their vibrational spectrum is broad and comprises various modes such as stretching modes of C-H and overtones. Two mains mechanisms involving interactions with vibration modes of the ligands have been identified :

1. Electronic-to-Vibrationnal Energy Transfer (EVET) processes. They consist in the conversion of the recombination energy from the annihilation of an electron-hole pair into the creation of quantum excitations of the surrounding ligands vibrational modes. In the large HgTe NCs studied here, the electronic states close to the bandgap (≈1 000-1 500 cm^{-1}) overlap the broad low-frequency ligand vibrational band (≈ 1 350 cm^{-1}) of the n-dodecanethiol ligands [49]. Thus, efficient hot carriers cooling through the direct energy transfer from the electronic transition to the ligand vibrational modes is expected [44, 77]. Also, previous works on smaller size NCs have observed that this resonant recombination process based on direct energy transfer occurs on typically few tens of picosecond timescales [49, 78], which is consistent with our measurements.

2. Non-resonant surface traps assisted recombination processes. In bulk semiconductor, the presence of disorder such as defects in the lattice can result in the existence of localized electronic states in the band gap that can trap charge carriers at different timescales. These so called "trap states" can be either "deep" if they lie in the middle of the band gap, or "shallow" if they lie close to a band edge. These trap states mediate new recombination channels for the carriers such as Shockley-Read-Hall recombination process, and thus strongly affect the carrier dynamics. In the case of HgTe NCs, the finite size of the particle causes the existence of shallow trap states at the surface of the particles. They are expected to be involved in efficient non-resonant non-radiative carrier recombination. Such process result from the coupling of core states with shallow trap states mediated via low energy non-zero angular momentum phonons, as detailed in Reference [79]. These populated trap states are localized on the surface of the NC, and thus strongly interact with vibrational modes of the ligands, forming a polaron. The polaron energy levels are equidistant, separated by a single ligand vibration mode energy. The energy of such vibration mode is lower than those involved in the EVET recombination, making the process non-resonant here. However, for a sufficiently strong coupling, the polaron energies can spread throughout the broad interval of forbidden energies. These energies appear as a staircase through which the carrier in the trap state can thermalize and finally recombine with a partner particle. The latter step is also probably mediated by additional interaction with phonons. The overall non-resonant recombination process is consistent with the increase of decay time observed with the increase of the pump fluence. Indeed, the process get bottlenecked as more phonons are needed for carriers of higher energy to be trapped by the shallow surface states.

To summarize this section, we attribute the main carrier recombination pathways to a resonant energy transfer from the electronic transition to the ligand vibrational modes and non-resonant non-radiative recombination channels assisted by surface traps. We also

highlight that Auger recombination is not the main relaxation mechanism at play in this system. Furthermore, recombination mechanisms in the few picosecond timescale supports our conclusion that collective excitations are negligible in self-doped large HgTe NCs since sub-picosecond decays are expected for photocarriers associated with the plasmonic absorption [80].

3.6 Dynamics as a function of temperature

Heat can also affect the dynamics of hot carriers as phonons are involved in scattering events, in this section, we study the influence of the temperature on the dynamics of hot carriers in large HgTe NCs. To this aim, we use the optical pump-THz probe set-up depicted in Figure 3.1 and place the HgTe NCs film sample into the liquid-helium cryostat.

Figure 3.8 reports $-\Delta t/t_0$ as a function of the pump-probe delay τ_2, for a fixed τ_1 set at the differential signal amplitude peak, at three distinct temperatures T=300 K, T=65 K ($T_{critical}$) and T=4 K . The measured dynamics of the differential transmission exhibit several noticeable features. First, we observe that the amplitude of the differential signal varies strongly with temperature, as expected, because it depends on the THz absorption, which has been shown to change significantly with temperature. We can also notice that the amplitude is maximum for T=$T_{critical}$=65K, temperature at which the THz absorption is minimal (cf Figure 2.22.b)). Figure 3.8.b) represents $-\Delta t/t_0$ as a function of τ_2 (for a fixed $\tau 1$) zoomed in the rise time of the differential transmission, i.e. in the first few picoseconds after pump excitation. The initial rise time changes with temperature : it is reduced from 2 ps at room temperature to 1.3 ps at T=65 K and increases again to 2.4 ps at T=4 K. One would expect slower relaxation of hot carriers as T decreases since the number of phonons available for electron-phonon scattering events is smaller. This is consistent with the results obtained at T=4 K. However, at T=65 K, we observe an acceleration of the intraband relaxation of hot carriers to lower energy states. We suggest that this trend could be the result of an increase in the number of optical phonons taking part in the relaxation process at this critical temperature for which the absorption by transverse optical phonons dominates the total intraband absorption.

If we now examine the decay times of $-\Delta t/t_0$, we also observe changes with temperature. At room temperature, we find τ_{300K}=8.9 ps± 200 fs. It shortens at lower temperatures as τ_{65K}=5.4 ps± 50 fs and τ_{4K}=6.3 ps± 300 fs. Moreover, we notice that, at T=4 K, $-\Delta t/t_0$ does not totally decay down to zero but reaches a constant value at long τ_2. The shortening of the decay times at low temperatures T=65 K and T=4 K indicates more efficient recombination processes. According to the scenarios developed in section 3.5, the non-resonant recombination mechanism could be reduced when less optical phonons are available, as it is the case at low temperature, leading to a lower coupling of the core states to the surface traps states. These original results will be the subject of further investigation, but appear to reveal that temperature changes the interplay between radiative and non-radiative recombination processes.

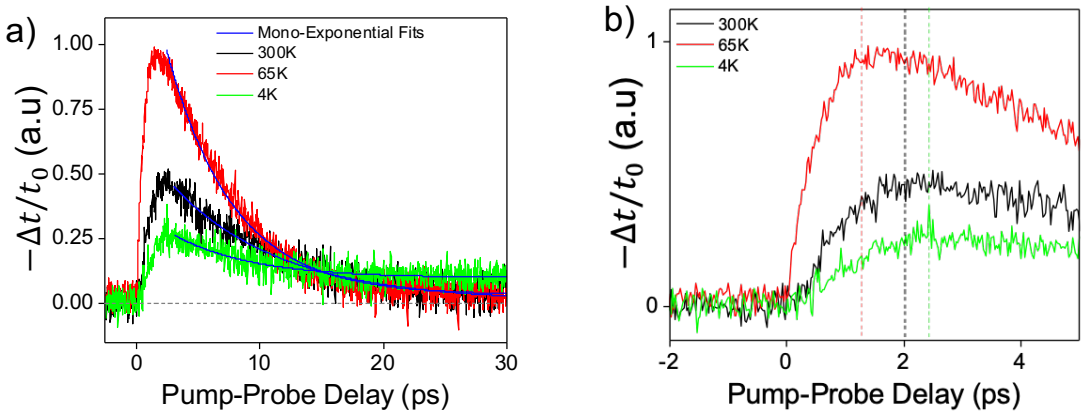

Fig. 3.8 *$-\Delta t/t_0$ as a function of pump probe delay for different temperatures T= 300K, 65K and 4K. The full dynamics is plotted in a) while b) is focused on the first few picoseconds after photo-excitation. At 4K, the system seem to remain out of equilibrium for a much longer time >30ps (green curve in a)).*

3.7 Conclusion

In this chapter, we have studied the photoresponse and the dynamics of hot carriers in large HgTe NCs film. Our results reveal recombination times of non-equilibrium carriers in the few picosecond timescale. We have highlighted that Auger recombination is not the main relaxation mechanism at play in this system. We attribute the main pathways of carrier recombination to two main non-radiative recombination processes resulting from interactions of NCs with their environnement. First, a resonant process, which consists of a direct energy transfer from the electronic transition to the ligand vibrational modes. Second, a non-resonant process also involving energy transfer to ligands vibrational modes, assisted by surface traps and mediated by optical phonons. Finally, we studied the influence of temperature on the hot carriers dynamics and and found a significant change with temperature. These are preliminary measurements that would require further investigation.

In the perspective of this work, making a film of HgTe NCs with a gate electrode to adjust the doping level would be very interesting to probe the dynamics of hot carriers when collective excitations are activated. Another investigation would be based on the surface chemistry of the NCs. Indeed, modifying the ligands should have a strong impact on the recombination processes of the carriers and should perhaps open the way to engineering the recombination times of the carriers.

Chapter 4

Coherent THz emission from HgTe NCs illuminated by optical pulses

In the previous chapters, we have shown that large HgTe NCs are very promising for THz technology as they exhibit broad THz absorption resonances and a carrier lifetime of a few picoseconds, as well as being easily fabricated using solution synthesis. In this chapter, we investigate their light emission properties in the THz spectral range, which has been up until now unexplored. Indeed, light emission from NCs is very well mastered in the visible range with applications for the display and lighting markets. Using narrow bandgap NCs, efforts have been devoted to obtain a light emission in the near and mid-infrared range. Tunable emission up to a wavelength of 5 μm has thus been demonstrated. The aim of this chapter is to investigate the possibility to push the light emission of colloidal NCs down to the THz spectral range.

In this chapter, we will first detail the THz emission spectroscopy set-up we have developed to measure coherent THz emission from large HgTe NCs excited by femtosecond optical pulses. We will then present the experimental study we have conducted on the properties of THz emission as a function of the characteristics of the incident optical pulses (angle, fluence, polarization). We will then focus on a model of the second order non-linear currents that may be at the origin of the THz radiation. Finally, we will discuss the confrontation of the model with experimental results, which allows to identify the main physical processes involved in the coherent THz emission from HgTe NCs. This chapter includes parts of our complete article [81].

4.1 Introduction

THz emission spectroscopy, based on coherent THz emission from materials excited by ultrashort optical pulses, is a very powerful and contactless tool to probe the ultrafast dynamics of current generation in materials [82] and to evaluate the potential of materials as active layers for the development of THz emitters. Under ultrafast laser excitation, transient carriers, polarisation oscillations, dipoles, phonons, excitons, and other quasi-particles are firstly generated in materials. Theses transient changes that can occur in a picosecond time scale act as sources radiating electromagnetic fields in the THz spectral range. The amplitude, phase,

duration, polarity, and polarization, of the emitted THz waveforms carry rich information on the materials such as the doping type, carrier mobility, carrier concentration, built-in fields, nonlinear susceptibility, crystal symmetry, surface and interface properties and so on [83]. For example, previous works have reported coherent THz emission induced by ultrafast photogalvanic and photon drag in topological materials [84, 85] and Weyl semimetals [86, 87], photon drag effects in graphene [88–90] and 2D materials [83], surface-plasmon-enhanced optical rectification in graphene [91], ultrafast injection and shift photocurrents in hybrid perovskites [92, 93], ultrafast spin current in spintronic structures [94, 95], photo-Dember field and surface depletion field in bulk semiconductors [96–98]. Each of these permits microscopic insights into the carrier generation and transport in their corresponding materials. Also, the study of THz emission properties from materials excited by ultrashort optical pulses plays an important role in the development of advanced THz sources such as recently demonstrated spintronic emitters that have considerably impacted the domain [94]. While THz emission from CdHgTe/HgTe quantum wells has been demonstrated previously [99, 100], coherent THz wave emission from large HgTe quantum dots excited by femtosecond optical pulses, and more generally from any quantum dots, remains unexplored to date.

4.2 THz Emission Spectroscopy set-up

THz emission spectroscopy is an analogy to the THz time-domain spectroscopy represented in section 2.3.2, except that the measured samples are in this case used as THz emitters.Therefore, the THz emission spectroscopy set-up we have developed is based on the same configuration as the THz-TDS experiment. In the THz emission spectroscopy, the incident optical pulses excite directly the samples under investigation, from which the emitted THz pulses are collected, collimated, and focused onto a detection electro-optic crystal by a pair of parabolic mirrors. The scheme of the set-up is presented in Figure 4.1. We use the same mode-locked Ti:Sa laser, which delivers red pulses of ∼20 fs duration, centered at 800 nm wavelength at a repetition rate of 80 MHz. As well, a beamsplitter is used to separate the optical pulses in two beam. A first beam is used to excite the sample and the second one is used for electro-optic probing. The excitation beam is focused onto the HgTe NCs films using a lens of focal length f=75mm lens, with a typical beam size of 200 μm. The emitted THz electric field is measured in a transmission configuration. We proceed to lock-in amplifying using an optical chopper to modulate the red beam at a frequency $f_{chopper}$=10 kHz. Since the electro-optic detection technique is only sensitive to synchronized THz radiation with femtosecond optical pulses, the incoherent thermal background is suppressed. All measurements are performed at room temperature.

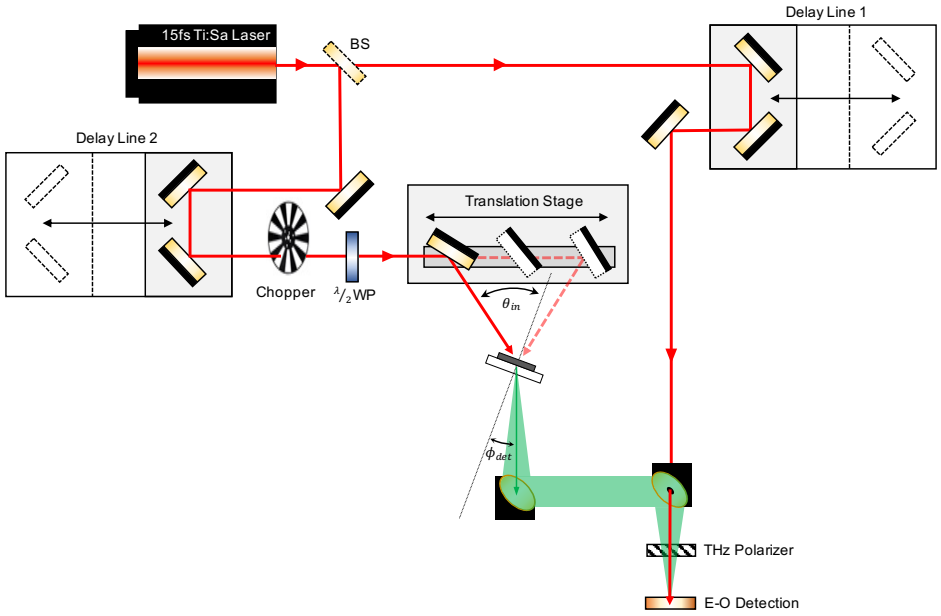

Fig. 4.1 *Schematic of the THz emission spectroscopy set-up. Only one delay-line is necessary but a second one has been added for the measurement presented in section 4.3.3*

The dependence of the emitted THz radiation on the incident optical fluence, incidence and detection angles and the polarization of the optical pulses provides insights into the ultrafast currents underlying the THz radiation. Thus, being able to adjust these parameters is essential. In our set-up, tuning the incidence angle θ_{in} of the excitation pulses onto the HgTe NCs film is achieved by a movable mirror set on a translation stage and positioned in front of the sample. The excitation pulses are linearly polarized, and their polarization angle is controlled using a $\lambda/2$ waveplate. We add an optical polarizer between the $\lambda/2$ waveplate and the samples to control the fluence of the incident optical pulses. Also, we can adjust the detection angle of the emitted THz pulses by rotating the HgTe NCs sample around the vertical axis (see Figure 4.1). The polarization state of the THz emitted electric field is characterized using a wire-grid polarizer and adjusting the electro-optic crystal orientation.

The three different frames involved in the measurements of the coherent THz emission are related to the incident beam, the sample and the detection beam as represented in Figure 4.2 and are defined as follows. The first frame $(\vec{x},\vec{y},\vec{z})$ is set according to the incident beam exciting the sample. The $\vec{z}$ axis corresponds to the direction of propagation of the optical pulses, i.e is collinear to the optical photon wavector $\vec{q}$. The optical pulses being linearly polarized, the electric field vector lies in the $(\vec{x},\vec{y})$ plane. It makes an angle α with respect to the $\vec{x}$ axis that is used to define the polarization of the optical pulses. $\alpha = 0°$ corresponds to p-polarized optical pulses while $\alpha = 90°$ corresponds to s-polarized pulses. The second frame (X,Y,Z) represents the HgTe sample coordinate framework. Y is the vertical axis and X the horizontal one. Z is perpendicular to the surface of the HgTe NCs film sample, and we define θ_{in} as the angle between Z and $\vec{z}$ which corresponds to the incidence angle of the

optical pulses. For θ_{in}=0, the optical excitation is at normal incidence. The third frame corresponds to the detection part of the set-up. It is defined by the three axis $(\vec{h},\vec{v},\vec{n})$ with $\vec{n}$ being the direction of propagation of the emitted THz beam that are propagating onto the detector. $\vec{n}$ makes an angle Φ_{det} with Z. In the actual configuration, the detector is fixed. In order to change the detection angle, we rotate the HgTe NCs sample around the Y axis. $\vec{h}$ and $\vec{v}$ are used to define the horizontal and vertical component of the emitted THz electric field.

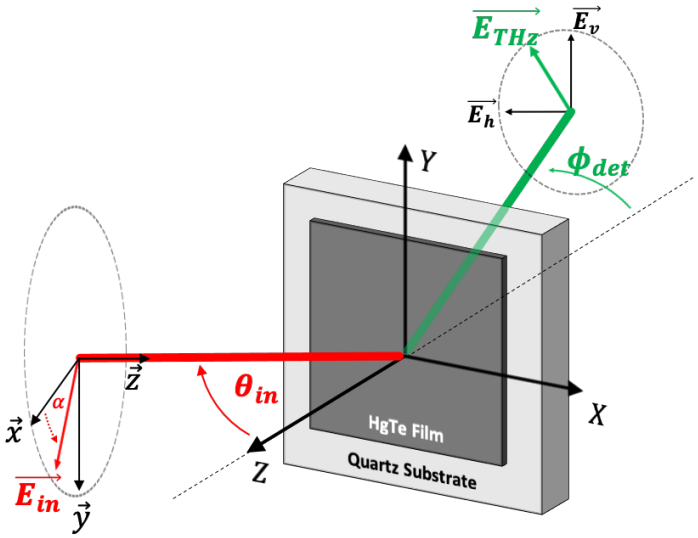

Fig. 4.2 *THz emission in a transmission configuration. (xyz), (XYZ) and (hvn) represent respectively the optical pump, sample and detector coordinates. The p-polarized and s-polarized optical excitations are along the x-axis and y-axis and correspond respectively to α=0° and α=90°.*

4.3 Experimental Results

4.3.1 Coherent THz Emission

For this study, we use a film of HgTe NCs similar to that in previous chapters. The NCs are capped with 1-dodecanethiol ligands so that these insulating long-chain organic ligands surrounded each HgTe NC strongly limit the carrier hopping between neighboring NCs. The typical mean size of the HgTe NCs in the film is L∼90 nm. The HgTe NCs film, of 13 μm-thick, is deposited on a 500 μm-thick quartz substrate, which is transparent in the optical and low-frequency THz spectral range.

The THz waveform generated by exciting the HgTe NCs film with p-polarized (α = 0°) optical pulses incident at θ_{in} =-45° and detected at Φ_{det}=45° is reported in Figure 4.3.a). We observe that the temporal signal is mainly unipolar, with a positive peak and almost no oscillation. The main peak has a full width at half maximum equal to 230 fs. The corresponding normalized amplitude spectrum obtained by FFT is shown in Figure 4.3.b).

It consists in a main broad peak centered at ∼0.7 THz. We also measured a reference THz waveform, generated by the low-temperature-grown GaAs photoconductive antenna, which has passed through a quartz substrate similar to the one used for the sample. The corresponding spectrum, plotted in Figure 4.3.b) (red dashed line), is broader with a peak centered at higher frequency and a spectral extension over 3 THz. This clearly indicates that the THz radiation emitted by the HgTe NCs is not limited by the detection bandwidth of our set-up. Also, we compare the amplitude of the THz radiation emitted by the HgTe NCs film with the reference THz waveform emitted from the low-temperature-grown GaAs photoconductive antenna and find a factor ∼ 1/60 (cf appendix A.1), indicating that the mean THz power emitted by the HgTe NCs film is in the range of 0.1 μW.

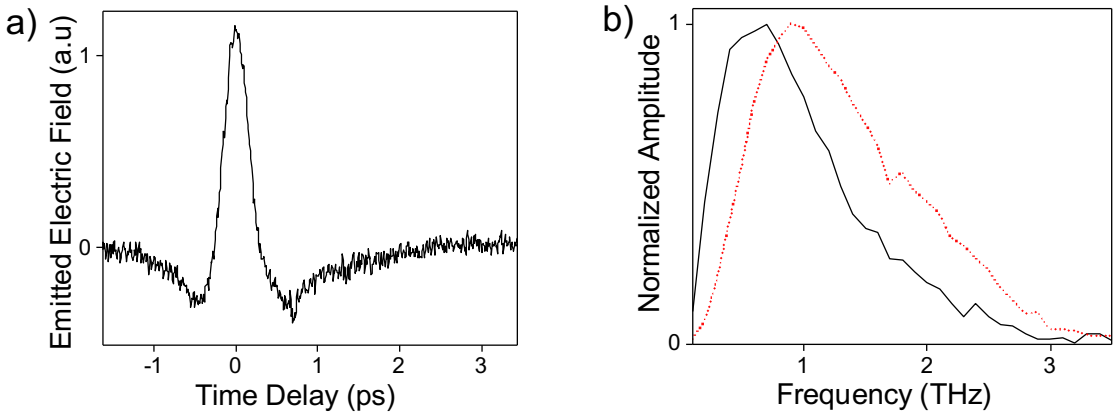

Fig. 4.3 *a) Temporal waveform of the emitted THz field for p-polarized optical pulses with an incident angle θ_{in}=-45° and a detection angle Φ_{det}=45°. b) Corresponding amplitude spectrum obtained by FFT. The red dashed line corresponds to the amplitude spectrum of signal generated by a low temperature-grown GaAs photoconductive antenna and propagated through a quartz substrate in the same configuration as the sample. It shows that the spectrum of the measured THz emission is not limited by the bandwidth of our set-up.*

4.3.2 Dependence of the THz radiation on the optical fluence

To get insight on the nature of the physical mechanisms responsible for the THz emission, we probe the dependence of the emitted THz radiation on the incident optical fluence. As depicted in Figure 4.4, the peak-to-peak amplitude of the emitted THz electric field scales linearly with the fluence (dashed black line) and thus quadratically with the incident optical electric field. We also observe in Figure 4.5.a) that the shape of the electric field waveforms and, therefore, of their amplitude spectra (see Figure 4.5.b)) remains essentially constant for all optical fluences.

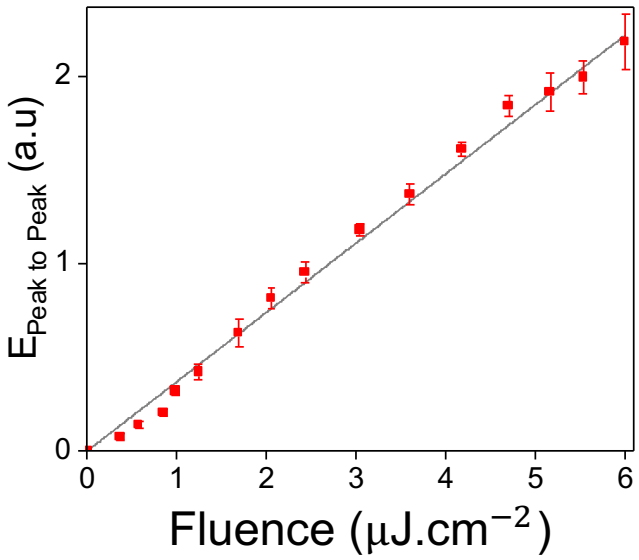

Fig. 4.4 *Peak to peak amplitude of the temporal waveform of the THz electric field emitted by the HgTe NCs film as a function of the optical fluence. Measurements were conducted with p-polarized optical pulses, incident angle θ_{in} =-45° and detection angle Φ_{det} =45°. The red squares are the experimental data, and the error bars show the standard deviation associated with noise fluctuations. The dashed line underlines the linear dependence. This linear scaling is the signature of a second order nonlinear effect.*

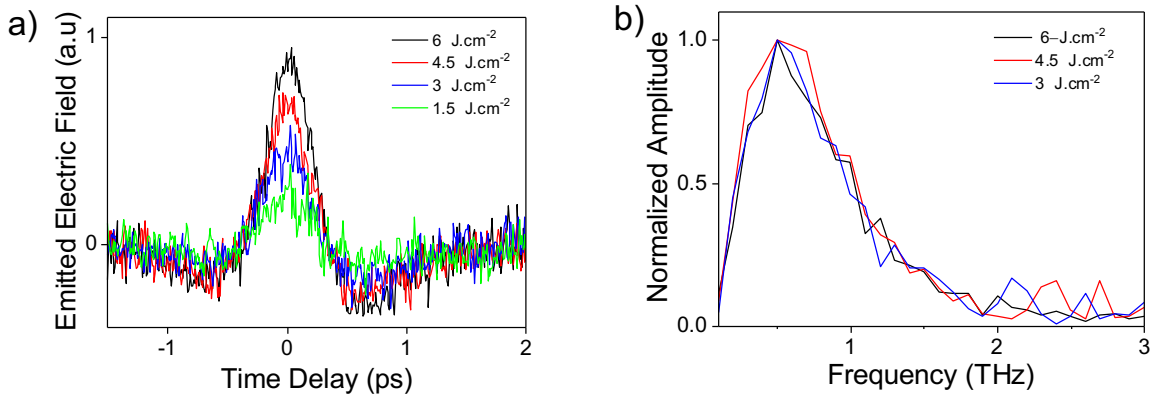

Fig. 4.5 *a) Temporal waveforms of the emitted THz field for several fluences of the incident optical pulses. Measurements were conducted with p-polarized optical pulses, incident angle θ_{in} =-45° and detection angle Φ_{det} =45°.b) Corresponding normalized amplitude spectra.*

4.3.3 Timing of the THz emission process

We then estimate the time delay between the optical excitation pulse and the THz emission by proceeding to two separate measurements After excitation of the sample, the THz pulse is generated and then propagates to the electro-optical crystal, where the temporal overlap with the optical detection pulse is achieved using a delay line (Delay Line 1 in Figure 4.1). To determine the time delay between the arrival of the optical excitation pulse on the sample and the THz emission process, we calibrate the delay of the arrival of the optical excitation pulse on the sample using a second delay line (Delay Line 2 in Figure 4.1). To do so, we use the THz pulse generated by the PCA antenna, which propagates to the sample along a distinct optical path.We set this second delay line so that the optical excitation pulse arrives on the sample simultaneously with a THz pulse generated by the conventional PCA antenna. From the sample up to the detector, both the pulses emitted by the sample and the PCA share the same optical path and thus, the propagation of both pulses take the same time. The delay between the two temporal waveforms can then be attributed to the time delay between the optical excitation pulse and the THz emission. The temporal overlap of the two waveforms presented in Figure 4.6 indicates THz emission by the sample is a quasi-instantaneous response of the HgTe NCs to the optical excitation.

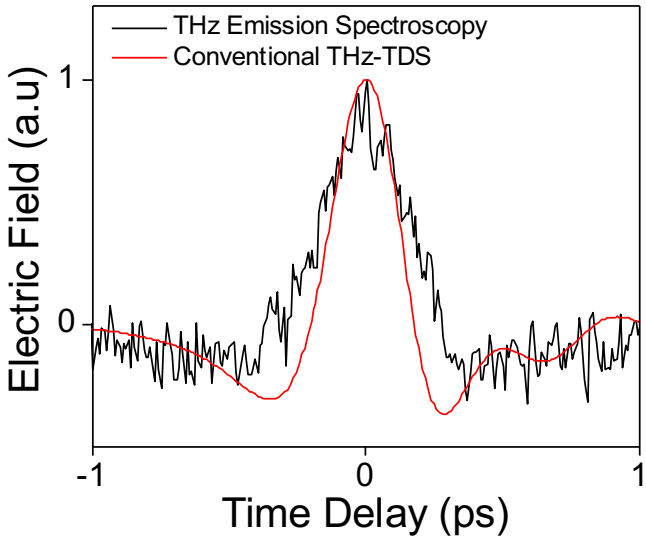

Fig. 4.6 *Normalized temporal waveforms emitted by the HgTe NCs film in emission spectroscopy configuration (black curve) and by the PCA antenna in conventional THz-TDS configuration and propagating through the sample. The set-up was calibrated so that the excitation optical pulse illuminates the sample simultaneously with the THz pulse generated by PCA antenna in THz-TDS configuration, and both measurements were performed separately.*

4.3.4 Influence of incidence and collection angles on THz radiation.

To get insight on the ultrafast currents underlying the THz radiation, we further probe the dependence of the THz radiation emitted from the HgTe NCs film on the detection and incidence angles. Figure 4.7.a) represents the THz waveforms emitted by the HgTe NCs film for various detection angles Φ_{det} where the incident angle θ_{in} is constant and equal to -15° and the optical excitation pulses are p-polarized. Such a measurement consists in successively rotating the sample and adjusting the angle of incidence accordingly by moving the mirror along the optical excitation beam path in front of the sample. One can note that the amplitude of the THz waveforms reaches a maximum when Φ_{det}=30°, and decreases as the detection angle gets larger. However, the most peculiar feature here is the polarity inversion for the negative angle Φ_{det}=-15°. Also, no signal is recorded for Φ_{det}=0°, i.e no THz radiation is emitted along the direction normal to the surface of the HgTe NCs film. Figure 4.7.b) shows the emitted waveforms obtained for two opposites incident angles θ_{in}=±15° for p-polarized optical pulses and a constant detection angle Φ_{det}=15°. In contrast, the waveforms do not exhibit polarity inversion for opposite incidence angle, but a significant change in amplitude. The largest amplitude is obtained when incident angle of the optical excitation is collinear with the detection angle.

Combining these results, we point out an another peculiar result that is the polarity inversion of the THz waveforms with similar amplitudes for both opposite and incidence angles, as presented in Figure 4.8. Note that the two configurations Φ_{det}=-θ_{in}=±45° are symmetrical with respect to the (YZ) plane.

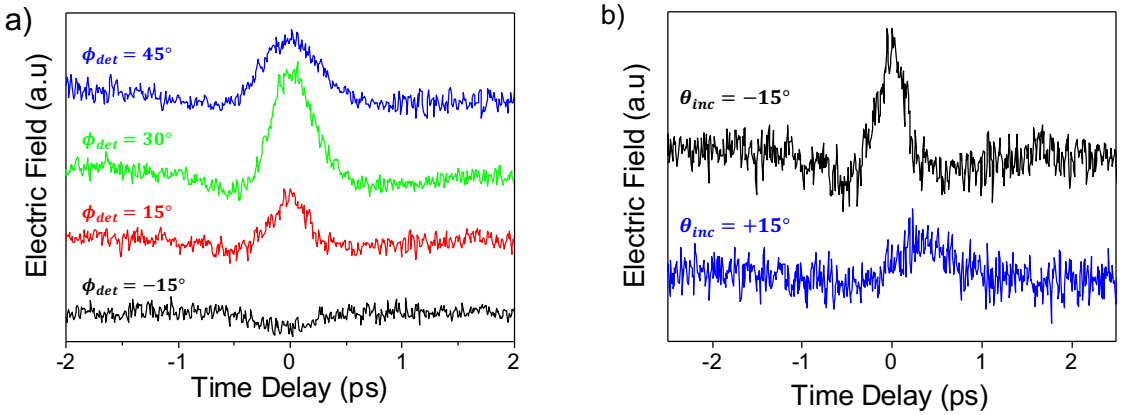

Fig. 4.7 *a) Time-resolved electric field profiles measured for various detection angles Φ_{det} under p-polarized optical pulses with a constant incident angle θ_{in}=-15°. Curves are shifted vertically for clarity. b) Time-resolved electric fields measured for two opposites incidence angles θ_{in}=±15°, under p-polarized optical pulses with a constant detection angle Φ_{det}=15°. Curves are shifted vertically for clarity.*

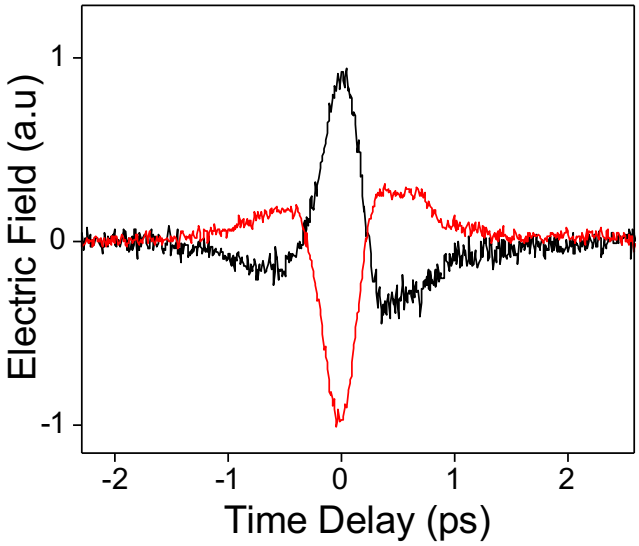

Fig. 4.8 *Time-resolved electric field profiles measured for both opposite incident and collection angles, Φ_{det}=-θ_{in}=45° in black, and Φ_{det}=-θ_{in}=-45° in red. The two waveforms have the same amplitude with inverted polarities.*

The peak amplitudes of the emitted THz waveforms for additional configurations are depicted in Figure 4.9. Most notably, we can note that no signal is measured for Φ_{det}=0°, while for a normal incidence of the optical excitation (i.e. θ_{in}=0°), a THz radiation is detected.

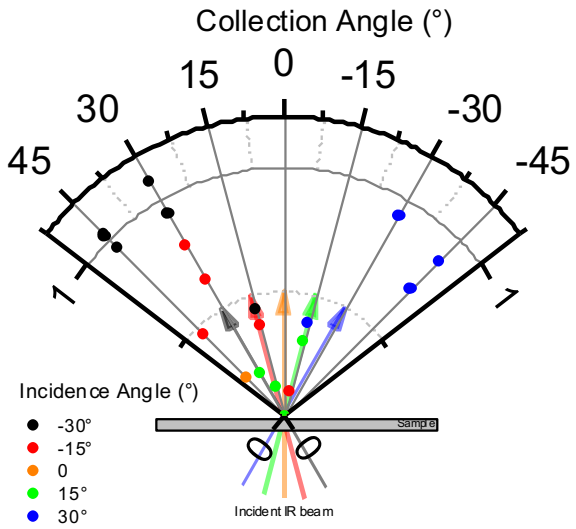

Fig. 4.9 *Absolute values of the peak to peak amplitudes of the emitted THz signals under various configurations for p-polarized optical excitations. Different colors corresponds to different angles of incidence of the optical pulses, which are illustrated by corresponding colored arrows.*

These properties of the THz waveforms provide key knowledge for the determination of the physical mechanisms involved in the emission processes, which we will detail in the next section. Indeed, these experimental features reveal that the emitted THz radiation comes from transient nonlinear photocurrents with several spatial components. Among these different components, the component of the photocurrent along the normal to the sample surface (along the Z axis on Figure 4.2) seems to be dominant.

4.3.5 Influence of the polarization of the optical excitation on THz radiation

The influence of the optical excitation wavevector has been investigated in the previous section by varying the incidence angle of the excitation pulses. However, second-order nonlinear effects can also depend on the orientation of the electric field vector $\overrightarrow{E_{inc}}$. Figure 4.10.a) represents the time-resolved electric field profiles measured for linearly polarized optical pulses but with different polarization angles, α. The waveforms have very similar shapes, which is confirmed by the spectra plotted in Figure 4.10.b) for p-polarized and s-polarized excitation pulses for two different incidence angles. Indeed, we observe only small variations in the amplitude spectra from p-polarized to s-polarized optical pulses.

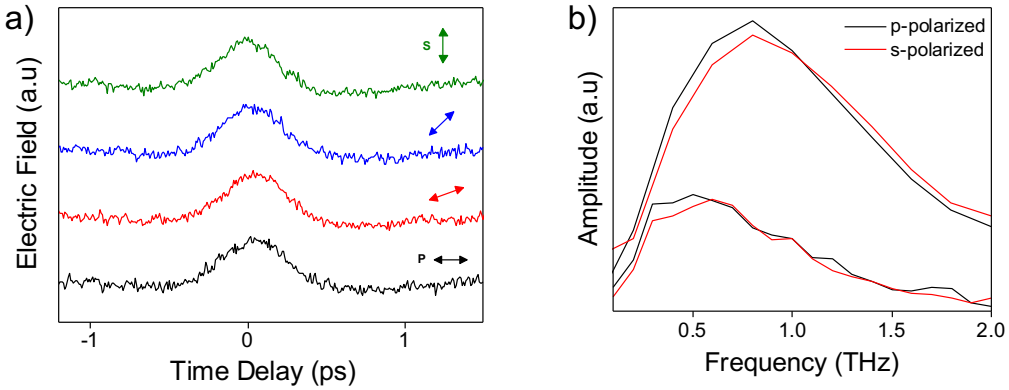

Fig. 4.10 *a) Time-resolved electric field profiles measured for different polarization angles α= 0° (p-polarized), 20°, 45° and 90° (s-polarized), for Φ_{det}=-θ_{in}=45°. Curves are shifted vertically for clarity. b) Amplitude spectra of the measured THz emitted electric field for p-polarized (black curves) and s-polarized (red curves) optical excitations. Measurements were conducted in two different configurations Φ_{det}=-θ_{in}=30° and 45°.*

4.3.6 Characterization of the emitted THz wavefrom polarization

We now focus on the polarization state of the emitted THz radiation. We probe the two components of the emitted THz electric field corresponding to the horizontal and vertical axis $\overrightarrow{h}, \overrightarrow{v}$, denoted E^h_{THz} and E^v_{THz} on the electro-optic detector. To this aim, we use a THz grid polarizer and adjust the azimutal angle of the electro-optic crystal. The two components E^h_{THz} and E^v_{THz} of the transient electric field onto the electro-optic detector for p-polarized optical pulses and Φ_{det}=-θ_{in}=45° are plotted in Figure 4.11.a). We observe that the component along the horizontal E^h_{THz} has an amplitude 3.8 times larger than the component along the vertical axis E^v_{THz}. Also, the spectral distribution of E^v_{THz} is shifted towards higher frequencies as depicted in the Figure 4.11.b). To determine the polarization state of the THz electric field emitted by the HgTe NCs film, we first experimentally calibrate the birefringence introduced by a bare 500 µm-thick quartz substrate in the same geometry, Φ_{det}=-θ_{in}=45°. We then calculate the THz electric field vector after its passage through the birefringent quartz substrate assuming that the THz emission at the output of the HgTe NCs film is fully polarized along the h-axis (E^v_{THz}=0). The calculated component E^v_{THz} (dashed red line) relatively well reproduces the measured E^v_{THz}, small deviation is attributed to uncertainty in the absolute orientation of the quartz substrate onto the sample holders. This observation indicates that, for p-polarized optical excitation, the emitted THz radiation is orientated along the h-axis (i.e. p-polarized) and that the measured component E^v_{THz} essentially results from the birefringence of the quartz substrate.

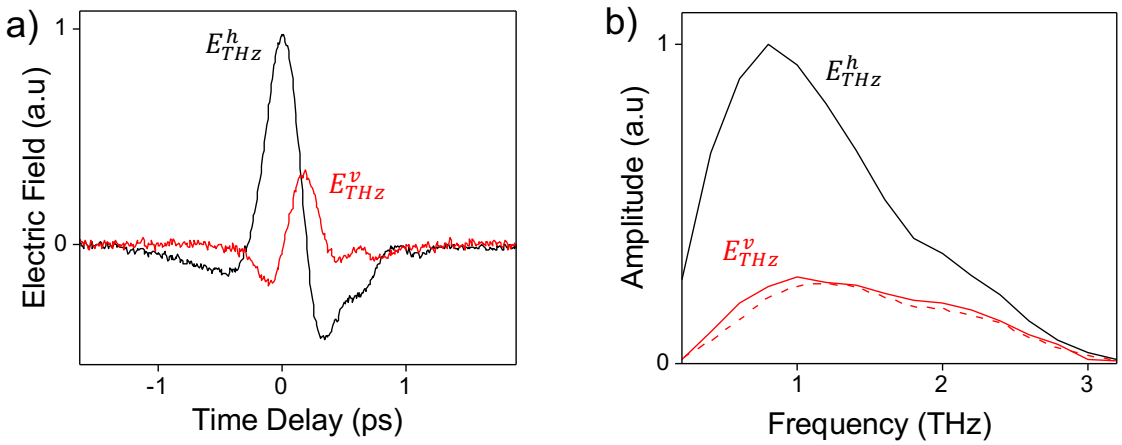

Fig. 4.11 *a) Electric field waveforms excited by p-polarized optical pulses and detected along the h-direction and v-direction on the electro-optic detector. b) Corresponding amplitude spectra. The red dashed curve represents the calculated amplitude spectrum.*

4.4 Physical processes involved in the coherent THz emission

4.4.1 Overview

In this section, we examine the potential mechanisms responsible for the observed coherent THz emission from HgTe NCs film under femtosecond optical pulse excitation. Coherent THz emission from material systems excited by femtosecond optical pulses is mainly due to the acceleration of charge carriers contained in the material. Indeed, a charge carrier with an accelerated motion radiates electromagnetic waves. If carriers accelerate over the picosecond time scale, they generate electromagnetic waves in the THz spectral range. Depending on the nature of the charge carriers, two formalisms are used to describe their motions: electrons in the conduction band move "freely" and are better described by a current $\mathbf{j}$, while bound electrons displace around an equilibrium position and a description in term of a polarization field $\mathbf{P}$ is more suitable. Note that the two approaches are yet formally equivalent, since an electric current can be seen as the time derivative of a polarization field $\mathbf{j} = \frac{\partial \mathbf{P}}{\partial t}$. Both the current and the polarization field oscillations act as electromagnetic waves sources, and based on Maxwell's equations, the radiated electric field $\mathbf{E}_{Radiated}$ can be described as follows [83]:

$$\mathbf{E}_{Radiated} \propto \frac{\partial^2 \mathbf{P}}{\partial t^2} + \frac{\partial \mathbf{j}}{\partial t} \tag{4.1}$$

with the bold-font corresponding to 3-dimensions vectors. As illustrated in Figure 4.12, THz generation from material systems under optical pulse excitation can arise from several physical processes at material surfaces and interfaces. In the following, we present the main physical mechanisms that can induce transient photocurrents or low frequency polarization oscillations that radiate in the THz spectral range.

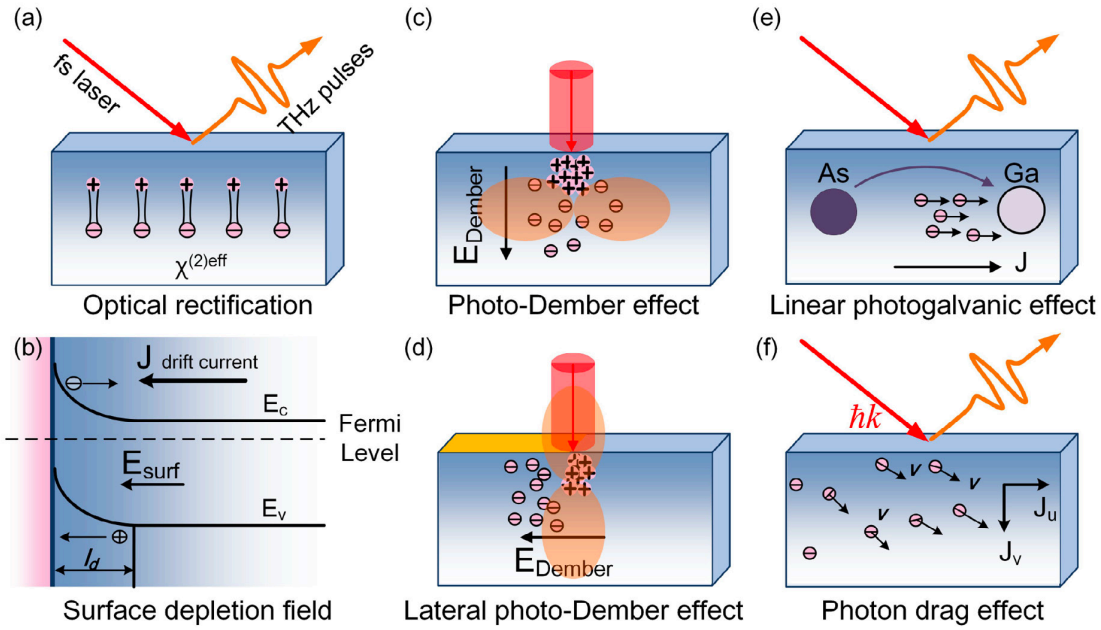

Fig. 4.12 *Schematic illustrations of physical processes at surfaces and interfaces generating THz radiation. (a) Optical rectification effect. (b) Surface depletion fields represented by n-type semiconductors with upward band bending, while downward band bending occurs in p-type semiconductors. (c) Photo-Dember effect and (d) lateral photo-Dember effect, which is introduced via adding a metallic strip on the material surface. The orange dumbbells indicate the THz radiation pattern from effective dipoles in photo-Dember fields. (e) Linear PhotoGalvanic Effect (PGE) represented by GaAs crystal. (f) Photon Drag Effect due to the momenta transfer from photons to electrons. Reproduced from [83].*

4.4.2 Ultrafast Charge Transport

For optical excitation of photon energy $\hbar\omega$ higher than the bandgap of the material, the incident electric field will generate electron-hole pairs due to interband absorption. These photocarriers can be accelerated or separated, and consequently radiate electromagnetic waves. These ultrafast charge transports are caused by two main mechanisms :

- Photo-Current Surge
  If a built-in static electric field is present in the material or if an external static electric field is applied, the photogenerated carriers accelerate, resulting in transient photocurrents varying on a picosecond timescale that therefore emit THz electromagnetic waves. This process is known as the photocurrent surge (see Figure 4.12.b)). For example, such photocurrent surge is involved in the THz generation by photoconductive antennas, as in our THz-TDS system where an external bias electric field is applied between electrodes lying on top of a low temperature grown Gallium Arsenide (LTG-GaAs) material illuminated by femtosecond optical pulses. This effect can also be significant in the case of built-in surface depletion fields that are present at the interfaces of semiconductors due to strong band bending at their surface.

- Photo-Dember Effect
  The other type of photocarrier separation occurs after the photogeneration of carriers at the surface of a semiconductor because of the difference of mobilities of the electrons and holes (see Figure 4.12.d)). Since the surface imposes boundary conditions, after photoexcitation, the photocarrier diffusion will have a net direction, that is normal to the surface. Electrons being generally more mobile than holes, they will diffuse faster from the surface to the bulk (see Figure 4.12.c)). The mobility difference results in a carrier density gradient, which induces a dipolar electric field parallel to the surface normal. This effect is called the Photo-Dember effect.

One can note the importance of the surface and interfaces in the appearance of such effects. Indeed, both surface built-in field and photo-Dember effects arise from the presence of an interface on a semiconductor.

4.4.3 Nonlinear Effects

Under optical illumination, charge carriers can also be accelerated because of the incident electromagnetic waves, which force electrons to move. While the energy of the optical photons is much higher than the energy of THz photons, the response of electrons to optical excitation can cause THz emission because of non-linear effects. Let us investigate the nonlinear response of electrons under an incident electric field $E(t)$. As previously mentioned, the carrier motions induced by the incident electric field can be described by either a (photoinduced) polarization field, P(t), or an electric (photo)current, j(t). It is convenient to express these two physical quantities as power series in the optical electric field strength $E(t)$, in order to reveal the nonlinearities of different orders [101] :

$$\begin{aligned} P(t) &= \epsilon_0 \left[\chi^{(1)}E(t) + \chi^{(2)}E^2(t) + \chi^{(3)}E^3(t) + ...\right] \\ &= P^{(1)}(t) + P^{(2)}(t) + P^{(3)}(t) + ... \end{aligned}$$

$$\begin{aligned} j(t) &= \sigma^{(1)}E(t) + \sigma^{(2)}E^2(t) + \sigma^{(3)}E^3(t) + ... \\ &= j^{(1)}(t) + j^{(2)}(t) + j^{(3)}(t) + ... \end{aligned}$$

The terms $\chi^{(n)}$ and $\sigma^{(n)}$ correspond to the different orders of the electrical susceptibility and the conductivity. For simplicity purposes, we use scalar quantities for $P(t)$, E(t) and j(t) in the previous equations. The general formulation of these equations with actual three-dimension vectors for the polarization $\boldsymbol{P}(t)$, the current $\boldsymbol{j}(t)$ and the electric field $\boldsymbol{E}(t)$ is more complex and requires tensor of order n+1 to describe the susceptibility and the conductivity of order n ($\chi^{(n)}$ and $\sigma^{(n)}$).

As in our experimental work, the amplitude of the emitted THz electric field is proportional to the square of the incident optical electric field amplitude, as depicted in Figure 4.4, we reduce the scope of our analysis to the 2^{nd} order terms. Considering the high photon energy ($\hbar\omega$=1.55 eV) of the optical excitation used in the experiment and the doped nature of the HgTe NCs, the description in term of nonlinear photocurrent is more appropriate.

Let us investigate the expression of the second-order nonlinear current $\boldsymbol{j}^{(2)}(t)$ for an incident optical electric field $\boldsymbol{E}$ defined as :

$$\boldsymbol{E}(\boldsymbol{r},t) = \boldsymbol{E}(\omega,\boldsymbol{q})e^{-i\omega t+i\boldsymbol{qr}} + \boldsymbol{E}^{*}(\omega,\boldsymbol{q})e^{i\omega t-i\boldsymbol{qr}}$$

with ω the angular frequency, $\boldsymbol{q}$ the wavevector and the bold-font corresponding to 3-dimensions vectors. A general tensorial formulation of the relation between $\boldsymbol{j}^{(2)}$ and $\boldsymbol{E}$ can be written :

$$\boldsymbol{j}^{(2)}(\boldsymbol{r},t) = \sigma^{(2)} : \boldsymbol{E}(\boldsymbol{r},t) \otimes \boldsymbol{E}(\boldsymbol{r},t) \tag{4.2}$$

where $\otimes$ is the tensorial product, $\boldsymbol{E}$ the electric field vector seen as a first order tensor, and : corresponding to the double dot product between the third rank tensor $\sigma^{(2)}$ and the second rank tensor $\boldsymbol{E}\otimes\boldsymbol{E}$. Equation 4.2 can also be expressed as a set a three scalar equations corresponding to the components of $\boldsymbol{j}^{(2)}$ along the three cartesian axis [90]:

$$j_{\alpha}^{(2)}(\boldsymbol{r},t) = \underbrace{\left[\sigma_{\alpha\beta\gamma}^{(2')}E_{\beta}(\omega,\boldsymbol{q})E_{\gamma}(\omega,\boldsymbol{q})e^{-2i(\omega t-\boldsymbol{qr})} + c.c\right]}_{\text{ac}} + \underbrace{\sigma_{\alpha\beta\gamma}^{(2)}E_{\beta}(\omega,\boldsymbol{q})E_{\gamma}^{*}(\omega,\boldsymbol{q})}_{\text{dc}} \tag{4.3}$$

where α, β and γ refer to cartesian coordinates, and c.c stands for "complex conjugate". Note that Equation 4.3 uses Einstein notation for α, β and γ which implies summation over indices that appear twice in any single term. A few important aspects are unveiled by Equation 4.3. The first term is oscillating at the pulsation 2ω while the second term is static. The radiated electric field in Equation 4.1 being linear in $\mathbf{j}$, the ac part of $j_{\alpha}^{(2)}$ will then generate electromagnetic waves oscillating at twice the frequency of the incident optical electric field, 2ω. This phenomena is referred to as Second Harmonic Generation (SHG). Similarly the appearance of a time-independent contribution yielding the directed (dc) current generation is an illustration of more generic phenomena called Difference Frequency Generation processes (DFG). More generally, an important aspect arising from the second-order nonlinear response of a material to an oscillating electric field is the ability to generate currents (or polarizations) oscillating at frequencies equal to the sum or difference of the incident electric field frequency.

The DFG processes are particularly relevant in our case. Indeed, the derivation of Equation 4.3 has been made for a single incident electromagnetic wave of pulsation ω. However, the optical excitation used in our experiment is a femto-second pulse whose spectrum spreads over a significant range of frequencies. Figure 4.13 represents the spectrum of the optical pulses used to illuminate our sample.

Thus, we now consider a total electric field composed of two electric field components oscillating at angular frequencies ω_1 and ω_2 :

$$\boldsymbol{E}(\boldsymbol{r},t) = (\boldsymbol{E_1}(\omega_1,\boldsymbol{q})e^{-i\omega_1 t+i\boldsymbol{qr}} + c.c) + (\boldsymbol{E_2}(\omega_2,\boldsymbol{q})e^{-i\omega_2 t+i\boldsymbol{qr}} + c.c)$$

The expression of Equation 4.3 considering the total electric field will present additional terms oscillating at the difference frequencies $\pm(\omega_1 - \omega_2)$. Even though these terms are oscillating, they are still related to $\sigma^{(2)}$ rather than $\sigma^{(2')}$ because they are DFG terms that originate from the product of $\boldsymbol{E_1}$ components with the c.c of those of $\boldsymbol{E_2}$ (or the opposite).

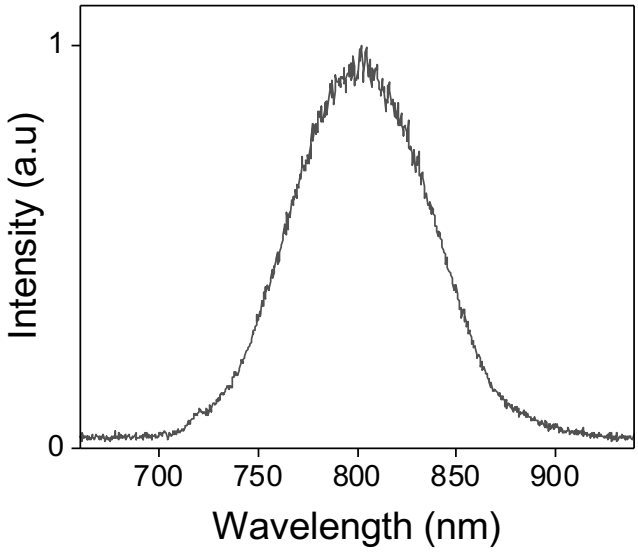

Fig. 4.13 *Intensity spectra of the optical pulse delivered by our femtosecond laser.*

One can note that $\sigma^{(2)}$ thus depends on the three quantities ω_1, ω_2 and $\omega_1 - \omega_2$. It is possible to roughly estimate the range of accessible frequencies $\omega_1 - \omega_2$ based on the DFG processes using the spectrum of the optical excitation pulses presented in Figure 4.13. Assuming the frequency difference defined by the full width at half maximum of the optical pulses, one should efficiently address DFG up to ∼40 THz. This overlaps the entire THz spectral range and DFG processes are thus particularly relevant for the analysis of our experimental results. Therefore, we focus on this "quasi-dc" part of the second-order nonlinear current to describe the THz radiation emitted from the HgTe NCs film driven by femtosecond optical pulses. The previous derivation was done for current $\boldsymbol{j}^{(2)}$, but a similar approach for polarization leads to an equivalent expression. Thus, it is possible to express the low frequency contribution of the second-order nonlinear current by the contribution of two incident waves as following :

$$j_\alpha^{(2)}(\omega_1 - \omega_2) = \sigma^{(2)}(\omega_1 - \omega_2,\omega_1,\omega_2)_{\alpha\beta\gamma} E_\beta(\omega_1) E_\gamma^*(\omega_2)$$
$$P_\alpha^{(2)}(\omega_1 - \omega_2) = \epsilon_0 \chi^{(2)}(\omega_1 - \omega_2,\omega_1,\omega_2)_{\alpha\beta\gamma} E_\beta(\omega_1) E_\gamma^*(\omega_2)$$

An important aspect of the second order nonlinear effects arises from symmetry considerations. Indeed, under spatial inversion, the current and the polarisation change sign, while the quadratic combinations $E_\beta(\omega_1)E_\gamma^*(\omega_2)$ remain invariant. This implies that second-order nonlinear effects occur only if $\sigma^{(2)}$ (i.e $\chi^{(2)}$) changes sign under spatial inversion, or in other words if $\sigma^{(2)}$ (i.e $\chi^{(2)}$), which have the symmetry of the material system, is not centro-symmetric. Thus, second-order nonlinear effects only occur for systems where the centro-symmetry is broken. The centro-symmetry can be broken in different ways [83], which correspond to different types of phenomena as described below, and represented in Figure 4.12 :

- Crystal Structure - Photo-Galvanic Effect and Optical Rectification

The first way a system can lack centrosymmetry is if the crystallographic structures of the materials do not possess centro-symmetry inversion property. This corresponds to 21 out of the 32 crystal classes that exist. This type of non-centrosymmetry is intrinsic, which means that such crystals can exhibit the associated 2^{nd} order nonlinear effects in their bulk form. Depending on the optical photon energy, one can distinguish two DFG nonlinear effects, which happen in non-centrosymmetric crystals:

- When the photon energy $\hbar\omega$ of the optical excitation is lower than the band gap of the material, the description in term of polarisation is better suited. It appears that a quasi-dc polarization is generated as the material is illuminated. This phenomenon is called *Optical Rectification* (see Figure 4.12.a)).
- When the photon energy $\hbar\omega$ of the optical excitation is higher than the bandgap of the material, or when the material is doped and intraband transitions can be addressed, quasi-dc currents are generated. This phenomenon is called the *Photo Galvanic Effect* (PGE) (see Figure 4.12.e)). PGE can be seen as a macroscopic manifestation of asymmetry of elementary processes such as the generation and recombination of electron-hole pairs or carriers scattering [102]. Indeed, such asymmetry in elementary processes in media lacking center of symmetry breaks down the overall compensation mechanisms when the system is brought out of equilibrium. For instance, the fluxes of particules with opposite momenta do not cancel each other anymore, which might give rise to a photocurrent in a privileged direction, i.e a photogalvanic current. Another part of the PGE also arises from the transfer of angular momenta of circularly polarized incident light, and will be detailed later.

- Photon Wavevector - Photon Drag Effect

  Breaking down the centro-symmetry of a system under optical illumination can also arises from the incident electric field itself. Indeed, the direction of propagation of incident light can induce a breakdown of the centro-symmetry of the system. More specifically, if the 2^{nd} order process of the ultrafast photocurrent generation also depends linearly on the photon wavevector $\mathbf{q}$, the condition on the change of sign of the conductivity tensor under spatial inversion is no longer required. This means that, since the asymmetry is caused by the incident electric field, such effects can also occur in centrosymmetric materials. This phenomenon is called *Photon-Drag Effect* (PDE) and can be described by a fourth order tensor as described below (see Figure 4.12.f)). PDE originates from the momentum transfer from the incident photons to the charge carriers in the material, that then move along the direction of the incident light. The resulting transient photocurrent thus depends linearly on the incident optical wavevector. Such effects are usually noticeable in materials with a significant amount of free carriers, such in doped semiconductors or metals.

- Interfaces - Surface PGE and Optical Rectification / EFIOR

  So far, the development was made for bulk materials, without consideration on the finite size and specific shape of the material. However, the presence of an interface can break the centro-symmetry of a bulk material. As a consequence, phenomena such as Surface Photo Galvanic Effect, or Optical Rectification at the material surface have

been observed, even in centro-symmetric materials [90, 103]. Also, the interfaces can cause the presence of a surface depletion field which breaks the symmetry of the system. Consequently, Electric-Field-Induced-Optical-Rectification (EFIOR) can happen at the interfaces of semiconductors with strong band bending at their surfaces. Such phenomena can be described by an effective 2^{nd} order nonlinear surface susceptibility tensor, that is actually the product of a third-order susceptibility tensor with a static electric field perpendicular to the surface E_{surf}, so that [103] :

$$\chi^{(2)}_{eff_{ijk}}(\omega_1 - \omega_2;\omega_1,\omega_2) = \chi^{(3)}_{ijk}(\omega_1 - \omega_2;\omega_1,\omega_2,0)E_{surf}$$

4.5 Application of the formalism to the experimental results

It is usually quite difficult to distinguish the respective contributions of the different ultrafast photocurrents in the emission of a THz electric field, as they may all be involved. However, by studying the properties of the emitted THz radiation as a function of macroscopic parameters such as the angles of incidence and of detection and the optical excitation polarization, it is possible to identify the physical processes involved using symmetry arguments without the necessity of microscopic description of the processes.

Let us now discuss on the measured THz emission from the optically excited HgTe NCs films, presented in the previous section. Among the different effects detailed above, it is possible to rule out photocurrents resulting from the acceleration of carriers by surface built-in field formed by either band bending at the surface or by the photo-Dember effect, because of the confinement of the carriers inside each NCs. Indeed, transport in HgTe NCs films occurs though hopping typically toward nearest neighbor at room temperature with a hopping time τ_{hop} given by [104]:

$$\tau_{hop} = \frac{eL^2}{6\mu k_B T} \tag{4.4}$$

with e being the electron charge, L the particle length, μ the carrier mobility. If we assume a typical value of μ=10^{-2}cm^2 V^{-1}s^{-1} for the mobility, this leads to τ_{hop} =16 ns, a timescale much longer than the relaxation mechanism under consideration here. This is reasonable to assume that all processes are intra nanocrystal processes [105]. Therefore, the observed coherent THz emission is attributed to second-order nonlinear effects and we reduce the scope of our study to second-order non-linear effects.

As presented earlier, the general second-order non-linear current density at the frequency difference for a monochromatic incident electromagnetic wave with a complex electric field component $\boldsymbol{E}(\boldsymbol{q},\omega)$ is expressed as:

$$j^{(2)}_{\alpha}(\boldsymbol{q}) = \sigma^{(2)}_{\alpha\beta\gamma}(\boldsymbol{q})E_{\beta}(\boldsymbol{q},\omega)E^{*}_{\gamma}(\boldsymbol{q},\omega) \tag{4.5}$$

where $\sigma^{(2)}(\boldsymbol{q})$ is the 2nd order conductivity tensor at the difference frequency $\Delta\omega = 0$, ω is the optical photon angular frequency, $\boldsymbol{q}$ the optical wavevector, and α, β, γ indices that run over the three cartesian coordinates X, Y and Z (see schematic presented in Figure 4.2). We will show later that the same approach is valid for $\Delta\omega \neq 0$ in the quasi-dc regime,

which corresponds to the experimentally investigated THz spectral range. Note that the dependence on the wavevector $\boldsymbol{q}$ has been taken into account in order to include potential Photon-Drag Effect. The tensor $\sigma^{(2)}(\boldsymbol{q})$ differs from that of the bulk HgTe and incorporates the microscopic properties of the materials.

In order to separate the Photo-Galvanic Effects from the Photon-Drag effects, it is convenient to expand the second-order conductivity to linear order in $\boldsymbol{q}$:

$$\sigma^{(2)}_{\alpha\beta\gamma}(\boldsymbol{q}) = \sigma^{(2)}_{\alpha\beta\gamma}(0) + \Phi_{\alpha\mu\beta\gamma} q_\mu \tag{4.6}$$

This leads to the two different contributions in the non-linear current density:

$$j^{(PG)}_\alpha(0) = \sigma^{(2)}_{\alpha\beta\gamma}(0) E_\beta(\boldsymbol{q},\omega) E^*_\gamma(\boldsymbol{q},\omega)$$
$$j^{(PD)}_\alpha(\boldsymbol{q}) = \Phi_{\alpha\mu\beta\gamma} q_\mu E_\beta(\boldsymbol{q},\omega) E^*_\gamma(\boldsymbol{q},\omega)$$

Both $j^{(PG)}_\alpha(0)$ and $j^{(PD)}_\alpha(\boldsymbol{q})$ are real quantities. As a consequence, we have $j^{(PG)*}_\alpha(0) = j^{(PG)}_\alpha(0)$ and $j^{(PD)}_\alpha(\boldsymbol{q}) = j^{(PD)*}_\alpha(\boldsymbol{q})$. It follows that $\sigma^{(2)*}_{\alpha\beta\gamma}(0) = \sigma^{(2)}_{\alpha\gamma\beta}(0)$ and $\Phi^*_{\alpha\mu\beta\gamma} = \Phi_{\alpha\mu\gamma\beta}$. It is possible to separate the contributions of $\sigma^{(2)}_{\alpha\beta\gamma}(0)$ and $\Phi_{\alpha\mu\beta\gamma}$ that are respectively symmetrical and anti-symmetrical with respect to the two last indices. These symmetrical and anti-symmetrical parts can be related to the contributions from respectively linearly and circularly polarized incident light, which leads to the following phenomenological expressions:

$$j^{(PG)}_\alpha(0) = \chi_{\alpha\beta\gamma} E_\beta(\boldsymbol{q},\omega) E^*_\gamma(\boldsymbol{q},\omega) + i\Gamma_{\alpha\mu} \left(\boldsymbol{E} \times \boldsymbol{E}^*\right)_\mu$$

$$j^{(PD)}_\alpha(\boldsymbol{q}) = T_{\alpha\mu\beta\gamma} q_\mu E_\beta(\boldsymbol{q},\omega) E^*_\gamma(\boldsymbol{q},\omega) + i R_{\alpha\mu\beta} q_\mu \left(\boldsymbol{E} \times \boldsymbol{E}^*\right)_\beta$$

where $\chi_{\alpha\beta\gamma}$ and $T_{\alpha\mu\beta\gamma}$ correspond to contributions from the linearly polarized excitation and are symmetrical with respect to the two last indices β and γ, and $\Gamma_{\alpha\mu}$ and $R_{\alpha\mu\beta}$ correspond to contributions from circularly polarized excitations and are anti-symmetrical with respect to the same indices. In our experimental set-up, optical pulses are linearly polarized. The circular polarization contributions associated with the tensors $\Gamma_{\alpha\mu}$ and $R_{\alpha\mu\beta}$ can then be dismissed.Thus, PGE and PDE are then only described by linear polarization contributions expressed using the two tensors $\chi_{\lambda\nu\eta}$ and $T_{\lambda\mu\nu\eta}$.

Since the (XYZ) coordinates are the natural framework to express the second-order conductivity tensor $\sigma^{(2)}(\boldsymbol{q})$ and make use of its symmetry properties, let us express $\boldsymbol{E}$ in this same framework. Taking into account the polarization angle α and the incident angle of the optical pulses onto the HgTe NCs film θ, it gives :

$$\boldsymbol{E} = E_0 \left(\cos\alpha \cos\theta \boldsymbol{X} - \sin\alpha \boldsymbol{Y} + \cos\alpha \sin\theta \boldsymbol{Z}\right)$$

To avoid confusion with the angle α in the following, we use the three indices λ, ν and η, running through the three spatial coordinates X, Y and Z. The derivation of the second-order non linear current density $\boldsymbol{j}^{(2)}(\boldsymbol{q})$ is detailed in appendix C.1 and yields to the following expression :

$$j^{(2)}_\lambda(\theta,\alpha) = j^{(2)}_{\lambda 0}(\theta) + j^{(2)}_{\lambda C}(\theta)\cos 2\alpha + j^{(2)}_{\lambda S}(\theta)\sin 2\alpha \tag{4.7}$$

which exhibits the different dependences on the polarization angle α, with :

$$j_{\lambda 0}^{(2)} = \frac{E_0^2}{2}\left[\sigma_{\lambda XX}^{(2)}(\boldsymbol{q})\cos^2\theta + \sigma_{\lambda ZZ}^{(2)}(\boldsymbol{q})\sin^2\theta + \sigma_{\lambda YY}^{(2)}(\boldsymbol{q}) + \sigma_{\lambda XZ}^{(2)}(\boldsymbol{q})\sin 2\theta\right]$$

$$j_{\lambda C}^{(2)} = \frac{E_0^2}{2}\left[\sigma_{\lambda XX}^{(2)}(\boldsymbol{q})\cos^2\theta + \sigma_{\lambda ZZ}^{(2)}(\boldsymbol{q})\sin^2\theta - \sigma_{\lambda YY}^{(2)}(\boldsymbol{q}) + \sigma_{\lambda XZ}^{(2)}(\boldsymbol{q})\sin 2\theta\right]$$

$$j_{\lambda S}^{(2)} = -\frac{E_0^2}{2}\left[2\sigma_{\lambda XY}^{(2)}(\boldsymbol{q})\cos\theta + 2\sigma_{\lambda YZ}^{(2)}(\boldsymbol{q})\sin\theta\right]$$

Let us detail Equation 4.7 for p-polarized light (i.e $\alpha = 0°$). It is simplified into the form:

$$j_{\lambda}^{(2)}(\boldsymbol{q},\alpha = 0) = E_0^2\left[\sigma_{\lambda XX}^{(2)}(\boldsymbol{q})\cos^2\theta + \sigma_{\lambda ZZ}^{(2)}(\boldsymbol{q})\sin^2\theta + \sigma_{\lambda XZ}^{(2)}(\boldsymbol{q})\sin 2\theta\right]$$

As in Equation 4.6, it is now convenient to separate the Photo-Galvanic and Photon-Drag effects to make use of symmetry arguments and simplify the previous expression.

$$j_{\lambda}^{(2)PG}(\boldsymbol{q}) = E_0^2\left[\chi_{\lambda XX}\cos^2\theta + \chi_{\lambda ZZ}\sin^2\theta + \chi_{\lambda XZ}\sin 2\theta\right]$$

$$j_{\lambda}^{(2)PD}(\boldsymbol{q}) = E_0^2\left[T_{\lambda\mu XX}q_\mu\cos^2\theta + T_{\lambda\mu ZZ}q_\mu\sin^2\theta + T_{\lambda\mu XZ}q_\mu\sin 2\theta\right]$$

Bulk HgTe is a non-centrosymmetric material with a zinc-blende structure which possesses a Td (eq $\bar{4}3m$) point group symmetry. However, the effective tensors $\chi_{\lambda\nu\eta}$ and $T_{\lambda\mu\nu\eta}$ locally describe microscopic properties of the HgTe NCs film. Thus, symmetries of an ensemble of HgTe NCs randomly arranged in the film have to be investigated in order to state on symmetries of the effective tensors. The size of the HgTe NCs are much smaller (≈90 nm) than both the optical beam size on the film (≈ 200 μm) and the optical and THz wavelengths. As a result, the HgTe NCs film is considered optically isotropic in the (XY) plane. This spatial symmetry consideration yields to an infinite number of mirror planes perpendicular to the HgTe NCs film, which correspond to ∞m symmetry class. On the other hand, there is no equivalence of Z and -Z directions because the HgTe NCs film is deposited on a substrate. For this symmetry group, the susceptibility tensor $\chi_{\lambda\nu\eta}$ has seven non-vanishing components with the following relations [101, 106]:

$$\chi_{ZXX} = \chi_{ZYY}$$

$$\chi_{ZZZ}$$

$$\chi_{XXZ} = \chi_{YYZ} = \chi_{XZX} = \chi_{YZY}$$

Based on the same symmetry considerations, the fourth-rank tensor $T_{\lambda\mu\nu\eta}$ has the following non vanishing components :

$$T_{XXXX} = T_{XXYY}$$

$$T_{XXZZ}$$

$$T_{XZXZ} = T_{XZZX} = T_{YZZY} = T_{YZYZ}$$

$$T_{ZZXX} = T_{ZZYY}$$

$$T_{ZXXZ} = T_{ZXZX}$$

$$T_{ZZZZ}$$

$$T_{YXYX} = T_{YXXY}$$

The derivation of the contribution of the PGE to the second-order nonlinear current density components for p-polarized optical excitations is straight forward and leads to :

$$j_X^{(2)PG}(0) = E_0^2(\omega)\left[\chi_{XXZ}\sin 2\theta\right]$$
$$j_Y^{(2)PG}(0) = 0$$
$$j_Z^{(2)PG}(0) = E_0^2(\omega)\left[\chi_{ZXX} - (\chi_{ZXX} - \chi_{ZZZ})\sin^2\theta\right]$$

The same derivation for the PDE requires a few extra steps that are detailed in appendix C.2, and yields to :

$$j_X^{(2)PD}(\boldsymbol{q}) = E_0^2(\omega)q_0\left[(T_{XXZZ} + 2T_{XZXZ} - T_{XXXX})\sin^3\theta + (T_{XXXX} - 2T_{XZXZ})\sin\theta\right]$$
$$j_Y^{(2)PD}(\boldsymbol{q}) = 0$$
$$j_Z^{(2)PD}(\boldsymbol{q}) = E_0^2(\omega)q_0\left[(T_{ZZZZ} - T_{ZZXX} - 2T_{ZXZX})\cos^3\theta + (2T_{ZXXZ} - T_{ZZZZ})\cos\theta\right]$$

Thus, the components of the total second-order nonlinear current density write :

$$j_X^{(2)}(\theta) = E_0^2[\chi_{XXZ}\sin 2\theta +$$
$$q_0(T_{XXZZ} + 2T_{XZXZ} - T_{XXXX})\sin^3\theta + q_0(T_{XXXX} - 2T_{XZXZ})\sin\theta]$$
$$j_Y^{(2)}(\theta) = 0$$
$$j_Z^{(2)}(\theta) = E_0^2(\omega)[\chi_{ZXX} - (\chi_{ZXX} - \chi_{ZZZ})\sin^2\theta +$$
$$q_0(T_{ZZZZ} - T_{ZZXX} - 2T_{ZXZX})\cos^3\theta + q_0(2T_{ZXXZ} - T_{ZZZZ})\cos\theta]$$

One can note that for p-polarized optical excitation, the $j_Y^{(2)}(\theta)$ contribution is reduced to zero.

At this point, we have the expressions of the current density along the three directions as a function of the incidence angle of the optical pulses. For later comparison with experimental results, we aim for an expression of the radiated THz electric field. The transient current induced THz emission can be described by a model of dipole radiation, $\boldsymbol{E_{THz}} \propto \frac{\partial \mathbf{j}}{\partial t}$ as expressed in Equation 4.1. The radiation is generated within the HgTe film, and has to propagate through successive medium (quartz substrate, air) before being recorded. By taking into account the transmission at different interfaces, it is possible to express the THz radiation emitted at an angle Φ_{det} from the normal surface of the HgTe NCs film as [107] :

$$E_{THz}^h \propto t_p^{quartz-air}\, t_p^{film-quartz}\left(\cos(\Phi_{in})\frac{\partial j_X}{\partial t} - \sin(\Phi_{in})\frac{\partial j_Z}{\partial t}\right) \tag{4.8}$$

$$E_{THz}^v \propto t_s^{quartz-air}\, t_s^{film-quartz}\left(\frac{\partial j_Y}{\partial t}\right) \tag{4.9}$$

These expressions make use of the Fresnel transmission coefficients defined as follows, involving different angles that are indicated in Figure 4.14 :

$$t_p^{quartz-air} = \frac{4\sin(\Phi_{det})\cos(\Phi_{quartz})}{\sin(2\,\Phi_{det}) + \sin(2\,\Phi_{quartz})}$$

$$t_p^{film-quartz} = \frac{4\sin(\Phi_{quartz})\cos(\Phi_{in})}{\sin(2\,\Phi_{quartz}) + \sin(2\,\Phi_{in})}$$

$$t_s^{quartz-air} = \frac{2\sin(\Phi_{det})\cos(\Phi_{quartz})}{\sin(\Phi_{quartz} + \Phi_{det})}$$

$$t_s^{film-quartz} = \frac{2\sin(\Phi_{quartz})\cos(\Phi_{in})}{\sin(\Phi_{in} + \Phi_{quartz})}$$

For a fixed angle Φ_{det}, Φ_{in} and Φ_{quartz} correspond to the internal angles of the radiated electric field respectively in the HgTe NCs film and in the quartz substrate. Both Φ_{in} and Φ_{quartz} can be expressed as function of Φ_{det} using Snell's laws: $\sin(\Phi_{in}) = (n_{quartz}/n_{film})\sin(\Phi_{quartz})$ and $\sin(\Phi_{quartz}) = (1/n_{quartz})\sin(\Phi_{det})$. Note that the proportionality factor in Equations 4.8 and 4.9 includes the effect the quartz birefringence.

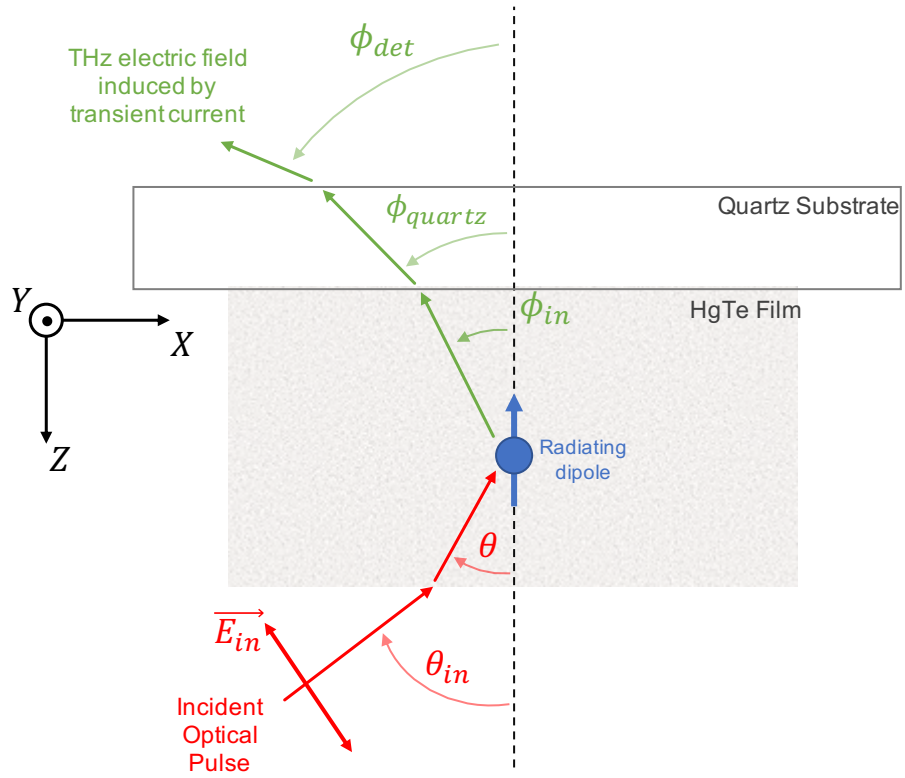

Fig. 4.14 *Sketch of the propagation of the optical and THz electric fields , with the associated angles indicated. The red color is used to depict propagation of the incident optical pulse, while the green one is used for the propagation of the transient current induced THz electric field detected at an angle* Φ_{det}.

We can then express the THz electric field at the electro-optic detector with separate terms corresponding to the different dependences on the angle θ :

$$E^h_{THz} \propto E_0^2(\omega)\left[A + B\cos\theta + C\sin\theta + D\sin 2\theta + E\cos^3\theta + F\sin^2\theta + G\sin^3\theta\right] \quad (4.10)$$

with :

$$A = -\sin(\Phi_{in})\chi_{ZXX}$$
$$B = -\sin(\Phi_{in})\, q_0\,(2\,T_{ZXZX} - T_{ZZZZ})$$
$$C = \cos(\Phi_{in})\, q_0\,(T_{XXXX} - 2\,T_{XZXZ})$$
$$D = \cos(\Phi_{in})\,\chi_{XXZ}$$
$$E = -\sin(\Phi_{in})\, q_0\,(T_{ZZZZ} - T_{ZZXX} - 2\,T_{ZXXZ})$$
$$F = \sin(\Phi_{in})(\chi_{ZXX} - \chi_{ZZZ})$$
$$G = -q_0\cos(\Phi_{in})(T_{XXXX} - 2\,T_{XZXZ} - T_{XXZZ})$$

The maximum achievable incident angle of the optical pulses in our experimental configuration is $|\theta_{in}| = 75°$, which corresponds to an incident angle in the HgTe NCs film of only $|\theta| = 24°$. We can thus neglect the $\sin^2$ and $\sin^3$ terms of Equation 4.11 in the following analysis of our datas. The expression is reduced to 5 independent parameters :

$$E^h_{THz} \propto E_0^2(\omega)\left[A + B\cos\theta + C\sin\theta + D\sin 2\theta + E\cos^3\theta\right] \quad (4.11)$$

4.6 Interpretation of experimental results

First analytical considerations indicate that the expression of E^h_{THz} (Equation 4.11) well explains some dependencies of the measured THz emission. Indeed, calculation predicts that $E^h_{THz}(\text{-}\Phi_{det},\text{-}\theta)=\text{-}E^h_{THz}(\Phi_{det},\theta)$, which is consistent with the reverse polarity observed experimentally in Figure 4.8. For a constant detection angle Φ_{det} but an opposite incident angle Φ_{in}, E^h_{THz} is reduced due to odd terms in Φ_{in} in the sum. Also, E^h_{THz} is predicted to cancel out for $\theta{=}\Phi_{det}{=}0°$, as observed experimentally. An interesting aspect of the Equation 4.11 is the fact that the coefficients A and D only depend on $\chi_{\lambda\nu\eta}$ and are thus related to PhotoGalvanic Effects while B, C and E only depend on $T_{\lambda\mu\nu\eta}$ and are related to Photon Drag Effects. This motivated more intensive measurements of the emitted THz electric field as function of the incident angle θ_{in}, in an attempt to gain insight into the relative contributions of PhotoGalvanic and Photon Drag currents underlying the THz emission by the HgTe NCs.

Figure 4.15.a) shows the emitted THz waveforms measured for several incident angles θ_{in} and a fixed detection angle $\Phi_{det}{=}45°$. The peak-to-peak E_{PP} amplitude of these waveforms shows a strong dependence on the inner incident angle θ and remains positive even at positive angle, as observed in Figure 4.15.b). We use the expression of E^h_{THz} from Equation 4.11 to fit the peak-to-peak amplitude as a function of θ, considering the coefficients A, B, C, D, E as mean values over all frequencies. It is worth noting the very good agreement between the theoretical expression of E^h_{THz} and the experimental trend. Most importantly, this good agreement could not be obtained with a single effect (i.e. by fixing either $A{=}D{=}0$

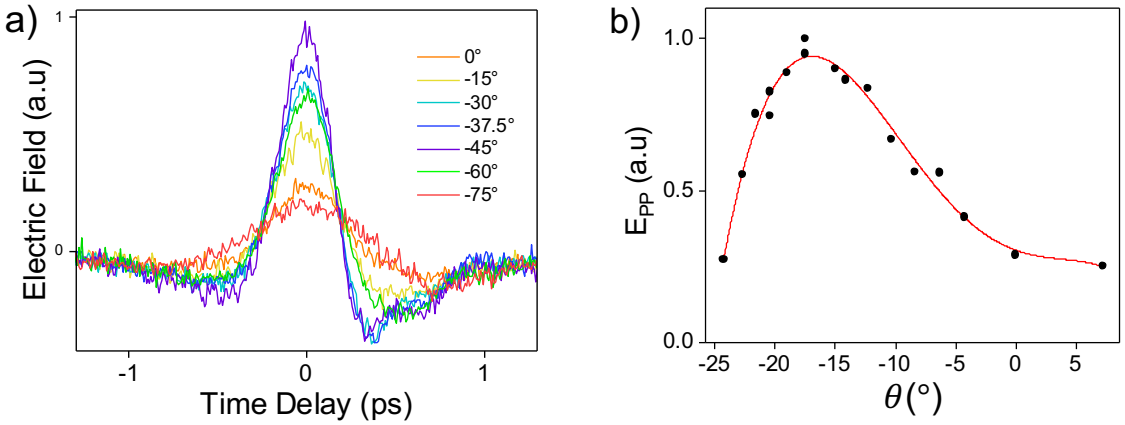

Fig. 4.15 *a) Time-resolved electric field profiles for different incident angles θ_{in} ranging from 0° to -75° under p-polarised excitation (α=0°), detected at fixed angle Φ_{det}=45°. b) Peak-to-Peak amplitude of the THz electric field profiles as a function of θ, the incidence angle within the HgTe NCs film. Black circles correspond to the experimental data and the red dashed line is the best-fit curve using Equation 4.11. We find the coefficients A=-377; B=575; C=-70; D=34 and E=-197.*

or B=C=E=0) showing the contribution of both Photon Drag and PhotoGalvanic Effects in the coherent THz emission process.

A few additional aspects can be pointed out. First, the weight of coefficients involved in j_X are smaller than those involved in j_Z revealing that the dominant transient photocurrent is along the direction normal to the HgTe NCs film surface. Also, the weak dependence of the emitted THz radiation on the polarization of the optical pulses observed in Figure 4.10 can be attributed, on the one hand, to the small angle of incidence of the optical pulses in the HgTe NCs film (θ of only -17.5° for θ_{in} = -45°), which strongly limits the Z-axis component of the optical electric field and, on the other hand, to the isotropy of the (X,Y) plane, which makes E_X and E_Y equivalent. Finally, the component of the emitted THz electric field along the vertical axis of the electro-optic detector results from birefringence effects in quartz substrate only, as $j_Y^{(2)}$=0.

The spectra derived from the emitted THz waveforms of Figure 4.15.a) are plotted in Figure 4.16 and exhibits interesting results. In particular, we observe a shift of the THz spectra in the range 0.4-0.8 THz by varying θ_{in}, leading to a tunability of the emitted THz radiation of $\Delta\omega/\omega$=50%. Such an optically controlled spectral tunability is not achievable in conventional THz emitters. This shift in frequency of the emission peak could be due to phase matching effects.

4.7 Conclusion

In conclusion, using THz emission spectroscopy, we have demonstrated THz emission from large HgTe NCs excited by femtosecond optical pulses induced by transient second-order

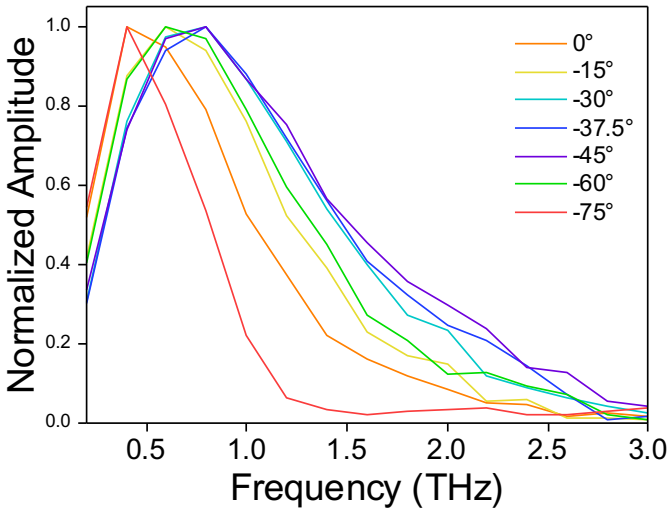

Fig. 4.16 *Normalized amplitude spectra of the THz electric field emitted by the HgTe NCs film, measured for different θ_{in} ranging from 0° to 75° under p-polarized optical excitation (α=0°), and detected at fixed angle Φ_{det}=45°.*

nonlinear photocurrents. We have highlighted the role of PhotoGalvanic and Photon Drag Effects underlying the nonlinear photocurrents and found that their main component is oriented in the direction normal to the HgTe NCs film. We have also shown the possibility to tune the THz emission in the range 0.4-0.8 THz by changing the incident angle of the optical pulses. Our work opens the perspective to study helicity-dependent nonlinear photocurrents in these HgTe NCs to probe their possible topological surface states and their potential to emit chiral THz waves. Also, the investigation of transient photocurrents and coherent THz emission from alternative nanocrystals and quantum dots could provide unique microscopic insights on their properties. This work represents an important step in colloidal quantum dot-based light emitters by extending their spectral range to THz frequencies. It therefore has important implications for THz technology with significant prospects in the development of novel THz emitters that can be easily integrated on various devices and towards the development of quantum THz devices.

Chapter 5

THz Spectroscopy of Graphene Quantum Dots

The lack of devices operating at THz frequencies keeps motivating both the research of new peculiar THz materials, and the development of new THz technologies.

In this context, the previous chapters dealt with the study of novel large HgTe nanocrsytals in the THz range, providing fundamental results on the absorption, the carriers dynamics and the non-linearites of these objects. It laid the groundwork for the comprehension of these state-of-art nanomaterials, which will hopefully lead to the development of NC based devices.

Concurrently to the fundamental work carried on the nanocrystals, an important and more technologically oriented part of my thesis was devoted to the study of graphene quantum dots (GQD). This part of my phD was motivated by the LEON project which aims to use GQDs as gain medium for the development of compact, powerful and efficient THz lasers operating at room temperature.

The previous section unveiled the peculiar properties of graphene sheet and established the motivation for the study of graphene quantum dots. Indeed, by taking advantage of the full discretization of their electronic states, one could possibly inhibit recombination processes that currently limit the optical gain in graphene sheet. However, due to the unusual gapless and linear energy dispersion of graphene, the effects of spatial confinement on the energy spectrum and the optical absorption might significantly differ from other regular materials used for THz applications.

In this chapter, we investigate the light matter interaction of arrays of graphene quantum dots in the THz range. We will first give a brief review of the potential of graphene quantum dots for THz lasing. We will then describe the energy level spectrum of GQDs from a theoretical perspective, as well as their absorption properties in the THz domain. Finally we will present the experimental investigations performed on GQD, which were made possible by the development of a fabrication process of the GQD arrays, and by improvements of the spectroscopy set-up.

5.1 Graphene for optoelectronic THz devices

This first section gives a brief overview of the important fundamentals of graphene, unveiling its potential to be used as a gain medium for THz lasers. It aims to give the reader

insights on the relevance of engineering GQD to enhance the limited lifetime of population inversion.

For this purpose, we start by quickly reviewing the peculiar linear band structure of graphene, and then describe its interaction with light in the THz range. Next, we present the relaxation and recombination dynamics of non-equilibrium carriers in graphene, resulting in a possible short-lived population inversion. We finally explain how graphene quantum dots could enhance the currently limited optical gain lifetime.

5.1.1 Electronic properties of graphene

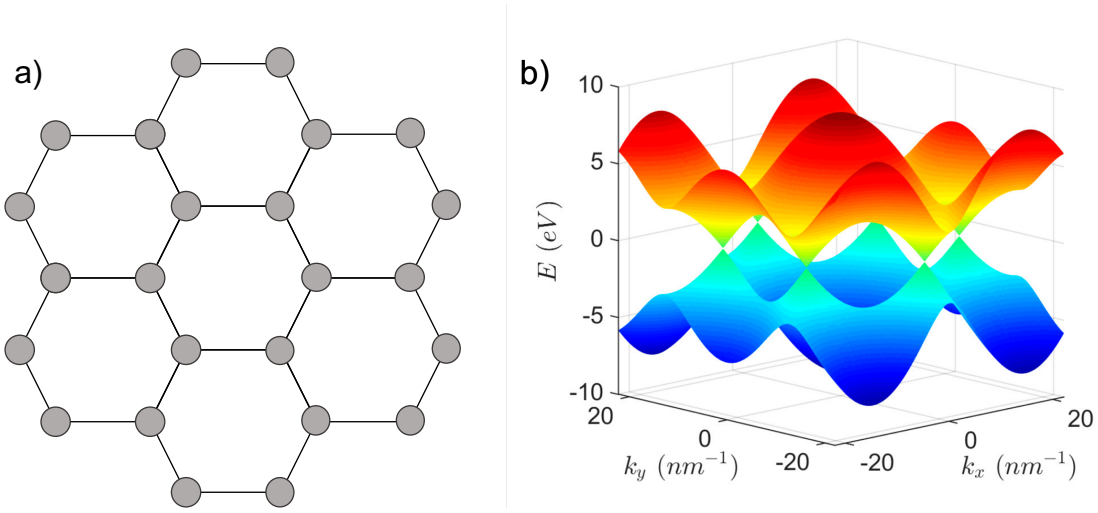

Fig. 5.1 *a) Representation of hexagonal honeycomb lattice of graphene. b) Graphene band structure within the nearest neighbour tight-binding model plotted within the first Brillouin zone. Adapted from [108].*

Graphene is a 2D material composed by carbon atoms arranged in a honeycomb lattice as represented in Figure 5.1.a). Carbons atoms have 4 valence electrons. Three of them form σ-bonds with neighboring atoms and are responsible for the mechanical properties of graphene. The remaining electron occupies a p_z orbital, which is oriented perpendicular to the plane, and forms weaker π-bonds. The only electrons contributing to the electronic properties of graphene are those in the π-bonds. They are delocalized over the whole graphene sheet, which enables a high electronic mobility.

The band structure of graphene is of particular interest. Using the tight-binding approximation, it is possible to derive the dispersion relation of a graphene monolayer, which writes [109, 110] :

$$E_{\pm}(\mathbf{k}) = \pm t\sqrt{1 + 4\cos\left(\frac{\sqrt{3}k_y a}{2}\right)\cos\left(\frac{k_x a}{2}\right) + 4\cos^2\left(\frac{k_x a}{2}\right)} \tag{5.1}$$

with t ≈2.eV is the transfer integral between first neighbors p_z-orbitals, $a = \sqrt{3}a_{CC}$ and a_{CC}=0.142 nm the carbon-carbon distance in graphene. The band structure of graphene is plotted in Figure 5.1.b). Like usual semiconductors, the band structure is mainly separated

in two bands. The lower energy one corresponds to the valence band and the higher energy one to the conduction band. Both bands are symmetrical with respect to E = 0 eV, where they touch each other at six points: **K**, **K'**, and the equivalent points obtained by $2\pi/3$-rotations. These 6 contact points are called the Dirac points.

In neutral graphene, the Fermi energy, E_F lies exactly at the Dirac points since each atom brings one electron, and each level is spin degenerated. Thus, the valence band is full and the conduction band is empty at T = 0 K and no carrier is able to take part in the charge transport even though there is no energy gap between the bands. Therefore, the graphene is often described as a semimetal or as a gapless semiconductor.

It is interesting to expend the Equation 5.1 in the vicinity of the points **K** and **K'**:

$$\mathbf{K/K'} = \frac{4\pi}{3a}(\eta,0) \text{ with } \eta = 1(-1) \text{ for } \mathbf{K}(\mathbf{K'}) \tag{5.2}$$

The first order development in **k** gives :

$$E_{\pm}(\mathbf{q}) = \pm\hbar v_f|\mathbf{q}| \tag{5.3}$$

where $\mathbf{q} = \mathbf{k}-\mathbf{K}(\mathbf{K'}$ and $v_f = \frac{\sqrt{3}ta}{2\hbar} \approx 10^6 \text{m.s}^{-1}$ is defined and referred to as the Fermi velocity. One can note that the dispersion relation in Equation 5.3 is linear in **q** in contrast with the usual parabolic dispersion relations of semiconductors. The low-energy band structure is then conical around the Dirac points, and is often referred to as the Dirac cones. From the computation of the density of states per unit area, it is possible to derive the charge carrier density n in graphene given by:

$$n = \frac{1}{\pi}\left(\frac{E_F}{\hbar v_F}\right)^2 \tag{5.4}$$

n is usually expressed in cm^{-2} and referred to as doping. The charge neutrality is reached when n=0, which corresponds to the energy level of the Dirac points E=0. By applying a gate voltage, it is possible to control the Fermi energy and tune the carrier density over large range. Such electric field effect in graphene could be very practical in our context as the interaction between graphene and THz photons strongly depends on the doping level, enabling the control of the strength of optical transitions through electrical gating, as it will be discussed in the following.

5.1.2 Optical properties of graphene at THz frequencies

Due to its particular linear dispersion relationship and gapless band structure, graphene has attracted a lot of interest from the THz scientific community, which has led to intense research on graphene-based THz devices [9, 111–113]. We present here some basic concepts concerning the optical properties of a graphene monolayer in the THz spectral range, in order to support the interpretation of the theoretical and experimental results obtained for graphene quantum dots (GQDs) which will be the subject of the following sections. In particular, we will highlight the crucial influence of the doping level of graphene and its temperature on its interaction with THz photons.

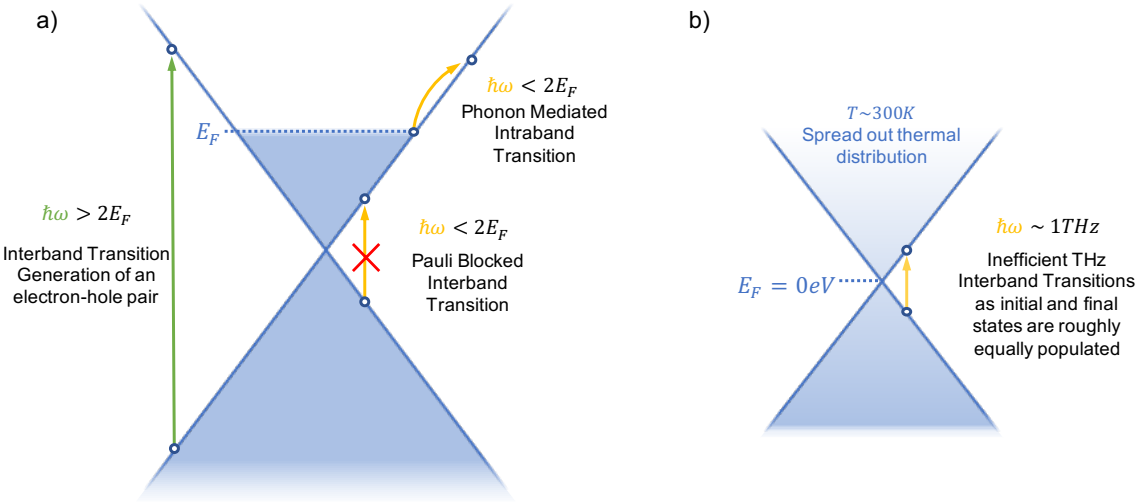

Fig. 5.2 *a) Sketch of Dirac cone of n-doped graphene over the entire linear energy range. b) Zoom in on the low energy range of the Dirac cone of undoped graphene to illustrate the effect of thermal distribution at T≈300 K on the efficiency of THz interband transitions.*

First, the linear dispersion relation of graphene (see Equation 5.3) is valid for energies up to ±1.5eV from the Dirac points [114]. The linear band structure is then valid to study interaction between graphene and photons with energies covering a wide range of the electromagnetic spectrum, from the visible down to the THz spectral range. Depending on the photon energy $\hbar\omega$ and the Fermi energy, two different types of transitions can be addressed, which are depicted in Figures 5.2 a) and b).

- **Interband Transitions**
  For $\hbar\omega > 2E_F$, interband transitions take place, leading to the creation of an electron-hole pair. Due to the peculiar linear band structure, interband transitions in graphene result in a frequency-independent absorption $A = \pi\alpha$=2.3% where $\alpha = (1/4\pi\epsilon_0)e2/\hbar c$ is defined as the fine constant structure. This regime mainly dominates in the infrared and visible spectral range. However, graphene being gapless, interband transitions at THz frequencies are also accessible, but are usually strongly limited by Pauli blocking due two reasons. The first one is the unintentional doping of graphene, preventing interband transitions for photons of energy $\hbar\omega < 2E_F$. Note that a Fermi level E_f as low as 20 meV causes Pauli blocking of interband transitions for frequencies lower than 10 THz. The second reason results from the thermal distribution of electrons. Indeed, at room temperature, even in undoped graphene, partial populations of states in the conduction and valence bands that could be involved in interband transitions at THz frequencies become almost equal. For instance, at T=300 K, for electronic states involved in the interband transitions at 1 THz, we have $|f_{FD,conduction} - f_{FD,valence}|$ = 0.04, which leads to efficient Pauli blocking of the transition [114]. Thus, interband transitions in the THz spectral range in graphene are accessible, but only if the Fermi level lies very close to the Dirac point, and at cryogenic temperature. For instance, S. Massabeau et al. have recently demonstrated interband transitions in multilayer

graphene at THz frequencies [108].

- **Intraband Transitions**
  For $\hbar\omega < 2E_F$, intraband transitions are possible and dominate in the THz range. Such transitions, also referred to as "free carrier absorption" correspond to the interaction of photons with carriers close to the Fermi level. These transitions are mediated by phonons or defects which ensure momentum conservation [115], as depicted in Figure 5.2.a). The optical response of free carriers is then well described by a Drude model, which leads to a conductivity expressed as:

$$\sigma(\omega) = \frac{\sigma_0}{1 + i\omega\tau} \tag{5.5}$$

  where σ_0 represents the DC conductivity and τ the electron scattering time. Note that, because of the graphene peculiar band structure, $\sigma_0 \propto \sqrt{n}$ with n the carrier density. Since the optical absorbance arising from the conductivity follows $A(\omega) \propto Re(\sigma(\omega)) \propto E_F$, the application of the gate voltage is an efficient way of modulating the intraband absorption of graphene at THz frequencies.

Thus, as soon as the temperature and/or the doping level of graphene increases, the "free carrier" absorption regime dominates in the THz range. These intraband transitions, although modified by the quantum confinement of the carriers, will be central in the next section of this chapter, section 5.3, which deals with the absorption at THz frequencies of GQDs.

5.1.3 Hot carrier dynamics in graphene

As mentioned previously, graphene has a great potential for the development of THz passive and active devices. Most notably, it is an excellent candidate for the realization of a THz laser based on a semiconductor-laser model scheme, which is still not available today [116]. The development of a compact, powerful THz laser would be greatly beneficial for THz technology since the current THz sources suffer from several limitations such as bulkiness, moderate output power or cryogenic operating temperature. Also, graphene is very promising for the realization of sensitive THz photodetectors owing to the high carrier mobility and its broad absorption spectrum.

An important aspect of the performance of graphene-based THz optoelectronic devices is the dynamics of non-equilibrium carriers in graphene. For instance, for the realization of a THz laser, carrier lifetimes of a few tens of picoseconds are needed to reach long-lived optical gain. The carrier lifetimes also strongly impact the sensitivity and speed of THz detectors. In this section, we briefly introduce the key features in the dynamics of non-equilibrium carriers in graphene.

The relaxation and recombination dynamics of non-equilibrium carriers in graphene have been intensively investigated [12, 117–120] and are sketched in Figure 5.3. Illumination of a graphene monolayer with femtosecond optical pulses generates non-equilibrium carriers

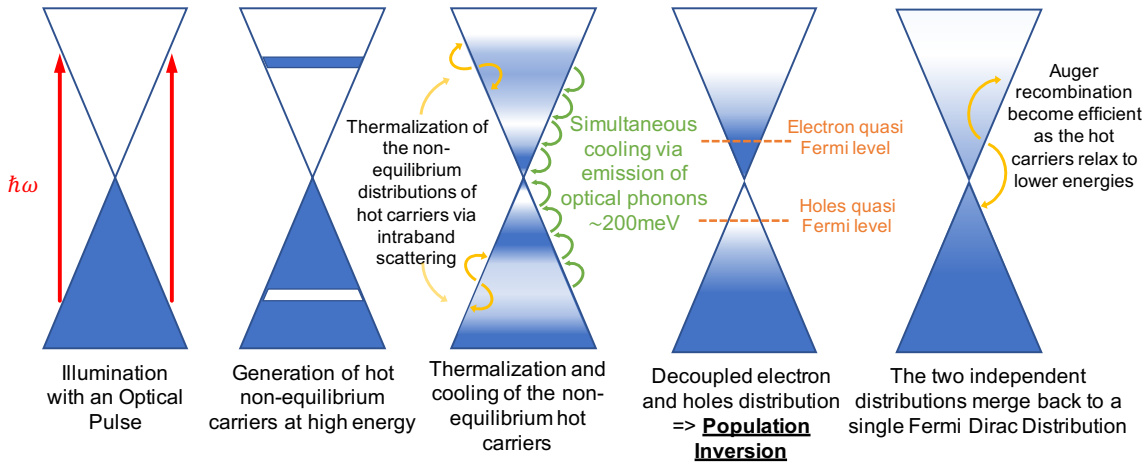

Fig. 5.3 *Scheme of the relaxation and recombination dynamics of non-equilibrium carriers in graphene probed by pump-probe experiments.*

at high energies. After photoexcitation, the hot electron/hole populations are both redistributed by energy-conserving intraband carrier–carrier scattering and relaxed via the emission of high energy-optical phonons (≈200meV), within the first tens of femtoseconds. It results in two independent lower-energy broad electron and hole distributions. Due to initially weak interband scattering, the valence and conduction bands are efficiently decoupled, which result in a short-lived inverted population [13]. As the hot carriers relax to lower energies, interband Auger recombination processes become efficient that quickly merge the separate electron and hole quasi-Fermi levels. Auger recombination is a scattering process in which the recombination of an electron–hole pair pushes another electron to higher energy. Auger process leads to a single Fermi-Dirac distribution for conduction and valence populations within typically 200 fs. A subsequent cooling process occurs mediated by interband optical phonon emissions within 1-2 ps and by less efficient intraband low-energy acoustical phonon scattering.

5.2 Graphene quantum dots for THz emitting devices

The existence of a transient population inversion near the Dirac point in graphene is very encouraging since it is a crucial building block for THz lasing. However, the optical gain lifetime is strongly limited by counteracting Auger recombination processes to a few hundred femtoseconds making it suitable only for amplification of short pulses. The strategy adopted in this thesis work to tackle this problem is to realize the full discretization of electronic states through Graphene Quantum Dots (GQD). Indeed, as the recombination of an electron–hole pair by Auger process requires another electron to be pushed to higher energy, one would expect that the full discretization of electronic states should significantly limit available final states for the scattered electron. A scheme diagram depicting the strategy adopted is presented in Figure 5.4.

Only a limited number of studies have been dedicated to GQD at THz frequencies. As

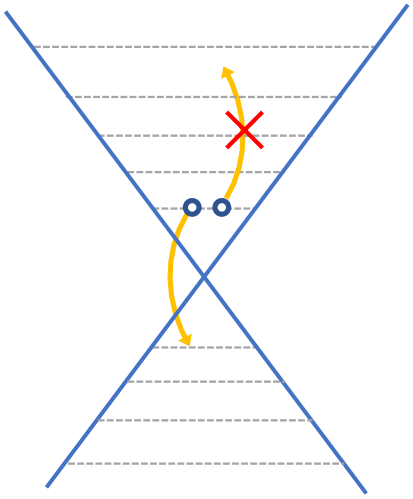

Fig. 5.4 *Illustration of the reduction of Auger recombination process by the full discretization of the electronic states in a GQD. The electron-hole recombination energy can not be transferred to another electron as no final state satisfies the energy conservation.*

will be detailed in the next section, for operation in the THz frequency range, large GQD with typical size of ∼100 nm have to be considered, i.e. such that the bandgap is ∼4 meV (1 THz). Few relevant experimental studies on large GQD have been focused on quantum transport phenomena in a single GQD. In particular, it has demonstrated charge carrier relaxation times of 60-100 ns, a very promising indication that long-lived optical gain at THz frequencies in GQDs is achievable [121]. Recently, large bolometric effects have been demonstrated in a single GQDs when illuminated with THz photons [122, 123]. Also, my thesis group has recently demonstrated the ultrasensitive photoresponse to thermal THz radiation of a hBN-encapsulated GQD in the Coulomb blockade regime at low temperature [124]. Also by investigating a quantum phototransport in single graphene quantum dot under coherent THz illumination my thesis group has demonstrated a large electric dipole of length d≈230 nm in a single graphene quantum dot [125]. Note that no experimental work has been reported so far on the reponse of an ensemble of GQDs at THz frequencies. The transition strengths between the confined states in GQD, the selection rules for optical absorption, as well as the link between the optical properties with their morphology have been restricted to theoretical studies. Regarding the dynamics of hot carriers in GQD, reported works are very limited so far, but several investigations support our innovative approach. Most notably, the study of Auger coupling in small GQD has been performed by Ozfidan *et al.*, which promisingly predicts the existence of of two electron-hole pair states stable against Auger recombination [126]. In addition, it has been shown in analogous systems that Auger coupling is decreased with increasing quantum dot size [127].

To conclude, the motivation of this thesis work to study GQDs is driven by their strong potential for the development of compact THz lasers. In the next sections, we will present a more in-depth theoretical analysis of the energy spectra of GQD and absorption spectra at low frequencies, which is essential for further GQD engineering. We will then describe the experimental implementations we performed in an attempt to study the optical absorption

of GQDs at THz frequencies, as a first step towards the study of THz optical gain and its lifetime in GQDS.

5.3 Theoretical analysis of GQD

Most of carried out theoretical studies on GQDs has only been devoted to small GQDs with optical response ranging from the visible range down to the mid-infrared range [128]. Very little work has been reported on the electronic and optical properties of larger GQDs, which is mainly due to computing issues associated with the important number of atoms in large GQDs. At this point, a theoretical study of the electronic levels and the optical properties of large GQDs is an important prerequisite for a relevant design, fabrication and characterization.

In this section we adapt the work of Sylvain Massabeau performed in his PhD thesis [108] in order to gain insight on the effect of carrier confinement in GQDs on the electronic states and optical absorption. The different models that are developed here allows for the prediction of energy spectra and optical response of large GQDs with radii over 25 nm. The first part presents a simplified description based on a continuous model using the assumption of a circular symmetry of the wavefunction. The second part presents a more accurate description based on the calculation of the GQD energy spectrum using the direct numerical diagonalization of the tight-binding Hamiltonian.

a)

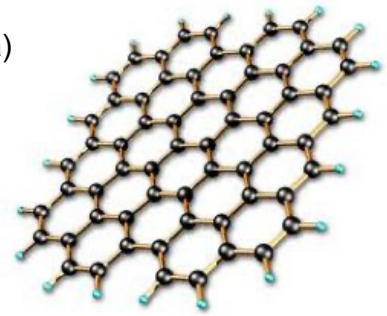

b)

Radius (*nm*)	3	7	11	15	19	25
N	1052	5850	14446	26936	43186	74866

Fig. 5.5 *a) Scheme of a graphene quantum dot. b) Number of carbon atoms for distinct GQD radii.*

5.3.1 Continuous model

In this section, we explore a method for the identification of the energy eigen values of a GQD based on a continuous model developed in reference [129]. Here the GQD is described as a 2D circular quantum well of radius R. We use the fact that at low energy, the Hamiltonian takes the form of a Dirac Hamiltonian, which writes :

$$H = \hbar v_f \begin{pmatrix} 0 & -i\left(\frac{\partial}{\partial x} - i\frac{\partial}{\partial y}\right) \\ -i\left(\frac{\partial}{\partial x} + i\frac{\partial}{\partial y}\right) & 0 \end{pmatrix} \tag{5.6}$$

We write the two-components wavefunction as :

$$\Psi(\mathbf{r}) = \begin{pmatrix} A(\mathbf{r}) \\ B(\mathbf{r}) \end{pmatrix} \tag{5.7}$$

where A and B correspond to the two atoms of the graphene unit cell. Using Equations 5.6 and 5.7, the eigenvalue equation for an energy E writes :

$$\Delta A(\mathbf{r}) = -\left(\frac{E}{\hbar v_f}\right)^2 A(\mathbf{r}) \tag{5.8}$$

Since we have made the assumption that the GQD have circular symmetry, we can assume the following convenient form for the wavefunction $A(\mathbf{r})$, expressed in the polar coordinates:

$$A(r,\varphi) = a(r)e^{im\varphi} \tag{5.9}$$

where m is an integer which stands for the eigenstate angular momentum. The solutions of eEquation 5.8 for the radial part $a(r)$ can be expressed using the m^{th} Bessel function of the first kind:

$$a(r) = J_m\left(\frac{Er}{\hbar v_f}\right) \tag{5.10}$$

The boundary conditions imposes $a(r = R) = 0$, leading to the discretization/quantization of the eingenvalues of Equation 5.8:

$$E_m = \frac{\hbar v_f \Theta_m^1}{R} \tag{5.11}$$

where Θ_m^1 is the first zero of the m^{th} Bessel function of the first kind J_m. The energy spectrum is plotted in Figure 5.6. The $\frac{1}{R}$ dependency is remarquable as it differs from the $\frac{1}{R^2}$ dependency obtained in Equation 1.10 for a NC made of a semiconductor with a parabolic dispersion relation. This continuous model provides first hints on the energy levels of a GQD. More particularly, it confirms that large GQD might actually exhibit transitions in the THz spectral range. Indeed, for a 50 nm radius GQD, typical energy level spacings is about 18 meV (eq.≈4 THz). However, the model shows limitations as it assumes an infinite potential well and thus does not take into account the edge states of GQD, which are expected to strongly affect the energy spectrum at low energy. The second model presented in the next section goes into more details, exhibiting a more complex energy spectrum of these GQD.

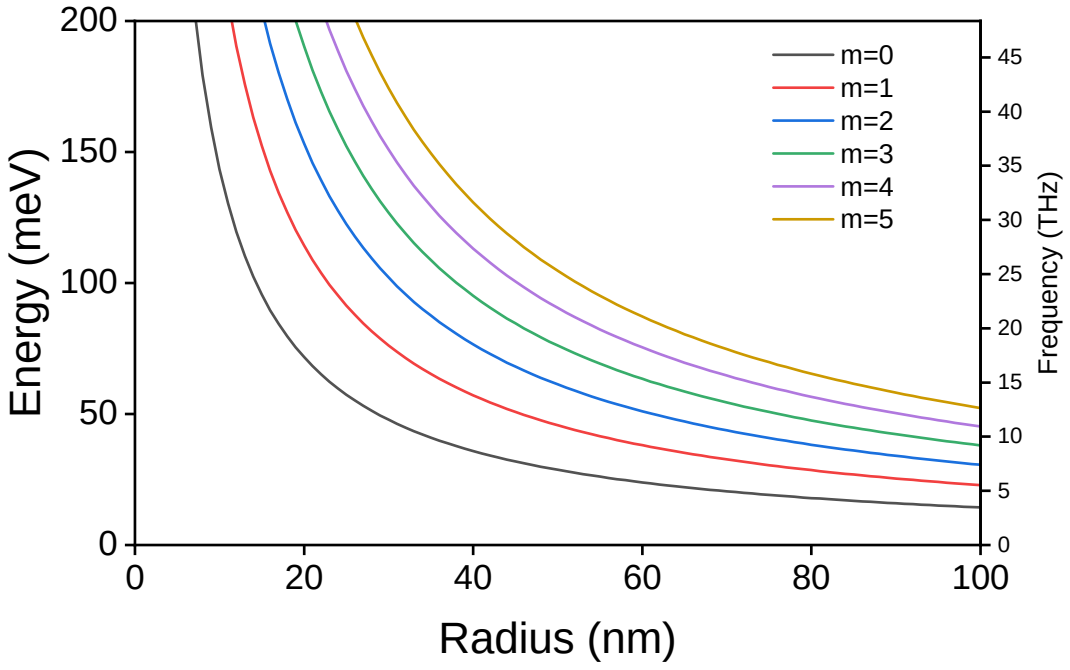

Fig. 5.6 *Eingenvalues E_m as function of radius from Equation 5.11 with increasing angular momentum m from bottom to top.*

5.3.2 Discrete tight-binding approach

The previous model takes into account the finite size of GQD, but neglects their microscopic structures, which would be incompatible with the circular symmetry assumption. More particularly, the model does not allow for the description of the GQD edge structures, which are expected to strongly affect the energy spectrum, as observed in the case of smaller GQD [130, 131]. Indeed, the two different types of graphene edge structure, either "zigzag" or "armchairs" as depicted in Figure 5.7, have a great influence on the low energy electronic states [132]. It is all the more crucial since it is geometrically not possible to have either defined armchair or zigzag edges in the case of a circular GQD.

Sylvain Massabeau in his thesis also proceeded to the rigorous calculation of the GQD energy spectrum based on the direct numerical diagonalization of the tight-binding hamiltonian, which accounts for the microscopic and edges structures. The geometrical definition of GQD does not impose any condition of the edge shape except cutting dangling bonds. These considerations are relevant from the fabrication perspective as simply connected carbon atoms in the border are not likely to remain after the lithography step, and since our fabrication process does not allow for the exact control of the edges shape. Also, note that the derivation of the wavefunctions from the direct numerical diagonalization of very large Hamiltanian was extremely demanding computing-wise, limiting the maximal radius of the studied GQD to 25 nm.

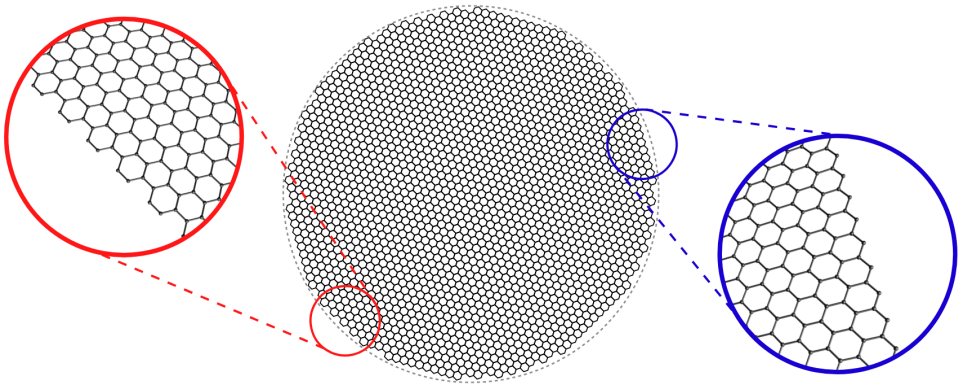

Fig. 5.7 *Sketch of a Graphene Quantum Dots exhibiting the different types of edges : red inset corresponds to an "armchair" configuration and blue inset to a "zigzag" configuration. Adapted from [133]*

Energy Spectra Figure 5.8 presents the energy spectra obtained for radii ranging from 17 nm to 25 nm. The results from the previous continuous model are also plotted in dashed lines for m=1 and m=2. The colors of the states correspond to the spatial extension of their wavefunctions, leading to the classification under three relevant categories : edge states, mixed states and edge states. Several aspects can be pointed out. First, one can note that the high energy states mostly consist of bulk states, and seem to follow the energy obtained from the previous continuous model described by Equation 5.11. The corresponding electronic density functions plotted on the right hand side of Figure 5.8, indicate that the bulk states exhibit smooth and large lobes almost entirely away from the GQD edges, in agreement with the boundary conditions imposed in Equation 5.11. Additionally, the energy spectra exhibit the presence of numerous states lying under the lowest energy solution (m=1) obtained from the continuous model, and spreading out down to the Fermi level E_F=0. These states arise from edge effects, which were previously not taken into account. The lower energy states, the edge states, are mainly localized at the GQD borders and supposedly result from the complex coupling of localized orbitals. At intermediate energy lie the mixed states, which are also localized at the GQD edge but with a non-negligible electronic density at the center of the dot.

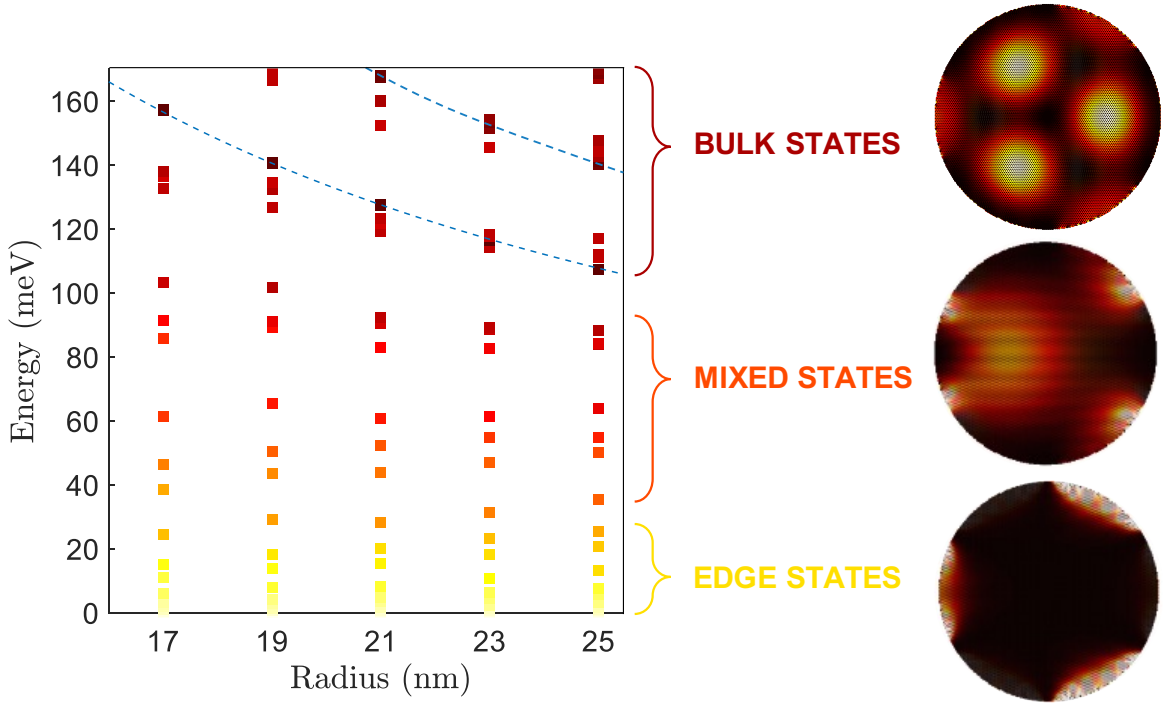

Fig. 5.8 *Energy spectra of GQD as function of the radius obtained from direct diagonalization of the tight-binding Hamiltonian. The color scale describes the spatial extension of the wavefunctions, from yellow (localised on the edge) to dark red (localised at the center). GQD can be classified into three categories : Bulk, Edge and Mixed States. Typical wavefunction density profiles for each type are depicted on the right. Dashed lines corresponds to the eigenvalues for m=1 and m=2 from Equation 5.11. Adpated from [108]*

Light Matter Interaction As these computation aim to provide preliminary results for future spectroscopic experiments, it is important to explore the theoretical interaction of these GQD with light. In the following, we investigate two insightful quantities that are the oscillator strength $f_{i,f}$ and the absorption probability $\alpha(\hbar\omega)$. Both quantities are calculated from the computation of the dipolar interaction Hamiltonian $H_I = \frac{e}{m_e}\mathbf{p}.\mathbf{A}$, with $\mathbf{p}$ the impulsion operator and $\mathbf{A}$ the vector potential of a plane wave at normal incidence.

Figure 5.9 represents the normalised $f_{i,f}$ restrained to pairs of initial and final states (E_i,E_f) so that $f_{i,f}$ is not negligible, i.e. $f_{i,f} \geq 10^{-2}$, for a GQD of radius R=25nm. The dark and red dashed lines represent the transitions such as E_f=E_i and E_f=-E_i respectively. Two different types of efficient transitions can be identified from this graph. First, the transitions corresponding to the points around the black dashed line, which are interband transitions. Second, the transitions concentrated in a line parallel to the red dashed curve. These transitions are intraband transitions and we observe that $E_f - E_i$ is roughly constant and matches the energy level spacings derived from Equation 5.11 $E_{m=2}(R = 25nm) - E_{m=1}(R = 25nm) \approx 30$ meV ≈7 THz. These intraband transitions are predicted to be much

more efficient than the interband transitions. These theoretical results are very promising as they predict the existence of very efficient THz intraband transitions in GQD of radius in the range 25 nm.

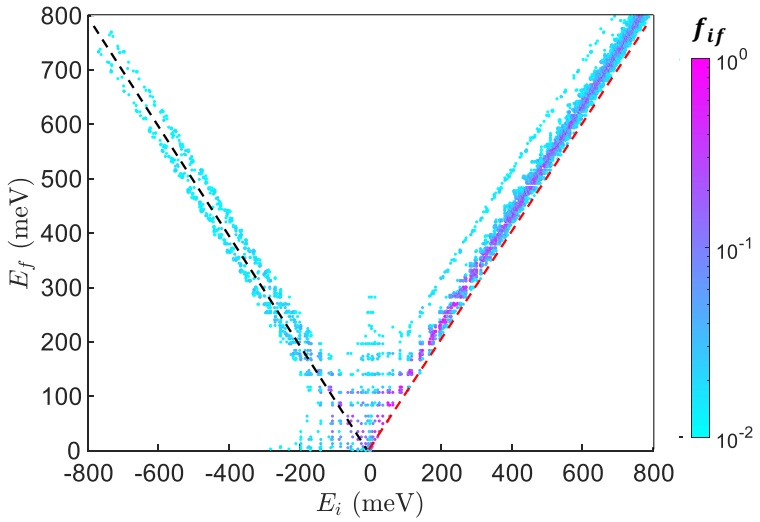

Fig. 5.9 *Oscillator strength $f_{i,f}$ for a GQD of radius R=25 nm, restricted to pairs of initial and final states (E_i,E_f) so that $f_{i,f}$ >10^{-2} and E_f>0. Reproduced from [108]*

Population effects strongly affect the optical response as, in a real system, the transitions are achievable if the initial state is occupied and the final state empty. Thus, we now focus on the absorption probability, which account for both the doping level and the Fermi-Dirac distribution of the carriers. For the calculation, we introduce as a phenomenological parameter, an energy level broadening Γ fixed at 5 meV. As seen on Figure 5.10, at T=4.7 K and E_F=0 eV, the model predicts a flat absorption $\alpha \approx \alpha_0 = 2.3\%$, indicating that the interband absorption of the GQD is close to the interband absorption of a graphene sheet considering the broadening effects. Also, we observe the same Pauli-blocking effect as described in section 5.1.2, which shifts the interband plateau towards energies satisfying $\hbar\omega$>$2E_F$ as the doping level is increased.

While the high-frequency interband absorption of the GQD is close to that of the graphene sheet, the low-frequency characteristics differ strongly from the conventional Drude-type response. Indeed, when the Fermi level is increased, an intense intraband absorption resonance arises at low energies, as observed in Figure 5.10. The center frequency of this absorption peak seems to be independent on the doping level but scales like $\frac{1}{R}$ as depicted in Figure 5.11.b). This strong low-frequency absorption resonance is very promising, as the extrapolation of its central frequency considering the $\frac{1}{R}$ dependence suggests that the peak frequency for a 50 nm radius GQD is about 4 THz, which fully reaches the THz spectral range. This low-frequency absorption resonance is induced by carrier confinement effects, which lead to previously mentioned very efficient intraband transitions, similarly to the intraband absorption resonance observed in large HgTe NCs in previous chapters.

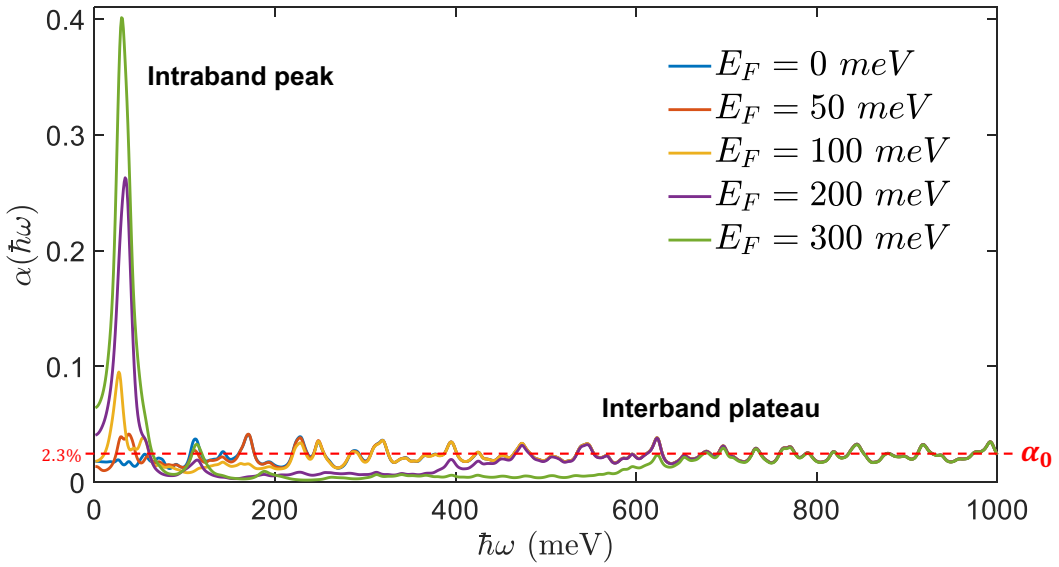

Fig. 5.10 *Absorption probability spectra for a GQD of radius R=25 nm, at T=0 K, for three doping values. Adapted from [108]*

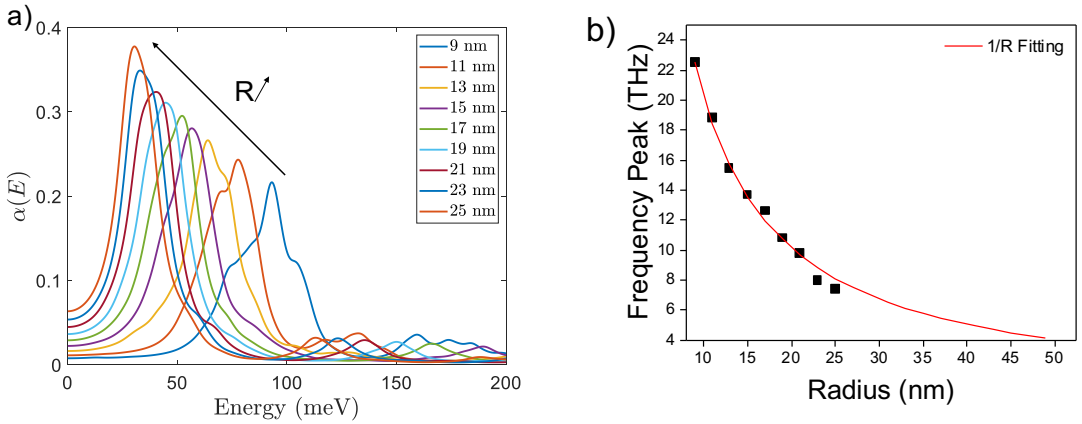

Fig. 5.11 *a) Theoretical absorption probability spectra $\alpha(\omega)$ of GQD for several radii ranging from 9 nm to 25 nm, E_F=200 meV and T=300 K. α is evaluated from the ratio of the GQD absorption cross section over the GQD surface area. Reproduced from [108] b) Frequency of the absorption peak from fitting of theoretical curves plotted in a). Adapted from [108].*

When the Fermi level increases, the number of activated transitions are increased by population effects, which results in the enhancement of the absorption resonance magnitude. However, in the case of low doping value, which is more likely to occur for our GQD sample as we will discuss later, the effect of quantization is supposedly still observable. Indeed, for $0 \leq E_F \leq 20$meV, an increase of the temperature leads to the activation of efficient intraband

transitions and thus an increase of the absorption around 30 meV (=7.2THz) for a GQD a radius R=25 nm as presented in Figure 5.12. In return, the absorption due to higher energy intraband transitions around 110 meV is reduced due to Pauli exclusion principle.

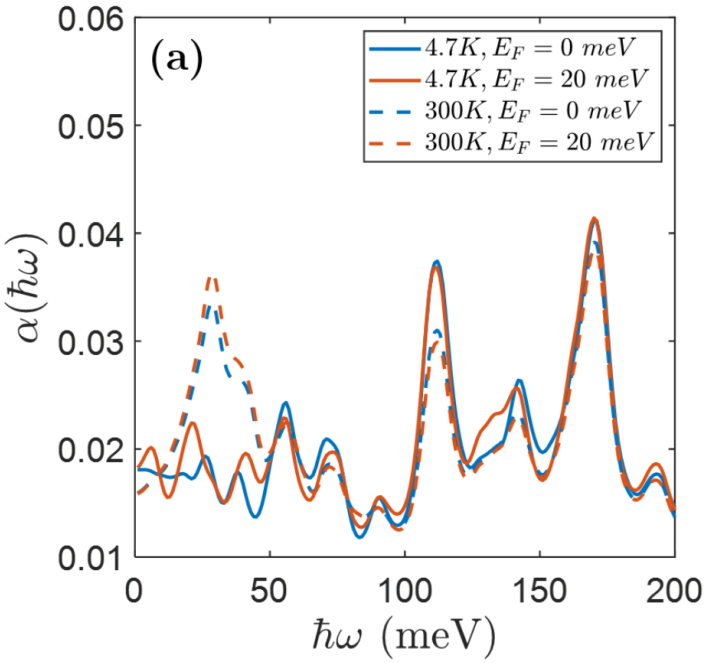

Fig. 5.12 *Absorption probability spectra for a GQD of radius R=25 nm with low doping values. Full line correspond to T=4.7 K and dashed lines to T=300 K. An in increase of the temperature leads to the activation of efficient intraband transitions and thus an increase of the absorption around 30 meV (=7.2 THz). Reproduced from [108]*

The results obtained from these theoretical studies are very promising. They predict a significant effect of the quantization of electronic levels in GQD, resulting in a singular absorption peak in the THz range caused by intraband transitions between these quantized states. The center frequency of the resonance thus depends on the size of the GQD, and has been well calculated for radius up to R=25 nm. Also, the magnitude of this absorption resonance strongly depends on the doping level, but is theoretically still observable even for low Fermi energy $0 \leq E_F \leq 20$meV at room temperature. All these predictions provide a strong basis for practical investigation of large GQDs since we now have a clear idea for where to seek for resonances depending on the GQD size and which absorption magitude to expect depending on the doping level. We will present in the following section the fabrication and experimental investigations performed on array of GQDs, and the challenges encountered in the measurement of this predicted intraband absorption resonance in the THz spectral range.

5.4 Fabrication and characterization of array of GQDs

The first section of this chapter presented the motivation for studying GQDs, unveiling the potential of their quantized electronic states for addressing the highly efficient Auger recombination problem that currently limits the lifetime of population inversion in a graphene sheet. Ideally, we shall aim for measurements of the recombination and relaxation dynamics of non-equilibrium carriers in GQDs. However, such measurements are not straightforward and require preliminary theoretical and experimental achievements. Therefore, the second section was devoted to theoretical investigations of the confinement effects in a circular GQDs with radii of a few tens of nanometers. Most notably we have demonstrated that such GQDs exhibit a singular absorption resonance in the THz spectral range. In this section we present the experimental work performed regarding the measurement of this intraband absorption resonance in such GQD.

It is worth noting that a first experimental issue stems from the size of the THz focused beam used as probe in the spectrometers. Indeed, even at the diffraction limit, their diameter is typically a few hundred microns which is very large compared to the few tens of nanometers radius of GQDs, making the characterization of a single GQD impossible. The strategy adopted here is to fabricate and probe arrays of GQDs with areas of $\sim$1 mm^2 in order to cover the entire THz focused beam and maximize the THz absorption, as shown in Figure 5.13. The number of GQDs in an array is typically 10^7.

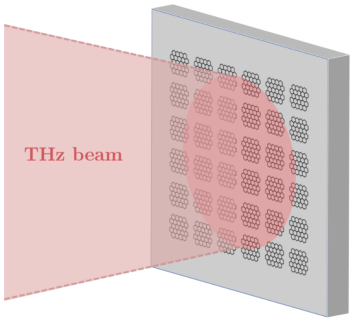

Fig. 5.13 *Sketch of a THz beam spot probing an array of GQDs. The array is designed to cover the entire THz beam to enhance the overall absorption of the GQDs array sample.*

In this third section, we present the experimental work that has been performed regarding the fabrication and the characterization of arrays of GQDs, in an attempt to measure the THz absorption resonance predicted by our microscopic model. The section is divided in two subsections, corresponding to the two main challenges that we have faced : first the fabrication of the GQD arrays, and second, the development of an adequate THz spectroscopy set-up to probe their absorption. Note that even though both aspects are presented in distinct sections, they are closely related and have been developed side-by-side, since the design of the GQD samples is both dictated by the performances of the spectroscopy set-up and constrained by the feasibility of nano-fabrication processes, as we will discuss in the following.

5.4.1 Fabrication of graphene quantum dot arrays

In this section we detail the fabrication procedure of arrays of graphene quantum dots, which has been developed by Michael Rosticher, an engineer working at the LPENS clean room, and Othmen Zied who worked as a post doctoral in our group. We opted for monolayer graphene sheets obtained by chemical vapour deposition (CVD) because of their low cost and easy availability from a large number of suppliers, which makes us completely autonomous for the fabrication of the samples and which is very relevant for the potential applications of these large GQDs. The fabrication procedure of arrays of GQD is mainly divided into two steps:

- Graphene Wet Transfer

The first part of the process, depicted in Figure 5.14, consists in wet transferring the graphene sheet initially deposited on a CVD catalyst copper foil to a convenient and processable substrate. For the substrate, we use 500 μm thick high-resistivity Si wafers coated with a 500 nm thick SiO_2 oxyde layer on one side. We start by spin-coating a poly(methyl methacrylate) (PMMA) layer, followed by an annealing, resulting in a top-layer of a few micrometers. This layer provides an top support for the graphene while the Cu catalyst foil is etched in a $(NH_4)SO_4$ solution. Once etching is complete, the graphene and the PMMA are washed several times in deionized water baths to remove any remaining copper ions. In parallel to these steps, a Si+Si0$_2$ wafer is cleaned in acetone and isopropanol (IPA) baths, followed by a reactive ion etching (RIE). The clean Si+Si0$_2$ substrate is then used to "fish out" the graphene & PMMA layers that float on the surface of the cleaning solution. They are then annealed to promote adhesion of graphene to the substrate and to remove any trapped water molecules. The top layer of PMMA is then removed with an acetone bath. Importantly, by successively repeating these steps with a substrate where graphene sheets have already been transferred, it is possible to obtain stacks of graphene layers. This was done to obtain the tri-layer graphene used in the following.

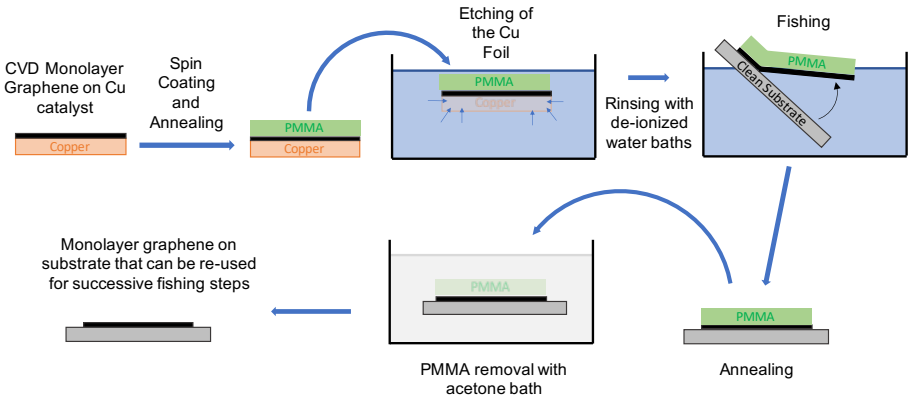

Fig. 5.14 *Sketch of the successive steps of the wet transfer of CVD graphene.*

- Nano-Patterning of arrays of GQD

The second part of the process consists in nano-patterning arrays of GQDs, and is depicted in Figure 5.15. We start by spin-coating a PMMA layer on the graphene, followed by an annealing. Next, an adhesion promoter is spin-coated and is later rinsed with H_2O. The structure is then left to dry, which is a crucial step. Indeed, it has been observed that remaining water molecules are very detrimental for the quality of the futur patterned QDs. We then proceed to the spin coating of a Hydrogen silsesquioxane (HSQ) resist mask, also followed by an annealing. We use electron beam lithography (EBL) to pattern an assembly of ∼50 nm diameter GQDs, separated by ∼100 nm (center-to-center distance) and covering an area of $\sim 1\text{mm}^2$. The EBL takes around 10 h due to the large number of GQDs to be patterned ($\sim 10^7$). Next, the resist is developed, which removes the HSQ that has not been patterned. This is followed by a RIE which etches both the PMMA and the graphene layer where the HSQ is missing. Finally, a PMMA lift-off is performed with an acetone bath followed by an IPA bath which supposedly to remove the HSQ dots by dissolving the PMMA in between the graphene and the HSQ layesr. This last step was motivated by the experimental observation of a non-negligible THz absorption by thin the HSQ film; this step is still under development as we will see later.

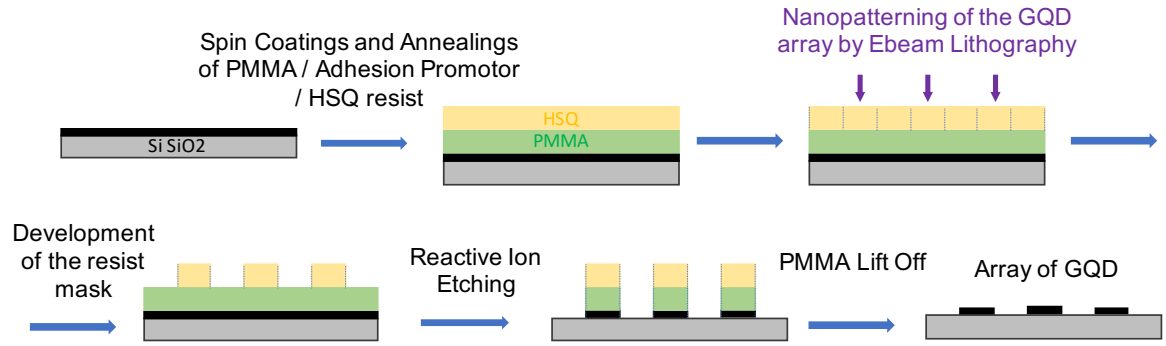

Fig. 5.15 *Sketch of the successive steps of the nanopatterning of array of GQDs.*

The SEM images presented in Figure 5.16 provide a snapshot of the GQD arrays after nano-processing. The full array consists of a 1 mm side square (see Figure 5.16.a)). Note that the GQDs have a satisfying circular shape of ∼54 nm. From Figure 5.16.b), we can estimate the filling factor η to be ≈23%. Moreover, Raman spectra tend to validate the success of the nanoprocess, in particular the fact that GQDs are well separated within the array.

The development of this whole fabrication process required significant efforts and successfully led to the possibility of nano-processing large arrays of GQDs without any residual resin. Preliminary characterizations (SEM and Raman spectroscopy) validate the good quality of the GQDs. Even tif the use of graphene by CVD was initially a technological challenge, it is now very beneficial. Indeed, in addition to the low cost and the wide availability of CVD graphene sheets, we can consider transferring them onto different substrates suitable for the development of futur devices, which is not be possible with graphene obtained by epitaxial growth. Such consideration are particularly relevant in the context of our project since our final goal is to integrate these GQDs into laser cavities. However, a crucial aspect that

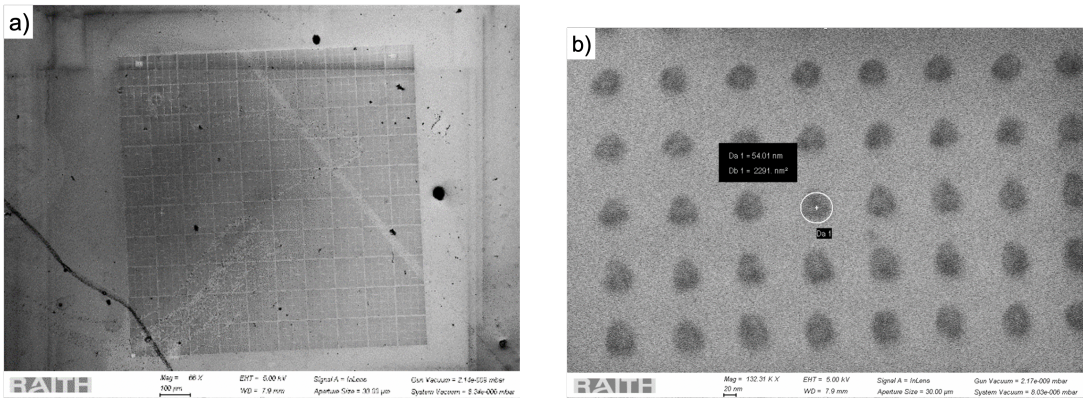

Fig. 5.16 *SEM images of an array of GQDs after nanoprocessing of a monolayer CVD graphene sheet. a) SEM Image showing the full 1 mm x1 mm array. b) SEM image focusing on the quantum dots, showing their circular shapes and the ∼ 54 nm diameter size.*

still remains unexplored from the fabrication perspective is the doping level of these GQDs, which is predicted to strongly affect the absorption resonance magnitude as presented in the previous section. Several fabrication steps have a potential impact on the doping level. For instance, hole-doping can be induced during the transfer of PMMA-covered graphene from the Cu tatalyst foils to the Si/SiO_2 substrates by residues of PMMA [114]. The effect of the environment, such as the dielectric substrate itself, molecules trapped between the graphene and the substrate, adsorption of impurities on the graphene surface, exposure to electron-withdrawing/donor species, are other exemples of potential contributions to the unintentional doping of CVD graphene [134, 135]. Typical unintentional doping of substrate-supported graphene is on the order of E_F=100 meV [114, 136]. Nevertheless, we cannot rule out the possibility of a very low doping value, which would result in a much lower absorption resonance. This motivated us to seek for very low absorption features during the characterization of the GQDs, as discussed in the next section.

5.4.2 Characterization of array of GQDs

The array of GQD being successfully fabricated, the next experimental step is to probe their absorption, in particular the THz absorption resonance predicted in section 5.3.2. Based on the SEM images of the arrays (See Figure 5.16.b)), we estimate the average diameter of the nano-patterned GQDs to be ∼ 54nm. Regarding the theoretical dependence of absorption spectra $\alpha(\omega)$ with the GQD radius presented in Figure 5.11 a) and b), we expect the absorption resonance of these GQD extending in between 7.3 THz and 8.2 THz. These frequencies are out of the range of our THz-Time Domain Spectroscopy set-up, but match the spectral bandwidth of the FTIR spectrometer. In this section, we present the calibration and optimization developments that we have performed on our FTIR spectroscopy set-up in order to be able to detect the weak THz absorption of GQD arrays.

The main challenge here is to enhance the sensitivity of FTIR experiments so that absorption resonances could be differentiated from noise and any experimental artifacts. Indeed,

in view of the $\alpha(\omega)$ calculations and the low filling factor $\eta \approx 23\%$, GQD arrays with even a relatively high doping value (typically 100 meV) are expected to absorb only ∼2.3 % of the incident electric field. Such variation in the FTIR transmittance spectra were not accurately detectable owing to the poor initial performances of the set-up as detailed below. Thus, before proceeding to further measurements on the GQD arrays, we first intended to reduce the noise and biases of the FTIR calibration transmittance spectra down to ∼0.2% which is supposedly required to differentiate the absorption resonance of GQDs with a low doping value.

Transmittance Spectra

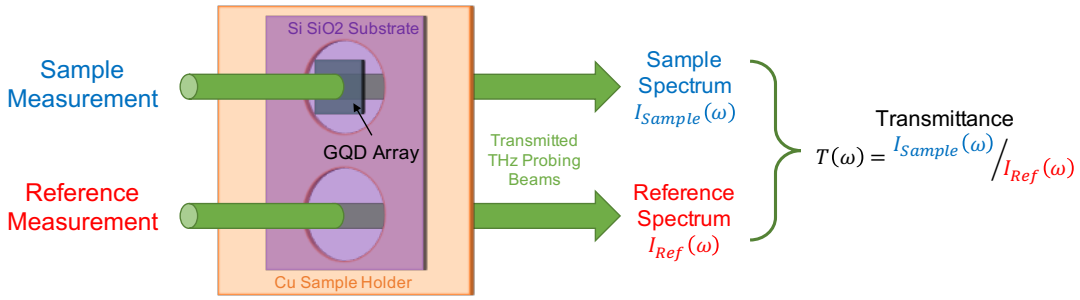

Fig. 5.17 *Sketch of the sample holding system developped for the measurements of transmittance spectra. We mount our samples on holed pieces of copper which allow for accurate positioning of the samples at the THz probe beam focal point. The sample is centered on the first hole, while the second one is covered by bare substrate belonging to the same piece of wafer. The two holes are separated by only 5 mm, which limit the variations between sample and reference substrates.*

For a better understanding of the experimental issues, we quickly review the process for measuring a transmittance spectra. We use the FTIR spectrometer in a transmission configuration, whose principle is presented in section 2.3.3. We add a beam condenser (accessory) that allows the examination of small samples (samples area from 0.5 to 3 mm) in reducing the normal sampling area by a factor 5. The reduction of the measurement spot is achieved by a stronger focus of the beam on the sample at the cost of an extremely limited sample space. To determine the transmission spectrum, we perform two successive measurements: one with the sample and one with a bare substrate used as a reference. The transmittance spectrum is defined as the ratio of these two recorded spectra. Ideally, the substrate used for the reference measurement should be identical to the one supporting the sample, and the performances of the set-up should not vary between the two measurements. To limit substrate variations between the sample and the reference, we probe the reference in close proximity to the sample, i.e. on the same piece of wafer. A sketch of the experimental configuration is depicted in Figure 5.17.

Development of a new module for sample positioning

The initial configuration of the FTIR, including the condenser accessory, did not allow the position of the sample holder to be changed from outside the FTIR chamber. Since the measurements are performed under vacuum, atmospheric pressure had to be restored in between sample and reference measurements. It was observed that the vacuum breaking and re-pumping intermediate steps had a detrimental effect on the reproducibility of the measurements as illustrated in Figure 5.19. This motivated the development of a new module allowing fexternal control of the sample holder position, which is shown in Figure 5.18. Using this new module, we measure a very flat transmittance spectrum between two bare holes of a sample holder (green curve in Figure 5.19), with variations and noise <0.2% that matches the level of accuracy we aim for.

Fig. 5.18 *Picture of the new FTIR module allowing for sample positioning from outside of the FTIR chamber, thus avoiding to break the vacuum between measurements.*

Sample Mounting

The other optimization concerned obtaining a flat transmittance with low noise for two measurements through the holes in the sample holder on which a piece of bare SiO_2/Si substrate is deposited. In this way, any variation in the transmittance spectrum of a sample with the GQDs array could be attributed to the absorption of the GQDs. At this point, we encounter issues with the sample mounting methods that are illustrated in Figure 5.20 a) and b). First, we identify that the PMMA layer we had previously used to glue the samples to the sample holder did not allow for similar transmission measurements through the two holes. The possible influence of the PMMA stains on the transmission spectrum raised the question of the transparency of the different resins used in the experiments and in the fabrication of the samples. As a result, we change the sample mounting method and optimize

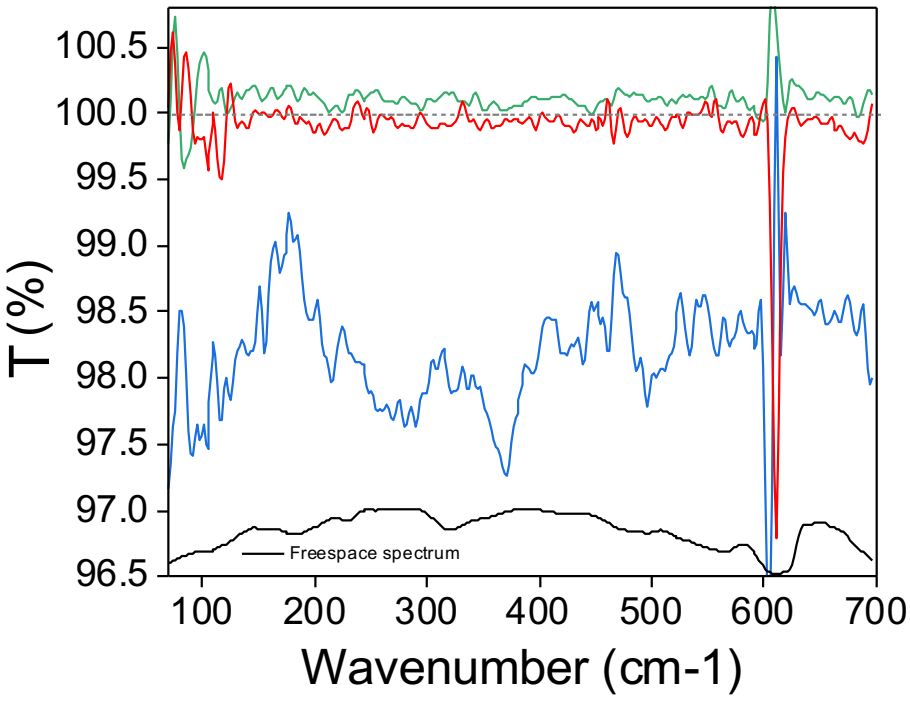

Fig. 5.19 *Red curve: ratio of two free-spaces spectra measured consecutively without vacuum breaking. Blue curve: ratio of two free-spaces spectra whose measurements were separated by vacuum breaking and re-pumpimp of FTIR chamber. The offset is important and one can note strong variation of ± 1% all over the spectrum. Green curve: ratio of two spectra measured for transmission through respectively each of the two bare holes of the sample holder, without intermediate breaking vacuum owing to the new sample positioning module. Black curve : FTIR free-space spectrum.*

the GQDs array fabrication process, with the goal of getting rid of the top layer of HSQ that remained on the GQDs after the initial processes. This step is now performed with the PMMA lift-off (see Figure 5.15). To stick the samples on the sample holder, we try to use double-sided adhesive tape, which results in oscillations in the spectra that we attribute to Fabry Perot effects between the sample holder and the substrate, caused by the width of the adhesive tape, as illustrated in Figure 5.20.b).

Finally, we mechanically press the sample on the sample holder using washers and clamps. This third method is much more satisfactory. Indeed, if we make two consecutive measurements through each hole covered with a single piece of SiO_2/Si substrate, the slow variations and oscillations of the spectrum are suppressed. However, we can note a slight resonance in the transmission, very wide, which extends from 320 cm^{-1} to 520 cm^{-1}. We observe this resonance in a systematic way. The contrast of this resonance is typically 1% when using two different pieces of substrate in front of each hole coming from distant parts of the wafer (see Figure 5.21.a)). This peak cannot be attributed to the main absorption resonances of SiO_2,

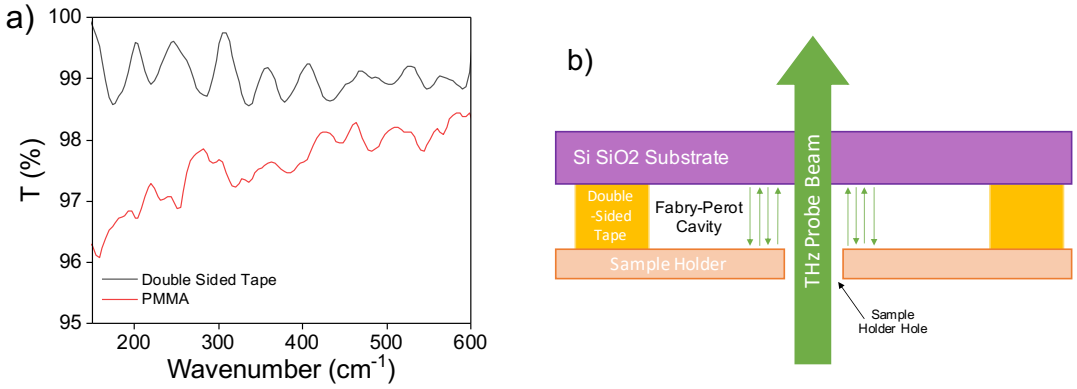

Fig. 5.20 *a) Transmittance spectra between the two holes of the sample holder covered by a piece of SiO_2/Si substrate, glued with PMMA (red curve) or sticked with double-sided tape (black curve). Black curve presents oscillations that we attribute to a Fabry-Perot cavity effect, sketched in b), since the oscillation period ($\approx 55cm^{-1}$) is consistent with the couple hundreds μm width of the double sided tape. b) Sketch of the Fabry-Perot cavity in between the sample holder and the substrate.*

clearly observed in Figure 5.21.b), we can however attribute to spatial inhomogeneity effects on the wafer, such as dopants introduced during growth. Thus, this resonance is reduced to typically 0.2% when using the same substrate.

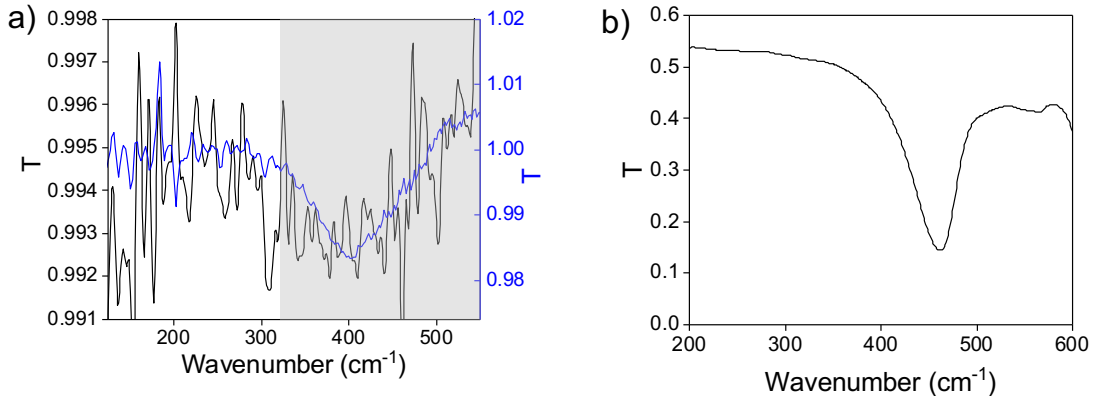

Fig. 5.21 *a) Transmittance spectra for two holes being covered by a single piece of SiO_2/Si wafer (black curve) and by two different pieces of SiO_2/Si (blue curve). b) Transmittance spectrum of the SiO_2/Si substrate, obtained using a free-space spectrum as reference.*

Transmittance Spectra of GQD array

Owing to the several optimization, the noise and the variations in the transmittance spectrum are low enough to measure transmission variations of the order of 0.3%, a typical value expected for arrays of GQDs with low doping values. We restrict our investigation to wavenumbers lower than 320 cm^{-1} to not overlap the resonance related to substrate inhomogeneities observed between 320 cm^{-1} and 520 cm^{-1} (see in Figure 5.21.a)). We thus proceed to the measurements of the transmittance of an array of GQDs at room temperature. Figure 5.22 shows the intensity spectra of a GQDs array, with the GQD mean radius of ∼27 nm and a filling factor $\eta \approx 23$ %, and of a SiO_2/Si wafer used as reference. The array of GQDs is made from an initial tri-layer graphene sheet, obtained by successive wet transfers and fabrication processes as described in section 5.4.1. We observe a reduced intensity from 240 cm^{-1} to 320 cm^{-1} for GQDs array compared to reference signal, revealing the absorption of the GQDs in this spectral region.

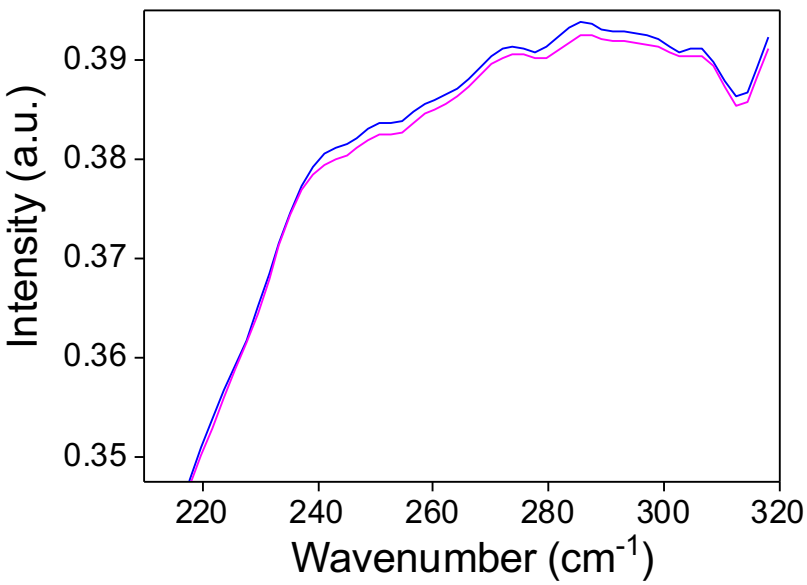

Fig. 5.22 *FTIR intensity spectra of a GQDs array, made from an initial tri-layer graphene sheet, with the GQD mean radius of ∼27 nm and a filling factor $\eta \approx 23$ % (magenta curve), and of a SiO_2/Si wafer used as reference (blue curve).*

Figure 5.23 presents the transmittance spectrum of the GQDs array, calculated from the recorded FTIR spectra. We observe a broad dip in the transmittance that appears to be centered around 300 cm^{-1}, i.e. 9 THz and results in a decrease in transmittance of ∼0.4 %. The evolution of transmittance as a function of frequency has an opposite trend to that of a 2D graphene layer governed by the Drude conductivity. Indeed, for a 2D graphene in the intraband regime, the transmittance increases as the frequency increases. Here, we observe that the transmittance of GQDs decreases when the frequency increases due to optical transitions between quantized electronic states (see Figure 5.23).

According to our predictions, the weak dip would indicate a low doping level. We thus

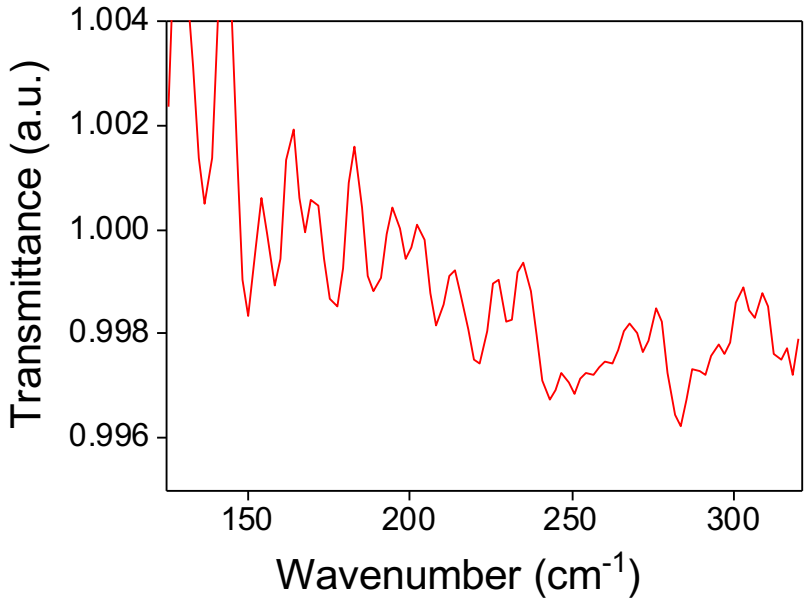

Fig. 5.23 *Experimental transmittance spectrum of a GQDs array, made from an initial tri-layer graphene sheet, with the GQD mean radius of ∼27 nm and a filling factor η ≈23 %.*

compare the measurements with the theoretical transmittance spectrum for a trilayer array of 25 nm radius GQDs with a doping level E_F=0 meV and a filling factor η=23% at T=300 K, as plotted in Figure 5.24. It is worth noting that the trend of the transmission decrease is in quite good agreement with the theoretical predictions. However, the predicted attenuation of 1.2 % is 3 times higher than that observed experimentally. This deviation from the theory could arise from several factors such as an over-estimation of the filing factor, partial degradation of the GQDs array during its manipulation or imprecision in the centering of the array over the middle of the sample holder holes. Concerning the dip frequency, the measurement gives a value slightly lower than the theoretical predictions, which is fully consistent with the SEM images (see Figure 5.16.b)) showing QD diameters of ∼54 nm which is a higher value than the one considered in the simulations (i.e. 50 nm).

These preliminary results showing the absorption of GQDs in the THz spectral range are new and very encouraging. It is also clear that the doping level is the next crucial aspect to enhance the absorption of the GQDs. This motivates the development of a system which would enable us to apply a gate voltage on the array, in order to take advantage of the electric field effect to tune the Fermi level in the dots. We are currently considering using an electrolytic solution deposited on the top of the sample that would make the application of a gate voltage possible, while still allowing for measurements in transmission configuration. The development of such a device requires several preliminary steps, such as the design of an electrical system connected to the sample that is easily mountable and manipulated in the set-up. Also, regarding the electrolytic solution, we have to characterize its response in

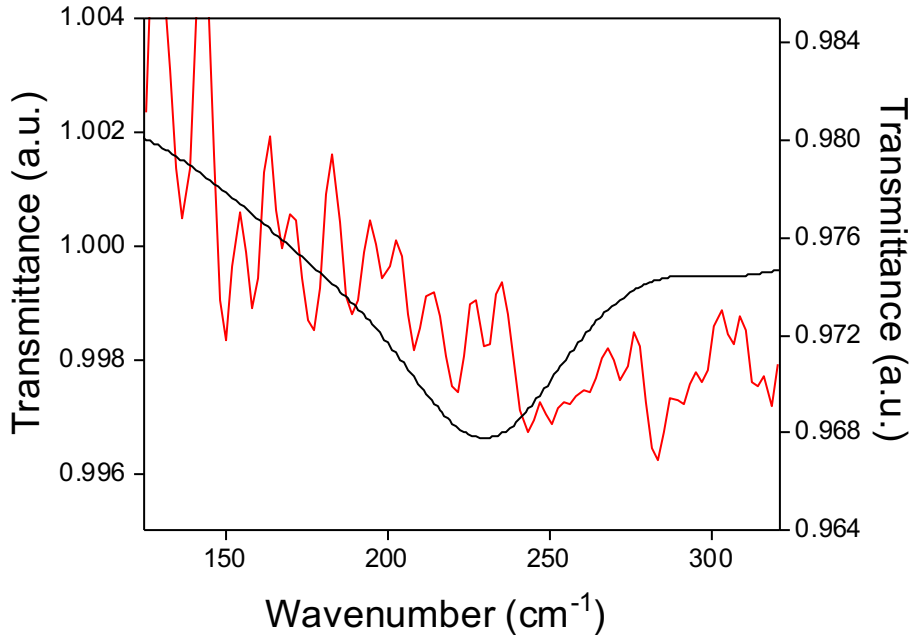

Fig. 5.24 *a) Comparison between experimental transmittance spectrum of a GQDs array, made from an initial tri-layer graphene sheet, with the GQD mean radius of ∼27 nm and a filling factor η ≈23 % and a computed transmittance of a tri-layer GQDs array with the same filling factor but a lower mean GQD radius size of 25 nm.*

the THz range, and check its compatibility with the current fabrication process. From the experimental perspective, connecting the sample to voltage source will require changes in the FTIR module.

It is also clear that the doping level is the next crucial aspect to improve the absorption of GQDs. An important perspective of this work is to develop a device that would allow us to apply a gate voltage to the GQDs array, in order to take advantage of the electric field effect to adjust the Fermi level in the GQDs. We plan to deposit the GQDs on a semi-transparent conductive layer, such as thin Ni/Cr (6 nm) or thin ITO (20 nm) and to use an electrolytic solution deposited on the GQDs array to apply a gate voltage, while allowing measurements in transmission configuration. Such a device will allow us to increase the Fermi level of the GQDs to reach Fermi levels of several hundreds of mV and thus to reach intraband absorptions of the order of ten %. We have also recently purchased CVD grapheme multilayers, 5 and 10 layers, available in the market today, which will also allow us to increase the absorption of the GQDs array by the increase of the number of layers.

In summary, the intense experimental work done in an attempt to measure the THz absorption resonance of GQDs has been very successful. It has laid the foundation for the

fabrication of GQDs arrays based on CVD graphene, which can now be pushed further by developing devices that allow modulation of the GQDs doping level and that contain a higher number of grapheme layers. Improvements to the experiment bench based on FTIR spectrometer will be of great value for future measurements, with the ability to detect optical responses of GQDs even for low Fermi levels.

5.5 Conclusion

In this chapter, we started by presenting the motivation for studying GQDs, and their potential for the realization of a THz laser. Indeed, the quantization of their electronic states could efficiently tackle the problem of very efficient Auger recombination that currently limits the lifetime of population inversion in graphene sheets. However, probing the effect of confinement on the dynamics of hot carriers in GQDs is not straightforward. It requires an in-depth theoretical understanding of the optical properties of GQDs, and an intense development concerning the experimental aspects. Thus, the second section was devoted to the theoretical study of confinement effects in a circular GQD of a few tens of nanometers radius. In particular, we have shown that the confinement of charge carriers in a circular GQD leads to very efficient intraband optical transitions at low frequencies and thus to an absorption resonance in the THz spectral range. The third section of this chapter presented the experimental work that has been done in an attempt to measure this THz absorption resonance that would pave the way for future measurements of hot carrier dynamics in GQDs. We started by presenting the top-down process that was developed, allowing the fabrication of large GQD arrays from CVD graphene. We then reviewed the successive improvements in the performance of our FTIR spectrometer-based experiment, in order to achieve very low noise and variation transmittance measurements of the GQDs array. Finally, we presented the transmittance spectrum of a GQD array, which reveals a weak THz absorption resonance in quite good agreement with theoretical prediction. We also suggested the development of an electric field gating system for GQDs array samples to fine tune the Fermi level of the GQDs and enhance the measured absorption. At this stage, the perspectives are very promising. Indeed, we now benefit from a good level of maturity both on the technological fabrication side and on the spectroscopy instrumentation side. Regarding the fabrication process, the electric field gating could be achieved by using an electrolytic solution deposited on the GQD arrays, themselves deposited on a semi-transparent conductive layer. On the experimental side, the FTIR spectroscopy setup has been fully optimized and is usable for future measurements.

Conclusion and Perspectives

My PhD work was devoted to the study of two different types of quantum dots: large HgTe Nanocrystals and Graphene Quantum Dots. The goal was to gain insight into their electronic and optic properties to evaluate their potential for the development of sources operating in the THz spectral range.

A first main part of this PhD work was dedicated to the study of large HgTe NCs. Our interest for these NCs has been motivated by several aspects. First, these NCs are state-of-the art, since their synthesis has been made possible only recently owing to a ground-breaking procedure developed by Goubet *et al.* [8]. Most importantly, they reported a significant absorption in the THz range, tunable down to 4 THz, and attributed to the self-doped nature of the NCs. This appeared particularly attractive as very few materials present tunable absorption in the THz spectral range. Also, from a technological perspective, colloidal quantum dots are very interesting owing to their low cost and easy fabrication and to their great manipulability.

- The first goal was to fully characterize the broad absorption at low frequencies and interpret the underlying physical mechanisms responsible for this absorption. We proceeded to Fourier Transform Infrared spectroscopy and THz Time Domain Spectroscopy measurements in order to measure the absorption spectrum of the large HgTe NCs over the full THz spectral range. These measurements have revealed a broad absorption resonance, centered at 4.5 THz with a FWHM of 5.5 THz. In order to interpret the physical mechanisms at stake in this feature, we have developed a quantum model that takes into account both the confinement of the carriers and their thermal distribution, the latter being justified by the low energy level spacing in these large NCs that is comparable to thermal energy at room temperature. The confrontation of this model with our data has enabled us to attribute this absorption to multiple intraband transitions between quantized states of confined carriers. Most notably, the plasmonic regime observed in smaller HgTe NCs with higher doping levels is negligible in the large HgTe NCs studied here. Also, our study indicates that confinement effects are still significant in these large NCs since their optical properties strongly differ from those of bulk HgTe. We also studied the dependence of the absorption on temperature and reported some surprising results. In particular, this study has highlighted a critical temperature T_C around 65K. Indeed, for temperatures above T_C, the variations of the absorption seem to be well described by the microscopic model we have developed, which is governed by the thermal broadening effects of the carrier distribution. However, at lower temperatures, the absorption differs strongly from the predictions

of our model.

- The second axis of investigation concerned the study of the photoresponse and the hot-carrier dynamics in these large HgTe NCs. Indeed, the dynamics of out-of-equilibrium carriers are crucial characteristics to evaluate the potential of these NCs for the realization of optoelectronics THz devices. For that purpose, we proceeded to optical-pump THz-probe measurements, which revealed recombination times of non-equilibrium carriers in the few picoseconds timescale. We have attributed the main pathways of carrier recombination to two main non-radiative recombination processes resulting from interactions of NCs with their environnement. First, a resonant process, which consists of a direct energy transfer from the electronic transition to the ligand vibrational modes. Second, a non-resonant process also involving energy transfer to ligands vibrational modes, assisted by surface traps and mediated by optical phonons. Also, the dependance of the recombination time with the optical fluence indicates that Auger recombination is not the main mechanism at stake in this system. Finally, we explored the influence of the temperature on the hot carrier dynamics.

- The third axis of investigation was devoted to expand the application fields of NCs towards the development of light emitters at THz frequencies. We have demonstrated coherent THz emission from HgTe NCs films under femtosecond optical excitation at room temperature. We performed several measurements under different experimental configurations to characterize the properties of the emitted THz radiation. We showed that the THz emission relies on a second-order nonlinear effects. We then developed a formalism describing the second-order nonlinear processes and we demonstrated that the physical phenomena involved in the detected THz coherent radiation are the photogalvanic and photon-drag effects in the HgTe NCs. We also highlighted the possibility to tune the emitted THz radiation in the range 0.4 - 0.8 THz by changing the incident angle of the optical pulses.

From a technological perspective, the results of our study performed on the large HgTe NCs over the course of this PhD are very encouraging. Indeed, these large HgTe NCs are very promising for the development of THz emitters and THz detectors as they exhibit a unique intense THz absorption and as they are easy to synthesize and manipulate. Also, the hot carriers dynamics of a few picoseconds is very encouraging for their integration into THz optoelectronic devices, and as the role of ligands has been pointed out in the relaxation mechanisms, their chemistry could allow for engineering of the carrier dynamics. Finally, the work carried on the THz emission under optical excitation represents an important step in colloidal quantum dot-based light emitters by extending their emitting spectral range down to THz frequencies. Also, these nanocrystals present an interesting optically controlled spectral tunability that is not achievable with conventional THz emitters. It therefore has important implications for THz technology with significant prospects in the development of novel THz emitters that can be easily integrated on various devices and towards the development of quantum THz devices.

The second part of this PhD work was devoted to the study of large circular graphene quantum dots, and was motivated by their great potential of being used as an efficient gain medium for the development of a THz laser. Indeed, quantum confinement is investigated

here as a way of tailoring the hot carriers dynamics in GQD, in order to inhibit Auger recombination processes that currently limit the lifetime of the population inversion in graphene sheet. In this study, we tried to gain insights into the confinement effects on the optical properties of large circular GQD at THz frequencies. In particular, we reported theoretical investigations that predict an absorption resonance in circular GQD, whose center frequency scales as $1/R$ in contrast with the $1/R^2$ of conventional semiconductors. Very promisingly, it indicates that the resonance falls in the THz range for sufficiently large GQD, with radius typically over 20 nm. We then tried to confront these predictions with experimental data. For this purpose, we developed a clean room procedure that allows for the fabrication of large arrays of GQDs with average diameter of around $\sim$ 50 nm. Regarding the experiments, due to the uncertainty on the doping level of the GQDs and the small variations expected in the transmittance spectra of the GQD arrays, we had to significantly optimize our experiment based on Fourier Transform Infrared spectroscopy. After advanced calibration, we proceeded to transmission measurements of an array of GQDs fabricated from a tri-layer graphene. The results are encouraging since a weak THz absorption resonance has been observed in the recorded spectra, in relatively good agreement with theoretical prediction. More generally, the work performed here has greatly enhanced our expertise and know-how on fabrication and characterization of large GQDs, as we are now able to easily and autonomously fabricate samples and accurately measure slight variations in their optical response.

An important perspective shared by the two types of quantum dots arises from the strong dependence of their optoelectronic properties on their doping level. Indeed, in the case of HgTe NCs, one might expect a plasmonic regime to occur for higher doping levels that would significantly impact the carrier dynamics. The control of the doping level in HgTe NCs is thus very promising for understanding the interaction between quantum mechanical transitions and collective excitations and to pave the way for on-demand activation of quantum collective effects. For GQDs, it is predicted that the amplitude of the absorption resonance is strongly increased with the doping level, which appears to be the next realization step to overcome the low absorption measured so far. Therefore, we are currently developing new devices that could be applied to both types of quantum dots, which include an electrolytic gate to control the chemical potential and thus the doping level in the quantum dots.

Bibliography

[1] R. M. Woodward, B. E. Cole, V. P. Wallace, R. J. Pye, D. D. Arnone, E. H. Linfield, and M. Pepper, "Terahertz pulse imaging in reflection geometry of human skin cancer and skin tissue," *Physics in Medicine & Biology*, vol. 47, no. 21, p. 3853, 2002. Cited page vi

[2] K. Kawase, Y. Ogawa, Y. Watanabe, and H. Inoue, "Non-destructive terahertz imaging of illicit drugs using spectral fingerprints," *Optics express*, vol. 11, no. 20, pp. 2549–2554, 2003. Not cited.

[3] E. National Academies of Sciences, Medicine, *et al.*, *Airport passenger screening using millimeter wave machines: Compliance with guidelines*. National Academies Press, 2018. Not cited.

[4] N. Nagai, M. Sumitomo, M. Imaizumi, and R. Fukasawa, "Characterization of electron- or proton-irradiated si space solar cells by thz spectroscopy," *Semiconductor science and technology*, vol. 21, no. 2, p. 201, 2006. Not cited.

[5] M. Tonouchi, "Cutting-edge terahertz technology," *Nature photonics*, vol. 1, no. 2, pp. 97–105, 2007. Not cited.

[6] B. Ferguson and X.-C. Zhang, "Materials for terahertz science and technology," *Nature materials*, vol. 1, no. 1, pp. 26–33, 2002. Cited page vi

[7] D. M. Mittleman, "Perspective: Terahertz science and technology," *Journal of Applied Physics*, vol. 122, no. 23, p. 230901, 2017. Cited page vi

[8] N. Goubet, A. Jagtap, C. Livache, B. Martinez, H. Portalès, X. Z. Xu, R. P. Lobo, B. Dubertret, and E. Lhuillier, "Terahertz hgte nanocrystals: beyond confinement," *Journal of the American Chemical Society*, vol. 140, no. 15, pp. 5033–5036, 2018. Cited pages vii, 10, 15, 16, 17, and 111

[9] B. Sensale-Rodriguez, R. Yan, M. M. Kelly, T. Fang, K. Tahy, W. S. Hwang, D. Jena, L. Liu, and H. G. Xing, "Broadband graphene terahertz modulators enabled by intraband transitions," *Nature communications*, vol. 3, no. 1, p. 780, 2012. Cited pages vii and 85

[10] M. Mittendorff, S. Li, and T. E. Murphy, "Graphene-based waveguide-integrated terahertz modulator," *Acs Photonics*, vol. 4, no. 2, pp. 316–321, 2017. Not cited.

[11] O. A. Azar, M. Abdi, and H. Baghban, "Graphene-based terahertz waveguide amplifier," *Procedia Materials Science*, vol. 11, pp. 270–274, 2015. Cited page vii

[12] K.-J. Tielrooij, J. Song, S. A. Jensen, A. Centeno, A. Pesquera, A. Zurutuza Elorza, M. Bonn, L. Levitov, and F. Koppens, "Photoexcitation cascade and multiple hot-carrier generation in graphene," *Nature Physics*, vol. 9, no. 4, pp. 248–252, 2013. Cited pages vii and 87

[13] T. Winzer, E. Malić, and A. Knorr, "Microscopic mechanism for transient population inversion and optical gain in graphene," *Physical Review B*, vol. 87, no. 16, p. 165413, 2013. Cited pages vii and 88

[14] I. Gierz, J. C. Petersen, M. Mitrano, C. Cacho, I. E. Turcu, E. Springate, A. Stöhr, A. Köhler, U. Starke, and A. Cavalleri, "Snapshots of non-equilibrium dirac carrier distributions in graphene," *Nature materials*, vol. 12, no. 12, pp. 1119–1124, 2013. Cited page vii

[15] R. S. Rawat, "Dense plasma focus - from alternative fusion source to versatile high energy density plasma source for plasma nanotechnology," *Journal of Physics: Conference Series*, vol. 591, p. 012021, mar 2015. Cited page 7

[16] A. Ekimov and A. Onushchehko, "Quantum size effect in three-dimensional microscopic semiconductor crystals," *ZhETF Pis ma Redaktsiiu*, vol. 34, p. 363, 08 1981. Cited page 6

[17] C. Murray, M. Nirmal, D. J. Norris, and M. Bawendi, "Synthesis and structural characterization of ii–vi semiconductor nanocrystallites (quantum dots)," *Zeitschrift für Physik D Atoms, Molecules and Clusters*, vol. 26, no. 1, pp. 231–233, 1993. Cited page 7

[18] Z. A. Peng and X. Peng, "Formation of high-quality cdte, cdse, and cds nanocrystals using cdo as precursor," *Journal of the American Chemical Society*, vol. 123, no. 1, pp. 183–184, 2001. Cited page 7

[19] C. Greboval, "Étude et contrôle de la densité de porteurs dans des nanocristaux à faible bande interdite : application à la détection infrarouge," *PhD thesis, Sorbonne Université*, 2015. Cited pages 7, 8, 12, and 13

[20] Y. Pu, F. Cai, D. Wang, J.-X. Wang, and J.-F. Chen, "Colloidal synthesis of semiconductor quantum dots toward large-scale production: a review," *Industrial & Engineering Chemistry Research*, vol. 57, no. 6, pp. 1790–1802, 2018. Cited page 7

[21] G. Kalyuzhny and R. W. Murray, "Ligand effects on optical properties of cdse nanocrystals," *The Journal of Physical Chemistry B*, vol. 109, no. 15, pp. 7012–7021, 2005. PMID: 16851797. Cited page 8

[22] N. Yazdani, S. Volk, O. Yarema, M. Yarema, and V. Wood, "Size, ligand, and defect-dependent electron–phonon coupling in chalcogenide and perovskite nanocrystals and its impact on luminescence line widths," *ACS Photonics*, vol. 7, no. 5, pp. 1088–1095, 2020. Cited page 8

[23] A. R. Khabibullin, A. L. Efros, and S. C. Erwin, "The role of ligands in electron transport in nanocrystal solids," *Nanoscale*, vol. 12, pp. 23028–23035, 2020. Cited page 8

[24] B. Martinez, *Étude des propriétés optoélectroniques de nanocristaux colloïdaux à faible bande interdite: application à la détection infrarouge*. PhD thesis, Sorbonne université, 2019. Cited page 9

[25] K. Sanderson, "Quantum dots go large: a small industry could be on the verge of a boom," *Nature*, vol. 459, no. 7248, pp. 760–762, 2009. Cited page 8

[26] G. Konstantatos and E. H. Sargent, "Nanostructured materials for photon detection," *Nature nanotechnology*, vol. 5, no. 6, pp. 391–400, 2010. Cited page 8

[27] W. A. A. Mohamed, H. A. El-Gawad, S. Mekkey, H. Galal, H. Handal, H. Mousa, and A. Labib, "Quantum dots synthetization and future prospect applications," *Nanotechnology Reviews*, vol. 10, no. 1, pp. 1926–1940, 2021. Cited page 8

[28] K. Bourzac *et al.*, "Quantum dots go on display," *Nature*, vol. 493, no. 7432, p. 283, 2013. Cited page 8

[29] Q. Zhang, J. Jie, S. Diao, Z. Shao, Q. Zhang, L. Wang, W. Deng, W. Hu, H. Xia, X. Yuan, *et al.*, "Solution-processed graphene quantum dot deep-uv photodetectors," *ACS nano*, vol. 9, no. 2, pp. 1561–1570, 2015. Cited page 9

[30] A. V. Barve, S. J. Lee, S. K. Noh, and S. Krishna, "Review of current progress in quantum dot infrared photodetectors," *Laser & Photonics Reviews*, vol. 4, no. 6, pp. 738–750, 2010. Not cited.

[31] C. Livache, B. Martinez, N. Goubet, C. Gréboval, J. Qu, A. Chu, S. Royer, S. Ithurria, M. G. Silly, B. Dubertret, *et al.*, "A colloidal quantum dot infrared photodetector and its use for intraband detection," *Nature communications*, vol. 10, no. 1, pp. 1–10, 2019. Cited page 9

[32] R. M. Crooks, M. Zhao, L. Sun, V. Chechik, and L. K. Yeung, "Dendrimer-encapsulated metal nanoparticles: synthesis, characterization, and applications to catalysis," *Accounts of chemical research*, vol. 34, no. 3, pp. 181–190, 2001. Cited page 9

[33] X. Michalet, F. F. Pinaud, L. A. Bentolila, J. M. Tsay, S. Doose, J. J. Li, G. Sundaresan, A. Wu, S. Gambhir, and S. Weiss, "Quantum dots for live cells, in vivo imaging, and diagnostics," *science*, vol. 307, no. 5709, pp. 538–544, 2005. Cited page 9

[34] D. Wang, J.-F. Chen, and L. Dai, "Recent advances in graphene quantum dots for fluorescence bioimaging from cells through tissues to animals," *Particle & Particle Systems Characterization*, vol. 32, no. 5, pp. 515–523, 2015. Cited page 9

[35] X. Gao, L. Yang, J. A. Petros, F. F. Marshall, J. W. Simons, and S. Nie, "In vivo molecular and cellular imaging with quantum dots," *Current opinion in biotechnology*, vol. 16, no. 1, pp. 63–72, 2005. Cited page 9

[36] S. R. Mudshinge, A. B. Deore, S. Patil, and C. M. Bhalgat, "Nanoparticles: emerging carriers for drug delivery," *Saudi pharmaceutical journal*, vol. 19, no. 3, pp. 129–141, 2011. Cited page 9

[37] D. Wang, L. Zhu, J.-F. Chen, and L. Dai, "Liquid marbles based on magnetic upconversion nanoparticles as magnetically and optically responsive miniature reactors for photocatalysis and photodynamic therapy," *Angewandte Chemie*, vol. 128, no. 36, pp. 10953–10957, 2016. Cited page 9

[38] P. V. Kamat, "Quantum dot solar cells. the next big thing in photovoltaics," *The journal of physical chemistry letters*, vol. 4, no. 6, pp. 908–918, 2013. Cited page 9

[39] E. H. Sargent, "Colloidal quantum dot solar cells," *Nature photonics*, vol. 6, no. 3, pp. 133–135, 2012. Cited page 9

[40] Y.-C. Lu, Z. Xu, H. A. Gasteiger, S. Chen, K. Hamad-Schifferli, and Y. Shao-Horn, "Platinum- gold nanoparticles: a highly active bifunctional electrocatalyst for rechargeable lithium- air batteries," *Journal of the American Chemical Society*, vol. 132, no. 35, pp. 12170–12171, 2010. Cited page 9

[41] A. Rogach, S. V. Kershaw, M. Burt, M. T. Harrison, A. Kornowski, A. Eychmüller, and H. Weller, "Colloidally prepared hgte nanocrystals with strong room-temperature infrared luminescence," *Advanced Materials*, vol. 11, no. 7, pp. 552–555, 1999. Cited pages 9 and 28

[42] S. Keuleyan, E. Lhuillier, and P. Guyot-Sionnest, "Synthesis of colloidal hgte quantum dots for narrow mid-ir emission and detection," *Journal of the American Chemical Society*, vol. 133, no. 41, pp. 16422–16424, 2011. Cited page 9

[43] H. Lu, G. M. Carroll, N. R. Neale, and M. C. Beard, "Infrared quantum dots: Progress, challenges, and opportunities," *ACS nano*, vol. 13, no. 2, pp. 939–953, 2019. Not cited.

[44] P. Geiregat, A. J. Houtepen, L. K. Sagar, I. Infante, F. Zapata, V. Grigel, G. Allan, C. Delerue, D. Van Thourhout, and Z. Hens, "Continuous-wave infrared optical gain and amplified spontaneous emission at ultralow threshold by colloidal hgte quantum dots," *Nature Materials*, vol. 17, no. 1, pp. 35–42, 2018. Cited page 54

[45] S. V. Kershaw, A. S. Susha, and A. L. Rogach, "Narrow bandgap colloidal metal chalcogenide quantum dots: synthetic methods, heterostructures, assemblies, electronic and infrared optical properties," *Chemical Society Reviews*, vol. 42, no. 7, pp. 3033–3087, 2013. Not cited.

[46] M. V. Kovalenko, E. Kaufmann, D. Pachinger, J. Roither, M. Huber, J. Stangl, G. Hesser, F. Schäffler, and W. Heiss, "Colloidal hgte nanocrystals with widely tunable narrow band gap energies: from telecommunications to molecular vibrations," *Journal of the American Chemical Society*, vol. 128, no. 11, pp. 3516–3517, 2006. Not cited.

[47] M. M. Ackerman, X. Tang, and P. Guyot-Sionnest, "Fast and sensitive colloidal quantum dot mid-wave infrared photodetectors," *ACS nano*, vol. 12, no. 7, pp. 7264–7271, 2018. Not cited.

[48] J. M. Pietryga, R. D. Schaller, D. Werder, M. H. Stewart, V. I. Klimov, and J. A. Hollingsworth, "Pushing the band gap envelope: mid-infrared emitting colloidal pbse quantum dots," *Journal of the American Chemical Society*, vol. 126, no. 38, pp. 11752–11753, 2004. Cited pages 9 and 28

[49] S. Keuleyan, J. Kohler, and P. Guyot-Sionnest, "Photoluminescence of mid-infrared hgte colloidal quantum dots," *The Journal of Physical Chemistry C*, vol. 118, no. 5, pp. 2749–2753, 2014. Cited pages 9, 53, and 54

[50] S. E. Keuleyan, P. Guyot-Sionnest, C. Delerue, and G. Allan, "Mercury telluride colloidal quantum dots: Electronic structure, size-dependent spectra, and photocurrent detection up to 12 μm," *ACS nano*, vol. 8, no. 8, pp. 8676–8682, 2014. Cited page 11

[51] M. Kopytko and P. Martyniuk, "Hgcdte mid-and long-wave barrier infrared detectors for higher operating temperature condition," in *Modeling and Simulation in Engineering Sciences*, IntechOpen, 2016. Cited page 11

[52] C. Livache, B. Martinez, N. Goubet, J. Ramade, and E. Lhuillier, "Road map for nanocrystal based infrared photodetectors," *Frontiers in chemistry*, vol. 6, p. 575, 2018. Cited page 11

[53] K. S. Jeong, Z. Deng, S. Keuleyan, H. Liu, and P. Guyot-Sionnest, "Air-stable n-doped colloidal hgs quantum dots," *The Journal of Physical Chemistry Letters*, vol. 5, no. 7, pp. 1139–1143, 2014. Cited page 11

[54] A. Robin, C. Livache, S. Ithurria, E. Lacaze, B. Dubertret, and E. Lhuillier, "Surface control of doping in self-doped nanocrystals," *ACS Applied Materials & Interfaces*, vol. 8, no. 40, pp. 27122–27128, 2016. PMID: 27640878. Cited page 11

[55] H. Liu, C. K. Brozek, S. Sun, D. B. Lingerfelt, D. R. Gamelin, and X. Li, "A hybrid quantum-classical model of electrostatics in multiply charged quantum dots," *The Journal of Physical Chemistry C*, vol. 121, no. 46, pp. 26086–26095, 2017. Cited page 11

[56] M. Chen and P. Guyot-Sionnest, "Reversible electrochemistry of mercury chalcogenide colloidal quantum dot films," *ACS Nano*, vol. 11, no. 4, pp. 4165–4173, 2017. PMID: 28314094. Cited page 12

[57] T. Apretna, S. Massabeau, C. Greboval, N. Goubet, J. Tignon, S. Dhillon, F. Carosella, R. Ferreira, E. Lhuillier, and J. Mangeney, "Few picosecond dynamics of intraband transitions in thz hgte nanocrystals," *Nanophotonics*, vol. 10, no. 10, pp. 2753–2763, 2021. Cited pages 15 and 18

[58] A. Jagtap, C. Livache, B. Martinez, J. Qu, A. Chu, C. Gréboval, N. Goubet, and E. Lhuillier, "Emergence of intraband transitions in colloidal nanocrystals," *Optical Materials Express*, vol. 8, no. 5, pp. 1174–1183, 2018. Cited page 16

[59] J. Neu and C. A. Schmuttenmaer, "Tutorial: An introduction to terahertz time domain spectroscopy (thz-tds)," *Journal of Applied Physics*, vol. 124, no. 23, p. 231101, 2018. Cited pages 20 and 23

[60] J. Dai, J. Zhang, W. Zhang, and D. Grischkowsky, "Terahertz time-domain spectroscopy characterization of the far-infrared absorption and index of refraction of high-resistivity, float-zone silicon," *JOSA B*, vol. 21, no. 7, pp. 1379–1386, 2004. Cited page 24

[61] C. Ro/nne, L. Thrane, P.-O. Åstrand, A. Wallqvist, K. V. Mikkelsen, and S. R. Keiding, "Investigation of the temperature dependence of dielectric relaxation in liquid water by thz reflection spectroscopy and molecular dynamics simulation," *The Journal of chemical physics*, vol. 107, no. 14, pp. 5319–5331, 1997. Not cited.

[62] S. Wen-Feng, W. Xin-Ke, and Z. Yan, "Measurement of refractive index for high reflectance materials with terahertz time domain reflection spectroscopy," *Chinese Physics Letters*, vol. 26, no. 11, p. 114210, 2009. Cited page 24

[63] A. Moritani, H. Sekiya, K. Taniguchi, C. Hamaguchi, J. Nakai, and R. Makabe, "Optical constants of hgte and hgse," *Japanese Journal of Applied Physics*, vol. 10, no. 10, p. 1410, 1971. Cited page 25

[64] M. El-Nahass, A. El-Salam, M. Seyam, *et al.*, "Optical and structural properties of flash evaporated hgte thin films," *Journal of materials science*, vol. 41, no. 11, pp. 3573–3580, 2006. Not cited.

[65] W. Szuszkiewicz, A. Witowski, and M. Grynberg, "The dynamic dielectric function in hgse and hgte," *physica status solidi (b)*, vol. 87, no. 2, pp. 637–645, 1978. Not cited.

[66] M. Secuk, M. Aycibin, B. Erdinc, S. Gulebaglan, E. Dogan, and H. Akkus, "Ab-initio calculations of structural, electronic, optical, dynamic and thermodynamic properties of hgte and hgse," *American Journal of Condensed Matter Physics*, vol. 4, no. 1, pp. 13–19, 2014. Cited page 25

[67] P. Rastogi, A. Chu, T. H. Dang, Y. Prado, C. Gréboval, J. Qu, C. Dabard, A. Khalili, E. Dandeu, B. Fix, *et al.*, "Complex optical index of hgte nanocrystal infrared thin films and its use for short wave infrared photodiode design," *Advanced Optical Materials*, vol. 9, no. 10, p. 2002066, 2021. Cited page 25

[68] G. Allan and C. Delerue, "Tight-binding calculations of the optical properties of hgte nanocrystals," *Phys. Rev. B*, vol. 86, p. 165437, Oct 2012. Cited page 30

[69] P. K. Jain, "Plasmon-in-a-box: on the physical nature of few-carrier plasmon resonances," *The Journal of Physical Chemistry Letters*, vol. 5, no. 18, pp. 3112–3119, 2014. Cited pages 31 and 34

[70] X. Fan, W. Zheng, and D. J. Singh, "Light scattering and surface plasmons on small spherical particles," *Light: Science & Applications*, vol. 3, no. 6, pp. e179–e179, 2014. Cited pages 34 and 37

[71] S. A. Maier *et al.*, *Plasmonics: fundamentals and applications*, vol. 1. Springer, 2007. Cited page 37

[72] A. M. Schimpf, N. Thakkar, C. E. Gunthardt, D. J. Masiello, and D. R. Gamelin, "Charge-tunable quantum plasmons in colloidal semiconductor nanocrystals," *ACS nano*, vol. 8, no. 1, pp. 1065–1072, 2014. Cited page 38

[73] J. Qu, P. Rastogi, C. Gréboval, D. Lagarde, A. Chu, C. Dabard, A. Khalili, H. Cruguel, C. Robert, X. Z. Xu, *et al.*, "Electroluminescence from hgte nanocrystals and its use for active imaging," *Nano Letters*, vol. 20, no. 8, pp. 6185–6190, 2020. Cited page 53

[74] J. Lim, Y. C. Choi, D. Choi, I.-Y. Chang, K. Hyeon-Deuk, K. S. Jeong, K. Kwak, and M. Cho, "Ultrafast intraband auger process in self-doped colloidal quantum dots," *Matter*, vol. 4, no. 3, pp. 1072–1086, 2021. Cited page 53

[75] C. Melnychuk and P. Guyot-Sionnest, "Auger suppression in n-type hgse colloidal quantum dots," *ACS nano*, vol. 13, no. 9, pp. 10512–10519, 2019. Cited page 53

[76] C. Melnychuk and P. Guyot-Sionnest, "Slow auger relaxation in hgte colloidal quantum dots," *The Journal of Physical Chemistry Letters*, vol. 9, no. 9, pp. 2208–2211, 2018. Cited page 53

[77] N. M. Abdelazim, Q. Zhu, Y. Xiong, Y. Zhu, M. Chen, N. Zhao, S. V. Kershaw, and A. L. Rogach, "Room temperature synthesis of hgte quantum dots in an aprotic solvent realizing high photoluminescence quantum yields in the infrared," *Chemistry of Materials*, vol. 29, no. 18, pp. 7859–7867, 2017. Cited page 54

[78] C. T. Smith, M. A. Leontiadou, R. Page, P. O'Brien, and D. J. Binks, "Ultrafast charge dynamics in trap-free and surface-trapping colloidal quantum dots," *Advanced Science*, vol. 2, no. 10, p. 1500088, 2015. Cited page 54

[79] Q. Wen, S. V. Kershaw, S. Kalytchuk, O. Zhovtiuk, C. Reckmeier, M. I. Vasilevskiy, and A. L. Rogach, "Impact of d2o/h2o solvent exchange on the emission of hgte and cdte quantum dots: Polaron and energy transfer effects," *ACS Nano*, vol. 10, no. 4, pp. 4301–4311, 2016. PMID: 26958866. Cited page 54

[80] J. Qu, C. Livache, B. Martinez, C. Gréboval, A. Chu, E. Meriggio, J. Ramade, H. Cruguel, X. Z. Xu, A. Proust, *et al.*, "Transport in ito nanocrystals with short- to long-wave infrared absorption for heavy-metal-free infrared photodetection," *ACS Applied Nano Materials*, vol. 2, no. 3, pp. 1621–1630, 2019. Cited page 55

[81] T. Apretna, N. Nilforoushan, J. Tignon, S. Dhillon, F. Carosella, R. Ferreira, E. Lhuillier, and J. Mangeney, "Coherent thz wave emission from hgte quantum dots," *Applied Physics Letters*, vol. 121, no. 25, p. 251101, 2022. Cited page 57

[82] X.-C. Zhang and D. Auston, "Optoelectronic measurement of semiconductor surfaces and interfaces with femtosecond optics," *Journal of applied physics*, vol. 71, no. 1, pp. 326–338, 1992. Cited page 57

[83] Y. Huang, Z. Yao, C. He, L. Zhu, L. Zhang, J. Bai, and X. Xu, "Terahertz surface and interface emission spectroscopy for advanced materials," *Journal of Physics: Condensed Matter*, vol. 31, no. 15, p. 153001, 2019. Cited pages 58, 68, 69, and 72

[84] S. Ruan, X. Lin, H. Chen, B. Song, Y. Dai, X. Yan, Z. Jin, G. Ma, and J. Yao, "Terahertz probe of nonequilibrium carrier dynamics and ultrafast photocurrents in the topological insulator sb2te3," *Applied Physics Letters*, vol. 118, no. 1, p. 011102, 2021. Cited page 58

[85] L. Braun, G. Mussler, A. Hruban, M. Konczykowski, T. Schumann, M. Wolf, M. Münzenberg, L. Perfetti, and T. Kampfrath, "Ultrafast photocurrents at the surface of the three-dimensional topological insulator bi2se3," *Nature communications*, vol. 7, no. 1, pp. 1–9, 2016. Cited page 58

[86] Y. Gao, S. Kaushik, E. Philip, Z. Li, Y. Qin, Y. Liu, W. Zhang, Y. Su, X. Chen, H. Weng, *et al.*, "Chiral terahertz wave emission from the weyl semimetal taas," *Nature communications*, vol. 11, no. 1, pp. 1–10, 2020. Cited page 58

[87] N. Sirica, R. Tobey, L. Zhao, G. Chen, B. Xu, R. Yang, B. Shen, D. Yarotski, P. Bowlan, S. Trugman, *et al.*, "Tracking ultrafast photocurrents in the weyl semimetal taas using thz emission spectroscopy," *Physical review letters*, vol. 122, no. 19, p. 197401, 2019. Cited page 58

[88] J. Maysonnave, S. Huppert, F. Wang, S. Maero, C. Berger, W. De Heer, T. B. Norris, L. De Vaulchier, S. Dhillon, J. Tignon, *et al.*, "Terahertz generation by dynamical photon drag effect in graphene excited by femtosecond optical pulses," *Nano letters*, vol. 14, no. 10, pp. 5797–5802, 2014. Cited page 58

[89] L. Zhu, Y. Huang, Z. Yao, B. Quan, L. Zhang, J. Li, C. Gu, X. Xu, and Z. Ren, "Enhanced polarization-sensitive terahertz emission from vertically grown graphene by a dynamical photon drag effect," *Nanoscale*, vol. 9, no. 29, pp. 10301–10311, 2017. Not cited.

[90] M. Glazov and S. Ganichev, "High frequency electric field induced nonlinear effects in graphene," *Physics Reports*, vol. 535, no. 3, pp. 101–138, 2014. Cited pages 58, 71, and 74

[91] Y.-M. Bahk, G. Ramakrishnan, J. Choi, H. Song, G. Choi, Y. H. Kim, K. J. Ahn, D.-S. Kim, and P. C. Planken, "Plasmon enhanced terahertz emission from single layer graphene," *ACS nano*, vol. 8, no. 9, pp. 9089–9096, 2014. Cited page 58

[92] B. Guzelturk, R. A. Belisle, M. D. Smith, K. Bruening, R. Prasanna, Y. Yuan, V. Gopalan, C. J. Tassone, H. I. Karunadasa, M. D. McGehee, *et al.*, "Terahertz emission from hybrid perovskites driven by ultrafast charge separation and strong electron–phonon coupling," *Advanced Materials*, vol. 30, no. 11, p. 1704737, 2018. Cited page 58

[93] P. A. Obraztsov, D. Lyashenko, P. A. Chizhov, K. Konishi, N. Nemoto, M. Kuwata-Gonokami, E. Welch, A. N. Obraztsov, and A. Zakhidov, "Ultrafast zero-bias photocurrent and terahertz emission in hybrid perovskites," *Communications Physics*, vol. 1, no. 1, pp. 1–7, 2018. Cited page 58

[94] T. Seifert, S. Jaiswal, U. Martens, J. Hannegan, L. Braun, P. Maldonado, F. Freimuth, A. Kronenberg, J. Henrizi, I. Radu, *et al.*, "Efficient metallic spintronic emitters of

ultrabroadband terahertz radiation," *Nature photonics*, vol. 10, no. 7, pp. 483–488, 2016. Cited page 58

[95] T. Dang, J. Hawecker, E. Rongione, G. Baez Flores, D. To, J. Rojas-Sanchez, H. Nong, J. Mangeney, J. Tignon, F. Godel, *et al.*, "Ultrafast spin-currents and charge conversion at 3 d-5 d interfaces probed by time-domain terahertz spectroscopy," *Applied Physics Reviews*, vol. 7, no. 4, p. 041409, 2020. Cited page 58

[96] M. E. Barnes, S. A. Berry, P. Gow, D. McBryde, G. J. Daniell, H. E. Beere, D. A. Ritchie, and V. Apostolopoulos, "Investigation of the role of the lateral photo-dember effect in the generation of terahertz radiation using a metallic mask on a semiconductor," *Optics express*, vol. 21, no. 14, pp. 16263–16272, 2013. Cited page 58

[97] E. A. P. Prieto, S. A. B. Vizcara, A. S. Somintac, A. A. Salvador, E. S. Estacio, C. T. Que, K. Yamamoto, and M. Tani, "Terahertz emission enhancement in low-temperature-grown gaas with an n-gaas buffer in reflection and transmission excitation geometries," *JOSA B*, vol. 31, no. 2, pp. 291–295, 2014. Not cited.

[98] B. Guzelturk, M. Trigo, O. Delaire, D. A. Reis, and A. M. Lindenberg, "Dynamically tunable terahertz emission enabled by anomalous optical phonon responses in lead telluride," *ACS Photonics*, vol. 8, no. 12, pp. 3633–3640, 2021. Cited page 58

[99] Y. B. Vasilyev, N. Mikhailov, G. Y. Vasilyeva, Y. L. Ivánov, A. Zakhar'in, A. Andrianov, L. Vorobiev, D. Firsov, M. Grigoriev, A. Antonov, *et al.*, "Terahertz emission from cdhgte/hgte quantum wells with an inverted band structure," *Semiconductors*, vol. 50, no. 7, pp. 915–919, 2016. Cited page 58

[100] V. V. Utochkin, K. E. Kudryavtsev, A. A. Dubinov, M. A. Fadeev, V. V. Rumyantsev, A. A. Razova, E. V. Andronov, V. Y. Aleshkin, V. I. Gavrilenko, N. N. Mikhailov, *et al.*, "Stimulated emission up to 2.75 μm from hgcdte/cdhgte qw structure at room temperature," *Nanomaterials*, vol. 12, no. 15, p. 2599, 2022. Cited page 58

[101] R. W. Boyd, *Nonlinear optics*. Academic press, 2020. Cited pages 70 and 76

[102] V. I. Belinicher and B. I. Sturman, "The photogalvanic effect in media lacking a center of symmetry," *Soviet Physics Uspekhi*, vol. 23, no. 3, p. 199, 1980. Cited page 73

[103] G. Mikheev, A. Saushin, V. Styapshin, and Y. P. Svirko, "Interplay of the photon drag and the surface photogalvanic effects in the metal-semiconductor nanocomposite," *Scientific Reports*, vol. 8, no. 1, p. 8644, 2018. Cited page 74

[104] P. Guyot-Sionnest, "Electrical transport in colloidal quantum dot films," *The Journal of Physical Chemistry Letters*, vol. 3, no. 9, pp. 1169–1175, 2012. Cited page 74

[105] J. Gao, A. F. Fidler, and V. I. Klimov, "Carrier multiplication detected through transient photocurrent in device-grade films of lead selenide quantum dots," *Nature Communications*, vol. 6, no. 1, p. 8185, 2015. Cited page 74

[106] J. Gielis, P. Gevers, I. Aarts, M. Van De Sanden, and W. Kessels, "Optical second-harmonic generation in thin film systems," *Journal of Vacuum Science & Technology A: Vacuum, Surfaces, and Films*, vol. 26, no. 6, pp. 1519–1537, 2008. Cited page 76

[107] M. B. Johnston, D. Whittaker, A. Corchia, A. Davies, and E. H. Linfield, "Simulation of terahertz generation at semiconductor surfaces," *Physical Review B*, vol. 65, no. 16, p. 165301, 2002. Cited page 77

[108] S. Massabeau, *THz Spectroscopy of Multilayer Epitaxial Graphene and Graphene Quantum Dots*. PhD thesis, LPENS, November 2020. Cited pages 84, 87, 90, 94, 95, 96, and 97

[109] P. R. Wallace, "The band theory of graphite," *Physical review*, vol. 71, no. 9, p. 622, 1947. Cited page 84

[110] A. C. Neto, F. Guinea, N. M. Peres, K. S. Novoselov, and A. K. Geim, "The electronic properties of graphene," *Reviews of modern physics*, vol. 81, no. 1, p. 109, 2009. Cited page 84

[111] Y. Wu, Y.-m. Lin, A. A. Bol, K. A. Jenkins, F. Xia, D. B. Farmer, Y. Zhu, and P. Avouris, "High-frequency, scaled graphene transistors on diamond-like carbon," *Nature*, vol. 472, no. 7341, pp. 74–78, 2011. Cited page 85

[112] F. Rana, "Graphene terahertz plasmon oscillators," *IEEE Transactions on Nanotechnology*, vol. 7, no. 1, pp. 91–99, 2008. Not cited.

[113] L. Ju, B. Geng, J. Horng, C. Girit, M. Martin, Z. Hao, H. A. Bechtel, X. Liang, A. Zettl, Y. R. Shen, *et al.*, "Graphene plasmonics for tunable terahertz metamaterials," *Nature nanotechnology*, vol. 6, no. 10, pp. 630–634, 2011. Cited page 85

[114] H. A. Hafez, S. Kovalev, K.-J. Tielrooij, M. Bonn, M. Gensch, and D. Turchinovich, "Terahertz nonlinear optics of graphene: from saturable absorption to high-harmonics generation," *Advanced Optical Materials*, vol. 8, no. 3, p. 1900771, 2020. Cited pages 86 and 101

[115] K. F. Mak, L. Ju, F. Wang, and T. F. Heinz, "Optical spectroscopy of graphene: From the far infrared to the ultraviolet," *Solid State Communications*, vol. 152, no. 15, pp. 1341–1349, 2012. Cited page 87

[116] T. Guo, L. Zhu, P.-Y. Chen, and C. Argyropoulos, "Tunable terahertz amplification based on photoexcited active graphene hyperbolic metamaterials," *Optical Materials Express*, vol. 8, no. 12, pp. 3941–3952, 2018. Cited page 87

[117] A. Tomadin, D. Brida, G. Cerullo, A. C. Ferrari, and M. Polini, "Nonequilibrium dynamics of photoexcited electrons in graphene: Collinear scattering, auger processes, and the impact of screening," *Physical Review B*, vol. 88, no. 3, p. 035430, 2013. Cited page 87

[118] M. T. Mihnev, F. Kadi, C. J. Divin, T. Winzer, S. Lee, C.-H. Liu, Z. Zhong, C. Berger, W. A. De Heer, E. Malic, *et al.*, "Microscopic origins of the terahertz carrier relaxation and cooling dynamics in graphene," *Nature communications*, vol. 7, no. 1, pp. 1–11, 2016. Not cited.

[119] S. Winnerl, F. Göttfert, M. Mittendorff, H. Schneider, M. Helm, T. Winzer, E. Malic, A. Knorr, M. Orlita, M. Potemski, *et al.*, "Time-resolved spectroscopy on epitaxial graphene in the infrared spectral range: relaxation dynamics and saturation behavior," *Journal of Physics: Condensed Matter*, vol. 25, no. 5, p. 054202, 2013. Not cited.

[120] J. H. Strait, H. Wang, S. Shivaraman, V. Shields, M. Spencer, and F. Rana, "Very slow cooling dynamics of photoexcited carriers in graphene observed by optical-pump terahertz-probe spectroscopy," *Nano letters*, vol. 11, no. 11, pp. 4902–4906, 2011. Cited page 87

[121] C. Volk, C. Neumann, S. Kazarski, S. Fringes, S. Engels, F. Haupt, A. Müller, and C. Stampfer, "Probing relaxation times in graphene quantum dots," *Nature Communications*, vol. 4, no. 1, p. 1753, 2013. Cited page 89

[122] A. El Fatimy, R. L. Myers-Ward, A. K. Boyd, K. M. Daniels, D. K. Gaskill, and P. Barbara, "Epitaxial graphene quantum dots for high-performance terahertz bolometers," *Nature nanotechnology*, vol. 11, no. 4, pp. 335–338, 2016. Cited page 89

[123] A. El Fatimy, A. Nath, B. D. Kong, A. K. Boyd, R. L. Myers-Ward, K. M. Daniels, M. M. Jadidi, T. E. Murphy, D. K. Gaskill, and P. Barbara, "Ultra-broadband photodetectors based on epitaxial graphene quantum dots," *Nanophotonics*, vol. 7, no. 4, pp. 735–740, 2018. Cited page 89

[124] E. Riccardi, S. Massabeau, F. Valmorra, S. Messelot, M. Rosticher, J. Tignon, K. Watanabe, T. Taniguchi, M. Delbecq, S. Dhillon, *et al.*, "Ultrasensitive photoresponse of graphene quantum dots in the coulomb blockade regime to thz radiation," *Nano Letters*, vol. 20, no. 7, pp. 5408–5414, 2020. Cited page 89

[125] S. Messelot, E. Riccardi, S. Massabeau, F. Valmorra, M. Rosticher, K. Watanabe, T. Taniguchi, J. Tignon, T. Boulier, V. Dauvois, *et al.*, "Large terahertz electric dipole of a single graphene quantum dot," *Physical Review Research*, vol. 4, no. 1, p. L012018, 2022. Cited page 89

[126] I. Ozfidan, M. Korkusinski, A. D. Güçlü, J. A. McGuire, and P. Hawrylak, "Microscopic theory of the optical properties of colloidal graphene quantum dots," *Physical Review B*, vol. 89, no. 8, p. 085310, 2014. Cited page 89

[127] V. I. Klimov, A. A. Mikhailovsky, D. McBranch, C. A. Leatherdale, and M. G. Bawendi, "Quantization of multiparticle auger rates in semiconductor quantum dots," *Science*, vol. 287, no. 5455, pp. 1011–1013, 2000. Cited page 89

[128] W.-d. Sheng, M. Korkusinski, A. D. Güçlü, M. Zielinski, P. Potasz, E. S. Kadantsev, O. Voznyy, and P. Hawrylak, "Electronic and optical properties of semiconductor and graphene quantum dots," *Frontiers of Physics*, vol. 7, no. 3, pp. 328–352, 2012. Cited page 90

[129] A. Matulis and F. M. Peeters, "Quasibound states of quantum dots in single and bilayer graphene," *Physical Review B*, vol. 77, no. 11, p. 115423, 2008. Cited page 90

[130] R. Pohle, E. G. Kavousanaki, K. M. Dani, and N. Shannon, "Symmetry and optical selection rules in graphene quantum dots," *Physical Review B*, vol. 97, no. 11, p. 115404, 2018. Cited page 92

[131] P. Bugajny, L. Szulakowska, B. Jaworowski, and P. Potasz, "Optical properties of geometrically optimized graphene quantum dots," *Physica E: Low-dimensional Systems and Nanostructures*, vol. 85, pp. 294–301, 2017. Cited page 92

[132] C. Mansilla Wettstein, F. P. Bonafé, M. B. Oviedo, and C. G. Sánchez, "Optical properties of graphene nanoflakes: Shape matters," *The Journal of Chemical Physics*, vol. 144, no. 22, p. 224305, 2016. Cited page 92

[133] S. Messelot, *Terahertz Tamm cavities for Light-Matter Coupling with Graphene Based Materials*. PhD thesis, LPENS, 12 2021. Cited page 93

[134] J. Basu, J. K. Basu, and T. K. Bhattacharyya, "The evolution of graphene-based electronic devices," *International Journal of Smart and Nano Materials*, vol. 1, no. 3, pp. 201–223, 2010. Cited page 101

[135] H. I. Wang, M.-L. Braatz, N. Richter, K.-J. Tielrooij, Z. Mics, H. Lu, N.-E. Weber, K. Müllen, D. Turchinovich, M. Kläui, *et al.*, "Reversible photochemical control of doping levels in supported graphene," *The Journal of Physical Chemistry C*, vol. 121, no. 7, pp. 4083–4091, 2017. Cited page 101

[136] H. A. Hafez, S. Kovalev, J.-C. Deinert, Z. Mics, B. Green, N. Awari, M. Chen, S. Germanskiy, U. Lehnert, J. Teichert, *et al.*, "Extremely efficient terahertz high-harmonic generation in graphene by hot dirac fermions," *Nature*, vol. 561, no. 7724, pp. 507–511, 2018. Cited page 101

[137] P. C. Planken, H.-K. Nienhuys, H. J. Bakker, and T. Wenckebach, "Measurement and calculation of the orientation dependence of terahertz pulse detection in znte," *JOSA B*, vol. 18, no. 3, pp. 313–317, 2001. Cited page 132

Appendices

Appendix A

Time Domain Spectroscopy

In this appendix, we give in-depths description of several parts of the Time Domain Spectroscopy presented in section 2.3.2

A.1 THz Generation

THz generation is done by making use of the ultrafast infrared pulses. Two main approaches exist. The first is based on non-linear effects, with techniques such as optical rectification, difference-frequency generation or optical parametric oscillation. The second is based on the acceleration of charge carrier under an applied field. In this work, we use photoconductive antennas (PCA) whose principle belongs to the second category. Our PCA consists of interdigitated electrodes lying on a top of a GaAs substrate. Using a low frequency generator, a voltage (10V) is applied resulting in a tension between the two electrodes. The PCA is illuminated with the 15 femtosecond infrared pulse. When the optical pulse hits the antenna, since infrared photons energy is larger than GaAs gap ($E_{800nm} = 1.55eV > E_{GaAs} = 1.424eV$ at room temperature), multiple electron-hole pairs are generated between the electrodes (cf figure A.1). These photo-generated carriers are then accelerated by the applied electric field in the opposite direction, which results in a transient current $J(t)$. The transient current generates an electric field accordingly to the relation :

$$\overrightarrow{E}_{\mathrm{THz}} \propto \frac{\partial \overrightarrow{J}}{\partial t}$$

The emitted electric field depends on both the lifetime of the photo-excited carriers and the duration of the infrared pulse. Indeed, at first, while the sample is illuminated, photo-carriers are generated, which results in an increase of the transient current $\overrightarrow{J}$, as it is represented in figure A.2. In a second time, photo-carriers recombine or are evacuated, and the current decrease. The radiated electric field is proportional to the time derivative of the transient current. Thus, as the transient current oscillates in a picosecond timescale, the generated field lies in the THz range.

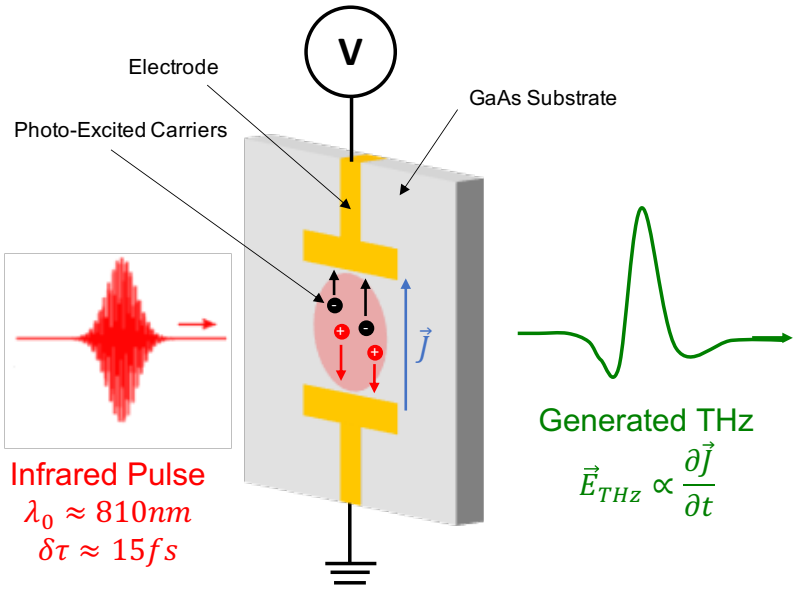

Fig. A.1 *Schema of a photoconductive antenna consisting of gold electrodes on a GaAs substrate. The femtosecond infrared pulse (in red) generates photo-carriers that are accelerated under the applied electric field, resulting in the generation of a THz pulse (in green).*

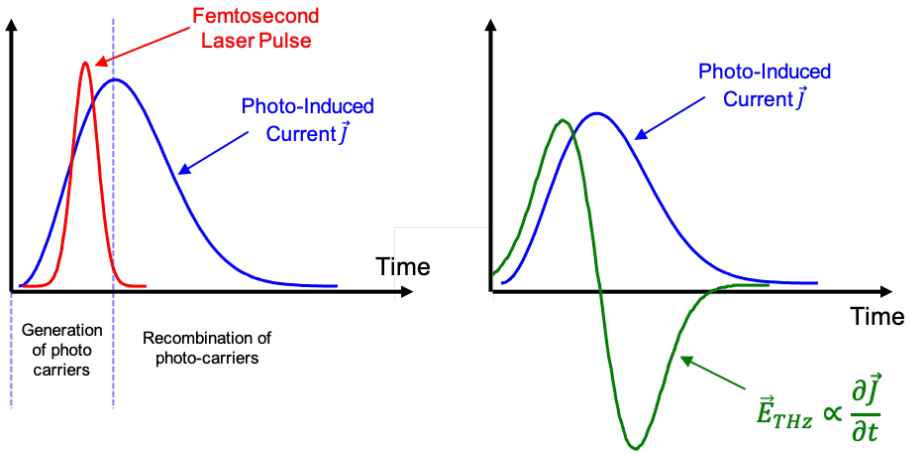

Fig. A.2 *Schemes of the mechanisms at stake in the generation of a THz pulse by a photoconductive antenna. While the sample is illuminated with the infrared pulse (red), the number of generated photo-carriers increases and so does the transient current J (blue). In a second time, photo-carriers recombine and are evacuated, which makes the transient current decrease. The radiated THz field is proportional to the time derivative of the transient current and is represented in green.*

A.2 THz detection

Several techniques exist for the detection of the THz pulse. For instance, it is possible to use the same PCA in the opposite way where photo-carriers are accelerated by the THz field and measured as an intensity. In our case, we proceed to electro-optic detection. This technique is based on the Pockels effect, which is a non-linear effect occurring in non-centrosymmetric crystal. The Pockels effect induces a birefringence when an electric field is applied. This effect is linear so that the induced birefringence is proportional to the electric field. It is possible to measure the amplitude of the birefringence by looking at the effect it has on the polarisation of a probe beam.

A.2.1 Electro-Optic Sampling

Let us describe how we take advantage of this effect in our set-up. The infrared pulse is initially split into two beams. The first one is used for the THz generation as described in the previous section. The second one propagates along "Probe Line". After the THz pulse has propagated through the sample, it is focused on to an electro-optic cristal. The "Probe Line" is set so that the second part of the infrared beam is also focused onto the cristal and superimposes both spatially and temporally with the THz pulse. The few picoseconds THz pulse duration is much longer than the infrared pulse of around 15fs. Thus, the THz electric field can be seen as a quasi static applied electric field, inducing a birefringence in the cristal, while the infrared pulse acts a a probe which undergoes a phase shift. The infrared probe provides a measurement of the electric field at a specific temporal overlap of the THz and infrared pulses. In order to obtain a full measurement of the THz pulse, a delay line is installed along the optical path of the probe line. The translation stage present in the probe arm of the TDS set ups can perform displacements with a micro-metric precision. These displacements correspond to variations of the optical paths, resulting in a tunable time delay of the infrared pulses with a precision of only a few fs and increments of around 10fs. Thus, by successively delaying the probing optical pulse, one can reconstruct a discrete time domain measurement of the THz field. (cf A.3), which can be later translated into a spectrum using Fast Fourier Transform. The resolution of the spectrum obtained by FFT is equal to the inverse of the measurements time window. In our TDS measurements, this resolution is limited by the time window performed in order to avoid aliasing in the spectrum due to internal reflexions.

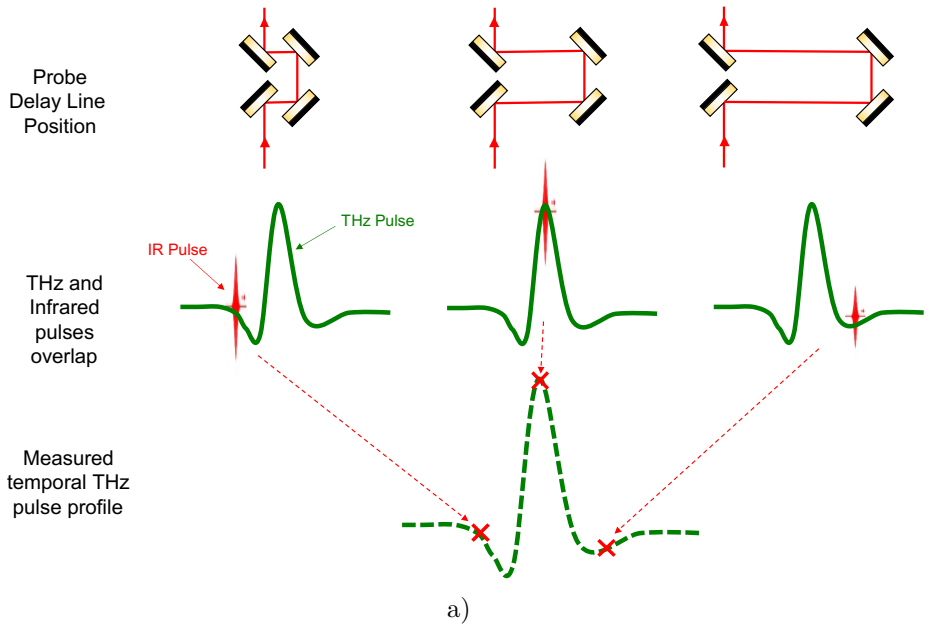

Fig. A.3 *Simplified illustration of the electro-optic sampling. The upper part represents the different positions of the probe delay line. The corresponding temporal overlap of the infrared and THz pulses are depicted in the second raw. The measured THz signal reconstructed from the different time delays is represented at the bottom of the scheme.*

A.2.2 Ellipsometry

The ellipsometry part of the set-up is represented in figure A.4. The infrared probe pulse is polarized horizontally.

In the absence of THz electric field, its polarization is not altered. A $\lambda/4$ waveplate is mounted after the crystal, and is oriented so that the polarisation becomes circular. A Wollaston prism projects two orthogonal components of the circular polarization in two different directions of space, and each beam is focused on balanced photodiodes. The balanced photodiode sends a signal that is proportional to the difference of intensity between the two diodes. Thus, in the absence of THz, the measured is null.

Let us now consider the case where the infrared and THz pulses overlap. The infrared polarisation is altered by the birefringence of the cristal, and exits the cristal and $\lambda/4$ waveplate with an elliptical polarization. The two projections after the Wollaston prism then have different intensities, and the measured signal is proportionnal to the degree of ellipticity. For the two types of electro-optic crystals used in the frame of this PhD, that are ZnTe and GaP, the intensity difference measured by the balanced photodiode is proportional to the amplitude of the THz electric field [137]. The amplitude of the measured signal also depends on the orientation of the electro-optic crystal and the polarizations angles. Both the incident THz and infrared pulses are polarized horizontally, and the crystal angle is set to achieve to maximum signal. An important advantage of this type of detection is the ability to measure the sign of the electric field. It enables the measurement of the time-dependent amplitude E(t) which captures the phase information.

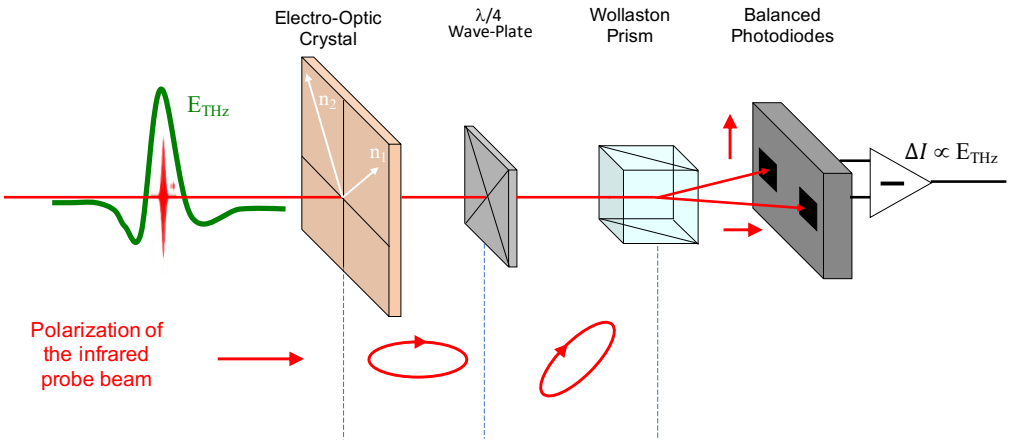

Fig. A.4 *Scheme of the electro-optical ellipsometry detection. The red arrows represent the polarization of the infrared probe beam in the plane perpendicular to the direction of propagation. The THz pulse (in green) induces a birefringence in the electro-optic crystal, which phase shifts the components of the infrared beam. The quarter waveplate is set so that in the absence of THz, the polarization that is exiting it is circular. The Wollaston prism projects two orthogonal components of the polarizations on two balanced photo-diodes. The measured intensity difference ΔI is proportional to the amplitude of the THz field E_{THz}, enabling the measurement of its sign.*

A.2.3 Lock-In Amplifying

The output signal of the balanced photodiode is very noisy. In order to improve the SNR, we proceed to lock-in amplifying by the modulation of the photo-conductive antennas. Indeed, one of the great advantage of the photo-conductive antenna is the possibility of switching on and off the applied voltage at the high frequencies associated with power supplies. In contrast, optical modulation required for generation techniques such as optical rectification implies an optical chopper whose achievable modulation frequencies are much lower ($\approx$ 10kHz max).

The lock-in amplyfing works as follows: A square waveform voltage between 0 and 10V is applied on the PCA by a power supplies, with a frequency equal to f_{PCA}=42kHz. While the voltage is set to 10V, the PCA emits THz at the same rate than repetition frequency of the laser (80MHz), which is much higher than the modulation frequency of 42kHz. When no voltage is applied, no THz is emitted. The modulation artificially makes the signal of interest periodic at the f_{PCA} frequency. Thus, the output signal can be written using Fourrier decomposition :

$$V_{Sig}(t) = a_0 + \sum_{n=1}^{\infty} A_n \sin(n\omega_{PCA}t + \theta_n)$$

Note that t here is the acquisition time of the set-up, and not the time delay used in other sections. $V_{Sig}(t)$ consists in a succession a measurements at the repetition rate of the photodiode. The lock-in amplifier takes the f_{PCA} frequency as a reference for an internal oscillator.

The signal of this internal oscillator $V_{Ref}(t)$ is then multiplied to $V_{Sig}(t)$. The signal out of the multiplier writes:

$$V_{Out}(t) = V_{Sig}(t)V_{Ref}(t)$$

$$V_{Out}(t) = [a_0 + \sum_{n=1}^{\infty} A_n \sin(n\omega_{PCA}t + \theta_n)]V_{Ref}\sin(n\omega_{PCA}t + \theta_{Ref})$$

$$V_{Out}(t) = a_0 V_{int}\sin(n\omega_{PCA}t + \theta_{Ref}) \tag{A.1}$$

$$+ \frac{1}{2}\sum_{n=1}^{\infty} A_n V_{Ref}\cos([n-1]\omega_{PCA}t + \theta_n - \theta_{Ref}) \tag{A.2}$$

$$+ \frac{1}{2}\sum_{n=1}^{\infty} A_n V_{Ref}\cos([n+1]\omega_{PCA}t + \theta_n + \theta_{Ref}) \tag{A.3}$$

The signal is passed through a low pass filter, removing the AC components. The only term that is left is n=1 in A.2, which leads to :

$$V_{Out}(t) = \frac{1}{2}A_1 V_{Ref} cos(\theta_1 + \theta_{Ref})$$

This is a DC signal, proportional to A_1. A_1 itself is proportional to E_{THz} by a factor depending on the balanced photo-diodes and their acquisition characteristics. Any other signal that is not periodic at a frequency f_{PCA} is removed by the low pass filter. This filtering efficiently removes most the noise outside of the low filter bandwidth. Thus, the ouput of the lock-in is thus a DC signal proportional to the E_{THz} cleaned from the intrinsic noise of the setup with a very good SNR.

Appendix B

Models

B.1 Quantum Model

We detail here the different steps of the derivation of the permittivity from the quantum model :

B.1.1 Equation of Evolution

From equation 2.9 to equation 2.11 :

We start with equation 2.8

$$\frac{\partial \hat{\rho}}{\partial t} = -\frac{i}{\hbar}[\hat{\mathrm{H}}, \hat{\rho}] - \gamma(\hat{\rho} - \hat{\rho}^{st})$$

We have $\frac{\partial \hat{\rho}^{(0)}}{\partial t} = 0$, thus :

$$\frac{\partial \hat{\rho}}{\partial t} = \frac{\partial \hat{\rho}^{(1)}}{\partial t} = -\frac{i}{\hbar}[\hat{H}_o + \hat{V}, \hat{\rho}^{(0)} + \hat{\rho}^{(1)}] - \gamma\hat{\rho}^{(1)}$$

$$= -\frac{i}{\hbar}\left\{\underbrace{[\hat{H}_o, \hat{\rho}^{(0)}]}_{(*)} + [\hat{H}_o, \hat{\rho}^{(1)}] + [\hat{V}, \hat{\rho}^{(0)}] + \underbrace{[\hat{V}, \hat{\rho}^{(1)}]}_{\text{second order}}\right\} - \gamma\hat{\rho}^{(1)}$$

$$(*)\quad \left.\begin{array}{l} \langle\Psi_f|\hat{H}_0\hat{\rho}^{(0)}|\Psi_i\rangle = E_i f_{\mathrm{FD}}(E_f)\delta_{i,f} \\ \langle\Psi_i|\hat{\rho}^{(0)}\hat{H}_0|\Psi_f\rangle = \langle\Psi_i|\hat{\rho}^{(0)}|\Psi_f\rangle\, E_f = E_i f_{\mathrm{FD}}(E_f)\delta_{i,f} \end{array}\right\} [\hat{H}_o, \hat{\rho}^{(0)}] = 0$$

By limiting ourselves to the first order terms, one can get rid of $[\hat{V}, \hat{\rho}^{(1)}]$.

$$\frac{\partial \hat{\rho}^{(1)}}{\partial t} \approx -\frac{i}{\hbar}\left\{[\hat{H}_o, \hat{\rho}^{(1)}] + [\hat{V}, \hat{\rho}^{(0)}] + \right\} - \gamma\hat{\rho}^{(1)}$$

$$\frac{\partial \rho^{(1)}_{i,f}}{\partial t} = -\frac{i}{\hbar}\left\{\underbrace{\langle\Psi_i|[\hat{H}_o, \hat{\rho}^{(1)}]|\Psi_f\rangle}_{1} + \underbrace{\langle\Psi_i|[\hat{V}, \hat{\rho}^{(0)}]|\Psi_f\rangle}_{2} + \right\} - \gamma\rho^{(1)}_{i,f}$$

$$
\begin{aligned}
1: \langle\Psi_i|[\hat{H}_o, \hat{\rho}^{(1)}]|\Psi_f\rangle &= E_i \langle\Psi_i|\hat{\rho}^{(1)}|\Psi_f\rangle - \langle\Psi_i|\hat{\rho}^{(1)}|\Psi_f\rangle E_f = (E_i - E_f)\ \rho_{i,f}^{(1)} \\
2: \ \langle\Psi_i|[\hat{V}, \hat{\rho}^{(0)}]|\Psi_f\rangle &= \langle\Psi_i|\hat{V}\hat{\rho}^{(0)}|\Psi_f\rangle - \langle\Psi_i|\hat{\rho}^{(0)}\hat{V}|\Psi_f\rangle \\
&= \langle\Psi_f|\hat{V} \quad \sum_k |k\rangle \underbrace{\langle k|\hat{\rho}^{(0)}|\Psi_f\rangle}_{f_{\mathrm{FD}}(E_k)\delta_{k,f}} - \langle\Psi_i|\hat{\rho}^{(0)} \sum_k |k\rangle \underbrace{\langle k|\hat{V}|\Psi_f\rangle}_{V_{k,f}} \\
&= \sum_k \left[V_{i,k} f_{\mathrm{FD}}(E_k)\delta_{k,f} - f_{\mathrm{FD}}(E_i)\delta_{i,k}V_{k,f}\right] \\
&= V_{i,f}\left(f_{\mathrm{FD}}(E_f) - f_{\mathrm{FD}}(E_i)\right)
\end{aligned}
$$

Thus

$$
\begin{aligned}
\frac{\partial \rho_{i,f}^{(1)}}{\partial t} &= -\frac{i}{\hbar}\underbrace{(E_i - E_f)}_{\hbar\omega_{i,f}}\rho_{i,f}^{(1)} - \frac{i}{\hbar}\left(f_{\mathrm{FD}}(E_f) - f_{\mathrm{FD}}(E_i)\right)V_{i,f} - \gamma\rho_{i,f}^{(1)} \\
&= -(i\omega_{if} + \gamma)\rho_{i,f}^{(1)} - \frac{i}{\hbar}\left(f_{\mathrm{FD}}(E_f) - f_{\mathrm{FD}}(E_i)\right)V_{i,f} \\
&= -i\tilde{\omega}_{i,f}\rho_{i,f}^{(1)} - \frac{i}{\hbar}\left(f_{\mathrm{FD}}(E_f) - f_{\mathrm{FD}}(E_i)\right)V_{i,f}
\end{aligned}
$$

Where $\tilde{\omega}_{i,f} = \omega_{i,f} - i\gamma$

B.1.2 Differential Equation

We have to solve the following equation :

$$
\frac{\partial \rho_{i,f}^{(1)}}{\partial t} = -\frac{i}{\hbar}(E_i - E_f - i\gamma\hbar)\rho_{i,f}^{(1)} - \frac{i}{\hbar}\left(f_{\mathrm{FD}}(E_f) - f_{\mathrm{FD}}(E_i)\right)ez_{i,f}E_0e^{-i\omega t}
$$

It is a first order differential equation on $\rho_{if}^{(1)}$. It has the following form : $\frac{\partial f}{\partial t} = af + b\mathcal{J}(t)$, $\mathcal{J}(t) = \tilde{\mathcal{J}}e^{-i\omega t}$, with the corresponding coefficients :

$a = -\frac{i}{\hbar}(E_i - E_f - i\gamma\hbar) = -i\tilde{\omega}_{i,f}$

$b = -\frac{ie}{\hbar}\left(f_{\mathrm{FD}}(E_f) - f_{\mathrm{FD}}(E_i)\right)z_{i,f}$

$\mathcal{J}(t) = E_0e^{-i\omega t}$

Such equations have a solution with the form $f(t) = be^{at}\int_{t_0}^{t} d\tau e^{-a\tau}\mathcal{J}(\tau)$ under the hyopthesis that $\mathcal{J}(t \to -\infty) = 0$. This hypothesis corresponds to an adiabatic start of the perturbation, which means that it is null at the beginning $t \to -\infty$. It is then possible to express $\rho_{i,f}^{(1)}(t)$ as :

$$
\rho_{i,f}^{(1)}(t) = -\frac{ie}{\hbar}\left(f_{\mathrm{FD}}(E_f) - f_{\mathrm{FD}}(E_i)\right)z_{i,f}e^{-i\tilde{\omega}_{i,f}t}\underbrace{\int_{t_0}^{t} d\tau e^{i\tilde{\omega}_{i,f}\tau}E_0e^{-i\omega_{i,f}\tau}}_{(*)}
$$

$$(*) : \int_{t_0}^{t} d\tau e^{i\tilde{\omega}_{nm}\tau} E_0 e^{-i\omega_{i,f}\tau} = E_0 \frac{e^{i(\tilde{\omega}_{i,f}-\omega)\tau}}{i(\tilde{\omega}_{i,f}-\omega)}\Big|_{t_0\to-\infty}^{t} = -\frac{E_0}{i(\tilde{\omega}_{i,f}-\omega)} e^{i(\tilde{\omega}_{i,f}-\omega)t}$$

$$\rho_{i,f}^{(1)}(t) = -\frac{e}{\hbar}\left(f_{\mathrm{FD}}(E_f) - f_{\mathrm{FD}}(E_i)\right)\frac{z_{i,f}}{\tilde{\omega}_{i,f}-\omega} E_0 e^{-i\omega t}$$
$$= eE_z(t)\frac{f_{\mathrm{FD}}(E_i) - f_{\mathrm{FD}}(E_f)}{E_i - E_f - \hbar\omega - i\hbar\gamma}$$

B.2 Matrix Element $z_{n'n}$

We detail the derivation of $z_{n'n}$ for the calculus of equation 2.18. Note that in this expression of $z_{n'n}$, the indices n' and n implicitly account for two triplets of quantum numbers corresponding to the wavefunctions $\psi_{l,m,n}$ and $\psi_{l,m,n'}$.

$z_{n'n}$ is defined as $\int \psi_{l,m,n}(z) \times z \times \psi_{l,m,n'}(z)dz$

Due to the normalization condition on the wavefunctions along the axis $\overrightarrow{e_x}$ and $\overrightarrow{e_y}$, $z_{n'n}$ can be simplified into

$$z_{n'n} = \frac{2}{L}\int_0^L \sin(\frac{n'\pi z}{L}) z \sin(\frac{n\pi z}{L})\mathrm{dz}$$

We have :

$$\int_0^L \sin(az)z\sin(bz)\mathrm{dz} = \frac{1}{2}\left[\frac{\cos(x(a-b))}{(a-b)^2} - \frac{\cos(x(a+b))}{(a+b)^2} + \frac{x\sin(x(a-b))}{a-b} - \frac{x\sin(x(a+b))}{a+b}\right]_0^L$$

We define :

$$B_{n'n} = \int_0^L \sin(\frac{\pi n'}{L}z) z \sin(\frac{\pi n}{L}z)\mathrm{dz}$$

$$\begin{aligned} B_{n'n} =& \frac{1}{2\pi}\left[\frac{L^2}{\pi(n'-n)^2}\cos x\frac{\pi(n'-n)}{L} - \frac{L^2}{\pi(n'+n)^2}\cos x\frac{\pi(n'+n)}{L}\right]_0^L \\ &+ \frac{1}{2\pi}\left[\frac{Lx}{(n'-n)}\sin x\frac{\pi(n'-n)}{L} - \frac{Lx}{(n'+n)}\sin x\frac{\pi(n'+n)}{L}{}_0^L\right]_0^L \\ =& \frac{L^2}{2\pi^2}\Big[\underbrace{(\cos(\pi(n'-n))-1)}_{a}\frac{1}{(n'-n)^2} + \underbrace{(1-\cos(\pi(n'+n))}_{b})\frac{1}{(n'+n)^2}\Big] \end{aligned}$$

1. n' and n ***are both even***, $n'+n = 2p$, $n'-n = 2p'\pi$ with $(p,p') \in \mathbb{Z}^2$:

$$a = \cos(2p\pi) - 1 = 0 \qquad b = 1 - \cos(2p'\pi) = 0$$

$\Rightarrow \mathcal{B} = 0.$

2. n' and n ***are both odd***, $n'+n = 2p$, $n'-n = 2p'\pi$ with $(p,p') \in \mathbb{Z}^2$:

$$a = \cos(2p\pi) - 1 = 0 \qquad b = 1 - \cos(2p'\pi) = 0$$

$\Rightarrow \mathcal{B} = 0.$

3. n' and n have different parities, $n'+n=2p+1$, $n'-n=2p+1$ with $(p,p')\in\mathbb{Z}^2$:

$$a=\cos(2p\pi+\pi)-1=\cos(\pi)-1=-2 \quad b=1-\cos(2p'\pi+\pi)=1-\cos(\pi)=2$$

$$\Rightarrow \mathcal{B}=\frac{L^2}{2\pi^2}\left[-\frac{2}{(n'-n)^2}+\frac{2}{(n'+n)^2}\right]$$

This leads to :

$$z_{n'n}=\begin{cases} 0 & \text{if } n \text{ and } n' \text{ have the same parity} \\ \frac{2L}{\pi^2}\left[\frac{1}{(n'+n)^2}-\frac{1}{(n'-n)^2}\right] & \text{otherwise} \end{cases}$$

We can see that the selection rules naturally appear from the derivation of the matrix element. The electric field is polarized along the $\overrightarrow{e_z}$ axis, the wavefunctions of the initial and the final states can not be different along the $\overrightarrow{e_x}$ and $\overrightarrow{e_y}$ directions. The electric field can only address transitions between states that have different parities.

Appendix C

Second order non-linearities

C.1 Derivation of the 2nd-order current density $\boldsymbol{j}^{(2)}$

We detail the derivation of the 2nd-order current density $\boldsymbol{j}^{(2)}$ for our experimental configuration.

The general form of $\boldsymbol{j}^{(2)}$ can be expressed using the Einstein notation :

$$j_\lambda^{(2)}(\boldsymbol{q}) = \sigma_{\lambda\nu\eta}^{(2)}(\boldsymbol{q}) E_\nu(\boldsymbol{q},\omega) E_\eta^*(\boldsymbol{q},\omega)$$

Where the subscripts correspond to the coordinate components of each physical quantity in the sample (XYZ) frame. It is possible to develop the previous expression, which leads to :

$$\begin{aligned} j_\lambda^{(2)}(\boldsymbol{q}) =& \sigma_{\lambda XX}^{(2)}(\boldsymbol{q}) E_X(\boldsymbol{q},\omega) E_X^*(\boldsymbol{q},\omega) + \sigma_{\lambda XY}^{(2)}(\boldsymbol{q}) E_X(\boldsymbol{q},\omega) E_Y^*(\boldsymbol{q},\omega) + \sigma_{\lambda XZ}^{(2)}(\boldsymbol{q}) E_X(\boldsymbol{q},\omega) E_Z^*(\boldsymbol{q},\omega) \\ & \sigma_{\lambda YX}^{(2)}(\boldsymbol{q}) E_Y(\boldsymbol{q},\omega) E_X^*(\boldsymbol{q},\omega) + \sigma_{\lambda YY}^{(2)}(\boldsymbol{q}) E_Y(\boldsymbol{q},\omega) E_Y^*(\boldsymbol{q},\omega) + \sigma_{\lambda YZ}^{(2)}(\boldsymbol{q}) E_Y(\boldsymbol{q},\omega) E_Z^*(\boldsymbol{q},\omega) \\ & \sigma_{\lambda ZX}^{(2)}(\boldsymbol{q}) E_Z(\boldsymbol{q},\omega) E_X^*(\boldsymbol{q},\omega) + \sigma_{\lambda ZY}^{(2)}(\boldsymbol{q}) E_Z(\boldsymbol{q},\omega) E_Y^*(\boldsymbol{q},\omega) + \sigma_{\lambda ZZ}^{(2)}(\boldsymbol{q}) E_Z(\boldsymbol{q},\omega) E_Z^*(\boldsymbol{q},\omega) \end{aligned}$$

or

$$\begin{aligned} j_\lambda^{(2)}(\boldsymbol{q}) =& \sigma_{\lambda XX}^{(2)}(\boldsymbol{q}) |E_X(\boldsymbol{q},\omega)|^2 + \sigma_{\lambda YY}^{(2)}(\boldsymbol{q}) |E_Y(\boldsymbol{q},\omega)|^2 + \sigma_{\lambda ZZ}^{(2)}(\boldsymbol{q}) |E_Z(\boldsymbol{q},\omega)|^2 \\ & + \sigma_{\lambda XY}^{(2)}(\boldsymbol{q}) E_X(\boldsymbol{q},\omega) E_Y^*(\boldsymbol{q},\omega) + \sigma_{\lambda XZ}^{(2)}(\boldsymbol{q}) E_X(\boldsymbol{q},\omega) E_Z^*(\boldsymbol{q},\omega) \\ & \sigma_{\lambda YX}^{(2)}(\boldsymbol{q}) E_Y(\boldsymbol{q},\omega) E_X^*(\boldsymbol{q},\omega) + \sigma_{\lambda YZ}^{(2)}(\boldsymbol{q}) E_Y(\boldsymbol{q},\omega) E_Z^*(\boldsymbol{q},\omega) \\ & \sigma_{\lambda ZX}^{(2)}(\boldsymbol{q}) E_Z(\boldsymbol{q},\omega) E_X^*(\boldsymbol{q},\omega) + \sigma_{\lambda ZY}^{(2)}(\boldsymbol{q}) E_Z(\boldsymbol{q},\omega) E_Y^*(\boldsymbol{q},\omega) \end{aligned}$$

In the (XYZ) frame, the electric vector of the optical pulses is given by :

$$\boldsymbol{E} = E_0 \left(\cos\alpha \cos\theta \boldsymbol{X} - \sin\alpha \boldsymbol{Y} + \cos\alpha \sin\theta \boldsymbol{Z} \right)$$

Then, the second-order nonlinear current density writes :

$$\begin{aligned} j_\lambda^{(2)}(\boldsymbol{q}) =& E_0^2(\sigma_{\lambda XX}^{(2)}(\boldsymbol{q})\,(\cos\alpha\cos\theta)^2 - \sigma_{\lambda XY}^{(2)}(\boldsymbol{q})\cos\theta\cos\alpha\sin\alpha + \sigma_{\lambda XZ}^{(2)}(\boldsymbol{q})\cos\theta\sin\theta\cos^2\alpha \\ & - \sigma_{\lambda YX}^{(2)}(\boldsymbol{q})\cos\theta\cos\alpha\sin\alpha + \sigma_{\lambda YY}^{(2)}(\boldsymbol{q})\sin^2\alpha - \sigma_{\lambda YZ}^{(2)}(\boldsymbol{q})\sin\theta\cos\alpha\sin\alpha \\ & + \sigma_{\lambda ZX}^{(2)}(\boldsymbol{q})\cos\theta\sin\theta\cos^2\alpha - \sigma_{\lambda ZY}^{(2)}(\boldsymbol{q})\sin\theta\cos\alpha\sin\alpha + \sigma_{\lambda ZZ}^{(2)}(\boldsymbol{q})\,(\sin\theta\cos\alpha)^2) \end{aligned}$$

It is possible to group the different terms according to their dependences on polarization angle α :

$$\begin{aligned} j_\lambda^{(2)}(\boldsymbol{q}) = E_0^2[\,&\cos^2\alpha\;(\sigma_{\lambda XX}^{(2)}(\boldsymbol{q})\cos^2\theta + (\sigma_{\lambda XZ}^{(2)}(\boldsymbol{q}) + \sigma_{\lambda ZX}^{(2)}(\boldsymbol{q}))\cos\theta\sin\theta + \sigma_{\lambda ZZ}^{(2)}(\boldsymbol{q})\sin^2\theta) \\ & + \sin^2\alpha\sigma_{\lambda YY}^{(2)}(\boldsymbol{q}) \\ & - \cos\alpha\sin\alpha((\sigma_{\lambda XY}^{(2)}(\boldsymbol{q}) + \sigma_{\lambda YX}^{(2)}(\boldsymbol{q}))\cos\theta + (\sigma_{\lambda YZ}^{(2)}(\boldsymbol{q}) + \sigma_{\lambda ZY}^{(2)}(\boldsymbol{q}))\sin\theta)] \end{aligned}$$

Since the incident optical pulses are linearly polarized, we have $\boldsymbol{E}^* = \boldsymbol{E}$, and thus the 2nd-order conductivity tensor $\sigma_{\lambda\nu\eta}^{(2)}(\boldsymbol{q})$ is symmetrical with respect to the two last indices. Using the trigonometric identities $\cos^2\alpha = \frac{1}{2}(1+\cos 2\alpha)$, $\sin^2\alpha = \frac{1}{2}(1-\cos 2\alpha)$ and $\cos\alpha\sin\alpha = \frac{1}{2}\sin 2\alpha$, the expression of $j_\lambda^{(2)}(\boldsymbol{q})$ can be rewritten as :

$$\begin{aligned} j_\lambda^{(2)}(\boldsymbol{q}) = \frac{E_0^2}{2}([&\sigma_{\lambda XX}^{(2)}(\boldsymbol{q})\cos^2\theta + \sigma_{\lambda ZZ}^{(2)}(\boldsymbol{q})\sin^2\theta + \sigma_{\lambda YY}^{(2)}(\boldsymbol{q}) + \sigma_{\lambda XZ}^{(2)}(\boldsymbol{q})\sin 2\theta] \\ & + \cos 2\alpha[\sigma_{\lambda XX}^{(2)}(\boldsymbol{q})\cos^2\theta + \sigma_{\lambda ZZ}^{(2)}(\boldsymbol{q})\sin^2\theta - \sigma_{\lambda YY}^{(2)}(\boldsymbol{q}) + \sigma_{\lambda XZ}^{(2)}(\boldsymbol{q})\sin 2\theta] \\ & - \sin 2\alpha[2\sigma_{\lambda XY}^{(2)}(\boldsymbol{q})\cos\theta + 2\sigma_{\lambda YZ}^{(2)}(\boldsymbol{q})\sin\theta]) \end{aligned}$$

Thus, the second-order current density is reduced to :

$$j_\lambda^{(2)}(\boldsymbol{q}) = j_{\lambda 0} + j_{\lambda C}\cos 2\alpha + j_{\lambda S}\sin 2\alpha$$

with :

$$j_{\lambda 0} = \frac{E_0^2}{2}\left[\sigma_{\lambda XX}^{(2)}(\boldsymbol{q})\cos^2\theta + \sigma_{\lambda ZZ}^{(2)}(\boldsymbol{q})\sin^2\theta + \sigma_{\lambda YY}^{(2)}(\boldsymbol{q}) + \sigma_{\lambda XZ}^{(2)}(\boldsymbol{q})\sin 2\theta\right]$$

$$j_{\lambda C} = \frac{E_0^2}{2}\left[\sigma_{\lambda XX}^{(2)}(\boldsymbol{q})\cos^2\theta + \sigma_{\lambda ZZ}^{(2)}(\boldsymbol{q})\sin^2\theta - \sigma_{\lambda YY}^{(2)}(\boldsymbol{q}) + \sigma_{\lambda XZ}^{(2)}(\boldsymbol{q})\sin 2\theta\right]$$

$$j_{\lambda S} = -\frac{E_0^2}{2}\left[2\sigma_{\lambda XY}^{(2)}(\boldsymbol{q})\cos\theta + 2\sigma_{\lambda YZ}^{(2)}(\boldsymbol{q})\sin\theta\right]$$

C.2 Photon-Drag Effect contribution to the second-order non linear current density components

For p-polarized optical pulses, the photon-drag effect contribution to the nonlinear photocurrent density is simplified into the form :

$$j_{\lambda}^{(2)PD}(\boldsymbol{q}) = E_0^2 \left[T_{\lambda\mu XX} q_\mu \cos^2\theta + T_{\lambda\mu ZZ} q_\mu \sin^2\theta + T_{\lambda\mu XZ} q_\mu \sin 2\theta \right] \tag{C.1}$$

Since the optical pulses propagate in the (XZ) plane, the wave vector $\boldsymbol{q}$ is expressed in the sample coordinate frame as :

$$\boldsymbol{q} = q_0 \left(\sin\theta, 0, -\cos\theta\right)$$

Symmetry considerations on the system leads to the following non-vanishing terms :

$$T_{XXXX} = T_{XXYY}$$
$$T_{XXZZ}$$
$$T_{XZXZ} = T_{XZZX} = T_{YZZY} = T_{YZYZ}$$
$$T_{ZZXX} = T_{ZZYY}$$
$$T_{ZXXZ} = T_{ZXZX}$$
$$T_{ZZZZ}$$
$$T_{YXYX} = T_{YXXY}$$

It is then possible to derivate the three components of $j_{\lambda}^{(2)PD}(\boldsymbol{q})$:

$$j_{X}^{(2)PD}(\boldsymbol{q}) = E_0^2(\omega) q_0 \left[T_{XXXX} \sin\theta\cos^2\theta + T_{XXZZ} \sin^3\theta - T_{XZXZ} \cos\theta \sin 2\theta \right]$$

Using the trigonometric identity cos(θ)sin(2θ) = cos(θ)2cos(θ)sin(θ) = 2cos^2(θ)sin(θ) = 2sin(θ) - 2sin^3(θ), we can write :

$$j_{X}^{(2)PD}(\boldsymbol{q}) = E_0^2(\omega) q_0 \left[(T_{XXZZ} + 2T_{XZXZ} - T_{XXXX}) \sin^3\theta + (T_{XXXX} - 2T_{XZXZ}) \sin\theta \right]$$

We proceed in the same way to express the components of $j_{\lambda}^{(2)PD}(\boldsymbol{q})$ along the Z axis :

$$j_{Z}^{(2)PD}(\boldsymbol{q}) = E_0^2(\omega) q_0 \left[T_{ZXXZ} \sin\theta \sin 2\theta - T_{ZZXX} \cos^3\theta - T_{ZZZZ} \sin^2\theta \cos\theta \right]$$

Which can also be simplified using sin(θ)sin(2θ) = sin(θ)2cos(θ)sin(θ) = 2sin^2(θ)cos(θ) = 2cos(θ) - 2cos^3(θ) :

$$j_{Z}^{(2)PD}(\boldsymbol{q}) = E_0^2(\omega) q_0 \left[(T_{ZZZZ} - T_{ZZXX} - 2T_{ZXZX}) \cos^3\theta + (2T_{ZXXZ} - T_{ZZZZ}) \cos\theta \right]$$

Finally, one can note that

$$j_{Y}^{(2)PD}(\boldsymbol{q}) = 0$$